Modelling and Optimisation of Ultra-wideband Optical Fibre Communication Systems

A thesis submitted to University College London (UCL) for the partial fulfilment of the requirements for the degree of Doctor of Philosophy (PhD)

by

Henrique Buglia

Optical Networks Group
Department of Electronic and Electrical Engineering
UCL

12th January 2025

Declaration

I, Henrique Buglia, confirm that the work presented in this thesis is my own. Where information has been derived from other sources, I confirm that this has been indicated in the thesis.

Abstract

Physical layer modelling has been an important topic for optical fibre communication systems. The possibility of correctly estimating the different noise sources in these systems has enabled to supply the worldwide demand for data traffic using the currently deployed network. This thesis describes notable advances in modelling these systems, complying with new technologies currently commercially available in the optical fibre industry. Novel nonlinear models are proposed to accurately cope with different amplifiers, fibres, transmitter and receiver technologies, especially in the context of next-generation ultra-wideband (UWB) systems, where signal transmission is performed using bandwidths exceeding the conventional 5 THz window.

These new models predict the amplified spontaneous emission (ASE) noise and the nonlinear distortions arising from the Kerr effect with low-computational complexity due to its semi-analytical formulation. Notably, this thesis presents the first UWB real-time semi-analytical model enabling performance estimation for ultra-low-loss fibres, links with arbitrary span length, and links composed of hybrid amplifiers, i.e., the utilisation of Raman together with rare-earth doped fibre amplifiers. These real-time models are obtained with the utilisation of closed-form expressions, and among its several possible utilisations, are used in this thesis to fasten optimisation algorithms, which enable transmission system designs tailored to suppliers' requirements; point-to-point and network-throughput maximisation through system parameter optimisation, such as launch power, pump power, and/or pump wavelength allocation; and experiment designs tailored with experimental constraints.

Experimental validations of these new closed-form models are presented, enabling to verify and confirm its accuracy in field-deployed systems. Optimisation of optical networks and topology designs using these models are also proposed. Furthermore, a theoretical investigation of the impact of transceiver (TRX) noise on the performance of transmission systems shows that sub-optimal solutions are close to optimum ones, with negligible error, for systems limited by this source of noise.

Impact statement

Internet applications and services have become an inherent part of modern society. These services are possible due to the global telecommunication infrastructure, underpinned by optical fibre networks, responsible for carrying 99 % of worldwide internet data traffic. Internet-device throughputs are forecast to continue to grow exponentially, driven by internet services including high-definition video streaming, cloud computing, artificial intelligence, Big Data and the Internet of Things. This urgently needs new advances in optical data transmission technologies to enable ultra-high throughput with minimal latencies, coping with data traffic demands.

Although silica-based optical fibres enable the possibility of transmitting large amounts of data given their higher bandwidth, the Kerr nonlinearity imposes fundamental physical limitations, setting an upper bound in the achievable information rates. There are two main possibilities to deal with this limitation and increase the total fibre throughput per individual fibre core. The first one is to increase the transmission bandwidth, achieved by transmitting multiple channels, modulated at different frequencies, known as UWB transmission. The second way is to improve the signal-to-noise ratio (SNR), achieved through improved detection schemes, advanced digital signal processing (DSP) techniques, and new amplifier, fibre and TRX technologies.

This thesis proposes new analytical models for UWB signal transmission able for the first time to predict the nonlinear signal distortion in links utilising any amplification technologies (such as Raman and/or lumped amplifiers) and fibres with arbitrary characteristics (such as arbitrary loss and span length). These new analytical models are obtained from the Gaussian noise (GN) and the Enhanced Gaussian noise (EGN) models, widely used to predict the transmission system performance in optical fibre cables. The GN and EGN models are integral models requiring high computational time and power, scaling in complexity with the transmission system bandwidth. The analytical models proposed in this thesis enable real-time system performance prediction, as integral expressions are replaced with approximate closed-form solutions. In the network, this feature enables an online assessment of the data rates, modulation formats, the number of channels, launch power profile, Raman

pump powers and wavelengths, given the fibre, the amplifier characteristics, allocated lightpaths, etc.

The new analytical models proposed in this thesis are tested in a wide range of scenarios and validated against UWB transmission experiments. The closed-form models are used to develop optimisation algorithms for launch power optimisation in lumped-amplified and hybrid-amplified links; Raman and lumped amplifier optimisation and design by finding the best pump allocation, i.e., the number of pumps, their power and wavelength, and their direction (forward (FW) and/or backward (BW)); optimisation of optical networks and topology designs. Another contribution of this thesis is an assessment of how the TRX impairments impact the total system performance. It is shown that for systems limited by this kind of noise (e.g. short-distance systems), launch power optimisation does not change the system performance, and spectrally uniform launch power profiles can maximise the total system throughput.

The results obtained in this thesis led to the publication of 23 papers, of which 7 journals. The analytical model accounting for Raman amplification (RA) described in this thesis led to a record throughput for unrepeated transmission links (see [P18]). The research led to an emerging scholar award given by the Pacific Telecommunications Council (PTC) recognising the top 6 PhD students in the world in the realm of information and communications technology. It also led to an IEEE Photonics Society award, given to the top 10 PhD students in the world. In addition, the research led to the 2023 Optical Fiber Communication Conference (OFC) best-poster award among 8 selected posters.

Acknowledgements

I am incredibly thankful to my supervisor Professor Polina Bayvel and my former supervisor Dr Lidia Galdino. I extend my thanks to Professor Robert Killey.

I gratefully acknowledge Microsoft Research and the Engineering and Physical Sciences Research Council (EPSRC) for generously funding this PhD research.

I want to thank the following past and present members of Optical Networks Group, Dr Eric Sillekens, Dr Daniel Semrau, Mindaugas Jarmolovičius, Dr Jiaqian Yang, Robin Matzner, Dr Anastasiia Vasylchenkova, Dr Callum Deakin, Dr Ronit Sohanpal, Dr Filipe Ferreira, Dr Hubert Dziecol, and Romulo Aparecido.

I also want to thank Professor Renato Lopes and Professor Darli Mello from the University of Campinas (UNICAMP).

I am deeply indebted to my parents, Fabio Buglia and Denise Vilela, and my brother Daniel Buglia.

Table of contents

List of figures

List of tables

List of terms and abbreviations

ADC analog-to-digital converter 32

AIR achievable information rate 28, 63, 65, 81, 132

ANN artificial neural network 124

AOM acousto-optic modulator 117, 119

ASE amplified spontaneous emission . 3, 32, 37, 39, 47, 75–79, 106, 115, 117–120, 128, 129, 131, 144, 147, 149–151, 155, 156, 158, 162, 168, 181

AT altered topology 169–171, 174

AWGN additive white Gaussian noise . 28, 33, 47, 48, 65, 75, 79–81, 125, 128, 137, 149

BDFA bismuth-doped fibre amplifier 30, 31, 99

BSF band-stop filter 128

BW backward 5, 31, 37, 39, 62, 70, 74, 76, 78, 99–103, 105–107, 109, 111, 112, 114–117, 120, 121, 123, 141–144, 147, 150, 151, 155, 156, 158, 162, 164–166, 175, 178, 179, 206

COI channel of interest 57, 59, 60, 70, 72, 73, 112, 179, 180, 201, 206, 211

CPU central processing unit 95, 115, 158

CW continuous-wave 59, 61

DAC digital-to-analogue converter 128, 175

DBP digital back propagation 81

DGE dynamic gain equaliser 128

ITU International Telecommunication Union 28

ITU-D ITU Telecommunication Development Sector 28

ITU-T ITU Telecommunication Standardization Sector . . . 55, 105, 109, 114, 148

JLT Journal of Lightwave Technology 98, 101, 123, 147

JOCN Journal of Optical Communications and Networking 123, 125

LA lumped amplification 33, 34, 74, 78, 101, 103, 105, 114, 119, 142, 143, 147, 148, 151, 155, 156, 158, 162, 164, 168, 177, 178, 181

LO local oscillator 128, 133

MB Maxwell-Boltzmann 80

MI mutual information 79–81

NF noise figure . 75, 76, 118, 120, 127–129, 131, 133, 134, 142, 148, 166, 168, 171, 181

NLI nonlinear interference 30, 32, 39, 47, 65–74, 78, 79, 83–85, 89, 90, 92, 95, 98, 99, 101, 102, 106, 108, 109, 111–113, 115, 117, 118, 120, 121, 124, 128, 129, 131, 140, 144, 147, 148, 150, 151, 155, 156, 158, 160, 162, 168, 178, 179, 200

NLSE nonlinear Schrödinger equation 32–34, 48, 50–52, 64–66, 68, 124

OFC Optical Fiber Communication Conference 5, 100, 123, 164

ONDM International Conference on Optical Network Design and Modelling 123, 125

OSA optical spectrum analyser 128

PhD Doctor of Philosophy 1, 5, 45, 55, 64, 74

PMD polarisation-mode dispersion 52

PS polarisation scrambler 117, 119

PSD power spectral density 66–70, 78, 85

PSO particle swarm optimisation . . 37, 124–126, 141–144, 149–151, 166, 175, 178

QAM quadrature amplitude modulation 37, 67, 73, 80, 81, 91, 92, 94, 100, 112, 114, 115, 117, 121, 127–129, 132, 133

QoT Quality of Transmission 36, 124, 134, 136–138, 141, 174, 175, 177, 178

QPSK quadrature phase shift keying 67, 73

RA Raman amplification 5, 11, 31, 33, 34, 37, 38, 56, 58, 61–63, 68–70, 74–78, 99–103, 105, 106, 109, 111–115, 120, 121, 142, 147, 149–151, 155, 156, 158, 162, 164, 166, 168, 174, 177, 181, 205, 206, 209

RIN relative intensity noise 76, 79

RP regular perturbation 65–67, 101

Rx receiver 31, 32, 45, 46, 70, 105, 115, 117, 128, 133

SDM space division multiplexing 29, 32, 36, 169–171, 174, 176, 179

SMF single-mode fibre 29, 38, 39, 53, 55–57, 60, 70, 71, 91, 117, 121, 128, 134, 148, 175, 177, 180

SNR signal-to-noise ratio 4, 28, 32, 33, 36, 38–40, 75, 78–81, 85, 89, 90, 92, 98, 106, 109, 111, 112, 115, 117, 118, 120–122, 124–128, 130–134, 136–138, 140–142, 144, 147, 149, 156, 158, 160, 162, 168, 170, 171, 174, 175, 177–179

SOA semiconductor optical amplifier 30, 31, 74, 99, 133

SPM self-phase modulation 57, 71–74, 85, 87–90, 95, 108, 179, 180, 200, 203, 204, 209, 213–215

SS spectrally shaped 128

SSFM split-step Fourier method . 32, 36, 37, 39, 52, 63, 64, 84, 91, 94–96, 98, 100, 109–112, 115, 116

TDFA thulium-doped fibre amplifier 30, 31, 74, 75, 99, 116, 117, 120, 121, 129, 133, 171, 175, 178, 181

TRX transceiver 3–5, 28, 30–34, 36, 38, 39, 46, 78, 79, 116, 118, 123–128, 130, 131, 133, 134, 136–138, 142, 147, 174, 175, 178, 180

Tx transmitter 31, 45, 46, 51, 66, 80, 128, 133

UCL University College London 1, 39

ULL ultra-low-loss 31–33, 53, 84, 91, 97, 98, 177

UWB ultra-wideband 3–5, 28, 30–40, 45, 57, 63, 68, 69, 74, 79, 83, 84, 98, 101, 120, 121, 123, 124, 126, 141, 164, 169–171, 174, 176–179, 181

VOA variable optical attenuator 117, 119

WDM wavelength division multiplexing 28, 33, 39, 40, 56, 60, 61, 68, 70, 71, 76, 77, 81, 85, 91, 102, 105, 109, 111, 114, 117, 118, 121, 124, 128, 133, 134, 143, 148, 150, 165, 168, 169, 179, 180, 206, 207

WSS wavelength selective switch 117–119, 171

XPM cross-phase modulation . 57, 71–74, 85, 87–90, 95, 108, 111, 150, 179, 180, 200–202, 209, 211, 212

List of symbols

t	time	s
f	frequency	s^{-1}
C	capacity	
S	number of spatial channels	
B	channel bandwidth	s^{-1}
ISD	information spectral density	bit
SNR	signal-to-noise ratio	
$x(t)$	continuous-time transmitted signal	Vm^{-1}
$y(t)$	continuous-time received signal	Vm^{-1}
d	transmitted data symbols	
d'	received data symbols	
$f(\cdot)$	nonlinear unitary function	
$q(\cdot)$	nonlinear unitary function	
$w(t)$	continuous-time noise signal generated in the span j	$V\mathrm{m}^{-1}$
β_2	second-order GVD parameter	$\mathrm{s}^2\mathrm{m}^{-1}$
β_3	third-order GVD parameter (slope)	$\mathrm{s}^3\mathrm{m}^{-1}$
β_4	fourth-order GVD parameter	$\mathrm{s}^4\mathrm{m}^{-1}$
z	distance	m^{-1}
T	reference time	s
γ	nonlinear coefficient	$\mathrm{W}^{-1}\mathrm{m}^{-1}$
j	imaginary unit or span index	
α	loss coefficient	Np m^{-1}
α'	loss coefficient	Np m^{-1}
$\tilde{\alpha}$	loss coefficient	Np m^{-1}
α_f	loss coefficient	Np m^{-1}
α_b	loss coefficient	Np m^{-1}
v_g	group velocity	m s^{-1}
T_r	Raman time constant	s
$\mathcal{F}\{\cdot\}$	Fourier transform	
$*$	convolution	
$\int$	integration	
$\frac{\partial}{\partial}$	partial derivative	

$E(\cdot)$	complex electric field	Vm^{-1}
$\overline{\cdot}$	complex conjugate	
$H(\cdot)$	impulse response of a filter	
$P(\cdot)$	power	W
L	fibre span length	m
D	chromatic dispersion parameter	$\mathrm{s\ m}^{-2}$
S	chromatic dispersion slope	$\mathrm{s\ m}^{-3}$
S_0	zero chromatic dispersion slope	$\mathrm{s\ m}^{-3}$
λ	wavelength	m
λ_0	zero-dispersion wavelength	m
λ_{ref}	reference wavelength	m
L_{eff}	effective length	m
$\tilde{L}_{\text{eff}}$	effective length	m
i	channel index	
k	channel index	
p	pump index	
n	number of spans	
$G_{\text{Tx}}(\cdot)$	Transmitted signal PSD	W s
$G_{\text{NLI}}(\cdot)$	NLI PSD	W s
N_{ch}	number of channels	
N_{p}	number of pumps	
$g(\cdot)$	Raman gain spectrum	$\mathrm{m}^{-1}\mathrm{W}^{-1}$
$g'(\cdot)$	generalised loss function	$\mathrm{Np\ m}^{-1}$
A_{eff}	effective core area	m^2
$\hat{D}$	dispersion operator	
$\hat{N}$	nonlinear operator	
h	SSFM step size	m
$\mathcal{O}(\cdot)$	high-order terms	
$\Gamma(\cdot)$	complex propagation constant	m^{-1}
$G(\cdot)$	lumped amplifier gain	
ξ_n	circular, complex Gaussian distributed symbol	
$\phi(\cdot)$	phase mismatch factor	
$\phi_i(\cdot)$	phase mismatch factor	$\mathrm{s}^2\ \mathrm{m}^{-1}$
$\phi_{i,k}(\cdot)$	phase mismatch factor	$\mathrm{s\ m}^{-1}$
$\tilde{\phi}(\cdot)$	phase mismatch factor	s^2
$\rho(\cdot)$	normalised signal power	
$\eta(\cdot)$	nonlinear coefficient	W^{-1}
C_r	Raman gain slope	$\mathrm{s\ W}^{-1}\ \mathrm{m}^{-1}$
C_f	Raman gain slope	$\mathrm{s\ W}^{-1}\ \mathrm{m}^{-1}$

C_b	Raman gain slope	s W^{-1} m^{-1}
ϵ	coherent factor	
Φ	excess kurtosis	
n_{sp}	spontaneous emission factor	
$\mathcal{X}$	photon occupancy factor	
T''	temperature	K
k_B	Boltzmann's constant	J K^{-1}
h	Plank constant	J s
$MI(\cdot)$	mutual information	bit
X	transmitted symbol random variable	
Y	received symbol random variable	
W	noise random variable	
$p_{X,Y}(x,y)$	joint probability distribution of X and Y	
$p_X(x)$	probability distribution of X	
$p_Y(y)$	probability distribution of Y	
$p_{\lambda_{MB}}(x)$	MB probability distribution	
$p_{v_1,v_2}(x)$	an optimised probability distribution	
$\Pi(\cdot)$	rectangular function	
Δ	difference/variation	
$\hat{f}$	average frequency	s^{-1}
P_f	channels total power + FW pumps total power	W
P_b	BW pumps total power	W
$\mathcal{X}(\cdot)$	phased-array term	

Chapter 1

Introduction

The exponential growth in the use of bandwidth-hungry internet services such as high-definition video streaming, cloud computing, artificial intelligence, Big Data and the Internet of Things requires new advances in optical data transmission technologies to achieve ultra-high throughputs and minimal latencies. This applies across all types of networks, from metro, access networks, and inter-data centre links through to wide-area terrestrial and ultra-long haul transoceanic systems. According to the International Telecommunication Union (ITU), under the ITU Telecommunication Development Sector (ITU-D) approximately 5.4 billion people were using the Internet in 2023. This represents 67 % of the world's population, corresponding to an increase of 45 % since 2018, with 1.7 billion people estimated to have come online during that period [1]. Ericsson predicts global mobile data traffic is expected to more than triple between 2023 and 2029 [2]. Over the last decades, optical fibre communications have driven this remarkable growth in data traffic through wavelength division multiplexing (WDM), improved fibre design and fabrication, optical amplification, coherent detection and digital signal processing (DSP), emerging as the key technology that supports the global information infrastructure. These systems are essential due to their ability to transmit data at ultra-high speeds with minimal loss over long distances, making them the foundation of today's digital infrastructure.

To achieve these high data rates, all the signalling dimensions, including bandwidth, information spectral density (ISD) and space, must be explored. The achievable information rate (AIR), or capacity, of a communications link is given by $C = S \cdot B \cdot \text{ISD}$, where B is the channel bandwidth, S is the number of spatial channels (included in this are the multiplexed spatial modes in each core), and the ISD is given per spatial channel. For additive white Gaussian noise (AWGN) channels, the ISD can be calculated analytically and the capacity is given by the well-known Shannon-Hartley formula: $C = S \cdot B \cdot \log_2(1 + \text{SNR})$, serving as a bound for the optical fibre channel. Advanced DSP techniques, new fibre technologies, low-noise transceivers (TRXs) and amplifiers achieve increased ISD values through SNR improvements. In contrast, ultra-wideband (UWB) transmission, enabled by WDM, aims to increase the $S \cdot B$ product. This requires extending channel bandwidth beyond

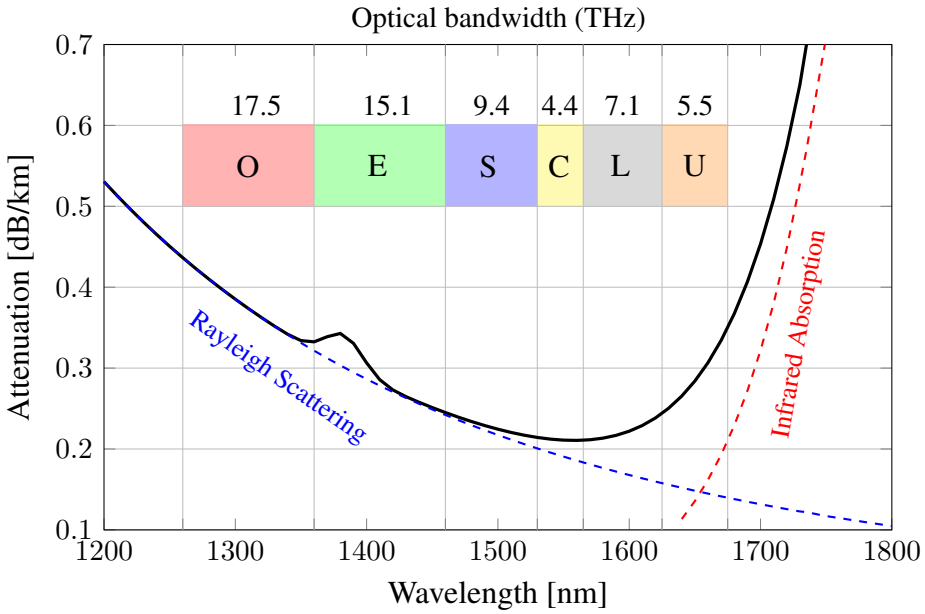

Fig. 1.1: Typical fibre attenuation spectrum for a low-water peak standard single-mode silica fibre and corresponding transmission bands from O- to U-band.

that of the well-established erbium-doped fibre amplifier (EDFA) in currently installed fibre links. This can be combined with space division multiplexing (SDM), based on multiple fibres (currently installed) or new multi-core/multi-mode fibres, making possible link capacities of tens of petabits per second.

The bandwidth of an optical fibre is defined by the low-attenuation window of silica, which is the range of wavelengths where the fibre has minimal attenuation and can transmit signals efficiently. This window generally ranges across the O-U band namely respectively the original (O), extended (E), short (S), conventional (C), long (L), and ultra-long (U) bands, as shown in Fig. 1.1; this corresponds to almost 60 THz available bandwidth. However, the majority of current systems operate over a relatively narrow bandwidth, limited to 11.5 THz within the C and L bands, corresponding to less than 20 % of the total available bandwidth. Experimental field trials have been exploring the utilisation of higher bands and alternative amplification technologies as enabling strategies to satisfy data traffic demands.

The current experimental record throughputs over single-mode fibre (SMF) are 74.38 Tb/s over 6300 km [20] and more recently, 46 Tb/s over 10072 km [14], using bandwidths of 11.1 THz, and 13.8 THz, respectively. The records throughput for medium haul (>100 km) currently stand at 264.7 Tb/s, using 27 THz signal bandwidth [5], and 110.7 Tb/s using 18.3 THz signal bandwidth [9], demonstrated experimentally over 200 km, and 1040 km, respectively. For short-distance links, the record throughput was achieved using O-, E-, S-, C-, L- and U-bands (37.6 THz) to reach 378 Tb/s [3], and E-, S-, C-, and L-bands (27.8 THz) to reach 301 Tb/s [4], both over

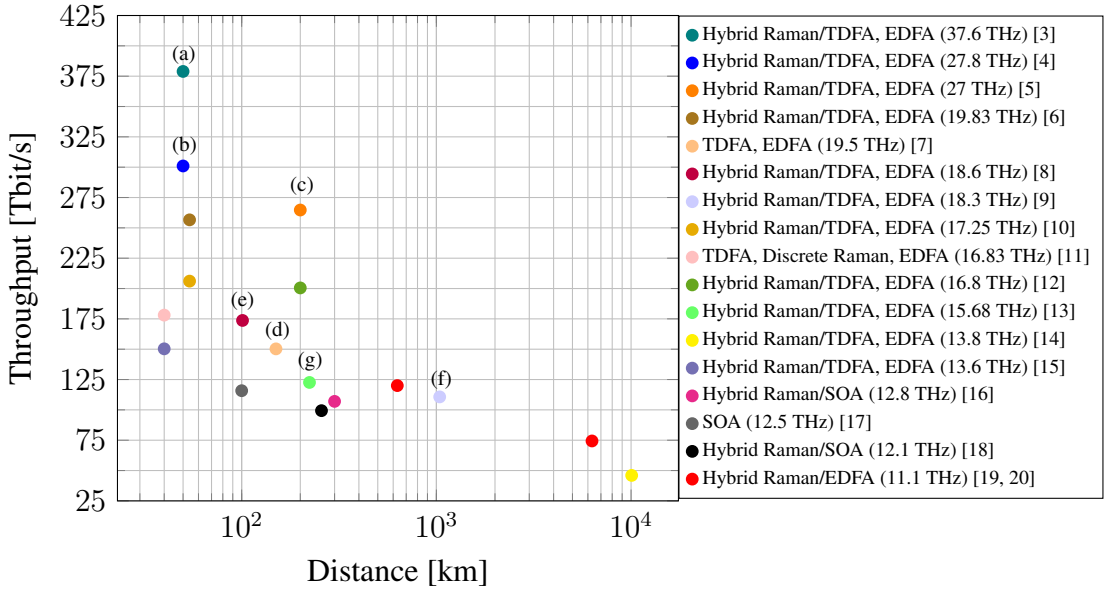

Fig. 1.2: Record data throughput versus distance for SMF using bandwidth > 10 THz, not including spectral gaps between amplifier gain bandwidths, with the most recent and key results highlighted in the figure: (a) [3] (b) [4], (c) [5], (d) [7], (e) [8], (f) [9], and (g) [13]. This figure also shows the different amplification technologies used to achieve these records.

50 km. Besides the wide bandwidth, these records are obtained utilising hybrid amplifier technologies, corresponding to Raman amplifiers combined with semiconductor optical amplifiers (SOAs), bismuth-doped fibre amplifiers (BDFAs) and rare-earth doped fibre amplifiers, such as EDFAs and thulium-doped fibre amplifiers (TDFAs).

To successfully use the full available fibre bandwidth in combination with different amplifier technologies such as lumped amplifiers (EDFAs, TDFAs, BDFAs and SOAs) and Raman amplifiers, mathematical modelling of optical fibre impairments, amplification technologies and TRXs is required. These models provide physical insight and allow quantification of nonlinear signal distortions in the optical transmission system, enabling performance improvements for the same utilised bandwidth and transmission distance. This thesis describes the development of new real-time models to predict nonlinear distortion in UWB transmission regimes with different amplification technologies using coherent detection.

The possibility of exhaustively predicting fibre noise sources in real-time for different user-case scenarios makes analytical models valuable and powerful tools. These models enable real-time estimation of the fibre nonlinear interference (NLI) noise, overcoming time-consuming simulations, even when using a state-of-the-art graphics processing unit (GPU). This enables an insightful understanding of how network throughputs scale with optical bandwidth and new technologies, ensuring

cost-effective solutions tailored to customer needs; network optimisation algorithms to improve system performance; better engineering system designs; and predictions of future optical technologies based on worldwide traffic demand forecasts, shaping the next-generation optical fibre industry, which includes new fibres, amplifiers, TRX, receiver (Rx) subsystems, etc.

Current analytical descriptions of nonlinear distortions in UWB transmission regimes are limited to lumped-amplified links. However, as shown in Fig. 1.2, high-capacity transmission systems have been shown to use hybrid-amplified technologies. This is because Raman amplifiers achieve better performance compared to EDFAs, TDFAs, BDFAs and SOAs. For UWB transmission employing distributed Raman amplification (RA), complex interactions between the fibre launch power, Raman pump powers and inter-channel stimulated Raman scattering (ISRS) effect must be analytically modelled. This is essential to achieve real-time system performance prediction enabling system optimisation to achieve ultra-high throughputs. This thesis presents the first closed-form model to estimate transmission system performance accounting for any amplifier technology in UWB transmission regimes, including RA. The model is validated numerically and experimentally using a recirculating loop transmission experiment.

For analytical models limited to lumped-amplified links, an additional limitation is their inaccuracy for fibres with short-span lengths (< 40 km) or extremely low losses (< 0.1 dB). A contribution of this thesis is a new analytical model tailored to lumped-amplified links and valid for any span length and fibre losses. This is particularly important for short-reach links, and new fibre technologies including ultra-low-loss (ULL) and hollow-core fibres.

A further contribution of this thesis is the integration of analytical models into optimisation algorithms. These algorithms are applied to power optimisation in both lumped-amplified and hybrid-amplified optical links, with and without transmitter (Tx) and Rx noise. This includes the optimisation and design of Raman and lumped amplifiers by determining the optimal pump configuration, specifically the number of pumps, their power levels, wavelengths, and direction (forward (FW) and/or backward (BW) propagation). Additionally, these algorithms are used for the optimisation of optical networks, including topology design, as well as practical applications that involve simulating real fibre cable operation under hybrid-amplification technologies, assessing their performance improvements compared to the same system operating over lumped amplifiers. The impact of ISRS effect is also analysed. It is shown that for systems limited by the TRX noise, launch power optimisation - done to compensate for ISRS and fibre-wavelength-dependent parameters - does not change the system performance, and spectrally uniform launch power profiles can maximise the total throughput.

1.1 Research problem

The instantaneous nonlinear fibre response imposes the most significant limitation in data throughput for silica-based optical fibres, known as the Kerr nonlinearity. The Kerr nonlinearity is proportional to the power launched in the fibre and its evolution with fibre distance. Because of it, the SNR in the Rx can not be arbitrarily increased leading to signal distortions that set an upper limit on the achievable total throughput for these systems. However, the capacity of an optical fibre system is bounded by the Shannon-Hartley formula [21], and according to it, further capacity can be obtained by increasing the number of spatial channels and the optical bandwidth, or through SNR improvements. UWB and SDM technologies aim to provide more capacity through bandwidth extension and increase in spacial channels respectively. On the other hand, SNR improvements can be achieved by alternative fibre technologies, such as ULL fibres and hollow-core fibres; improved TRX technologies, such as photonics analog-to-digital converters (ADCs) and high baud-rate TRXs; alternative amplifier technologies, such as Raman amplifiers; advanced DSP, including nonlinear mitigation techniques, constellation shaping and improved detection techniques.

To understand the limitations caused by the Kerr nonlinearity and its implications in data transmission, the evolution of the guided electrical field in an optical fibre must be simulated. This is important as technologies which aim to increase the total system throughput, also affect the electrical field evolution along the fibre distance, inducing different Kerr nonlinear distortions. In this category, UWB transmission through the ISRS effect can be cited; Raman amplifiers, through the complex interactions between pump wavelengths, powers and ISRS effect; and also ULL fibres through their lower attenuation. While increasing the bandwidth through UWB transmission technologies yields higher NLI contributions to the total SNR due to the additional channels, the gain is still positive because Shannon-Hartley capacity bound formula [21] scales linearly with bandwidth and logarithmic with SNR. In the case of Raman amplifiers and ULL fibres, additional NLI is generated because of the pump powers injected in the fibre and the fibre low loss respectively; however, this is compensated through a reduction in the amplified spontaneous emission (ASE) noise contribution in both cases to the total SNR. These will be the main strategies analysed throughout this thesis.

The evolution of the electrical field in an optical fibre obeys the nonlinear Schrödinger equation (NLSE) [22], and it is commonly obtained using split-step Fourier method (SSFM) simulations [22]. However, the computational complexity of this strategy scales with the optical bandwidth and becomes unmanageable for UWB systems even using state-of-the-art GPUs. To tackle this, mathematical assumptions and approximations have been introduced in the NLSE and simpler but sub-optimal nonlinear models have been published [23, 24, 25, 26, 27, 28, 29, 30, 31]. This is the

case with conventional transmission systems, which consist of modelling the optical fibre channel as an AWGN channel. This greatly simplifies the channel modelling as the characteristics of an AWGN channel are well known [32] and Shannon‘s information theory gives a complete description of the optimum coding, modulation, and detection strategies which should be used to achieve the so-called AWGN capacity [21]. The most widely known channel model relying on this approach is the frequency domain model known as Gaussian noise (GN) model [27] and its extensions [28, 33]. Because of the integrals involved in this model, it is also referred to as the integral model.

Even approximating the NLSE, these frequency-domain AWGN-like channel models [27, 28, 33] are time-consuming models because of the integrals involved in their computations. However, using function approximations, closed-form solutions can be obtained yielding real-time prediction of the optical system performance. These models can be embedded in optimisation algorithms to tackle problems such as network optimisation, and capacity maximising system designs by optimising amplifiers, modulation formats, launch power, etc.

The ISRS effect, an essential physical effect for systems operating beyond the C-band was for the first time included in the GN model in [33]. Closed-form expressions of this model were further developed in [34, 35, 36, 37, 38] for lumped amplification (LA) only. Among the limitations of these formulae are their non-validity for arbitrary span lengths and fibre losses; and their non-validity for Raman or hybrid amplified links, because of the approximations used to derive them. New closed-form models have to be derived to account for those scenarios, especially in next-generation optical networks, where throughput is enhanced by different amplification technologies such as RA combined with rare-earth doped fibre amplifiers; and the utilisation of ULL fibres.

In UWB systems, i.e., systems operating beyond the C-band, because of the combination of signal power transfer due to ISRS together with wavelength-dependent attenuation, amplifier noise, and for hybrid amplified links, the additional interaction between pump powers and wavelengths, each WDM channel experiences different accumulated distortions [39, 40, 41]. Thus the optimum launch power for each channel varies and launch power optimisation has to be performed. Additionally for hybrid-amplified links, pump power and wavelength optimisation is essential to achieve the maximum system throughput. The impact of the TRX subsystem has to be accounted for in the estimation of the system performance, as this component is also a fundamental contributor to the total received SNR with a larger impact for short-reach systems.

This thesis describes the research carried out during this PhD research, which involves the development and application of accurate new closed-form models to predict performance limitations in the next-generation optical communication

networks, comprising the use of UWB technologies combined with different kinds of amplification technologies, such as Raman, lumped, and hybrid amplifiers. New closed-form expressions have been proposed for these scenarios and used for system parameter optimisation, such as optimum Raman amplifier design to achieve performance maximisation. Newly derived models have also been applied for network optimisation, amplifier design, and to evaluate the impact of the TRX subsystem and launch power optimisation in links operating with different amplification technologies.

1.2 Chapter overview

The remaining chapters in this thesis cover the following topics:

Chapter 2 introduces the fundamental concepts of optical communications, the theory needed to understand propagation effects in optical fibre cables and the basic physics of optical amplifiers. This chapter gives a mathematical understanding of the state-of-the-art modelling of conventional optical systems and reviews the literature on this topic. UWB analytical models are presented in this chapter and their limitations are discussed.

Chapter 3 describes a new semi-analytical model to evaluate the system performance for optical links operating with LA in UWB regime. The new model removes the limitations of a previous approach extending it to support arbitrary span lengths and fibre losses. Its accuracy is validated against the NLSE and the integral version of this model.

Chapter 4 describes the first real-time semi-analytical model to evaluate the optical system performance for hybrid-amplified links, i.e., links consisting of Raman combined with rare-earth doped fibre amplifiers. The model is validated against the NLSE, its integral version, and with a recirculating-loop experiment using hybrid amplification.

Chapter 5 describes the application of real-time models in optimisation algorithms to maximise the system throughput. The new proposed model in Chapter 4 is used to derive UWB throughput-maximising Raman amplifiers by optimising launch power, pump powers and wavelengths. This model is used for practical link design simulations, analysing the benefits of RA compared to LA, and further evaluating the impact of launch power optimisation in hybrid-amplified links. Additionally, analytical models from Chapter 2 are embedded in optimisation algorithms and used to evaluate how the TRX noise impacts the gains obtained by launch power optimisation

in UWB lumped-amplified links. These models are also used to understand the impact of topology redesign using space and wavelength domains on network throughput.

Chapter 6 concludes the thesis, highlights its most important contributions, and suggests possible future works.

1.3 Key contributions

The key contributions of this thesis are listed below, the citations in this section refer to the list of publications in Sec. 1.4 resulting from this PhD research.

- The analytical nonlinear model presented in Sec. 2.7 was used to predict the results of the experiment published in [11]. The analysis concluded that for this particular 40 km transmission system, the TRX noise was the predominant noise source, and as a consequence launch power optimisation had negligible impact on the per channel and overall system performance. This led to the publication of [P8] which was selected as a top-scored conference paper and invited for an extended journal publication. This journal paper was published in [P1], where for the first time the impact of launch power, TRX noise and ISRS effect on the system Quality of Transmission (QoT) was evaluated for an UWB transmission systems using different bandwidths and span lengths. It was found that the ISRS effect degrades the QoT and increases the gains in performance obtained by optimising the launch power, while the TRX noise reduces these gains and the SNR variation across the bandwidth, with a major impact over short distances. Part of these results were also published in [P10].

- The impact of topology redesign using SDM and UWB technologies on network throughput was studied. To that end, 200 topologies were generated from a geometric generative graph model and per-channel optimum launch power was calculated for each topology maximising the total system throughput. These optimisations were enabled by the speed of computation of the analytical models in Sec. 2.7. Different throughputs and costs with and without topology redesign for SDM and UWB technologies were analysed and the results were published in [P16].

- A limitation of the semi-analytical model presented in Sec. 2.7 is their non-validity for arbitrary fibre span lengths and fibre losses. More specifically, these models are not valid for short-span lengths (< 40 km) and extremely low losses (< 0.1 dB). For the first time, a new UWB model was proposed, removing these constraints. The model was published at [P2] and [P9] and was described in Chapter 3. The model was applied in this same chapter for an S+C+L band (20 THz) transmission system and its accuracy were verified through comparisons with results obtained using the integral model and SSFM simulations, showing good agreement for most scenarios simulated.

- The first UWB semi-analytical model supporting hybrid-amplified links for any pump configuration was proposed in [P3] and [P12], and is described in

Secs. 4.1 and 4.2. Previous models were limited to specific RA scenarios (such as FW pump or C-band transmission only), or restricted for lumped-amplified links, such as the ones in Chapters 2 and 3. The publications in [P3] and [P12] support an arbitrary number of FW and BW pumps including their co-propagation, wavelength-dependent fibre parameters, variable per-channel launch powers and channel bandwidths. These new closed-form expressions are valid for Gaussian constellations and are based on a semi-analytical approach for the power evolution along the fibre distance in the presence of RA. The accuracy of these expressions was confirmed using the integral model and SSFM simulations over 10 THz and 13 THz optical bandwidth.

- The model described in Secs. 4.1 and 4.2 was extended to account for arbitrary modulation formats and the results were described in Sec. 4.3 and published in [P14]. The new semi-analytical model is the first UWB model to account for any setup of hybrid-amplified links with any modulation format, including shaped or unshaped constellations, including square quadrature amplitude modulation (QAM) formats. The model accuracy was confirmed using SSFM simulations over 20 THz optical bandwidth.

- The ASE noise generated by hybrid amplifiers (see Sec. 2.8) was for the first time included in the model described in Chapter 4 and results were published in [P17]. This new model was used to simulate and optimise launch power, pump power and pump wavelength of an optical link with parameters similar to the MAREA submarine cable, operating with lumped amplifiers only, and in a hybrid-BW amplifier configuration. This work was described in Sec. 5.5 and results showed an increasing throughput by 12% for the optimised hybrid link compared to the same link using EDFAs only.

- The model described in Chapter 4 with the ASE noise inclusion as per Sec. 2.8 was used to design capacity-maximising hybrid Raman amplifiers based on particle swarm optimisation (PSO) algorithm, where the semi-analytical nonlinear model in Chapter 4 was used to achieve real-time optimisation. The baseline system under consideration was a multi-span 18.4 THz transmission system (with 80-km spans), and results were validated using the integral model. The analysis was published in [P6] and described in Sec. 5.4. An extensive theoretical investigation of different system configurations, ranging from short to metro, long-haul, and trans-Atlantic links was described, demonstrating the trade-off between the various sources of noise and amplifier technologies.

- The first analysis of the gains obtained by per-channel launch power optimisation in hybrid links was performed in Sec. 5.3 and published in [P19]. It was found

that compared with lumped-amplified links, these gains are smaller because the pumps injected in the transmission fibre can compensate for power variations induced by the wavelength dependence fibre parameters and the ISRS effect. The system used an ideal TRX, 13 THz optical bandwidth and 10 x 100 km optical link length. Compared to using the optimum spectrally uniform launch power, an average SNR gain of 0.13 dB is obtained against 0.56 dB for the same system operating with lumped amplifiers only.

- The first optimised O-to-U band ($\approx$ 60 THz) simulation was published in [P5]. To enable such simulation, the integral model in Sec. 2.6 was implemented on multiple GPUs to demonstrate a 589×96 GBaud channel transmission with optimised per-channel launch power profile. This is the first model predicting the performance of a fully loaded O-to-U band transmission without guard bands at zero-dispersion wavelength. This model was further applied to quantify the achievable throughput under total optical power constraints for systems ranging from C-band to fully populated OESCLU bands using optimum launch powers. Results were published in [P20] and showed conditions when expanding bandwidth provides minor additional throughput.

- The real-time model in Chapter 4 was used to reproduce experimental results of a UWB transmission over E-, S-, C- and L- band with hybrid Raman amplifier. This work was published in [P4]. The amplifier consisted of two stages: a distributed RA over a 50 km SMF and two discrete RA stages with 7.5 km inverse dispersion fibres. The semi-analytical model was further used to study the system performance with additional pump configurations, enabling the analysis of future experimental setup upgrade, not presently possible experimentally due to equipment limitations.

- An experimental comparison of the performance of probabilistic and geometric shaping was performed for the first time and published in [P15]. The transmission experiment was carried out for distances of 232.5, 1007.5 and 3022.5 km SMF, using a recirculating loop with 4 channels. The experimental results were validated using the Enhanced Gaussian noise (EGN) model described in Sec. 2.6. For 64-ary constellations over 3022.5 km, probabilistic shaping outperformed geometric shaping by 0.17 bit/(4D symbol). For short distance (232.5 km) and 1024 constellation points, this advantage diminishes due to increased TRX noise, and both schemes performed similarly.

- The closed-form expressions developed in Chapter 4 were used to model a world record unrepeated transmission experiment, which achieved 122.6 Tbit/s over 223 km fibre (see Fig. 1.2). The record experiment was enabled by using the

semi-analytical model to plan the experiment by estimating the system performance for various experimental setups, including different fibre lengths and launch power profiles, to find in which configuration a record transmission experiment could be achieved. The chosen transmission setup was further optimised experimentally and the results were published in [P7] and selected as a top-scored publication, further extended to a journal paper in [P18] where the closed-form model in Chapter 4 was used to verify the experimental results. In this validation, it was shown average SNR difference between model prediction and measured results were only 0.56 dB across all WDM channels.

- The closed-form model developed in Chapter 4 was experimentally validated in a 12.4 THz S+C+L band WDM transmission with BW Raman pumping. The validation was described in Sec. 4.4 and published in [P22]. The experimental setup used 4 BW Raman pumps with a total power of up to 1.5 W. The TRX noise was minimised by using a relatively low symbol rate of 32 GBaud per WDM channel to highlight the impact of accumulated ASE and NLI noise on the overall performance in the recirculating loop transmission. It was found that the model accurately estimates the nonlinear interference and ASE noise with an average SNR difference between the experiment and model of less than 0.38 dB and 0.60 dB over 355 km and 1065 km SMF transmission, respectively.

- A record transmission experiment of 202.3 Tbit/s over 39 km field-deployed fibre connecting University College London (UCL), London, UK to Telehouse datacentre in East London, UK was achieved using 15.6 THz S+C+L-bands. The record was possible after using the models in Chapter 2, 3 and 4 to plan the experiment by estimating approximate values of the per-channel launch power, required power tilt, and the transmission distance of which a record could be achieved, given the experimental equipment constraints. These parameters were further optimised experimentally and the results were published in [P23].

- The first UWB semi-analytical model supporting O-band transmission for lumped-amplified links was published in [P21]. The formulae in Sec. 2.7 were extended to include four-wave mixing (FWM) effects (see Secs. 2.4.3 and 6.2) and accurately operate in the O-band, including the zero-dispersion regime. The accuracy of the derived equations was validated and confirmed via comparisons with the SSFM and the integral model over a single 80 km fibre span and 10 THz optical bandwidth with channels centred at 1302.3 nm.

- Using the semi-analytical models in Sec. 2.7, the ISRS effect was studied and techniques to compensate for this effect were proposed focusing on new transmission performance metrics. More specifically, launch power optimisation

and constellation shaping were proposed to achieve uniform SNR spectral distribution for all the WDM channels, rather than maximising total system throughput. It is shown that under this metric the S-band (the most affected band by the ISRS effect) can perform 3x higher in terms of SNR, compared to the same system optimised to achieve the maximum throughput. The results were published in [P11].

- New and sub-optimal techniques to overcome the computational complexity of per-channel launch power optimisation techniques in UWB transmission systems were proposed using the semi-analytical models in Sec. 2.7. The impact of experimental equipment constraints on these techniques was also studied. Two cases were considered: using constant launch power per groups of WDM channels, and random power deviations from the per-channel optimum launch power (emulating equipment imperfections). Performance losses were computed for several different scenarios, and results were published in [P13]. It was shown that sub-optimal techniques exhibit performance close to that of optimal techniques under specific conditions.

1.4 List of publications

A subset of the work presented in this thesis was first published in the following publications:

Journal papers

(P1) **H. Buglia**, E. Sillekens, A. Vasylchenkova, P. Bayvel and L. Galdino, "On the impact of launch power optimization and transceiver noise on the performance of ultra-wideband transmission systems [Invited]," in Journal of Optical Communications and Networking, vol. 14, no. 5, pp. B11-B21, May 2022, doi: 10.1364/JOCN.450726.

(P2) **H. Buglia**, M. Jarmolovičius, A. Vasylchenkova, E. Sillekens, L. Galdino, R. I. Killey and P. Bayvel, "A Closed-Form Expression for the Gaussian Noise Model in the Presence of Inter-Channel Stimulated Raman Scattering Extended for Arbitrary Loss and Fibre Length," in Journal of Lightwave Technology, vol. 41, no. 11, pp. 3577-3586, 1 June1, 2023, doi: 10.1109/JLT.2023.3256185.

(P3) **H. Buglia**, M. Jarmolovičius, L. Galdino, R. I. Killey and P. Bayvel, "A Closed-Form Expression for the Gaussian Noise Model in the Presence of Raman Amplification," in Journal of Lightwave Technology, vol. 42, no. 2, pp. 636-648, 2024, doi: 10.1109/JLT.2023.3315127.

(P4) P. Hazarika, **H. Buglia**, M. Jarmolovičius, E. Sillekens, M. Tan, A. Donodin, I. Phillips, P. Harper, R. I. Killey, P. Bayvel and W. Forysiak, "Multi-Band Transmission Over E-, S-, C- and L-Band With a Hybrid Raman Amplifier," in Journal of Lightwave Technology, vol. 42, no. 4, pp. 1215-1224, 2024, doi: 10.1109/JLT.2023.3328836.

(P5) M. Jarmolovičius, D. Semrau, **H. Buglia**, M. Shevchenko, F. M. Ferreira, E. Sillekens, P. Bayvel and R. I. Killey, "Optimising O-to-U Band Transmission Using Fast ISRS Gaussian Noise Numerical Integral Model," in Journal of Lightwave Technology, vol. 42, no. 20, pp. 7095-7103, 2024, doi: 10.1109/JLT.2024.3417696.

(P6) **H. Buglia**, R. I. Killey and P. Bayvel, "Ultra-wideband Modelling of Optical Fibre Nonlinearity in Hybrid-amplified Links," in Journal of Lightwave Technology, 2024, doi: 10.1109/JLT.2024.3439999.

(P7) J. Yang, **H. Buglia**, M. Jarmolovičius, R. Aparecido, P. Hazarika, E. Sillekens, R. Sohanpal, M. Tan, D. Pratiwi, R. S. Luis, B. J. Puttnam, Y. Wakayama, R.

Stolte, W. Forysiak, P. Bayvel, and R. I. Killey, "122.6 Tb/s S+C+L Band Unrepeatered Transmission over 223 km Link with Optimised Bidirectional Raman Amplification," in Journal of Lightwave Technology, 2024, doi: 10.1109/JLT.2024.3521233.

Peer-reviewed conference papers published in conference proceedings

(P8) **H. Buglia**, E. Sillekens, A. Vasylchenkova, W. Yi, R. I. Killey, P. Bayvel and L. Galdino, "Challenges in Extending Optical Fibre Transmission Bandwidth Beyond C+L Band and How to Get There," 2021 International Conference on Optical Network Design and Modeling (ONDM), Gothenburg, Sweden, 2021, doi: 10.23919/ONDM51796.2021.9492434.

(P9) **H. Buglia**, E. Sillekens, A. Vasylchenkova, R. I. Killey, P. Bayvel and L. Galdino, "An Extended Version of the ISRS GN model in Closed-Form Accounting for Short Span Lengths and Low Losses," 2022 European Conference on Optical Communication (ECOC), Basel, Switzerland, 2022.

(P10) **H. Buglia** and L. Galdino, "Unleashing the Optical Fiber Transmission Bandwidth: From Theory to Experiments," in Optica Advanced Photonics Congress 2022, Technical Digest Series (Optica Publishing Group, 2022), paper SpTh2J.7.

(P11) A. Vasylchenkova, **H. Buglia**, E. Sillekens, L. Galdino, R. I. Killey, and P. Bayvel, "Analytical modelling of system impairments in ultrawideband transmission context," in Optica Advanced Photonics Congress 2022, Technical Digest Series (Optica Publishing Group, 2022), paper NeTu3D.1.

(P12) **H. Buglia**, M. Jarmolovičius, A. Vasylchenkova, E. Sillekens, L. Galdino, P. Bayvel and R. I. Killey, "A Closed-form Expression for the ISRS GN Model Supporting Distributed Raman Amplification," 2023 Optical Fiber Communications Conference and Exhibition (OFC), San Diego, CA, USA, 2023, pp. 1-3, doi: 10.1364/OFC.2023.W2A.29.

(P13) A. Vasylchenkova, **H. Buglia**, E. Sillekens, R. I. Killey and P. Bayvel, "Launch power optimisation for ultrawideband transmission: achievable throughput improvement under practical constraints," 49th European Conference on Optical Communications (ECOC 2023), Hybrid Conference, Glasgow, UK, 2023, pp. 1051-1054, doi: 10.1049/icp.2023.2432.

(P14) **H. Buglia**, M. Jarmolovičius, L. Galdino, R. I. Killey and P. Bayvel, "A modulation-format dependent closed-form expression for the Gaussian noise

model in the presence of Raman amplification," 49th European Conference on Optical Communications (ECOC 2023), Hybrid Conference, Glasgow, UK, 2023, pp. 64-67, doi: 10.1049/icp.2023.1848.

(P15) E. Sillekens, **H. Buglia**, P. Bayvel and R. I. Killey, "Experimental comparison of probabilistic and geometric shaping in transmission," 49th European Conference on Optical Communications (ECOC 2023), Hybrid Conference, Glasgow, UK, 2023, pp. 1019-1022, doi: 10.1049/icp.2023.2424.

(P16) R. Matzner, **H. Buglia** and P. Bayvel, "Evolving optical core networks: understanding the impact of topology redesign using space and wavelength domains on network throughput," 49th European Conference on Optical Communications (ECOC 2023), Hybrid Conference, Glasgow, UK, 2023, pp. 1043-1046, doi: 10.1049/icp.2023.2430.

(P17) **H. Buglia**, E. Sillekens, L. Galdino, R. Killey and P. Bayvel, "Throughput Maximisation in Ultra-wideband Hybrid-amplified Links," 2024 Optical Fiber Communications Conference and Exhibition (OFC), San Diego, CA, USA, 2024, pp. 1-3.

(P18) J. Yang, R. Aparecido, **H. Buglia**, P. Hazarika, E. Sillekens, R. Sohanpal, M. Tan, D. Pratiwi, R. S. Luis, B. J. Puttnam, Y. Wakayama, W. Forysiak, P. Bayvel and R. I. Killey, "122.6 Tb/s S+C+L Band Unrepeated Transmission over 223 km link with Optimised Bidirectional Raman Amplification," 2024 Optical Fiber Communications Conference and Exhibition (OFC), San Diego, CA, USA, 2024, pp. 1-3.

(P19) **H. Buglia**, E. Sillekens, L. Galdino, R. I. Killey, and P. Bayvel, "Impact of launch power optimisation in hybrid-amplified links," 2024 European Conference on Optical Communication (ECOC), Frankfurt, Germany, 2024.

(P20) M. Jarmolovičius, **H. Buglia**, E. Sillekens, P. Bayvel, and R. I. Killey, "Ultrawideband optical fibre throughput in the presence of total optical power constraints from C to OESCLU spectral bands," 2024 European Conference on Optical Communication (ECOC), Frankfurt, Germany, 2024.

(P21) F. Balasis, D. J. Elson, M. Jarmolovičius, **H. Buglia**, E. Sillekens, R. I. Killey, P. Bayvel, N. Yoshikane, T. Tsuritani and Y. Wakayama, "An Extended Closed Form of the ISRS GN Model for the Zero-Dispersion Regime," 2024 European Conference on Optical Communication (ECOC), Frankfurt, Germany, 2024.

(P22) J. Yang, **H. Buglia**, E. Sillekens, M. Tan, P. Hazarika, D. Pratiwi, R. Sohanpal, M. Jarmolovičius, R. Aparecido, R. Stolte, W. Forysiak, P. Bayvel, and R. I.

Killey, "Experimental validation of the closed-form GN model accounting for distributed Raman amplification in an S+C+L-band hybrid amplified long-haul transmission system," 2024 European Conference on Optical Communication (ECOC), Frankfurt, Germany, 2024.

(P23) J. Yang, E. Sillekens, B. J. Puttnam, R. Sohanpal, M. Jarmolovičius, R. Aparecido, **H. Buglia**, R. S. Luis, R. Stolte, P. Bayvel, and R. I. Killey, "Record 202.3 Tb/s Transmission over Field-Deployed Fibre using 15.6 THz S+C+L-Bands," 2024 European Conference on Optical Communication (ECOC), Frankfurt, Germany, 2024.

Chapter 2

Optical fibre channel modelling

This chapter describes the optical fibre channel and how it is conventionally modelled. Several approximations are made to obtain a simple and practical description of this channel, referred to as the conventional approach. The basic theory of optical propagation and amplification effects are presented together with the most used nonlinear channel model to estimate the optical system performance. Semi-analytical expressions of this model are presented. Modulation formats are reviewed and particular emphasis is given to UWB signal transmission. The theory in this chapter presents the background to understand the research conducted during this Doctor of Philosophy (PhD) research.

2.1 Optical fibre communication system

An optical fibre communication system is schematically represented in Fig. 2.1. It consists of a Tx device that modulates the data stream through optical modulators and converts the electrical signal into a light signal exploiting amplitude, phase and the polarisation state of the electric field. The light is carried by an optical fibre, followed by an optical amplifier which recovers the transmitted signal level, which was attenuated due to propagation. The optical link consists of n optical fibre spans followed by n optical amplifiers. The number n depends on the distance covered by the optical transmission link, ranging from short (<100 km) to transoceanic (>6000 km) distances. After propagation, an optical coherent Rx detects the light signal and converts it back into an electrical signal through coherent detection [42], where the signal is mixed with a local oscillator and converted to the electrical domain using

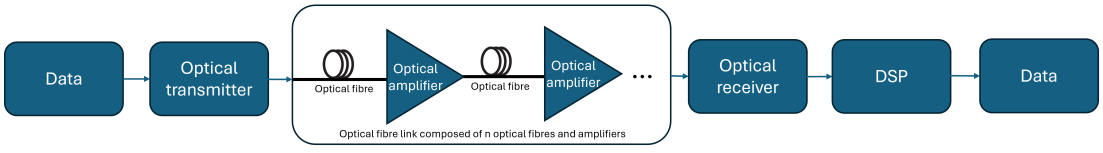

Fig. 2.1: Schematic of an optical fibre transmission system.

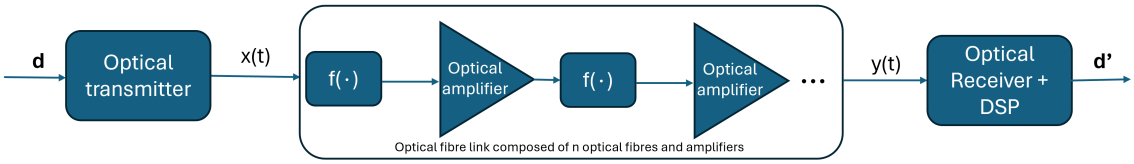

Fig. 2.2: Schematic of an optical fibre transmission system with the optical fibre represented as a nonlinear function.

photodiodes (other detection strategies are also possible, in this thesis coherent detection is used). The received electrical signal is processed using DSP [43] algorithms and the data stream is recovered with errors originating from the optical Tx and Rx, i.e., the TRX sub-system and from the optical link. Errors originating from the optical link are due to optical amplifiers and propagation effects discussed in the next sections.

2.2 Optical fibre channel

The optical fibre link is a nonlinear channel represented in Fig. 2.2 through the unitary nonlinear function $f(\cdot)$ (normalised to the fibre loss). In summary, a set of data symbols represented as a vector **d** is modulated through the optical Tx to obtain a continuous-time signal represented as $x(t)$. The signal $x(t)$ is transmitted through the optical fibre link. After transmission, a noisy and distorted signal $y(t)$ is obtained, which is received by the optical Rx and after digitisation and DSP treatment a vector of noisy and distorted data symbols is obtained represented as **d'**.

Because of the nonlinear nature of the optical fibre link, an explicit and practically implementable relation between **d** and **d'** (same for $x(t)$ and $y(t)$) is not possible to obtain. This is because the equation governing the propagation of the signal in optical fibres has no integral or analytical solution. Thus, approximations and assumptions are made to obtain an easier and implementable description of this channel. Currently deployed optical systems rely on these approximations and are referred to as conventional systems.

The first approximation usually made is to assume the ideal Tx and Rx, such that $x(t)$ is a noiseless signal and no further noise other than the in-line optical amplifier noise is added to $y(t)$. The TRX noise is added later, as an independent noise contribution to the system (see Sec. 2.9). Each amplifier placed after the j $^{\text{th}}$ fibre span generates a noise $w_j(t)$, where $j = \{0, \cdots, n\}$. The signal $x(t)$ after the first span is written as $f(x(t)) + w_1(t)$. Thus, the signal $x(t)$ after n spans, i.e., the signal $y(t)$ can

be represented as

$$y = \underbrace{f(\cdots f(f(f(x) + w_1) + w_2) + w_3 \cdots)}_{\text{n times}} + w_n. \tag{2.1}$$

The second assumption is to assume that the amplifier noise in each span w_j is independent of the function $f(\cdot)$. In an optical fibre system, this is equivalent to neglecting all the noise-signal and noise-noise interactions due to the nonlinear nature of $f(\cdot)$. It is also equivalent of assuming that the noise is independent of the fibre dispersion, which is shown to be the case in [29]. Furthermore, the optical amplifier restores the noise level after each span. Under this assumption, Eq. (2.1) can be written as

$$y = \underbrace{f(\cdots f(f(f(x))) \cdots)}_{\text{n times}} + \sum_{j=1}^{n} w_j = f^n(x) + \sum_{j=1}^{n} w_j, \tag{2.2}$$

where $f^n(\cdot)$ represents the n^{th} application of the function $f(\cdot)$. The third assumption is the hypothetical possibility of writing $f^n(x)$ as a summation of the signal and a nonlinear function of it, i.e., $f^n(x) = x + q(x)$, where $q(x)$ is a nonlinear function (both normalised to the fibre loss and thus, unitary) of the transmitted signal. Thus, Eq. (2.2) can be written as

$$y(t) = x(t) + q(x(t)) + \sum_{j=1}^{n} w_j(t) = x(t) + w'(t), \tag{2.3}$$

where $w'(t) = q(x(t)) + \sum_{j=1}^{n} w_j(t)$ represents the additive noise in the system, which depends on the transmitted signal $x(t)$ and on the optical amplifier noise $w_j(t)$. In an optical fibre system, $q(x(t))$ is referred to as the NLI noise due to the optical fibre nonlinearities and $\sum_{j=1}^{n} w_j(t)$ is referred to ASE noise from optical amplifiers. Note that, using these approximations, the ASE and NLI noise can be assumed as additive noise sources impairing the transmitted signal $x(t)$.

Indeed, an important feature of Eq. (2.3) is the simple description of the channel, where the transmitted optical signal $x(t)$ is impaired by additive noise contributions. Combined with this, the last assumption is that the noise $w'(t)$ is Gaussian distributed and assumed to be locally white, i.e., white within the bandwidth of a single channel i. By doing so, Eq. (2.3) represents an additive GN channel, where the variance of the noise $w'(t)$ depends on the transmitted signal statistics, because of the nonlinear nature of $q(\cdot)$ inherited from $f(\cdot)$. Another advantage of this description, which greatly simplifies the complexity of the channel, is that the characteristics of AWGN channels are well known [32] (at least for the ones where the noise does not depend on the transmitted signal) and Shannon‘s information theory gives a complete description of the optimum coding, modulation, and detection strategies which should be used to

achieve the capacity of these channels. The most widely known optical fibre channel model relying on the assumptions described in this chapter is the GN model, summarised in [27, 44], which is the focus of this thesis.

It is important to note that applying the AWGN channel theory to the optical fibre channel gives an upper bound on the achievable capacity of these channels because of the approximations described in this section. Even for the channel described by Eq. (2.3), the AWGN theory and capacity formula [32] is also an upper bound because $w'(t)$ depends on the transmitted signal $x(t)$. Indeed, capacity exceeding the AWGN capacity formula for channels modelled as Eq. (2.3), were obtained by nonlinear shaping strategies in [45] (see also Sec. 2.10). Furthermore, other types of channel models are also possible (but usually more complex) [46]; for instance, non-AWGN channel characteristics that can be exploited to achieve higher performances [47, 48, 49, 50], such as by considering the memory induced by dispersion and nonlinear effects, and performing a joint detection (rather than symbol by symbol) [51], or by considering other channel models rather than additive noise only, such as phase-and-additive noise models [52]. The higher performance obtained by these non-AWGN-like channels is achieved by capturing some of the effects presented in Eq. (2.1) which were neglected in Eq. (2.3).

Despite that, the approach described in this section, i.e. an AWGN-like model, is easy to implement, understand, and facilitate the transmission and detection strategies; plus it is used in the currently installed optical fibre systems because of its simplicity. Since the model used in this thesis relies on these assumptions and thus is an AWGN-like channel, a brief review of modulation and coding for this channel type is presented later in this chapter in Sec. 2.10.

2.3 Derivation of the nonlinear Schrödinger equation

This section describes the derivation of the NLSE, which describes the propagation of the guided electric field $\tilde{E}(z,t)$ through an optical fibre. The derivation starts with the wave equation

$$\nabla^2\tilde{\mathbf{E}} - \frac{1}{c^2}\frac{\partial^2\tilde{\mathbf{E}}}{\partial t^2} = \mu_0\frac{\partial^2\mathbf{P}_L}{\partial t^2} + \mu_0\frac{\partial^2\mathbf{P}_{NL}}{\partial t^2}, \tag{2.4}$$

where $\tilde{\mathbf{E}}(\mathbf{r},t)$ represents the electric field as a function of position $\mathbf{r}$ and time t, c is the speed of light, μ_0 is the vacuum magnetic permeability, while $\mathbf{P}_L$ and $\mathbf{P}_{NL}$ are the linear part and the nonlinear part of the induced electric polarisation vector $\mathbf{P}$, respectively. Assume that each of the vectors above are aligned along the generic direction $\hat{\mathbf{x}}$, such that $\tilde{\mathbf{E}}(\mathbf{r},t) = \tilde{E}(\mathbf{r},t)\hat{\mathbf{x}}$ and $\mathbf{P}(\mathbf{r},t) = P(\mathbf{r},t)\hat{\mathbf{x}}$. This corresponds to an assumption of isotropy of the optical fibre medium, which can be considered valid only locally [22].

Under this assumption, Eq. (2.4) can be reduced to a scalar equation given by

$$\nabla^2 \tilde{E} - \frac{1}{c^2}\frac{\partial^2 \tilde{E}}{\partial t^2} = \mu_0 \frac{\partial^2 P_L}{\partial t^2} + \mu_0 \frac{\partial^2 P_{NL}}{\partial t^2}. \tag{2.5}$$

The linear component $P_L(\mathbf{r}, t)$ and nonlinear component $P_L(\mathbf{r}, t)$ of $\mathbf{P}(\mathbf{r}, t)$ are related to $\tilde{E}(\mathbf{r}, t)$ by

$$P_L(\mathbf{r}, t) = \varepsilon_0 \int_{-\infty}^{\infty} \chi_{xx}^{(1)}(t - t')\, \tilde{E}(\mathbf{r}, t')\, dt', \tag{2.6}$$

and

$$\begin{aligned} P_{NL}(\mathbf{r}, t) = \varepsilon_0 \int_{-\infty}^{\infty}\int_{-\infty}^{\infty}\int_{-\infty}^{\infty} \chi_{xxxx}^{(3)}(t - t_1, t - t_2, t - t_3) \\ \tilde{E}(\mathbf{r}, t_1)\, \tilde{E}(\mathbf{r}, t_2)\, \tilde{E}(\mathbf{r}, t_3)\, dt_1 dt_2 dt_3, \end{aligned} \tag{2.7}$$

where ε_0 is the vacuum dielectric constant while $\chi_{xx}^{(1)}$ and $\chi_{xxxx}^{(3)}$ are components of the first-order and third-order susceptibility tensors, respectively. Several different nonlinear optical effects arising in an optical fibre can be described by the third-order tensor component $\chi_{xxxx}^{(3)}$. In the following, it is assumed that $\chi_{xxxx}^{(3)}$ is composed by an instantaneous and a delayed component. The physical phenomenon associated with the instantaneous component of $\chi_{xxxx}^{(3)}$ is the well-known Kerr effect [22], which yields a local change of the fibre refractive index due to the optical field intensity. The physical phenomenon associated with the delayed component of $\chi_{xxxx}^{(3)}$ is the Raman effect (see Sec. 2.4.4).

Eq. (2.4) cannot be easily treated without some further simplifying assumptions. A common approach takes into account the nonlinear part of the equation P_{NL} as a perturbation of the solution for the linear case ($P_{NL} = 0$). Furthermore, $\tilde{E}(\mathbf{r}, t)$ is assumed to be a quasi-monochromatic signal. This means that $\tilde{E}(\mathbf{r}, t)$ (and $P(\mathbf{r}, t)$) can be expressed as

$$\tilde{E}(\mathbf{r}, t) = \frac{1}{2}\left[\tilde{E}(\mathbf{r}, t)\exp(-j\omega_0 t) + \overline{\tilde{E}(\mathbf{r}, t)}\exp(j\omega_0 t)\right], \tag{2.8}$$

where $\tilde{E}(\mathbf{r}, t)$ is a slowly-varying complex envelope (compared to the frequency of oscillation ω_0). Under the above conditions, the method of the separation of the variables can be used to solve Eq. (2.4). According to this method, the generic solution can be expressed in the form

$$\tilde{E}(\mathbf{r}, t) = F(x, y)E(z, t)\exp(j\beta_0 z), \tag{2.9}$$

where β_0 is the wave number at frequency $\omega = 0$. The frequency ω is related to the frequency f as $\omega = 2\pi f$. Substituting Eq. (2.9) into Eq. (2.4) and switching to the

Fourier domain (see Fourier transform definition in Sec. 2.4), we obtain a pair of equations with decoupled variables [22, Sec. 2.3]

$$\frac{\partial^2 F}{\partial x^2} + \frac{\partial^2 F}{\partial y^2} + \left[\varepsilon(\omega) k_0^2 - \tilde{\beta}\right] F = 0, \tag{2.10}$$

$$2i\beta_0 \frac{\partial E}{\partial z} + \left(\tilde{\beta}^2 - \beta_0^2\right) E = 0, \tag{2.11}$$

where $E \triangleq E\left(z, \omega - \omega_0\right)$ is the Fourier transform of $E(z,t)$, $\tilde{\beta}(\omega)$ is the wave number as a function of frequency, and z is the propagation distance. In order to obtain Eq. (2.11), a partial second derivative in z is neglected as a result of the slowly-varying envelope assumption. This set of equations admits solutions only for specific values of $\tilde{\beta}$ referred to as eigenvalues. Such solutions are called eigenfunctions. The pair eigenvalue and eigenfuction is referred to as a propagation mode.

The wave number $\tilde{\beta}$ can be obtained solving the eigenvalue equation in Eq. (2.11) and contains two terms

$$\tilde{\beta}(\omega) = \beta(\omega) + \Delta\beta \tag{2.12}$$

The term $\Delta\beta$ includes the attenuation effect and the nonlinearity induced by P_{NL} in Eq. (2.4), and it is typically expressed as

$$\Delta\beta = j\frac{\alpha}{2} + \gamma|E|^2 + T_r \frac{\partial}{\partial t}|E|^2 \tag{2.13}$$

where α, γ and T_r are referred to as attenuation coefficient or fibre loss, nonlinearity coefficient and Raman time constant, respectively. Separating the two components of the wave number in Eq. (2.11) and rearranging, we obtain

$$\frac{\partial E}{\partial z} = j\left[\beta(\omega) + \Delta\beta - \beta_0\right] E, \tag{2.14}$$

where $\tilde{\beta}^2 - \beta_0^2$ was approximated by $2\beta_0\left(\tilde{\beta} - \beta_0\right)$. The linear wave number $\beta(\omega)$ is not in general an analytical known function, as it depends on the fibre index profile. However, it can be expanded in Taylor series around ω_0 as

$$\beta(\omega) = \beta_0 + \beta_1\left(\omega - \omega_0\right) + \frac{1}{2}\beta_2\left(\omega - \omega_0\right)^2 + \frac{1}{6}\beta_3\left(\omega - \omega_0\right)^3 + \cdots \tag{2.15}$$

where β_i for $i = 0, 1, 2, \ldots$ represents the i-th derivative of $\beta(\omega)$ evaluated in $\omega = \omega_0$. Recalling the assumption on the quasi-monochromatic envelope, Eq. (2.15) can be truncated to the second-order without significant loss in accuracy. Substituting the truncated version of Eq. (2.15) into Eq. (2.14), using $\Delta\beta$ as Eq. (2.13), and switching back to the time domain, Eq. (2.14) becomes Eq. (2.16) (see Sec. 2.4), which is commonly referred to as NLSE and it is considered to be the key equation to

understand fibre propagation effects as described in Sec. 2.4.

2.4 Propagation effects

This section describes the impairments affecting the complex envelope of the guided electric field $E(z,t)$, in the optical fibre after a single-span transmission before optical amplification and considering an ideal Tx. Equivalently the function $f(\cdot)$ in Sec. 2.2 is characterised. The propagation of the guided electric field $E(z,t)$ obeys the NLSE, which is given in the time domain by [22]

$$\begin{aligned}\frac{\partial E(z,T)}{\partial z} = &\underbrace{-\frac{\alpha}{2}E(z,T)}_{\text{Loss}} \underbrace{-j\frac{\beta_2}{2}\frac{\partial^2 E(z,T)}{\partial T^2}+\frac{\beta_3}{6}\frac{\partial^3 E(z,T)}{\partial T^3}}_{\text{Dispersion}} \\ &+j\gamma\Bigg(\underbrace{|E(z,T)|^2E(z,T)}_{\text{Kerr}}\underbrace{-T_r\left\{\frac{\partial}{\partial T}|E(z,T)|^2\right\}E(z,T)}_{\text{Raman}}\Bigg)\end{aligned} \tag{2.16}$$

where β_2 is the second-order dispersion coefficient or the group velocity dispersion (GVD) parameter at reference wavelength and β_3 is the third-order dispersion coefficient or dispersion slope, $T = t - \frac{z}{v_g}$ is the time of the reference time window moving at group velocity v_g. The Raman time constant is related to the slope of the Raman gain $T_r = \frac{1}{2\pi\gamma f_r}\frac{\partial}{\partial f}g_r(f)\Big|_{f=0}$ with the fractional contribution of the delayed nonlinear response f_r [53].

The Raman gain spectrum $g_i(|\Delta f|)$, describes the power coupling of two frequency components as a function of their frequency separation (see Fig. 2.7 and Sec. 2.4.4). The Raman gain becomes relevant for bandwidths beyond 5 THz and is only valid for bandwidths up to the peak of the Raman gain coefficient (approximately 13.5 THz). Beyond 13.5 THz, an integral form of the Raman term has to be considered (see [54] and [22, Sec. 2.3.2] for details), and $\Delta\beta$ in Eq. (2.13) has to be updated. This integral term, models both the real and imaginary parts of the Raman response. The imaginary part of its Fourier transform, referred to as the Raman gain spectrum, which is included as an approximation in Eq. (2.16) (see [22, Sec. 2.3.2] for details), leads to ISRS effects. On the other hand, the impact of the real part of its Fourier transform was shown to be negligible in [53] for S+C+L band fully populated transmission systems.

Additionally in Eq. (2.16), other high-order nonlinear effects as a result of the third-order tensor component $\chi^{(3)}_{xxxx}$ in Eq. (2.7), such as self-steepening, which is relevant for ultra-short pulse (< 1 ps), were neglected. This is because modern and future optical transmission systems operate with symbol rates such as 10, 25, 32, 64,

100, 120, 200 Gbaud, corresponding to relatively long pulse widths of 100, 40, 31.25, 15.625, 10, 8.33, 5 ps. Moreover, Eq. (2.16) is valid for single polarisation only. For the case of dual polarisation, the nonlinear term in Eq. (2.16) has to be multiplied by $\frac{8}{9}$ and polarisation-mode dispersion (PMD) effect has to be included [22]. Despite dealing with dual polarisation signals, PMD is neglected in this thesis.

The Fourier transform $\mathcal{F}\{\cdot\}$ of $E(z,t)$ is defined as $E(z,f) = \mathcal{F}\{E(z,T)\} = \int_{-\infty}^{\infty} E(z,t)\exp(-j2\pi ft)dt$. The inverse Fourier transform $\mathcal{F}^{-1}\{\cdot\}$ is defined as $E(z,T) = \mathcal{F}^{-1}\{E(z,f)\} = \int_{-\infty}^{\infty} E(z,f)\exp(j2\pi ft)df$. Applying this definition to Eq. (2.16), yields the NLSE in frequency domain as

$$\frac{\partial E(z,f)}{\partial z} = \underbrace{-\frac{\alpha}{2}E(z,f)}_{\text{Loss}} + \underbrace{\left(j2\pi^2\beta_2 f^2 + j\frac{4}{3}\pi^3\beta_3 f^3\right)E(z,f)}_{\text{Dispersion}}$$
$$+ j\gamma\Bigg(\underbrace{E(z,f) * \overline{E(z,-f)} * E(z,f)}_{\text{Kerr}} - \underbrace{jT_r(2\pi f(E(z,f) * \overline{E(z,-f)}) * E(z,f))}_{\text{Raman}}\Bigg), \tag{2.17}$$

where $\overline{E(\cdot)}$ denotes the complex conjugate of $E(\cdot)$, and $u(\cdot)*v(\cdot) = \int_{-\infty}^{\infty} u(\tau)v(t-\tau)d\tau$ defines the convolution operation between $v(\cdot)$ and $u(\cdot)$.

The solution of Eq. (2.16) for an initial condition $x(t) = E(0,t)$ gives the evolution of the propagating signal $x(t)$ along the fibre length z. As in Sec. 2.2, this solution corresponds to $f(x(t))$. It is worth noting that solutions of Eqs. (2.16) and (2.17) are only possible using numerical methods as this equation is not integrable. The most widely used numerical method to solve it is called SSFM method [22] (see Sec. 2.5), however, the non-explicit representation of its solutions together with the implementation complexity of SSFM method push the developments of approximations of this equation enabling both integral (i.e., a formulation containing integrals) and closed-form (i.e., a formulation without integrals, containing only analytical functions) solutions; these approaches speed up the computation of the optical system performance and provide a mathematical understanding on how the physical effects scale with the optical transmission setup because of their description using explicit or closed-form expression solutions.

The effects on the transmitted signal $x(t)$ of each one of the terms shown in Eqs. (2.16) and (2.17) are described in the next sections. The following analysis enables an understanding of how each one of the effects in Eqs. (2.16) and (2.17), separately, change the signal $x(t)$ after fibre propagation. It also offers an initial insight into how these effects jointly modify the signal after propagation.

2.4.1 Fibre loss

The optical fibre loss is a linear effect. Neglecting dispersion, Kerr and Raman effects in Eq. (2.17), yields to

$$\frac{\partial E(z,f)}{\partial z} = -\frac{\alpha}{2}E(z,f), \tag{2.18}$$

with the solution of the electrical field given by

$$E(z,f) = E(0,f)\exp\left(-\frac{\alpha(f)}{2}z\right), \tag{2.19}$$

where $\alpha(f)$ is the fibre attenuation coefficient. In terms of optical power $P(z,f) = |E(z,f)|^2$, this equation is rewritten as

$$P(z,f) = P(0,f)\exp\left(-\alpha(f)z\right). \tag{2.20}$$

Eq. (2.20) shows that the optical signal power propagating in the fibre experiences a loss of intensity. These losses can be introduced by the intrinsic characteristics of the fibre, such as Rayleigh scattering, infrared absorption, and the presence of OH^- ions absorbed in certain spectrum regions, for instance in the E-band (1360 nm - 1460 nm) due to chemical reactions or environmental humidity during the manufacturing process [22]. Extrinsic effects, such as bending and connector loss also introduce losses in the fibre. Because of the dependency of these loss mechanisms on frequency, the attenuation $\alpha(f)$ is a frequency-dependent parameter. The intrinsic loss profile of a silica-based standard SMF is shown in Fig. 1.1 achieving its lowest value at the C-band at around 0.2 dB/km. Silica-based ULL fibres are also produced with state-of-art losses at around 0.14 dB/km [55]. Other fibre types, such as hollow core fibres, have recently achieved a state-of-art loss of 0.11 dB/km [56].

2.4.2 Fibre dispersion

Another linear effect changing the characteristics of the input electrical field in an optical fibre is the fibre dispersion. Neglecting the loss, Kerr and Raman effects. Eq. (2.17) is rewritten as

$$\frac{\partial E(z,f)}{\partial z} = \left(j2\pi^2\beta_2 f^2 + j\frac{4}{3}\pi^3\beta_3 f^3\right)E(z,f), \tag{2.21}$$

of which its solution in frequency domain is given by

$$E(z,f) = E(0,f)\exp\left(j[2\pi^2\beta_2 f^2 + \frac{4}{3}\pi^3\beta_3 f^3]z\right). \tag{2.22}$$

Eq. (2.22) shows that the input electrical field in frequency domain $E(0, f)$ experiences a frequency-dependent phase change refereed as chromatic dispersion, while its amplitude remains constant. Dispersion leads to different frequency components of a pulse travelling at slightly different speeds along the fibre because of GVD. In the time domain, this corresponds to the input signal $x(t) = E(0, t)$ experiencing a pulse broadening. The pulse can maintain its width only if all spectral components arrive together. Any time delay in the arrival of different spectral components leads to pulse broadening [22].

If dispersion is left uncompensated, the pulse broadening effect translates itself into an inter-symbol interference effect in the time domain. This effect however is partly compensated by passing the received signal $E(L, f)$ through a filter with impulse response $H(f)$ given by

$$H(f) = \exp\left(- j[2\pi^2\beta_2 f^2 + \frac{4}{3}\pi^3\beta_3 f^3]L\right), \tag{2.23}$$

where L is the full fibre span length. This compensation is done digitally at the DSP block for systems using coherent detection techniques (which detect both phase and amplitude of the received signal). However, because all the effects on Eq. (2.17) act jointly in the transmitted signal, interactions between linear and nonlinear effects cause remaining nonlinear effects that depend on the dispersion; for systems described using the approach in Sec. 2.2, these effects are captured by the function $q(x)$.

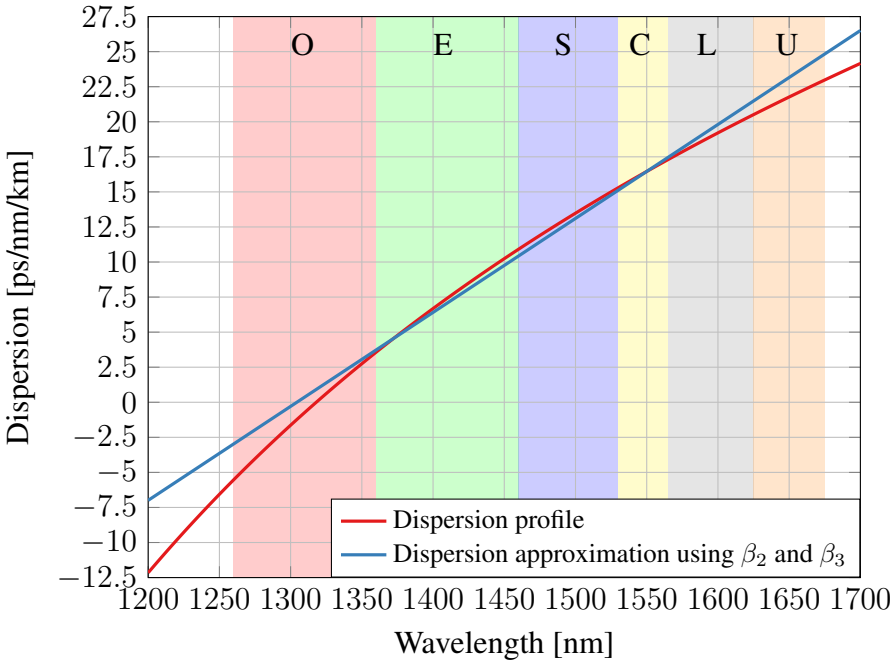

Fig. 2.3: Dispersion profile calculated using Eq. (2.24) with λ_0 = 1314 nm and $S_0 = 0.089\ \frac{\text{ps}}{\text{nm}^2\cdot\text{km}}$, and dispersion approximation using $D = 16.5\ \frac{\text{ps}}{\text{nm}\cdot\text{km}}$ and $S = 0.067\ \frac{\text{ps}}{\text{nm}^2\cdot\text{km}}$ at 1550 nm. Both profiles characterise an ITU-T G652.D fibre.

The frequency-dependent chromatic dispersion profile, or the parameter D, of a standard silica-based optical fibre, is shown in Fig. 2.3 (red curve) for different wavelengths, following the ITU Telecommunication Standardization Sector (ITU-T) G.652 recommendation [57]. It is obtained considering a common expression of this parameter reported by standard SMF fibre producers, which is given by [58]

$$D(\lambda) = \frac{S_0}{4}\left(\lambda - \frac{\lambda_0^4}{\lambda^3}\right), \tag{2.24}$$

where S_0 is the zero dispersion slope and λ_0 is the zero-dispersion wavelength. In Fig. 2.3, λ_0 = 1314 nm and $S_0 = 0.089 \frac{\text{ps}}{\text{nm}^2\cdot\text{km}}$ which are values within the common tolerance ranges of commercial standard SMF [58].

The frequency variation of the dispersion profile is taken into account using a linear approximation via coefficients β_2 and β_3 (see Eq. (2.17)) obtained from a 1$^{\text{st}}$-order Taylor expansion of the frequency-dependent propagation constant $\beta(\lambda)$ [22]. $\beta_2(\lambda)$ and $\beta_3(\lambda)$ are obtained from the dispersion parameter D and dispersion slope S at the reference wavelength $\lambda_{\text{ref}} = 1550$ nm as

$$\beta_2(\lambda) = -\frac{D\lambda^2}{2\pi c}, \tag{2.25}$$

and

$$\beta_3(\lambda) = \frac{\lambda^3}{(2\pi c)^2}\left(2D + S\lambda\right), \tag{2.26}$$

where c is the vacuum speed of light. S is related to the dispersion parameter D as

$$S \triangleq \left(\frac{\partial D}{\partial \lambda}\right)_{\lambda=\lambda_{\text{ref}}}, \tag{2.27}$$

where λ_{ref} is the reference wavelength, usually taken to be 1550 nm. SMFs have typical D values varying from 16 to 20 $\frac{\text{ps}}{\text{nm}\cdot\text{km}}$, and S values around 0.067 $\frac{\text{ps}}{\text{nm}^2\cdot\text{km}}$ at 1550 nm [59]. The dispersion approximation using $D = 16.5$ $\frac{\text{ps}}{\text{nm}\cdot\text{km}}$ and $S = 0.067$ $\frac{\text{ps}}{\text{nm}^2\cdot\text{km}}$ at 1550 nm is shown in Fig. 2.3 (blue curve). Fig. 2.3 shows that the linear approximation of the dispersion is fairly accurate for ESCL-band simulations, but lacks accuracy when adding U- and/or O-band. To accurately reproduce OESCLU-band simulations, β_4 must be included [60, 61]. This parameter was included for the first time in the model described in Sec. 2.6 during this PhD research in [60] but is not included in this thesis.

To analyse the impact of dispersion, a useful parameter is the dispersion length, defined as $L_{\text{D}} = \frac{T_0^2}{|\beta_2|}$ [22], where T_0 is the pulse width (and $\frac{1}{T_0}$ the symbol rate). It provides the length scales over which dispersive effects become important for pulse

evolution. For modern communications operating in the C-band, assuming rectangular pulses, using $\beta_2 = 17.5\ \frac{\text{ps}^2}{\text{km}}$, and a symbol rate of 32 Gbaud and 100 Gbaud, dispersion lengths of approximately 55.8 km and 5.71 km are obtained. For each case, this shows that dispersion are negligible for fibre lengths $L < 55.8$ km and $L < 5.71$ km. Consequently, dispersion compensation becomes critical for modern fibre communication systems, where link lengths typically span from tens to thousands of kilometers.

2.4.3 Kerr effect

Fibre loss and dispersion are linear optical fibre impairments and can be partially compensated by linear filtering and equalisation (total compensation would only be possible if Eq. (2.16) were made only of linear impairments). On the other hand, Kerr and Raman effects are nonlinear effects. To understand the Kerr effect, loss, dispersion and Raman effects are neglected in Eq. (2.16) yielding

$$\frac{\partial E(z,T)}{\partial z} = j\gamma |E(z,T)|^2 E(z,T), \tag{2.28}$$

with the solution given by

$$E(z,T) = E(0,T) \exp\left(j\gamma |E(0,T)|^2 z\right). \tag{2.29}$$

From Eq. (2.29) it is possible to note that the received electrical field $E(z,T)$ experiences a phase in the time domain proportional to its instantaneous power $|E(0,T)|^2$. The higher the input power, the higher the nonlinear phase shift experienced by the signal. For lumped-amplified links, most of the nonlinear phase shift interaction happens in the first portions of the fibre. This is because of the fibre loss, which attenuates the nonlinear phase shift along the fibre length. For these systems, the effective fibre length represents the portion of the fibre span where the majority of phase shift interactions occur. For a standard SMF with a hypothetical average loss $\alpha = 0.18$ dB/km, the effective length $L_{\text{eff}} = \frac{1-e^{-\alpha L}}{\alpha} \approx \frac{1}{\alpha} = 24.13$ km, which means that most of the nonlinear effects occur in the first kilometres of the fibre span. However, in the more general case where gains from distributed amplification techniques such as RA, or power transfer from ISRS effect, happen in the transmission fibre (see Sec. 2.4.4), the nonlinear phase shift interactions happen around all portions of the fibre length, depending on the signal power evolution along the optical fibre length. This is because, for these systems, the loss term α in Eq. (2.16) is replaced by the generalised loss function $g'(z,T)$, which is calculated based on this power profile evolution (see Sec. 2.4.4 for details).

In a WDM transmission, where each wavelength or channel transmits independent

data, the channel of interest (COI) experience additional phase shit depending on the instantaneous power of the remaining channels. To visualise it, consider an electrical field E composed of N_{ch} independent channels, i.e.,

$$E = \sum_{i=1}^{N_{ch}} E_i. \tag{2.30}$$

Replacing Eq. (2.30) in Eq. (2.28), separating and taking the equation related to the COI E_1 yields

$$\frac{\partial E_1}{\partial z} = j\gamma \left| \sum_{i=1}^{N_{ch}} E_i \right|^2 E_1. \tag{2.31}$$

It seems the nonlinear phase shift increases indefinitely with the number of channels. However, this is not the case as dispersion leads to the walk-off between channels decreasing the nonlinear phase shift. In the frequency domain, the time-phase shift experienced by the signal creates additional spectral components. This process is known as FWM because it involves the interaction of four spectral frequencies. A new frequency component f is created by the interaction of frequencies at f_1, f_2 and f_3. This process satisfies the relation [22]

$$f = f_1 + f_2 - f_3. \tag{2.32}$$

If f_1, f_2 and f_3 are frequencies in the spectral range of the COI and whose interference coherently adds up at frequencies of the same channel, this process is referred to as self-phase modulation (SPM). Similarly, if the component f generated in the COI is a result of the beating frequencies f_1, f_2 and f_3 belonging either to the COI or one, and only one other channel, this process is referred to as cross-phase modulation (XPM). The remaining frequency component f generated in the COI involving at least two channels, other than the centre channel (the latter may or may not be involved), is also referred to as FWM.

The fibre nonlinear contribution is mathematically weighted within the pulse propagation equation (Eq. (2.16)) by the nonlinear parameter, γ. This parameter quantifies the strength of SPM, XPM, and FWM effects. Typical value of this parameter at $\lambda = 1550$ nm for SMF is $\gamma \approx 1.25 \frac{1}{\text{W·km}}$. For UWB systems, where several channels with different wavelengths are launched into the fibre, this parameter experiences a notable variation across the O to U bands. This variation is shown in Fig. 2.4, calculated following the equations in [58, 60].

Fig. 2.4 shows that at the shortest wavelength of the S band ($\lambda = 1460$ nm), $\gamma = 1.49 \frac{1}{\text{W·km}}$. At the longest wavelength of the L band ($\lambda = 1625$ nm), $\gamma = 1.1 \frac{1}{\text{W·km}}$. Over the SCL band, this corresponds to a nonlinear parameter variation of

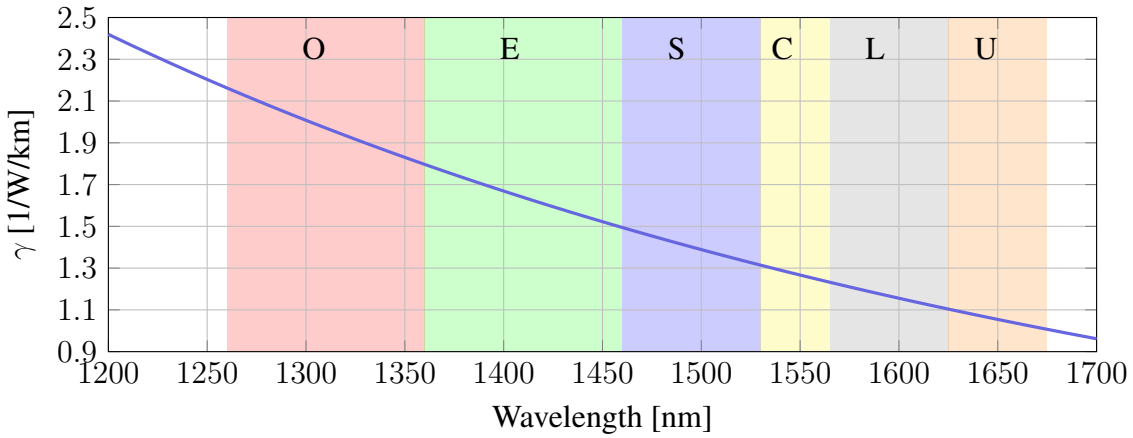

Fig. 2.4: Calculated wavelength-dependent nonlinear parameter of an ITU-T G652.D fibre.

approximately $0.4\frac{1}{\text{W·km}}$. Extending this analysis to the OESCLU band, a variation of $1.46\frac{1}{\text{W·km}}$ is obtained between the shortest wavelength of O-band ($\lambda = 1260$ nm) and the longest wavelength of the U-band ($\lambda = 1675$ nm).

As mentioned in this section, the nonlinear Kerr effect is proportional to the instantaneous power. To analyse its impact, a useful parameter is the nonlinear length, defined as $L_{\text{NL}} = \frac{1}{\gamma P}$ [22], where P is the pulse power. It provides the length scales over which nonlinear effects become important for pulse evolution. Similar to the analysis in Sec. 2.4.2, for modern communications operating in the C-band, using $\gamma = 1.25\frac{1}{\text{W·km}}$, and channel power of 2 dBm, assuming duty cycle of $\frac{1}{2}$, nonlinear length $L_{\text{NL}} = 252.4$ km. This shows that nonlinear impairments are not the main contributing factor for fibre lengths L <252.4 km. However, as launch power increases, nonlinear effects become significant and need to be modelled and evaluated, particularly in modern optical fibre communications, where high-power amplification technologies such as Raman amplifiers are employed to enhance system performance.

2.4.4 Stimulated Raman scattering effect

Another nonlinear effect described by Eq. (2.16) is the stimulated Raman scattering. It leads to a power transfer from shorter-wavelength channels to longer-wavelength channels, and it is also responsible for one of the most important amplification techniques in optical fibres, the Raman amplification or RA. By neglecting fibre dispersion, Kerr effect and writing explicitly the convolution between $E(z, f)$, $\overline{E(z, -f)}$ and $E(z, f)$, Eq. (2.17) can be rewritten as (the z dependence of $E(z, f)$ has been omitted for simplicity)

$$\frac{\partial E(f)}{\partial z} = -\frac{\alpha}{2}E(f) - 2\pi\gamma T_r \iint f_2 E(f_1) * \overline{E(f_1 - f_2)} * E(f - f_2)\, df_1\, df_2. \quad (2.33)$$

Considering a transmitted signal made of two continuous-wave (CW) tones located at relative frequencies 0 and f_k with powers $P_1 = |E_1|^2$ and $P_k = |E_k|^2$, i.e.,

$$E(f) = E_1\delta(f) + E_k\delta(f - f_k), \tag{2.34}$$

where $\delta(\cdot)$ is the Dirac delta function. Substituting Eq. (2.34) in Eq. (2.33), yields to

$$\begin{aligned}&\frac{\partial}{\partial z}[E_1\delta(f) + E_k\delta(f - f_k)] = -\frac{\alpha}{2}[E_1\delta(f) + E_k\delta(f - f_k)]\\ &- 2\pi\gamma T_r \iint f_2[E_1\delta(f_1) + E_k\delta(f_1 - f_k)]\\ &[E_1\delta(f_1 - f_2) + E_k\delta(f_1 - f_2 - f_k)][E_1\delta(f - f_2) + E_k\delta(f - f_2 - f_k)]\, df_1\, df_2.\end{aligned} \tag{2.35}$$

The convolution integrals in Eq. (2.35) are only non-zero for the frequency combinations $\{f_1 = 0 \text{ and } f_2 = -f_k\}$ and $\{f_1 = f_k \text{ and } f_2 = f_k\}$. This yields to

$$\begin{aligned}&\frac{\partial}{\partial z}[E_1\delta(f) + E_k\delta(f - f_k)] = -\frac{\alpha}{2}[E_1\delta(f) + E_k\delta(f - f_k)]\\ &- 2\pi\gamma T_r f_k \left[|E_k|^2 E_1\delta(f) - |E_1|^2 E_k\delta(f - f_k)\right].\end{aligned} \tag{2.36}$$

Eq. (2.36) can be written as two coupled equations because of the orthogonality property of delta functions and further translated to the power evolution of the CW tones using the relation $\frac{\partial P}{\partial z} = \frac{\partial \overline{E}}{\partial z}E + \frac{\partial E}{\partial z}\overline{E}$, yielding to

$$\begin{aligned}\frac{\partial}{\partial z}P_1 &= -\alpha P_1 \overbrace{+4\pi\gamma T_r f_k P_k P_1}^{\text{Power gain}}\\ \frac{\partial}{\partial z}P_k &= -\alpha P_k \underbrace{-4\pi\gamma T_r f_k P_1 P_k}_{\text{Power loss}}.\end{aligned} \tag{2.37}$$

Eq. (2.37) shows that the Raman effect translates into a transfer of power. The channel located at the frequency $f = f_k$ provides gain to the channel at the frequency $f = 0$ at the cost of its depletion, i.e., that of $f = f_k$. This analysis can be generalised for an input field consisting of $\mathrm{N_{ch}}$ equally-spaced CW tones, i.e., $E(f) = \sum_{i=1}^{\mathrm{N_{ch}}} E_i\delta(f - f_i)$, with each channel power $P_i = |E_i|^2$. The following yields to the so-called coupled Raman equations. For the COI i, this equations is:

$$\frac{\partial P_i}{\partial z} = \underbrace{-\sum_{k=i+1}^{\mathrm{N_{ch}}} \frac{f_k}{f_i} g_i(|\Delta f|) P_k P_i}_{\text{ISRS power loss}} + \underbrace{\sum_{k=1}^{i-1} g_i(|\Delta f|) P_k P_i}_{\text{ISRS power gain}} \overbrace{-\alpha_i P_i}^{\text{Fibre loss}}, \tag{2.38}$$

where, P_i, f_i are the power and frequency of the COI, P_k, f_k are the power and frequency of the remaining WDM channels, $g_i(|\Delta f|)$ is the wavelength-dependent polarisation averaged, normalised (by the wavelength-dependent $A_{\text{eff},i}$) Raman gain spectrum for a frequency separation $|\Delta f| = |f_i - f_k|$ and α_i is the wavelength-dependent attenuation coefficient. In Eq. (2.38), the COI located at frequency f_i receives power from channels located at wavelengths shorter than $\lambda_i = \frac{c}{f_i}$ (or frequencies higher than f_i). Similarly, the COI provides power at the cost of its depletion for channels located at wavelengths longer than λ_i (or frequencies lower than f_i). This effect happens in all the WDM channels and is known as the ISRS effect, and is illustrated in Fig. 2.5. It can be seen that, shorter-wavelength channels transfer

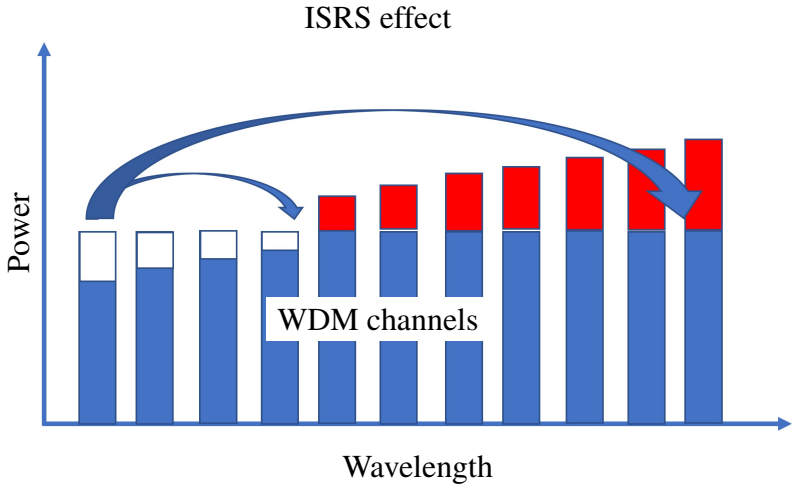

Fig. 2.5: Illustration of the ISRS effect.

power to longer-wavelength channels. The amount of power that is transferred from one channel to another follows the Raman gain spectrum $g_i(|\Delta f|)$. This gain is normalised to the fibre-effective core area A_{eff} [58]. Similarly to the nonlinear parameter γ, the effective area experiences a notable variation over frequency. A typical A_{eff} profile for a standard SMF is shown in Fig. 2.6, calculated following the equations in [58, 60]. Because of such variation, the Raman gain spectrum also varies for each channel. A typical Raman gain profile for three different channels at $\lambda = 1370$ nm, $\lambda = 1495$ nm and $\lambda = 1620$ nm is shown in Fig. 2.7,also calculated using equations in [58, 60]. This figure shows that the gain/loss of one channel to another depends on their frequency separation. The maximum Raman gain is achieved at a channel frequency separation of around 13.4 THz. From Eq. (2.38), the term $g_i(|\Delta f|)P_kP_i$ shows that the amount of gain/loss also depends on the power of the two involved channels. For a uniform launch power, the channel located at $\lambda = 1550$ nm ($f = 193.41$ THz) will receive the most power gain from a channel located at $f = 193.41 + 13.5 = 206.81$ THz ($\lambda = 1450$ nm). Similarly, it will experience a maximum power loss for a channel located at $\lambda = 1665$ nm. Additionally, the effective

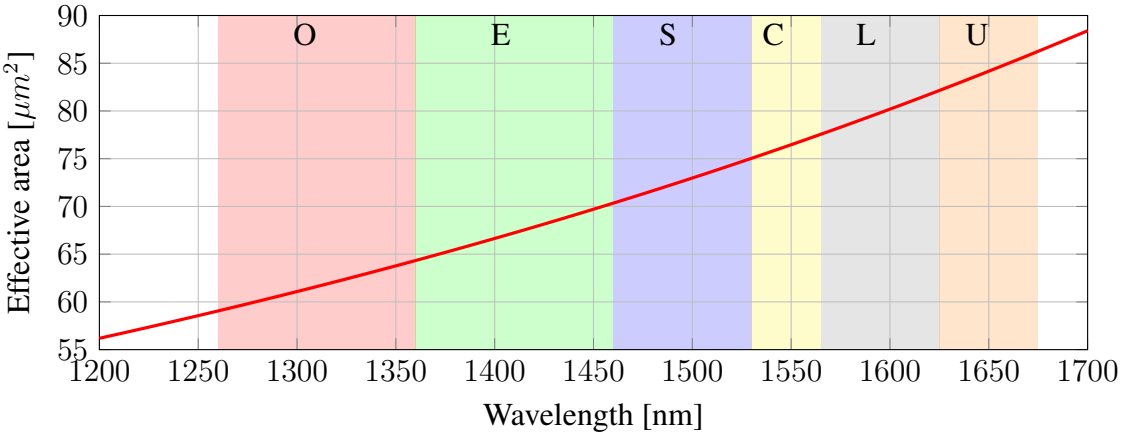

Fig. 2.6: Calculated wavelength-dependent effective area of an ITU-T G652.D fibre.

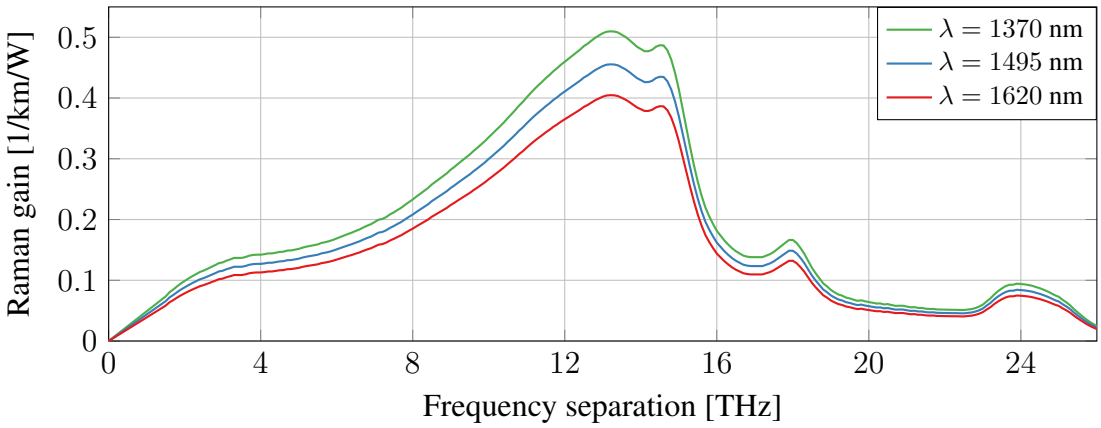

Fig. 2.7: Calculated Raman gain spectrum of an ITU-T G652.D fibre for three different wavelengths.

area profile has a substantial variation over the OESCLU band reflecting a higher Raman gain for short-wavelength channels compared to the long-wavelength ones as shown in Fig. 2.7.

The Raman effect in an optical fibre can also be used to amplify the WDM signal. This is done by placing high power CW pumps at shorter wavelength channels to amplify the WDM channels. This strategy is known as RA. To that end, Eq. (2.38) can be further generalised when pumps are presented in the input electrical field $E(f)$, i.e., $E(f) = \sum_{i=1}^{\mathrm{N_{ch}}} E_i \delta(f - f_i) + \sum_{p=1}^{\mathrm{N_p}} E_p \delta(f - f_p)$, where each pump carries a power

$P_p = |E_p|^2$. This yields to the Raman equations in the presence of RA, given by

$$\pm\frac{\partial P_i}{\partial z} = \overbrace{-\sum_{k=i+1}^{N_{ch}} \frac{f_k}{f_i} g_i(|\Delta f|) P_k P_i}^{\text{ISRS loss}} \overbrace{- \sum_{p:f_i>f_p} \frac{f_p}{f_i} g_i(|\Delta f|) P_p P_i}^{\text{RA loss}} \underbrace{+\sum_{k=1}^{i-1} g_i(|\Delta f|) P_k P_i}_{\text{ISRS gain}} \underbrace{+ \sum_{p:f_i<f_p} g_i(|\Delta f|) P_p P_i}_{\text{RA gain}} \underbrace{- \alpha_i P_i}_{\text{Fibre loss}}, \tag{2.39}$$

where P_p and f_p are the power and the frequency of the pumps, $|\Delta f|$ is generalised to include pumps, i.e., $|\Delta f| = |f_i - f_l|$, $l = k, p$. Pumps can be launched in the fibre with the signals at the fibre input, and/or in the opposite direction of the signal, i.e., in the fibre output. These are respectively known as FW-RA and BW-RA. In Eq. (2.39) this is captured by the symbol $\pm$, which represents the pump under consideration, i.e., $+$ for signals and FW-pump, and $-$ for BW-pump configurations.

RA has a similar effect when compared to the ISRS effect. It also produces a power transfer, but from pumps to the channels. When acting jointly with the ISRS effect, this transfer of power occurs in all directions, i.e., from pumps to pumps, pumps to channels and channels to channels, illustrated in Fig. 2.8.

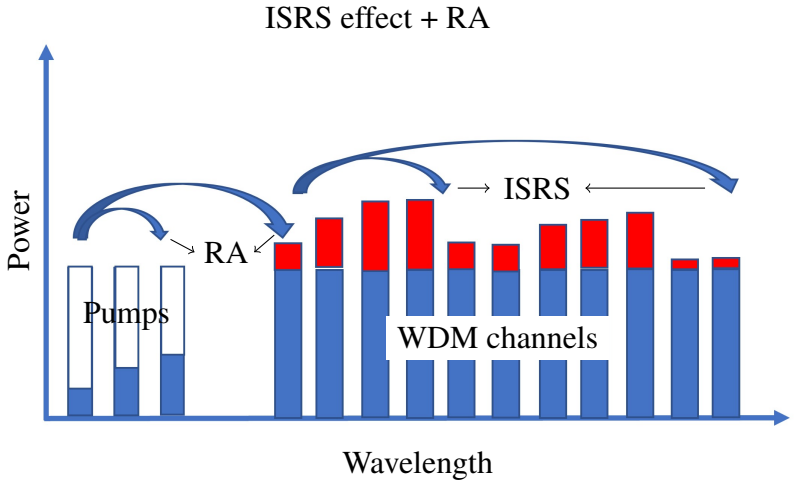

Fig. 2.8: Illustration of the ISRS effect jointly with RA.

RA also follows the Raman gain spectrum in Fig. 2.7 and in this case, the amount of power transferred from the pumps to each channel will be dependent on the pump wavelengths and their powers. The pumps are usually chosen to give gains in the specific portions of the signal spectrum. This selection is done by placing the pumps at an approximate spacing of 13.4 THz from the desired regions of the signal spectrum to be amplified. However, this spacing can vary significantly when multiple pumps are introduced into the transmission system, as numerous interactions (as per Eq. (2.39))

occur between the pumps and the signal. This requires the use of optimisation algorithms to determine the optimal pump wavelength and power allocation to maximise the gain in the desired region of the signal spectrum.

The Raman effect is taken into account as power-dependent loss in Eq. (2.16). This equation is then simplified to yield

$$\frac{\partial E(z,T)}{\partial z} = \frac{g'(z,T)}{2}E(z,T) - j\frac{\beta_2}{2}\frac{\partial^2 E(z,T)}{\partial T^2} + \frac{\beta_3}{6}\frac{\partial^3 E(z,T)}{\partial T^3} + j\gamma|E(z,T)|^2 E(z,T), \tag{2.40}$$

where $g'(z,T)$ is a generalised loss function related with the solution of Eq. (2.39) (which is given by $P(L)$) as $\rho(L,T) = \frac{P(L)}{P(0)} = e^{\int_0^L g'(z,T)\,dz}$, where $P(0) = P_i$ is the input or per-channel launch power. Eq. (2.40) is used to calculate fibre propagation effects in the presence of RA and ISRS. For UWB transmission systems, the effect of ISRS on the Kerr nonlinearity was previously studied in [33].

The research described in this thesis was focused on the analysis of the more general case involving RA jointly with the ISRS effect as outlined in Chapter 1. More importantly, new analytical real-time models are developed in Chapters 3 and 4 and used in Chapter 5 for nonlinear optimisation routines. Moreover, these models can assess the impact of RA and ISRS in the AIR of optical systems, enabling throughput maximisation, and optimised system design.

2.5 Split-step Fourier method

So far propagation effects included in Eq. (2.16) have been described but the solution of this equation has not been given. Its approximate solution is obtained through stimulation using the SSFM. This method has been used throughout this research to validate the proposed analytical models. The main disadvantage of SSFM is the computational resources needed to perform such simulations, which exponentially scale with the number of channels and optical bandwidth. Thus, especially for UWB transmission systems, analytical models must be derived to achieve a feasible assessment of the system performance for multiple transmission scenarios, and thus, have been the main goal of this research. The SSFM gives the approximate solution of the propagated field at the end of the fibre, i.e., $E(L)$ for an input signal $E(0)$ by solving Eq. (2.40). In the context described in Sec. 2.2, this is equivalent to finding the signal $f(x)$ for a single span or $f^n(x)$ for multiple spans.

The SSFM is a pseudo-spectral numerical method used to solve nonlinear partial differential equations, like that in Eq. (2.40). The approach is to write this equation as

$$\frac{\partial E(z,T)}{\partial z} = (\hat{D} + \hat{N})E(z,T), \tag{2.41}$$

where $\hat{D} = \frac{g'(z,T)}{2} - j\frac{\beta_2}{2}\frac{\partial^2}{\partial T^2} + \frac{\beta_3}{6}\frac{\partial^3}{\partial T^3}$ is the dispersion operator and $\hat{N}(z) = j\gamma|E(z,T)|^2$ is the nonlinear operator. The SSFM results in an approximate solution by assuming that in propagating the optical field over a small distance h, the dispersion and the nonlinear operators act independently. In the first step, $\hat{D} = 0$ in Eq. (2.41). In the second step, $\hat{N}(z) = 0$ in Eq. (2.41). Thus, after a small distance h, the solution of this equation is given by

$$E(z+h,T) \approx e^{\int_z^{z+h} h\hat{N}(z)\,dz} e^{h\hat{D}} E(z,T), \tag{2.42}$$

where the linear operator in the right-hand side of Eq. (2.42) is evaluated in the Fourier domain as

$$e^{h\hat{D}} E(z,T) = \mathcal{F}^{-1}\{e^{h\mathcal{F}\{\hat{D}\}}\mathcal{F}\{E(z,T)\}\}. \tag{2.43}$$

This procedure is applied repeatedly, with the solution of the previous step as an initial condition for the following step. The algorithm ends when the full fibre length is covered, i.e., $z = L$. The solution obtained by this method converges to the exact solution of Eq. (2.41) in the limit of $h \to 0$, however, the smaller the step size h, the higher the computational complexity.

Different implementations of the SSFM algorithm are possible [60, 62] to increase its accuracy and speed up computations. In the research described in this thesis, SSFM simulations were used to validate the accuracy of the proposed analytical models in Chapters 3, 4, 5. To that end, SSFM were implemented ensuring simulations with small step size h converging to the exact solution of Eq. (2.41). The SSFM algorithm used in this thesis is based on the approach outlined in [60, 62]. It incorporates modifications to the original algorithm described in this section, including parallelisation across multiples GPUs to speed up computations, enabling the results presented in this PhD research.

2.6 The Gaussian noise model

As described in the previous section, the solution of the NLSE in Eq. (2.40) can be obtained via simulation using SSFM. This is because, in its current form, Eq. (2.40) has no explicit solution, i.e., solutions containing integrals or analytical functions. The possibility of obtaining an explicit solution enables understanding how fibre propagation effects scale with fibre parameters such as bandwidth, span length, etc. Furthermore, integral solutions allow the derivation of closed-form or analytical models to overcome the computational complexity of integral calculations and SSFM simulations. These integral solutions yield approximate descriptions of the optical

fibre channel, serving as bounds to the maximum AIR [63]. These descriptions are provided by nonlinear models which approximate the NLSE to some extent.

To obtain an explicit solution of the NLSE, several nonlinear models have been proposed to date, based on approximate solutions of NLSE, for instance, using regular perturbation (RP) [25, 26, 27, 28, 29], logarithmic perturbation [30], or Volterra series [64, 65]. For the case of using RP theory, the NLSE is approximate to 1$^{\text{st}}$-order around some fibre parameter and an approximate explicit solution of this equation containing integrals is obtained. Models relying on this approach can be found in [27, 29, 28, 31, 33]. An advantage of this approach is the possibility of approximating the NLSE as a linear equation perturbed with a nonlinear term, which is the idea behind Eq. (2.3), and thus, the NLI can be treated as an additive noise term and eventually assumed as AWGN. This is the case, for instance, of the GN and also of the EGN models [27, 28, 33]. Both models are derived using a 1$^{\text{st}}$-order perturbation approach with respect to the nonlinear parameter γ in the frequency domain together with additional assumptions and approximations. Following this approach, the optical link can be considered an AWGN channel, for which efficient coding, modulation, and detection techniques are available, and system performance and channel capacity can be computed in closed form. Because of their simplicity and efficiency, these are the reference models presented and used in this thesis to derive closed-form solutions.

A brief description of the GN and EGN models is described. Within the 1$^{\text{st}}$-order RP approach, the electric field is written as a perturbation series with respect to the nonlinear parameter γ as

$$E(z,f) = E^{(0)}(z,f) + \gamma E^{(1)}(z,f) + \mathcal{O}(\gamma^2). \tag{2.44}$$

In Eq. (2.44), the electrical field $E(z,f)$ is described as $E^{(0)}(z,f)$ plus an additional perturbation $E^{1}(z,f)$, which is scaled by the nonlinear parameters γ. The following approximation is accurate provided that the perturbation term $\gamma E^{(1)}(z,f)$ is small compared to $E^{(0)}(z,f)$. This is not the case for scenarios of extremely low fibre loss (see Sec. 3.2.2), high power spectral density (see [60]), or high values of γ; in these scenarios, higher-order terms have to be included in Eq. (2.44). However, currently deployed optical systems operate with fibre parameters and power levels within the range of validity of Eq. (2.44). Additionally, note that, in the context of Sec. 2.2, Eq. (2.44) represents the necessary step to obtain Eq. (2.3) from Eq. (2.2).

Let $\Gamma(z,f) = \int_0^z \tilde{\Gamma}(\zeta,f)\,d\zeta$, with $\tilde{\Gamma}(\zeta,f) = \frac{g'(\zeta,f)}{2} + j2\pi^2\beta_2 f^2 + j\frac{4}{3}\pi^3\beta_3 f^3$. Inserting Eq. (2.44) in Eq. (2.40), neglecting 2$^{\text{nd}}$-order terms $\mathcal{O}(\gamma^2)$ and separating 0$^{\text{th}}$

and 1st-order terms yields

$$\begin{aligned}\frac{\partial E^{(0)}(z,f)}{\partial z} &= \tilde{\Gamma}(z,f)E^{(0)}(z,f),\\ \frac{\partial E^{(1)}(z,f)}{\partial z} &= \tilde{\Gamma}(z,f)E^{(1)}(z,f) + jE^{(0)}(z,f) * \overline{E^{(0)}(z,-f)} * E^{(0)}(z,f).\end{aligned} \tag{2.45}$$

The 0th-order solution of Eq. (2.45) is simply the linear part of the NLSE and its solution is given by

$$E^{(0)}(L,f) = E(0,f)e^{\Gamma(L,f)}, \tag{2.46}$$

where $E(0,f)$ is the input electrical field, or the transmitted signal. Using the initial condition for the 1st-order field $E^{(1)}(0,f) = 0$, the 1st-order solution $E^{(1)}(z,f)$ is given by

$$E^{(1)}(L,f) = e^{\Gamma(L,f)} \int_0^L \frac{jE^{(0)}(\zeta,f) * \overline{E^{(0)}(\zeta,-f)} * E^{(0)}(\zeta,f)}{e^{\Gamma(\zeta,f)}}\, d\zeta. \tag{2.47}$$

The derivation of Eq. (2.47) can be found in Appendix A of [33]. This equation represents the solution of the NLSE using the 1st-order RP approach. Based on Eq. (2.44), the received electrical field is impaired by a nonlinear term $E^{(1)}(z,f)$. The actual transmitted signal is $E^{(0)}(0,f)$, and is easily recovered from $E(L,f)$ (see Eq. (2.46)) after DSP, i.e., by filtering $E(L,f)$ using Eq. (2.23). To compute the amount of NLI presented in the signal, the power spectral density (PSD) of $\lambda E^{(1)}(L,f)$ has to be computed. Consider that the transmitted signal is made up of an infinitely narrow frequency comb, spectrally shaped according to the PSD of the transmitted signal and where each spectral line carries a complex symbol ξ_n. This assumption is the basis of the EGN and GN models and greatly simplifies the mathematical steps required to obtain the NLI PSD of $\lambda E^{(1)}(L,f)$. Using this assumption, the transmitted field $E(0,f)$ is written as

$$E(0,f) = \sqrt{f_0 G_{\text{Tx}}(f)} \sum_{n=-\infty}^{\infty} \xi_n \delta(f - nf_0), \tag{2.48}$$

where $f_0 \to 0$ and $G_{\text{Tx}}(f)$ is the PSD of the signal at the Tx. Consider each symbol ξ_n to be a complex circular Gaussian distributed symbol, which is the main assumption of the GN model, then by inserting Eq. (2.48) in Eq. (2.47) and exploiting the statistical independence of the symbols at different frequencies, the NLI PSD

$G_{\text{NLI}}(f) = \mathbb{E}(|\lambda E^{(1)}(L,f)|^2)$ can be expressed as [33]

$$G_{\text{NLI}}(f) = \frac{16}{27}\gamma^2 \int\int G_{\text{Tx}}(f_1)G_{\text{Tx}}(f_2)G_{\text{Tx}}(f_1+f_2-f) \left|\int_0^L \frac{\rho(\zeta,f_1)\rho(\zeta,f_2)\rho(\zeta,f_1+f_2-f)}{\rho(\zeta,f)} e^{j\phi(f_1,f_2,f,\zeta)} d\zeta\right|^2 df_1 df_2, \tag{2.49}$$

where $\phi(f_1,f_2,f,\zeta) = -4\pi^2(f_1-f)(f_2-f)[\beta_2+\pi\beta_3(f_1+f_2)]\zeta$, and $\rho(z,f) = \frac{P(z)}{P(0)}$ is the normalised signal power profile. For multi-span systems, where each span is assumed to have identical fibre parameters and signal power profiles, the phased-array term $\mathcal{X}(f_1,f_2,f)$, given by

$$\mathcal{X}(f_1,f_2,f) = \frac{\sin\left[\frac{1}{2}n\phi(f_1,f_2,f,L)\right]}{\sin\left[\frac{1}{2}\phi(f_1,f_2,f,L)\right]}, \tag{2.50}$$

must be inserted into the integral in Eq. (2.49). This term models the coherent accumulation of the NLI over the fibre spans. For multi-span systems with non-identical fibre parameters, including different per-channel launch powers, the phased-array term given by Eq. (2.50) cannot be used, as this expression assumes identical fibre parameters for each span. For non-identical fibre parameters, some valid approximations and equations for the phase-array term can be found in [33, 44] and are described in Chapter 3.

The NLI PSD given by the GN model is given by Eq. (2.49) and its derivation can also be found in Appendix A of [33]. Because it was assumed that each symbol ξ_n in Eq. (2.48) is Gaussian distributed, representing a Gaussian random process, the GN model described by Eq. (2.49) is valid for Gaussian modulated signals only. In [66], it was shown that arbitrary signals using different modulation formats other than Gaussian, do not converge to a joint Gaussian process due to fibre propagation (even in the presence of dispersion only). Indeed, Eq. (2.49) overestimates the amount of NLI for other constellations such as shaped or unshaped/square QAM or quadrature phase shift keying (QPSK) formats. To correctly account for arbitrary constellation formats, the GN model was extended in [28] yielding to the so-called EGN model. This model accounts for arbitrary modulation formats, including shaped and square constellations, by including further integral terms in addition to the one in Eq. (2.49). Various limitations and shortcomings of these models have been pointed out, and some of these are summarised in [67]. Yet, because of its simplicity compared to other nonlinear models the GN model is the most widely used NLI model for fibre propagation. It should be noted that Eq. (2.49) was first published in 1993 [68], and later presented in other works and summarised in a more detailed and complete form in [27].

It should finally be highlighted, that the statistics of NLI in Eq. (2.49) is assumed to be Gaussian, and based on the RP approach is also additive. Indeed, the statistic of the

perturbation term of the received signal $E^{(1)}(L, f)$ and its PSD (Eq. (2.49)) are assumed to be Gaussian - this is one of the main assumptions of the GN and EGN models and its accuracy was validated for high-dispersive links in [69]. On the other hand, the statistic of the input signal $E(0, f)$ is Gaussian for the GN model and arbitrarily for the EGN model.

The model described in Eq. (2.49), is an integral model requiring a lot of computational resources to solve the integrals involved in its calculation. Additionally, its computational complexity scales with the number of channels. For UWB systems, where multiple WDM channels are transmitted, the computational time to solve Eq. (2.49) easily becomes unmanageable for optimisations and real-time applications. In Chapters 3 and 4, new proposed analytical models of GN and EGN models are described. In Chapter 5, analytical models are applied in optimisation algorithms to achieve transmission system throughput maximisation.

2.7 Analytical models

The EGN and GN models, described in Sec. 2.6, are models in an integral formulation. Fig. 2.9 presents a chart on the differences between the various frequency domain GN-based nonlinear models, and how each one of them differs in their formulation, i.e., from the NLSE whose solution is obtained via simulation, to the integral and analytical or closed-form formulations of GN and EGN models.

For these models, the calculation of the NLI PSD (e.g. for Gaussian signals in Eq. (2.49)) depends on the normalised power profile evolution along the fibre, captured by the function ρ (see in Eq. (2.49)). The first integral GN model, obtained in [27] and derived for C-band systems only, is valid if the only effect changing the transmitted power profile of the fibre is the wavelength-dependent fibre loss. The same happens for the first EGN model in [28]. These integral models were further extended in [33, 70] to include the ISRS effect in the function ρ (essential for UWB transmission, i.e., bandwidths larger than 5 THz), leading to Eq. (2.49) valid for Gaussian signals only. The extension for arbitrary constellations was further developed in [37] taking into account the most impactful integral contribution term to NLI in [28]. The versatility of the model in [33] also enables the inclusion of RA effects but yet in an integral formulation only as opposed to a closed-form expression or analytical formulation.

When it comes to the analytical expressions for the EGN and GN models, valid for UWB systems, their validity range is limited compared to the integral formulations. This is because of the approximations required to obtain these closed-form solutions. Numerous closed-form expressions have been proposed to date [71]. Closed-form formulae of the integral GN/EGN model in the presence of ISRS [33, 37] were developed in [34, 35, 37]. These formulae can account for ISRS effect using a

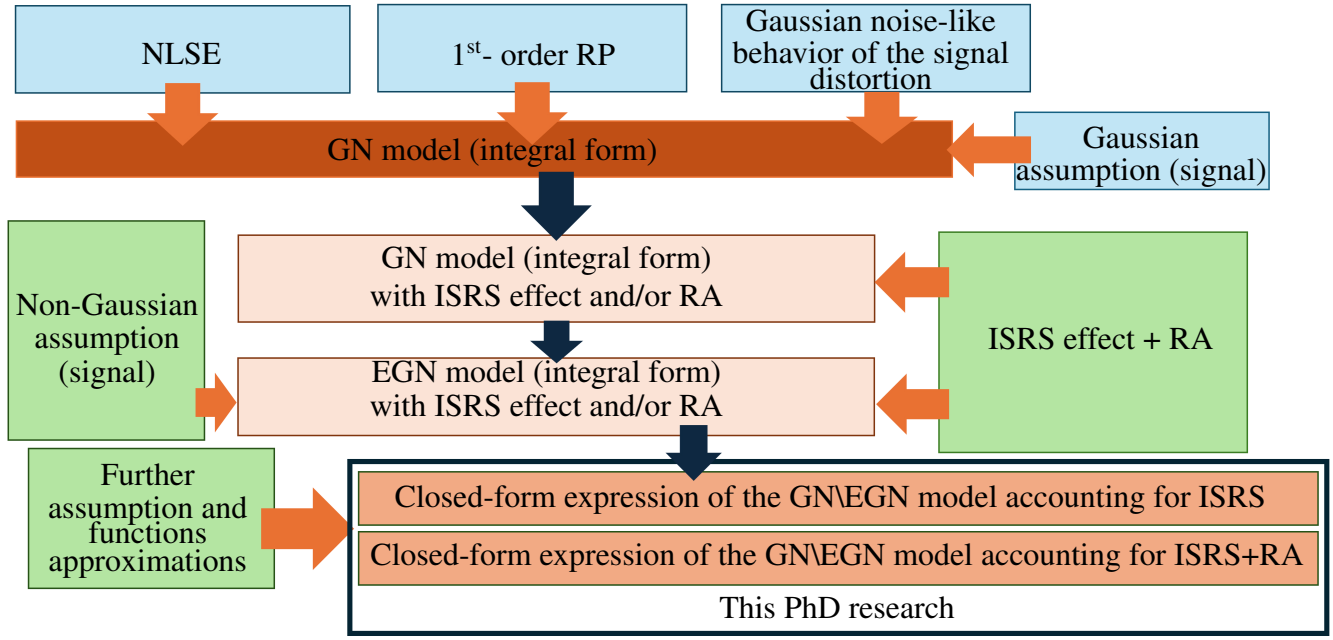

Fig. 2.9: Nonlinear models based on GN and EGN models.

semi-analytical approach, where a suitable exponential function is used to reproduce the function ρ. The formulae in [35, 37] have different mathematical derivations and assumptions when compared to the one in [34] but account for the same scenarios, i.e., they are able to accurately predict the ISRS effect, essential for UWB transmission as discussed in Sec. 2.4.4.

In this thesis, the mathematical approach used to derive the new closed-form expressions follows the basis of the approach in [35, 37]. A fundamental step in deriving any closed-form expression is to reproduce the signal profile given by Eq. (2.38) in the case of ISRS effect only and in Eq. (2.39) for the more general case of ISRS + RA. This is because the NLI PSD in Eq. (2.49) depends on the normalised signal profile given by the function ρ. In the case of models derived in [34, 35, 37], analytical or semi-analytical expressions of equation Eq. (2.38) were obtained. For the models in [35, 37], this expression is

$$\rho(z, f_i) = \frac{P(z, f_i)}{P(0, f_i)} \approx e^{-\alpha_i z}[1 - C_r P_{\text{tot}} L_{\text{eff}}(z) f_i], \tag{2.51}$$

where $L_{\text{eff}}(z) = \frac{1-e^{-\alpha_i' z}}{\alpha_i'}$, C_r is the slope of the linear regression of the normalised Raman gain spectrum, and P_{tot} is the total transmitted optical power. Note that, α' is also the fibre loss, but it is different from α because it is an optimisation parameter.

Indeed, because Eq. (2.51) are not fully able to reproduce analytically all the effects of the solution of Eq. (2.38), α, α' and C_r are parameters which are fitted to correctly reproduce this solution. A more complex function rather than the one in Eq. (2.51) may be able to fully analytically capture the effects of Eq. (2.38), however, it would complicate the obtention of an analytical expression for Eq. (2.49). This is the main reason why Eq. (2.51) is chosen as a set of exponential functions - they are easily integrable and the fitting optimisation (which yields a semi-analytical function for Eq. (2.51)) enables its application in a broad range of scenarios with the ISRS effect. Details of this approach are given in [33] and in Chapters 3 and 4.

Fig. 2.10 shows an example of power profile evolution with distance in fibre obtained using Eq. (2.38), and the semi-analytical solution shown in Eq. (2.51). The analysis uses a standard 80 km SMF with wavelength-dependent attenuation profile shown in Fig. 3.1. The Raman gain spectrum is considered to be the same for all the channels and is shown in Fig. 3.2 (details on how this profile is obtained can be found in Chapter 3). The system consisted of a WDM transmission with N_{ch}=181 channels spaced by 100 GHz and centred at 1540 nm. Each channel carried 1 dBm launch power and was modulated at the symbol rate of 96 GBd, resulting in a total bandwidth of 18 THz. Longer-wavelength channels receive power from shorter-wavelength channels due to the ISRS effect, yielding higher power propagating through the fibre for these channels. Note that Eq. (2.51) is an exponential decay only, and thus is unable to reproduce scenarios given by RA shown in Eq. (2.39), for instance in BW pumping schemes where exponential signal power growth happens at the end of the fibre. In Chapter 4, a new semi-analytical function is proposed to account for cases where RA is used.

Semi-analytical descriptions of the NLI are described next. The NLI noise is defined as

$$P_{\text{NLI}} = \eta_n(f_i) P_i^3, \tag{2.52}$$

where $\eta_n(f_i)$ is the nonlinear coefficient obtained at the end of the n^{th} span. The nonlinear coefficient can be simply obtained by integrating the NLI PSD in Eq. (2.49) over the COI bandwidth and normalising by the channel launch power as

$$\eta_n(f_i) = \frac{1}{P_i^3} \int_{-\frac{B_i}{2}}^{\frac{B_i}{2}} |H(f)|^2 G_{\text{NLI}}(f) df \approx \frac{B_i}{P_i^3} G_{\text{NLI}}(f_i), \tag{2.53}$$

where $H(f)$ is the transfer function of the matched filter at the Rx given by Eq. (2.23). The filter $H(f)$ is inside the "Optical Receiver + DSP" block shown in Fig. 2.2. The approximation in Eq. (2.53) assumes a rectangular transfer function with COI bandwidth B_i. It also assumes the NLI is uniformly distributed over the COI

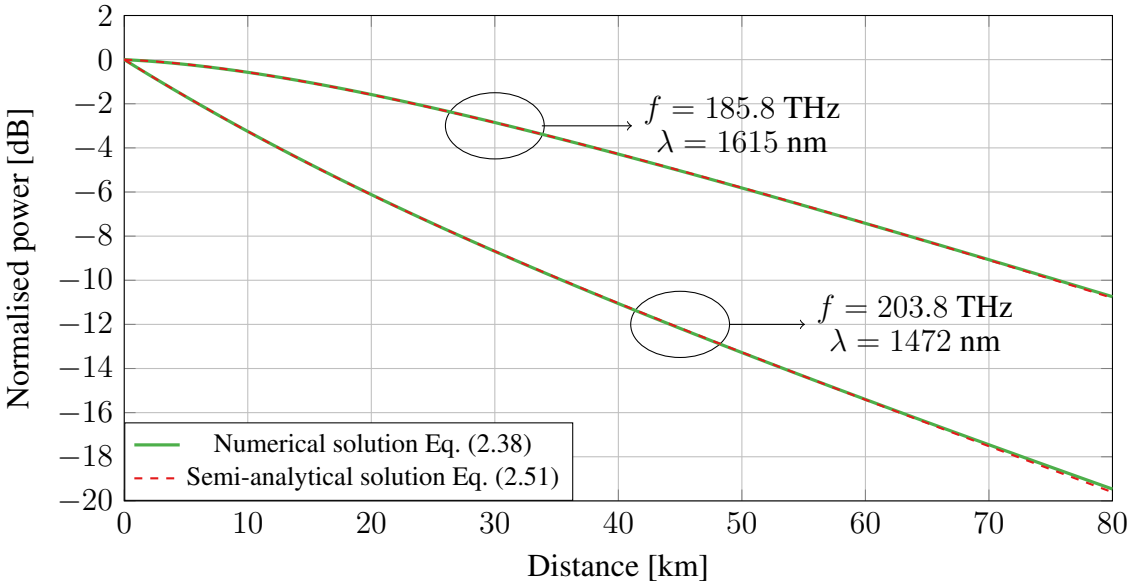

Fig. 2.10: Signal power evolution along the fibre length obtained using the numerical solution of the Raman differential equations in the presence of ISRS effect only in Eq. (2.38), and the semi-analytical solution shown in Eq. (2.51).

bandwidth. The approximation in Eq. (2.53) is useful to obtain closed-form expressions as arbitrary matched filter shapes are difficult to include analytically. Moreover, the approximation error is negligible in WDM systems with channel spacing close to the channel baud rate (e.g. Nyquist-spaced channels).

The nonlinear coefficient obtained at the end of the n-th span, $\eta_n(f_i)$, can be written as [28, Eq. 1],

$$\eta_n(f_i) = \eta_{\text{GN},n}(f_i) + \eta_{\text{corr,n}}(f_i), \tag{2.54}$$

where $\eta_{\text{GN},n}(f_i)$ and $\eta_{\text{corr,n}}(f_i)$ are respectively the nonlinear coefficient contributions accounting for Gaussian modulated symbols [33], i.e., a contribution from GN model and its correction term accounting for the dependence of the NLI on the modulation format [37], which is a contribution from the EGN model. For Gaussian modulated signals, the correction term $\eta_{\text{corr,n}}(f_i)$ vanishes and one obtains the model in [33], also given by Eq. (2.49).

The integral version of the GN model contribution (Eq. (2.49)), accounts for all the nonlinear interactions, namely SPM, XPM and FWM, as discussed in Sec. 2.4.3. To obtain a closed-form solution, it greatly simplifies the derivation if FWM contributions are neglected. This approach is shown to be accurate for systems operating with SMF in the ESCLU band, where dispersion values $D \gtrapprox |5|$. The approach however is not valid for O-band transmission as $D \lessapprox |5|$. Thus, by neglecting FWM contributions,

$\eta_{\text{GN},n}(f_i)$ in Eq. (2.54) can be approximated as [35, Eq. 5]

$$\eta_{\text{GN},n}(f_i) \approx \sum_{j=1}^{n} \left(\frac{P_{i,j}}{P_i}\right)^2 \cdot [\eta_{\text{SPM}_j}(f_i) n^{\epsilon} + \eta_{\text{XPM}_j}(f_i)], \tag{2.55}$$

where $\eta_{\text{SPM}_j}(f_i)$ is the SPM contribution and $\eta_{\text{XPM}_j}(f_i)$ is the total XPM contribution to the NLI, both generated in the j-th span. $P_{i,j}$ is the power of channel i launched into the j-th span. The accumulation of the NLI with the number of spans (described by Eq. (2.50)), is taken into account using the so-called coherent factor ϵ [27, Eq. 22] as opposed to the phase-array term in Eq. (2.50). This factor models the coherent accumulation of the NLI in a simplified way, allowing the use of this model in network scenarios, where, for instance, different launch power per channel and add-drop channels are considered [72]. In Eq. (2.55), the SPM is assumed to accumulate coherently along the fibre spans, while the XPM is assumed to accumulate incoherently - the accuracy of these assumptions was validated in [35]. For notation convenience, the j dependence of the SPM and XPM contribution is suppressed below.

The XPM contribution in Eq. (2.55), $\eta_{\text{XPM}}(f_i)$, is obtained by summing over all COI-interfering pairs present in the transmitted signal, i.e.,

$$\eta_{\text{XPM}}(f_i) = \sum_{k=1,k\neq i}^{\text{N}_{\text{ch}}} \eta_{\text{XPM}}^{(k)}(f_i), \tag{2.56}$$

where $\eta_{\text{XPM}}^{(k)}(f_i)$ is the XPM contribution of a single interfering channel k on channel i.

A closed-form expression expression of $\eta_{\text{SPM}_j}(f_i)$ is given by [35, Eq. (10)]

$$\eta_{\text{SPM}}(f_i) = \frac{4}{9}\frac{\gamma_i^2}{B_i^2}\frac{\pi}{\phi_i \alpha'(2\alpha+\alpha')}\left[\frac{T_i' - \alpha^2}{\alpha}\operatorname{asinh}\left(\frac{\phi_i B_i^2}{\pi\alpha}\right) + \frac{A^2 - T_i'}{A}\operatorname{asinh}\left(\frac{\phi_i B_i^2}{\pi A}\right)\right] \tag{2.57}$$

with $\phi_i = \frac{3}{2}\pi^2(\beta_2 + 2\pi\beta_3 f_i)$, $A = \alpha + \alpha'$, and $T_i' = (\alpha + \alpha' - P_{\text{tot}} C_r f_i)^2$. The closed-form approximation for the total XPM, $\eta_{\text{XPM}}(f_i)$ is given by

$$\begin{aligned}\eta_{\text{XPM}}(f_i) = \frac{32}{27}\sum_{k=1,k\neq i}^{\text{N}_{\text{ch}}}\left(\frac{P_k}{P_i}\right)^2 \frac{\gamma_i^2}{B_k \phi_{i,k}\alpha'(2\alpha+\alpha')} \\ \left[\frac{T_k' - \alpha^2}{\alpha}\operatorname{atan}\left(\frac{\phi_{i,k} B_i}{\alpha}\right) + \frac{A^2 - T_k'}{A}\operatorname{atan}\left(\frac{\phi_{i,k} B_i}{A}\right)\right]\end{aligned} \tag{2.58}$$

with $\phi_{i,k} = 2\pi^2 (f_k - f_i)[\beta_2 + \pi\beta_3 (f_i + f_k)]$. The proof of Eqs. (2.57) and (2.58) are given respectively, in Appendices B and A of [35]. Note that, in Eqs. (2.57) and (2.58), γ_i was made wavelength-dependent following the approach in [60].

These formulae are valid for Gaussian constellations only. The more general case

Table 2.1: Excess kurtosis of selected modulation formats.

Modulation format	Excess kurtosis Φ
QPSK	-1
16-QAM	-0.6800
64-QAM	-0.6190
256-QAM	-0.6050
1024-QAM	-0.6012
Uniform distribution (∞-QAM)	-0.6000
Gaussian distribution	0

accounting for any modulation format can be included by using $\eta_{\text{corr,n}}(f_i)$ in Eq. (2.54). This correction term is only one of the terms from the EGN model [28] and a closed-form expression for this particular term was obtained in [37] by considering only the XPM contribution to $\eta_{\text{corr,n}}(f_i)$, i.e., neglecting SPM and FWM. The XPM contribution for $\eta_{\text{corr,n}}(f_i)$ can be written as the sum over all COI-interfering-channel pairs present in the transmitted signal,

$$\eta_{\text{corr,n}}(f_i) = \sum_{k=1,k\neq i}^{\text{N}_{\text{ch}}} \eta_{\text{corr,n}}^{(k)}(f_i), \tag{2.59}$$

where $\eta_{\text{corr,n}}^{(k)}(f_i)$ is the XPM contribution of a single interfering channel k on channel i. Using further approximations described in [37], a closed-form expression of Eq. (2.59) can be obtained as [37, Eq. (15)]

$$\eta_{\text{corr,n}}(f_i) = \frac{80}{81}\Phi \sum_{k=1,k\neq i}^{\text{N}_{\text{ch}}} \left(\frac{P_k}{P_i}\right)^2 \frac{\gamma_i^2}{B_k} \left\{ \frac{1}{\phi_{i,k}\alpha'(2\alpha+\alpha')} \left[\frac{T_k' - \alpha^2}{\alpha} \operatorname{atan}\left(\frac{\phi_{i,k}B_i}{\alpha}\right) + \frac{A^2 - T_k'}{A} \operatorname{atan}\left(\frac{\phi_{i,k}B_i}{A}\right) \right] + \frac{2\pi\bar{n}T_k'}{|\phi|B_k^2\alpha^2A^2} \left[(2|\Delta f| - B_k) \log\left(\frac{2|\Delta f| - B_k}{2|\Delta f| + B_k}\right) + 2B_k \right] \right\}, \tag{2.60}$$

where $\tilde{n} = 0$ for a single span or $\tilde{n} = n$ otherwise, $\phi = -4\pi^2[\beta_2 + \pi\beta_3(f_i + f_k)]L$, $\Delta f = f_k - f_i$. In Eq. (2.60) γ_i is a wavelength-dependent parameter (see Fig. 2.4 and [60]).

The term Φ is the so-called excess kurtosis, defined as $\Phi = \frac{\mathbb{E}[X^4]}{\mathbb{E}^2[X^2]} - 2$. This factor takes into account different modulation formats. Table 2.1 shows the typical values of the excess kurtosis for common modulation formats. It can be seen that the kurtosis of common modulation formats is negative, meaning that the NLI is reduced for QAM, QPSK and shaped constellations when compared to the Gaussian constellations where the kurtosis is zero (and thus $\eta_{\text{corr,n}}(f_i) = 0$). The derivation of Eq. (2.60) can be found in Appendices A and B of [37].

The closed-form formulae in Eqs. (2.57), (2.58) and (2.60), however, are not able

to account for RA because the analytical function used to calculate ρ in Eq. (2.51) is not able to correctly reproduce the signal evolution along the fibre in the case where arbitrary pumps in arbitrary direction (FW or BW) are injected in the transmission fibre. This is because the function in Eq. (2.51) is an exponential decay only. The first closed-form formula able to account for any RA setup was developed and validated experimentally during this PhD and is presented in Chapter 4.

Furthermore, the closed-form formulae in [35, 37, 34] are not able to correctly reproduce the NLI for UWB cases of short-span lengths and extremely low losses, due to a fundamental approximation made in deriving $\eta_{\text{SPM}}(f_i)$ and $\eta_{\text{XPM}}(f_i)$ in Eqs (2.57) and (2.58) (see Sec. 3.3 for details). The first closed-form expression able to account for arbitrary span lengths and arbitrary losses was developed in this PhD and in present in Chapter 3.

Closed-form expressions are essential for optimisation routine and real-time applications. In Chapter 5, the closed-form formulae developed during the research described in this thesis are used for launch power optimisation routines and amplification design. Based on these analytical-formula-aided optimisations, throughput maximisation is obtained for systems operating with lumped and Raman amplifiers.

2.8 Optical amplifiers

As shown in Fig. 2.2, optical amplifiers are fundamental components of any optical fibre transmission system. These devices amplify the received signal which loses power due to fibre propagation effects such as fibre loss and the Raman effect discussed in Secs. 2.4.1 and 2.4.4. The amplification occurs directly in the fibre medium, eliminating the need for complex electronic conversions. This technology underpins modern telecommunications networks, providing high gain, low noise, and broad bandwidth. These extremely important devices support the long-distance optical communication networks of today enabling signal transmission over thousands of kilometers. Optical amplifiers can be classified into three main categories: rare-earth doped fibre amplifiers (including EDFAs and TDFAs), SOAs, and Raman amplifiers. Each type offers unique advantages and is employed in various applications within optical communication systems. More broadly, amplification techniques can use a different fibre with a short length to provide the desired signal amplification, named LA, or the same fibre of which the signal is being transmitted, i.e., the transmission fibre itself, named distributed amplification. Examples of the first are rare-earth doped fibre amplifiers, SOAs and discrete Raman amplifiers, whereas the later distributed Raman amplifiers are used. For LA techniques, an amplifier is placed at the end of every fibre span, for distributed RA, or just RA, pumps are injected into the

transmission fibre and signal amplification is achieved via stimulated RA (see Sec. 2.4.4). This section focuses on rare-earth doped fibre amplifiers and distributed RA.

2.8.1 Rare-earth-doped fibre amplification

Rare-earth-doped fibre amplifiers play a crucial role in enhancing the performance of optical fibre communication systems. For this technology, the fibre is doped with rare-earth elements like erbium for EDFAs or thulium for TDFAs. EDFAs are primarily used in the C-band (1530 - 1565 nm) and L-band (1565 - 1625 nm) of the optical spectrum. The typical gain of an EDFA ranges from 20 to 40 dB, depending on the specific design, input signal power, and the length of the doped fibre. TDFAs, on the other hand, operate in the S-band (1460 - 1530 nm). The typical gain of a TDFA is slightly lower than that of an EDFA, usually ranging from 15 to 30 dB.

The amplifier characteristics is usually measured in terms of amplifier noise figure (NF), defined as

$$\frac{\text{SNR}_{\text{in}}}{\text{SNR}_{\text{out}}} = \text{NF} = \frac{1}{G_i}[1 + 2n_{sp,i}(G_i - 1)], \tag{2.61}$$

where $n_{sp,i}$ is the spontaneous emission factor at the frequency of the i^{th} channel, $G_i = P_i(L)/P_i(0)$ is the amplifier gain where $P_i(0)$ and $P_i(L)$ are the powers of channel i at the input and output of the considered span, respectively. SNR_{in} and SNR_{out} are the SNR before and after the amplifier. The theoretical minimum NF for an ideal optical amplifier, assuming a perfect device with no excess noise sources other than quantum noise, is 3 dB. In practice, due to additional sources of noise (like excess thermal noise, non-idealities in the amplifier design, and implementation losses), the actual NF of optical amplifiers reaches higher values than the quantum limit.

In both EDFAs and TDFAs, ASE noise is a significant concern as it degrades the quality of optical signals by introducing unwanted noise. ASE noise arises from the spontaneous emission of photons by the doped ions within the fibre, which is amplified along with the signal. This noise degrades the SNR and limits the overall system performance. In the context of Sec. 2.2, this noise is represented by $w_j(t)$, which is the ASE noise generated by each amplifier. In EDFA, ASE noise results from spontaneous photon emission by erbium ions, leading to a NF typically between 4 and 6 dB. TDFAs exhibit a higher NF, generally ranging from 6 to 8 dB, due to similar ASE processes involving thulium ions. The ASE noise can be effectively modelled as AWGN, and its noise power across both polarisations can be approximated as

$$P'_{\text{ASE},i} = 2(G_i - 1)n_{sp,i}hf_iB_i, \tag{2.62}$$

where h is the Plank's constant.

2.8.2 Distributed Raman amplification

Distributed RA is a technology used in optical fibre communication systems where the optical fibre itself serves as the gain medium for amplifying signals. The amplification is distributed along the length of the transmission fibre, rather than being concentrated in a specific component, like in conventional lumped amplifiers. The amplification principle is stimulated Raman scattering, where a high-power pump laser injects light into the fibre. This pump light interacts with the optical signal, transferring energy to it and thereby amplifying the signal as it propagates through the fibre (see Sec. 2.4.4). Different configurations are possible including FW pumping, BW pumping or co-propagating pumps, where both FW pumping, BW pumping are used. Typically, BW pumping is employed to reduce the relative intensity noise (RIN) [73].

Distributed Raman amplifiers have a lower NF compared to lumped amplifiers primarily because their distributed gain reduces the accumulation of noise over distance, which generates less ASE noise. The typical NF for Raman amplifiers is generally in the range of 1.5 dB to 4.5 dB, depending on various factors such as the pump configuration, fibre type, and system design. These values are generally lower than those for EDFAs, making Raman amplifiers especially advantageous in applications requiring low noise and high signal quality over long distances. Another advantage is their broad wavelength coverage: Raman amplifiers can provide amplification across a wide range of wavelengths, from the S-band to the L-band and even into other bands, depending on the pump wavelength used. This makes them highly flexible and suitable for WDM systems where multiple channels at different wavelengths need to be amplified.

For Raman-amplified links, Eq. (2.39), is a simplified way of describing the power evolution of the transmitted signal along the power distance. In its original form, the power evolution in Eq. (2.39) is coupled with the ASE noise generated by Raman amplifiers and is written as [74]

$$\begin{aligned}\pm\frac{\partial P_i}{\partial z} = &-\sum_{k=i+1}^{\mathrm{N_{ch}}}\frac{f_k}{f_i}g_i(|\Delta f|)(P_k+P_{\mathrm{ASE},k})P_i-\sum_{p:f_i>f_p}\frac{f_p}{f_i}g_i(|\Delta f|)(P_p+P_{\mathrm{ASE},p})P_i\\&+\sum_{k=1}^{i-1}g_i(|\Delta f|)(P_k+P_{\mathrm{ASE},k})P_i+\sum_{p:f_i<f_p}g_i(|\Delta f|)(P_p+P_{\mathrm{ASE},p})P_i-\alpha_i P_i,\end{aligned} \tag{2.63}$$

where $P_{\mathrm{ASE},k}$ and $P_{\mathrm{ASE},p}$ are respectively the ASE noise from channel k and the pump p. The ASE noise is calculated similarly to Eq. (2.39): its power at the frequency of the i^{th} channel, P_{ASE_i}, is calculated as the solution of the following coupled differential

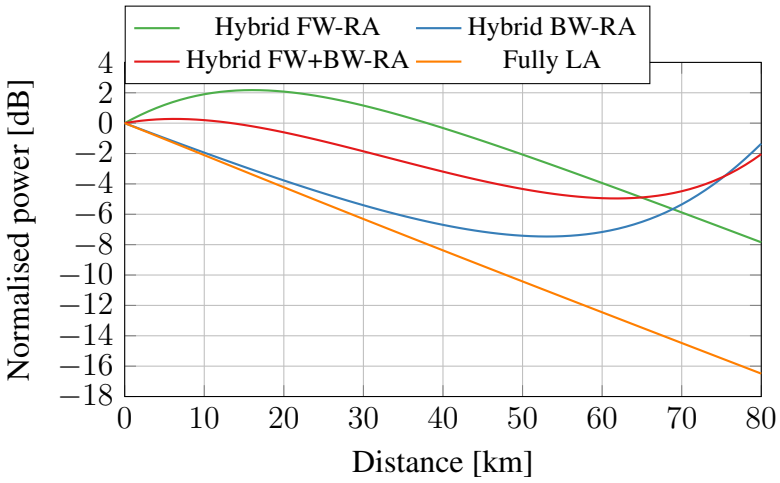

Fig. 2.11: Signal power evolution along the fibre length obtained for LA (orange curve) using Eq. (2.38), and for different cases of RA (remaining curves) using Eq. (2.39).

equations [74]:

$$\begin{aligned}\frac{\partial P_{\text{ASE},i}}{\partial z} = &- \sum_{k=i+1}^{N_{ch}} \frac{f_k}{f_i} g_i(|\Delta f|)(P_k + P_{\text{ASE},k})(P_{\text{ASE},i} + 2h\kappa B_i f_i) - \\ &- \sum_{p:f_i>f_p} \frac{f_p}{f_i} g_i(|\Delta f|)(P_p + P_{\text{ASE},p})(P_{\text{ASE},i} + 2h\kappa B_i f_i) + \\ &+ \sum_{k=1}^{i-1} g_i(|\Delta f|)(P_k + P_{\text{ASE},k})(P_{\text{ASE},i} + 2h\kappa B_i f_i) + \\ &+ \sum_{p:f_i<f_p} g_i(|\Delta f|)(P_p + P_{\text{ASE},p})(P_{\text{ASE},i} + 2h\kappa B_i f_i) - \alpha_i P_{\text{ASE},i},\end{aligned} \tag{2.64}$$

where κ is related to the photon occupancy factor χ as

$$\kappa = 1 + \chi = \frac{1}{1 - e^{-\frac{h\Delta f}{k_B T''}}}, \tag{2.65}$$

where T'' is the temperature of the system and k_B is Boltzmann's constant. The ASE equations for the remaining WDM channels and pumps are obtained by setting $i = k$ and $i = p$ respectively. Eqs. (2.63) and (2.64) are solved for each one of the spans with initial conditions at the beginning of the first span as $P_{\text{ASE},i} = P_{\text{ASE},k} = P_{\text{ASE},p} = 0$, and P_i, P_k the corresponding channel launch power. Eq. (2.39) is valid and accurate for most transmission scenarios, and coupling the ASE noise in that equation (as per Eq. (2.63)) may not be necessary. An analysis of the validity of approximating Eq. (2.63) by Eq. (2.39) is given in Sec. 5.4.3 and results are shown in Fig. 5.18.

For hybrid-amplified links, the ASE noise generated by distributed RA, obtained from Eq. (2.64), is amplified by the ideal lumped amplifier gain (G_i) placed at the end

of the fibre. The total ASE noise is then given by

$$P''_{\text{ASE},i} = G_i P_{\text{ASE},i} + P'_{\text{ASE},i}. \tag{2.66}$$

Lumped amplifiers are located at the ends of fibre spans, thus, the signal propagating through the fibre is just changed by the optical fibre attenuation and the ISRS effect as per Eq. (2.38). On the other hand, distributed Raman amplifiers use the optical fibre itself as the gain medium, distributing the amplification along the length of the transmission fibre rather than concentrating it in a discrete component. For RA the total gain can be tailored by adjusting the pump power and wavelength as per Eq. (2.39). Fig. 2.11 shows an example of signal propagation using LA and various types of RA. For the case of RA the signal experiences gain at every portion of the fibre span due to the pumps injected in the FW and BW directions. For the case of LA the signal experiences a simple exponential decay and thus an exponential function is sufficient to reproduce the signal propagation evolution along the optical fibre. In contrast, for RA more sophisticated analytical functions have to be used. An analytical function able to reproduce RA cases is one of the novelties presented in this thesis and one of the key approximations to derive the semi-analytical model in Chapter 4.

2.9 Transmission system performance

In Sec. 2.2 a description of the optical fibre channel was presented. Eq. (2.3) showed that the transmitted signal $x(t)$ is impaired by additive noise sources represented by $w(t)$. Because of this, the system performance in terms of SNR for the channel i can be calculated as

$$\text{SNR}_i = \frac{\mathbb{E}[|X|^2]}{\mathbb{E}[|W|^2]} = \frac{\mathbb{E}[|X|^2]}{\mathbb{E}[|X-Y|^2]}, \tag{2.67}$$

where X, W and Y are random variables representing the transmitted symbols, noise, and received symbols after DSP is applied, respectively. The variance of the noise is simply given by $\sigma^2 = \mathbb{E}[|W|^2] = \mathbb{E}[|X-Y|^2]$.

In Sec. 2.6, the variance or PSD of the nonlinear noise was defined in Eq. (2.52). Similarly, the variance of the ASE noise was defined in Sec. 2.8 using Eq. (2.66). Thus, $\mathbb{E}[|W|^2]$ can be simply written as $\mathbb{E}[|W|^2] = P''_{\text{ASE},i} + P_{\text{NLI},i}$. The channel optical transmitted power is given by $P_i = \mathbb{E}[|X|^2]$ and then the total SNR can be conveniently written as

$$\text{SNR}_i^{-1} = \text{SNR}_{\text{ASE},i}^{-1} + \text{SNR}_{\text{NLI},i}^{-1} = \left(\frac{P_i}{P''_{\text{ASE}_i} + \eta_n(f_i) P_i^3} \right)^{-1}, \tag{2.68}$$

where $\text{SNR}_{\text{ASE},i} = P_i / P''_{\text{ASE}_i}$ and $\text{SNR}_{\text{NLI},i} = P_i / P_{\text{NLI}_i}$. In Eq. (2.68), the impact of the TRX was neglected. In real systems, TRX noise can significantly affect the performance

of an optical communication system and must be included in the SNR calculation. This noise originates from various types of noise introduced by the optical TRX such as quantisation noise, thermal noise, shot noise, RIN, laser phase noise, etc. The TRX noise is typically added in Eq. (2.68) as another additive noise term such that SNR_i is calculated as

$$\text{SNR}_i^{-1} \approx \text{SNR}_{\text{TRX}}^{-1} + \text{SNR}_{\text{ASE}}^{-1} + \text{SNR}_{\text{NLI}}^{-1} = \left(\frac{P_i}{\kappa_i P_i + P''_{\text{ASE}_i} + \eta_n(f_i) P_i^3} \right)^{-1}, \tag{2.69}$$

where $\text{SNR}_{\text{TRX},i} = P_i/\kappa_i P_i$ (or $\kappa = 1/\text{SNR}_{\text{TRX},i}$). $\text{SNR}_{\text{TRX},i}$ is the TRX noise, also called back-to-back implementation penalty. $\eta_n(f_i)$ is obtained from Eq. (2.53). Eq. (2.69) assumes that all noise sources are AWGN and is used to calculate the optical system performance for channels described by the conventional system approach described in Sec. 2.2.

An important feature of Eq. (2.69) is that the NLI noise increases with launch power ($P_{\text{NLI}} \propto P_i^3$), thus, every optical fibre transmission system exhibits an optimal per-channel launch power profile $P_{\text{opt},i}$, leading to an optimal per-channel SNR_i. In UWB systems and hybrid-amplified links, however, this optimal launch power has no analytical solution and has to be found using optimisation algorithms [75]. For the special case of C-band systems operating with lumped amplifiers only, an analytical solution can be obtained. This solution is given by

$$P_{\text{opt},i} = \sqrt[3]{\frac{P_{\text{ASE},i}}{2\eta_n(f_i)}}. \tag{2.70}$$

Launch power optimisation techniques in UWB system operating with different amplification technologies are explored in Chapter 5.

2.10 Modulation and capacity bound for the optical AWGN channel

Modulation is the process of converting digital data into an optical signal that can be transmitted over the fibre. The modulation format determines how the bits are mapped to the optical signal, and different modulation formats use different constellations to represent data symbols. The constellation refers to the graphical representation of the signal states (amplitude and phase) that correspond to the different symbols in the modulation scheme. For a chosen constellation and channel, the amount of information that can be transmitted through this channel can be estimated using the mutual information (MI), which, assuming continuous distributions, is given by [63]

$$\text{MI}(X,Y) = \int\int p_{X,Y}(x,y) \log_2 \left(\frac{p_{X,Y}(x,y)}{p_X(x) p_Y(y)} \right) dx\, dy, \tag{2.71}$$

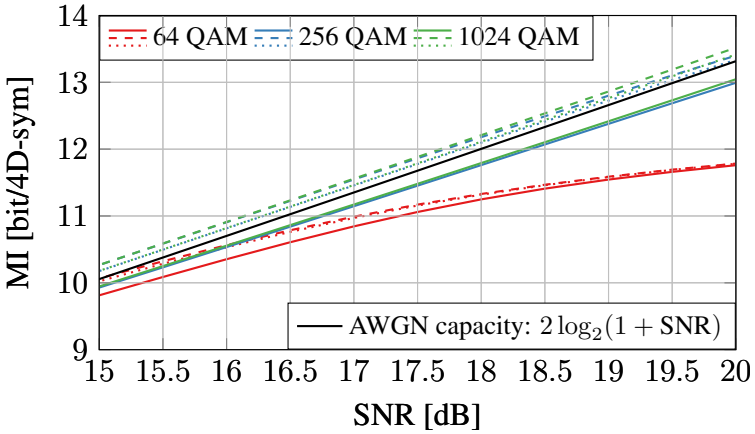

Fig. 2.12: MI as a function of SNR at optimal launch power for square/uniformly distributed 64-QAM, 256-QAM and 1024-QAM (red, blue and green continuous lines) and shaped according to MB distribution (dotted lines) and optimised distribution (dashed lines). The AWGN channel capacity is also shown as the continuous black line. Additional details are given in [76].

where $p_{X,Y}(x,y)$ is the joint probability distribution of X and Y and $p_X(x)$, $p_Y(y)$ are the marginal probability distributions.

For the optical AWGN channel described in Sec. 2.2 and modelled according to Eq. (2.69), different values of MI are shown in Fig. 2.12, for different shaped and unshaped modulation formats. Red, blue and green continuous lines show standard unshaped (or square) QAM constellations. For an AWGN channel where the additive GN is independent of the Tx symbol, the maximum MI, also called AWGN capacity, is achieved for a Gaussian distribution (which has zero excess kurtosis, $\Phi = 0$) at the input symbols. This is shown as the continuous black line in Fig. 2.11 with its capacity given analytically by

$$C = \max_{p_X(x)} \text{MI} = 2\log_2(1+\text{SNR}). \tag{2.72}$$

The optical AWGN channel however has the particular feature that the AWGN noise is dependent on the transmitted symbols through their higher-order statistics (see for instance the excess kurtosis in Table 2.1 and high-order statistics in [28]). Because of it, Eq. (2.72) serves as a bound only and different distributions can achieve higher MI. Indeed, a common example is to achieve shaped constellations according to a Maxwell-Boltzmann (MB) distribution, which is given by

$$p_{\lambda_{MB}}(x) = \frac{e^{-\lambda_{MB}|x|^2}}{\sum_{\forall x' \in X} e^{-\lambda_{MB}|x'|^2}}, \tag{2.73}$$

where λ_{MB} is the shaping parameter that is optimised for a given SNR. This distribution has $\Phi = -0.15$ [76]. The MI achieved by these shaped constellations is shown in Fig. 2.12 as dotted lines. Another possible shaped constellation is given by

the following optimised distribution

$$p_{v_1,v_2}(x) = \frac{e^{-v_1|x|^2 - v_2|x|^4}}{\sum_{\forall x' \in X} e^{-v_1|x'|^2 - v_2|x'|^4}}, \tag{2.74}$$

where v_1 and v_2 are also shaping parameters that is optimised for a given SNR. This distribution has $\Phi = -0.25$ [76]. An example of the MI achieved by these shaped constellations is shown in Fig. 2.12 as dashed lines. Details of results of Fig. 2.12 are given in [76]. Compared to uniform M-QAM constellations, Gaussian distributions achieve a maximum of 1.53 dB shaping gain in the high-SNR regime [32]. Other distributions like the ones shown in Eqs. (2.73) and (2.74) can achieve higher shaping gains. Further analysis on this topic can be found in [45]. Note that, despite Eq. (2.72) being only a bound to the AIR, most of the total throughput estimations in this thesis are estimated using this equation. This is because of its simplicity: this equation gives an approximation of the total throughput and the only parameter needed for its calculation is the SNR for each WDM channel.

2.11 Final considerations

This chapter presented the definitions and tools, which were used in the research described in this thesis, to derive the analytical models in Chapters 3 and 4, and the optimisation algorithms in Chapter 5. It should be pointed out that, the properties of the optical fibre channel are different from the classical AWGN channel. The primary challenge in identifying an optimal model for the optical fibre channel lies in the fact that an exact and explicit input-output relationship for this channel, without any approximations, has not been determined due to its nonlinear nature. Specifically, there is no analytical or integral solution to Eq. (2.16). Because of its AWGN-like formation, the model presented in Sec. 2.2 is only an approximation of this channel. It has been shown that the optical fibre AIR is ultimately limited by signal-noise and noise-noise interactions [77, 78]. Additionally, It has been shown that higher values of AIR can be achieved by using other descriptions of the optical fibre channel, such as by considering the memory introduced through the dispersion and its interaction with the fibre nonliterary, using nonlinear compensation methods such as digital back propagation (DBP), and improved detection strategies [79, 80, 81, 51]; however, such types of channel descriptions usually rely on time-consuming algorithms for nonlinear equalisation and detection, increasing the complexity of the system. Finally, despite being sub-optimal, the approach described in Sec. 2.2 is advantageous given its AWGN-like simplicity and is the most widely adopted model for estimating the performance of optical fibre transmission systems. In this thesis, new semi-analytical models of the approach described in Sec. 2.2, coping with next-generation optical fibre

systems were derived and validated, and are described in Chapters 3 and 4. These models were used in Chapter 5 for optimisation algorithms to achieve optimal system design, such as optimum amplification setup and launch power profiles.

Chapter 3

A closed-form expression for the Gaussian noise model extended for arbitrary loss and fibre length

Following the theoretical background detailed in Chapter 2, the novel contributions from this research are presented and discussed. To address the current capacity limitations in the installed optical network infrastructure, new technologies are being explored to extend the optical transmission bandwidth beyond the conventionally used C+L band [75, 82, 83, 84]. Although bandwidth expansion can lead to higher data throughputs, several challenges arise in modelling UWB transmission (see also Sec. 2.4). Among these challenges, the wavelength-dependent optical fibre parameters, described in Sec. 2.4 and also modelled in [85, 86, 87], together with the ISRS effect [39, 40, 41] described in Sec. 2.4.4, play a significant role. In contrast to conventional C-band systems where these effects are negligible, they must be taken into account for UWB systems. The combination of these effects, together with their Kerr-induced nonlinear interaction leads to additional signal degradation and variations in performance between channels. Some studies and strategies to address these effects have been proposed in [82, 88, 89, 90, 91].

Associated with this, research in adaptive network planning tools aims to introduce intelligence in the network and deliver capacity when and where it is needed [92, 93]. This is an essential step to achieve efficient resource-utilisation [94] and to build a self-controlled network infrastructure. To cope with this, one requirement is to bring physical layer awareness to the control plane level [95] enabling it to account for inline signal impairments, to predict failures, and to avoid wasting resources. To achieve this, an efficient, fast and accurate model to estimate NLI at *any portion* of the optical fibre link is essential.

As mentioned in Chapter 2, to enable real-time prediction of the UWB system performance, formulations in closed form are needed. These formulations must offer a fast, yet accurate, evaluation of the network characteristics, so that they can be widely used for network optimisation purposes [75, 82]. The closed-form expressions derived using the ISRS GN model [33] given by Eq. (2.52) and described in Sec. 2.7 are a starting point due to their simplicity and efficiency in estimating NLI in UWB systems, and numerous closed-form equations have been developed to date [34, 35, 37, 96].

However, these studies can provide models for NLI estimation for a subset of scenarios only. The proposed formulae do not account for the cases of short-span lengths and extremely low losses, due to the approximations made in their derivation. The first case is essential for estimating the NLI in every portion of the fibre span, predicting failures, and introducing intelligence in the network. It is also important for modelling short-reach transmission systems and fibre cables connecting data centres. The second case is essential for fibre technologies such as ULL fibres and hollow core fibres. It can be also used as a starting point for modelling Raman amplified links, in which the effective attenuation is much lower than the intrinsic fibre attenuation, however a more complete model for Raman-amplified links is given in Chapter 4. The closed-form formulae proposed in [97, 98] do account for short span lengths and extremely low-losses but do not include the ISRS effect, and hence are not suitable for UWB modeling in conventional optical fibres, which is rapidly gaining interest now.

This chapter describes the first analytical model able to accurately estimating the NLI in the presence of ISRS for any fibre span length and for fibres with extremely low losses (~ 0.04 dB/km). This represents a key result of the research described in this thesis, and is significant in the modelling of UWB transmission systems. Particularly, the derivation of this model was enabled by removing one of the main approximations used in deriving the formulae described in Sec 2.7 and published in [35, 37, 99]. This chapter presents all the assumptions and the mathematical derivations used to obtain the closed-form expression, and various case scenarios of it demonstrating the multiple applications of the proposed closed-form expression. A discussion on the validity range of this closed-form formula compared with those in [33, 37, 99] is also presented. The proposed closed-form expression accounts for all modulation formats, wavelength-dependent attenuation and dispersion, and its accuracy was compared with the ISRS GN model in integral form [33, 37] and SSFM simulations.

The material presented in this chapter was published in peer-reviewed conferences and journals [P2, P9], referenced in this thesis as [100, 101].

3.1 The derivation of the closed-form expression for NLI-induced SNR

This section describes the closed-form expression used to analytically estimate the NLI supporting any span length and fibre losses. The integral model and the closed-form expression obtained from this model are presented. The steps used to derive this closed-form expression are also detailed in this section.

3.1.1 Integral expressions

After coherent detection and electronic dispersion compensation, the total received SNR for the i-th WDM channel (SNR$_i$) after n spans can be estimated as Eq. (2.69). To calculate the NLI noise PSD, $P_{\text{NLI}} = \eta_n(f_i)P_i^3$, the ISRS GN model approach was considered, which is an extension of the GN model [27] accounting for the ISRS effect, it was proposed in [33, 37] and is given by Eq. (2.49). This model also accounts for the modulation dependence of the NLI in the input symbol distribution [28, 29, 66]. This dependence is accounted for by calculating one of the NLI correction terms in [28] in the presence of ISRS. In the integral equations shown in this section, the nonlinear parameter is considered wavelength-dependent and denoted as γ_i following the approach in [60].

Following Eq. (2.52), the nonlinear coefficient obtained at the end of the n-th span, $\eta_n(f_i)$, can be written as Eq. (2.54). To obtain a closed form expression for the Gaussian contribution to $\eta_n(f_i)$, i.e., $\eta_{\text{GN},n}(f_i)$, the integral expressions presented in [33] are first introduced. $\eta_{\text{GN},n}(f_i)$ is divided in their XPM and SPM contributions as per Eq. (2.55). The total XPM contribution $\eta_{\text{XPM}}(f_i)$ can be written as the sum of the XPM contribution of each single interfering channel k as per Eq. (2.56), where $\eta_{\text{XPM}}^{(k)}(f_i)$ is given in integral form by [35, Eq. 8]

$$\eta_{\text{XPM}}^{(k)}(f_i) = \frac{32}{27}\frac{\gamma_i^2}{B_k^2}\left(\frac{P_k}{P_i}\right)^2 \int_{\frac{-B_i}{2}}^{\frac{B_i}{2}} df_1 \int_{\frac{-B_k}{2}}^{\frac{B_k}{2}} df_2 \, \Pi\left(\frac{f_1+f_2}{B_k}\right) \mu(f_1+f_i, f_2+f_k, f_i), \tag{3.1}$$

the integral expression for the SPM contribution is given by

$$\eta_{\text{SPM}}(f_i) = \frac{1}{2}\eta_{\text{XPM}}^{(i)}(f_i), \tag{3.2}$$

where $\eta_{\text{XPM}}^{(i)}(f_i)$ is given by Eq. (3.1) with the index k replaced by i. $\Pi(x)$ denotes the rectangular function. $\mu(f_1, f_2, f_i)$ is the so-called link function or FWM efficiency [27], which is given by [33, Eq. (4)]

$$\mu\left(f_1, f_2, f_i\right) = \left| \int_0^L d\zeta \sqrt{\frac{\rho(\zeta, f_1)\rho(\zeta, f_2)\rho(\zeta, f_1+f_2-f_i)}{\rho(\zeta, f_i)}} e^{j\phi(f_1,f_2,f_i)\zeta} \right|^2 \tag{3.3}$$

where $\phi = -4\pi^2\left(f_1 - f_i\right)\left(f_2 - f_i\right)\left[\beta_2 + \pi\beta_3(f_1+f_2)\right]$, and $\rho(z, f_i) = \frac{P(z,f_i)}{P(0,f_i)}$ is the normalised signal power profile obtained by solving for instance, Eqs. (2.38) or (2.39).

The correction term contribution to the total nonlinear coefficient, $\eta_{\text{corr,n}}(f_i)$ which accounts for different modulation formats, can be estimated using Eq. (2.59) i.e., by considering only the XPM contribution of each single interfering channel k on the

channel i (the accuracy of this assumption was demonstrated in [37]). The correction term of a single interfering channel k on channel i, $\eta^{(k)}_{corr,n}(f_i)$ is given in integral form by [37, Eq. (4)]. As shown in detail in [37], [37, Eq. (4)] can be accurately approximated as

$$\eta^{(k)}_{corr,n}(f_i) \approx \underbrace{\left(\frac{P_{i,1}}{P_i}\right)^2 \eta^{(k)}_{corr,1}(f_i)}_{\text{1 st span correction term}} + \underbrace{\sum_{j=2}^{n}\left(\frac{P_{i,j}}{P_i}\right)^2 \cdot \eta^{(k)}_{corr,a}(f_i)}_{\text{asymptotic correction term}}, \tag{3.4}$$

where the dependence of $\eta_{corr,a}(f_i)$ in the index j is omitted for convenience. The term $\eta^{(k)}_{corr,1}(f_i)$ is a correction term originating in the first span and $\eta^{(k)}_{corr,a}(f_i)$ is an asymptotic correction term originating in the limit of large span number. $\eta^{(k)}_{corr,1}(f_i)$ and $\eta^{(k)}_{corr,a}(f_i)$ are given respectively by [37, Eqs. (9), (12)]

$$\eta^{(k)}_{corr,1}(f_i) = \left(\frac{P_k}{P_i}\right)^2 \frac{80}{81}\frac{\gamma_i^2\Phi}{B_k}\int_{\frac{-B_i}{2}}^{\frac{B_i}{2}} df_1\, \mu(f_1+f_i, f_k, f_i), \tag{3.5}$$

and

$$\eta^{(k)}_{corr,a}(f_i) = \left(\frac{P_k}{P_i}\right)^2 \frac{80}{81}\frac{\gamma_i^2\Phi}{B_k}\mu(f_i, f_k, f_i)\frac{2\pi}{|\phi|B_k^2}\left[(2\Delta f - B_k)\ln\left(\frac{2\Delta f - B_k}{2\Delta f + B_k}\right) + 2B_k\right], \tag{3.6}$$

where $\tilde{\phi} = -4\pi^2\left[\beta_2 + \pi\beta_3(f_i+f_k)\right]L$. It should be pointed out that Eqs. (3.1), (3.2), (3.5) and (3.6) are valid for arbitrary values of loss and also arbitrary values of span lengths. These expressions, however, are given in an integral formulation and thus are not suitable for real-time optimisation. The closed-form solution of these equations given by Eqs. (2.58), (2.57) and (2.60) (also presented in [35, 37]) do not support extremely low losses and short span lengths because of the approximations, discussed in Sec. 3.3, made to derive them. In the following, these approximations are discussed and one of the novelties of the research carried out in this thesis is presented, which is the derivation of a closed-form expression supporting these scenarios and thus overcoming the limitations of [35, 37], i.e., Eqs. (3.1), (3.2), (3.5) and (3.6).

3.1.2 Signal power profile and fitting optimisation routine

The first step in deriving a closed-form expression for Eqs. (3.4), (3.5) and (3.6) is to derive a closed-form expression for the link function in Eq. (3.3). To that end, the normalised power evolution along the fibre $\rho(z, f_i)$ was considered as the semi-analytical solution of the Raman differential equations [102, 103], approximated by a Taylor series to the first order as in [35], which is given by Eq. (2.51) (also [35, Eq. (17)] and [99, Eq. (2)]). Eq. (2.51) is obtained by considering several assumptions, firstly, as by [102, 103], a constant attenuation profile, a triangular approximation of

the Raman gain spectrum, and the approximation $\frac{f_k}{f_i} \approx 1$ were assumed in Eq. (2.38). Afterwards, in the equations derived in [102, 103], a spectrally uniform launch power profile was assumed, and a first-order Taylor expansion was used in [35] leading to Eq. (2.51) (see [35, Sec II-E] for further discussion of these assumptions).

To overcome the restrictive assumptions described above, a fitting strategy was used, whereas in Eq. (2.51), as in [35], two different loss coefficients were considered (α_i and $\tilde{\alpha}_i$) and together with $C_{r,i}$ were treated as channel-dependent fitting parameters and matched using a fitting algorithm to reproduce the true power profile, which was obtained by numerically solving the Raman differential equations in Eq. (2.38) [103] using the Raman profile shown in Fig. 2.7. Also, the use of two separate loss coefficients (α_i and $\tilde{\alpha}_i$) enables an increase in the dimension of the optimisation space.

Because of the fitting optimisation routine, Eq. (2.38) is referred to as a semi-analytical solution. Moreover, the fitting algorithm can overcome all the assumptions used to derive Eq. (2.51) as shown in Sec. 2.7, Sec. 3.2 and [35, 37, 100, 101], making this equation valid for a wide range of simulation scenarios, including nonuniform launch power profiles, wavelength-dependent attenuation, non-triangular Raman gain spectrum, etc. Note that, in its current form, for each new link configuration, the fitting optimisation needs to be performed again, however, scaling rules of such fitting coefficients with the physical parameters might also be exploited.

3.1.3 Closed-form expressions

The new equations arising from this research w.r.t. the ones in [35, 37, 99] and described in Sec. 2.7 are now introduced. The derivations in this section were carried out as part of this PhD research and represent novel work. However, to improve readability they were moved to dedicated appendices. One of the main novelties is a new approximation shown in this section, performed to overcome the restive assumptions of these formulae which did not allow them to account for short-span lengths and arbitrary fibre losses. This new approximation is the key enabling step that allows the derivation of the new closed-form equations for the SPM and XPM contributions in Eqs. (3.1), (3.2), (3.5) and (3.6).

The first step was to derive a closed-form expression for the link function in Eq. (3.3). Let $\tilde{T}_i = -\frac{P_{\text{tot}} C_{r,i}}{\tilde{\alpha}_i} f_i$, $T_i = 1 + \tilde{T}_i$ and $\alpha_{l,i} = \alpha_i + l\tilde{\alpha}_i$. By assuming the normalised power evolution along the fibre $\rho(z, f_i)$ as Eq. (2.51), the link function in Eq. (3.3) could be approximated in closed form as

$$\mu\left(f_1, f_2, f_i\right) \approx \left| -T_i \sum_{0 \leq l \leq 1} \left(\frac{-\tilde{T}_i}{T_i} \right)^l \left(\frac{1 - e^{-(\alpha_{l,i} - j\phi)L}}{-\alpha_{l,i} + j\phi} \right) \right|^2 . \tag{3.7}$$

If the approximation $e^{-\alpha_{l,i}L} \ll 1$ is assumed in Eq. (3.7), such that $1-e^{-(\alpha_{l,i}-j\phi)L} \approx 1$, the closed-form formulae published in [35, 37, 99] are obtained. This assumption is generally satisfied for relatively long span lengths (> 40 km) and losses greater than 0.1 dB/km. In order to remove the above-mentioned limitation and obtain a set of new closed-form formulae which accurately account for any span lengths and any values of fibre loss in the presence of ISRS, the approach in [97] was considered and the fraction presented in Eq. (3.7) was approximated as

$$\frac{1-e^{-(\alpha_{l,i}-j\phi)L}}{-\alpha_{l,i}+j\phi} \approx \frac{\kappa_{l,i}}{-\tilde{a}_{l,i}+j\phi}, \tag{3.8}$$

where $\kappa_{l,i}$ and $\tilde{a}_{l,i}$ are chosen such that the first-order Taylor approximation of both the left and the right side of Eq. (3.8) around the variable $\phi = 0$ become equal. This yields

$$\tilde{\alpha}_{l,i} = \frac{\alpha_{l,i}(1-e^{-\alpha_{l,i}L})}{1-e^{-\alpha_{l,i}L}-\alpha_{l,i}Le^{-\alpha_{l,i}L}} \tag{3.9}$$

and

$$\kappa_{l,i} = \frac{\tilde{\alpha}_{l,i}(1-e^{-\alpha_{l,i}L})}{\alpha_{l,i}}. \tag{3.10}$$

The proposed approximation presented in Eq. (3.8) captures the effect of the attenuation in the oscillatory term $e^{-(\alpha_{l,i}-j\phi)L}$ and enables accurate modelling of fibres made of arbitrary span lengths and arbitrary fibre losses. Note that, this approximation is reflected in all mathematical derivations in this chapter to obtain a closed-form expression for Eqs. (3.1), (3.2), (3.5) and (3.6).

Inserting the approximation from Eq. (3.8) into Eq. (3.7), and calculating the modulus, yields to

$$\mu\left(f_1,f_2,f_i\right) \approx T_i^2 \sum_{\substack{0\le l\le 1\\ 0\le l'\le 1}} \left(\frac{-\tilde{T}_i}{T_i}\right)^{l+l'} \left[\frac{\kappa_{l,i}\kappa_{l',i}(\tilde{\alpha}_{l,i}\tilde{\alpha}_{l',i}+\phi^2)}{(\tilde{\alpha}_{l,i}^2+\phi^2)(\tilde{\alpha}_{l',i}^2+\phi^2)}\right]. \tag{3.11}$$

The proof of Eq. (3.11) is given in Appendix A. The coefficients $\tilde{\alpha}_{l',i}$ and $\kappa_{l',i}$ are respectively the same as those in Eqs. (3.9) and (3.10) with the indices l replaced by l'. The same is valid for the variable $\alpha_{l',i}$ (see Appendix A for details).

The next step was to use Eq. (3.11) to derive closed-form expressions for the XPM and SPM NLI contributions given by Eqs. (3.1), (3.2), respectively. Using Eq. (3.11) as an analytical solution of the link function, a closed-form expression for the Gaussian

contribution of the XPM and SPM are given respectively by

$$\eta_{\text{XPM}}^{(k)}(f_i) = \frac{32}{27}\frac{\gamma_i^2}{B_k}\left(\frac{P_k}{P_i}\right)^2 T_k^2 \sum_{\substack{0\le l\le 1\\ 0\le l'\le 1}} \left(\frac{-\tilde{T}_k}{T_k}\right)^{l+l'} \frac{2\kappa_{l,k}\kappa_{l',k}}{\phi_{i,k}(\tilde{\alpha}_{l,k}+\tilde{\alpha}_{l',k})}\left[\operatorname{atan}\left(\frac{\phi_{i,k}B_i}{2\tilde{\alpha}_{l,k}}\right)+\operatorname{atan}\left(\frac{\phi_{i,k}B_i}{2\tilde{\alpha}_{l',k}}\right)\right] \tag{3.12}$$

and

$$\eta_{\text{SPM}}(f_i) = \frac{16}{27}\frac{\gamma_i^2}{B_i^2}T_i^2 \sum_{\substack{0\le l\le 1\\ 0\le l'\le 1}} \left(\frac{-\tilde{T}_i}{T_i}\right)^{l+l'} \frac{2\kappa_{l,i}\kappa_{l',i}\pi}{\phi_i(\tilde{\alpha}_{l,i}+\tilde{\alpha}_{l',i})}\left[\operatorname{asinh}\left(\frac{3\phi_i B_i^2}{8\pi\tilde{\alpha}_{l,i}}\right)+\operatorname{asinh}\left(\frac{3\phi_i B_i^2}{8\pi\tilde{\alpha}_{l',i}}\right)\right], \tag{3.13}$$

with $\phi_i = -4\pi^2\left(\beta_2 + 2\pi\beta_3 f_i\right)$ and $\phi_{i,k} = -4\pi^2\left(f_k - f_i\right)\left[\beta_2 + \pi\beta_3\left(f_i + f_k\right)\right]$. The proof of Eqs. (3.12) and (3.13) are given respectively in Appendix B and C.

The final step was to derive closed-form expressions for the correction terms, which account for the dependence of the NLI on the modulation format, i.e., a closed-form expression for the terms given in Eqs. (3.5) and (3.6). For Eq. (3.5), a similar integral has already been solved in Appendix B for the XPM contribution, the solution is given by Eq. (B.4). Thus, Eq. (3.5), in closed form is given by

$$\eta_{corr,1}^{(k)}(f_i) = \frac{80}{81}\frac{\gamma_i^2\Phi}{B_k}\left(\frac{P_k}{P_i}\right)^2 T_k^2 \sum_{\substack{0\le l\le 1\\ 0\le l'\le 1}} \left(\frac{-\tilde{T}_k}{T_k}\right)^{l+l'} \frac{2\kappa_{l,k}\kappa_{l',k}}{\phi_{i,k}(\tilde{\alpha}_{l,k}+\tilde{\alpha}_{l',k})}\left[\operatorname{atan}\left(\frac{\phi_{i,k}B_i}{2\tilde{\alpha}_{l,k}}\right)+\operatorname{atan}\left(\frac{\phi_{i,k}B_i}{2\tilde{\alpha}_{l',k}}\right)\right]. \tag{3.14}$$

For Eq. (3.6), it is enough to note that when substituting identical arguments, i.e., $\mu(f_i, f_k, f_i)$, yields $\phi(f_i, f_k, f_i) = 0$ in Eq. (3.11). Thus, Eq. (3.6) could be written in closed form as

$$\eta_{corr,a}^{(k)}(f_i) = \frac{80}{81}\frac{\gamma_i^2\Phi}{B_k}\left(\frac{P_k}{P_i}\right)^2 T_k^2 \sum_{\substack{0\le l\le 1\\ 0\le l'\le 1}} \left(\frac{-\tilde{T}_k}{T_k}\right)^{l+l'} \left[\frac{2\pi\kappa_{l,k}\kappa_{l',k}}{|\phi|B_k^2\tilde{\alpha}_{l,k}\tilde{\alpha}_{l',k}}\cdot\left((2\Delta f - B_k)\ln\left(\frac{2\Delta f - B_k}{2\Delta f + B_k}\right)+2B_k\right)\right]. \tag{3.15}$$

To calculate the SNR_{NLI} in Eqs. (2.68) and (2.69) in closed form, Eqs. (3.12), (3.13), (3.14) and (3.15) were then used. To write the complete equation for SNR_{NLI} in Eq. (2.69) and simplify the notation, it was assumed that the optical link

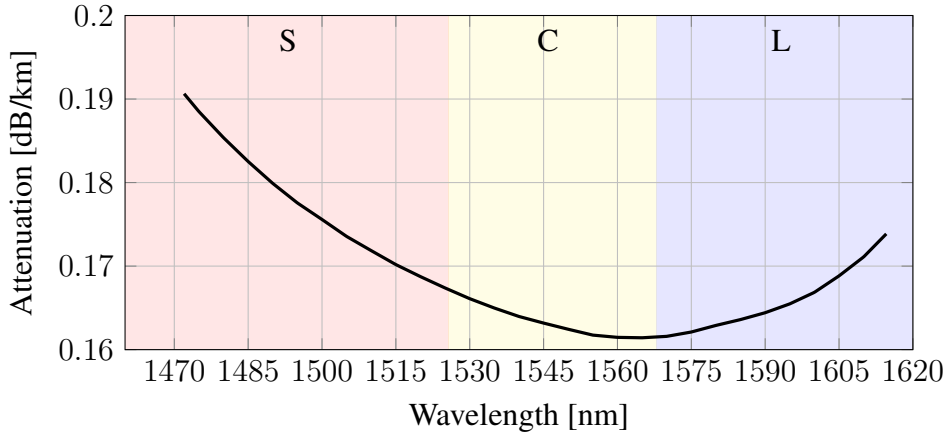

Fig. 3.1: Experimentally measured attenuation coefficient of a Corning© SMF-28© ULL fibre.

under study is made up of identical spans in terms of fibre parameters, also called the homogeneous link assumption. This is equivalent of assuming that $\eta_{\text{SPM}}(f_i)$, $\eta_{\text{XPM}}(f_i)$, and $\eta^{(k)}_{corr,a}(f_i)$ are independent of the fibre span j, and $\sum_{j=1}^{n}(P_{i,j}/P_i)^2 = n$ in Eqs. (2.55) and (3.4). Under this condition, the SNR_{NLI} can be written as

$$\begin{aligned}\text{SNR}_{\text{NLI},i}^{-1} \approx{}& \frac{16}{27}\frac{\gamma_i^2 P_i^2}{B_i^2} T_i^2 \sum_{\substack{0\le l\le 1\\ 0\le l'\le 1}} \left(\frac{-\tilde{T}_i}{T_i}\right)^{l+l'} \frac{2\pi\kappa_{l,i}\kappa_{l',i} n^{1+\epsilon}}{(\tilde{\alpha}_{l,i}+\tilde{\alpha}_{l',i})\phi_i} \left[\operatorname{asinh}\left(\frac{3\phi_i B_i^2}{8\pi\tilde{\alpha}_{l,i}}\right) + \operatorname{asinh}\left(\frac{3\phi_i B_i^2}{8\pi\tilde{\alpha}_{l',i}}\right)\right] \\ &+ \frac{32}{27}\sum_{k=1,k\neq i}^{N_{\text{ch}}} \frac{\gamma_i^2 P_k^2}{B_k} T_k^2 \sum_{\substack{0\le l\le 1\\ 0\le l'\le 1}} \left(\frac{-\tilde{T}_k}{T_k}\right)^{l+l'} 2\kappa_{l,k}\kappa_{l',k} \left\{\frac{n+\frac{5}{6}\Phi}{(\tilde{\alpha}_{l,k}+\tilde{\alpha}_{l',k})\phi_{i,k}} \left[\operatorname{atan}\left(\frac{\phi_{i,k}B_i}{2\tilde{\alpha}_{l,k}}\right)\right.\right. \\ &\left.\left. + \operatorname{atan}\left(\frac{\phi_{i,k}B_i}{2\tilde{\alpha}_{l',k}}\right)\right] + \frac{5}{6}\frac{\Phi\pi\tilde{n}}{|\phi|\, B_k^2\tilde{\alpha}_{l,k}\tilde{\alpha}_{l',k}} \left[(2|f_k-f_i|-B_k)\ln\left(\frac{2|f_k-f_i|-B_k}{2|f_k-f_i|+B_k}\right)+2B_k\right]\right\},\end{aligned} \tag{3.16}$$

where $\tilde{n} = 0$ for a single span or $\tilde{n} = n$ otherwise. Also, the indices i and k were included in all the variables to show their channel dependence explicitly. Moreover, if the homogeneous and transparent link assumption is removed, those variables becomes also span-dependent. Finally, note that, in the limit $\alpha_{l,i}L \to \infty$, Eq. (3.16) converges to that in [99].

3.2 Applications and validation of the accuracy of the closed-form expression

This section describes the numerical validation of the closed-form expression described in Sec. 3.1.3. To that end, Eq. (3.16) were compared with the ISRS GN model in integral form for Gaussian constellations [33] given by Eq. (2.49), and with the modulation format correction contribution [37] given by Eqs. (3.5) and (3.6). The results were also

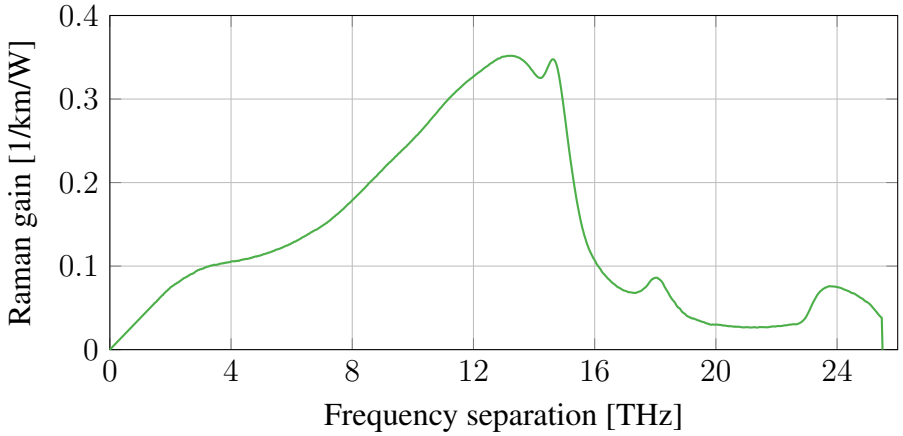

Fig. 3.2: Experimentally measured Raman gain spectrum of a Corning© SMF-28© ULL fibre for a pump wavelength at 1457 nm and $A_{\text{eff}} = 80\ \mu\text{m}^2$.

compared with SSFM simulations described in Sec. 2.5, for the transmission system described in Sec. 3.2.1.

3.2.1 Transmission system

The baseline transmission system, over which the derived expressions were validated, consisted of a WDM transmission with N_{ch}=181 channels spaced by 100 GHz and centred at 1540 nm. Each channel was modulated at the symbol rate of 96 GBd. This resulted in a total bandwidth of 20 THz (158 nm), ranging from 1470 nm to 1615 nm, corresponding to the transmission over the S- (1470 nm - 1530nm), C- (1530 nm - 1565nm) and L- (1565 nm - 1615nm) bands. Spectral gaps of 10 nm and 5 nm were assumed between the S-/C- and C-/L- bands, respectively. The channels were transmitted over 5 spans using a SMF where the span length is varied to show the accuracy of the derived expressions for different span lengths. It was assumed that each amplifier fully compensates for the span losses (the transparent link assumption). A spectrally uniform input launch power profile was used, with each channel having a launch power of 1 dBm. A realistic wavelength-dependent attenuation profile and Raman gain spectrum (considering a constant $A_{\text{eff}} = 80\ \mu\text{m}^2$ for all the channel) were measured from a Corning© SMF-28© ULL fibre as shown in Figs. 3.1 and 3.2 and were used in this section for the closed form expression validations. Dispersion parameter and dispersion slope were $D = 16.5\ \frac{\text{ps}}{\text{nm}\cdot\text{km}}$, $S = 0.067\ \frac{\text{ps}}{\text{nm}^2\cdot\text{km}}$ and a constant nonlinear parameter for all the channels $\gamma_i = 1.03 \frac{1}{\text{W}\cdot\text{km}}$ (see Secs. 2.4.2 and 2.4.3) was assumed.

To verify the accuracy of the proposed closed-form expression, a variety of span lengths and losses were also considered; these values are described in detail in Sec. 3.2.2. Additionally, Gaussian modulated and 64-QAM symbols were also used. For the latter, this was achieved by setting the excess kurtosis in Eq. (3.16) to $\Phi = -0.6190$, against $\Phi = 0$ for the former.

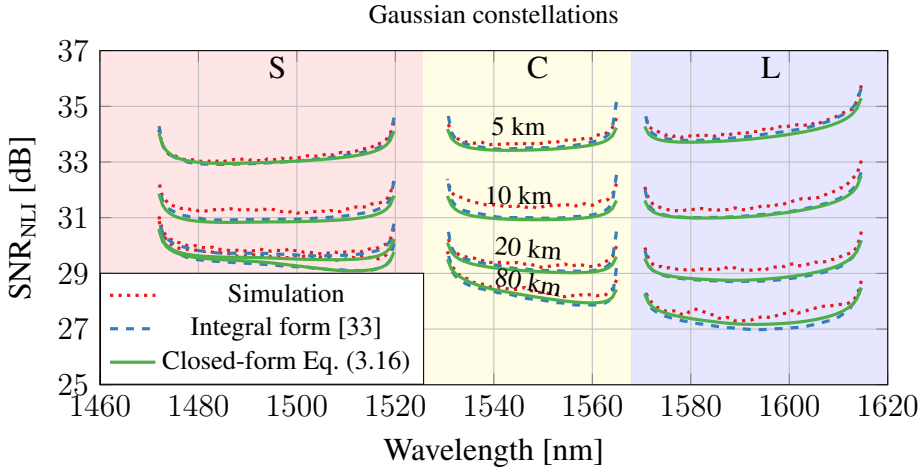

Fig. 3.3: Nonlinear performance for Gaussian constellations after 5 spans for different spans lengths using the closed-form formula in Eq. (3.16) (green), the ISRS GN model in integral form (blue) and the SSFM simulation (red). The attenuation profile used is shown in Fig. 3.1.

3.2.2 Numerical validation

The transmission system performance estimation using the proposed closed-form formula, i.e., Eq. (3.16), was carried out for two different scenarios using the transmission setup described in Sec. 3.2.1. The scenarios were chosen to assess the formula for short-span lengths and low losses. For the first scenario, a variety of span lengths were chosen. These results are shown in Fig. 3.3 for Gaussian constellations and in Fig. 3.4 for 64-QAM constellations. More specifically, span length values of 5 km, 10 km, 20 km and 80 km were chosen to show the accuracy of the proposed closed-form for short and long-span lengths. For these scenarios, the attenuation profile used is shown in Fig. 3.1.

In the second scenario the span length was fixed to a value of 80 km and different spectrally uniform loss profiles were used. These results were also shown for Gaussian constellations in Fig. 3.5 and for 64-QAM constellations in Fig. 3.6.

The interaction between fibre attenuation, dispersion and normalised ISRS-power evolution profile, led to the $\mathrm{SNR}_{\mathrm{NLI}}$ profile as shown in Figs. 3.3, 3.4, 3.5 and 3.6. The higher dispersion towards the L-band reduced the NLI for the long-wavelength channels. This reduction however was counter-balanced by the ISRS-transferred power from short to long wavelength channels, increasing the NLI for these channels, and thus reducing the $\mathrm{SNR}_{\mathrm{NLI}}$. In the case of Figs. 3.3 and 3.4, the effect of ISRS was increasingly seen as the span length increases. This is because the longer the span length, the greater the power which was transferred due to ISRS effect. In the case of Figs. 3.5 and 3.6, the same trend was observed among the curves, with a larger tilt due to the ISRS in the case of links with lower losses.

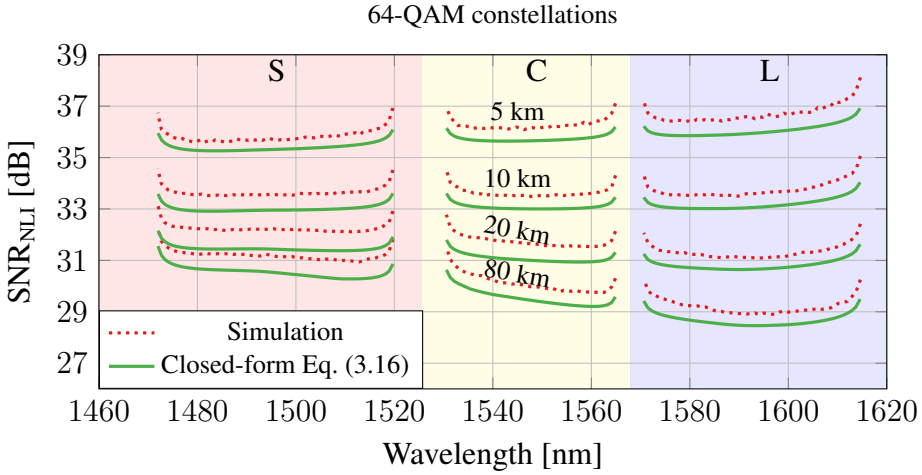

Fig. 3.4: Nonlinear performance for 64-QAM constellations after 5 spans for different spans lengths using the closed-form formula in Eq. (3.16) (green), the ISRS GN model in integral form (blue) and the SSFM simulation (red). The attenuation profile used is shown in Fig. 3.1.

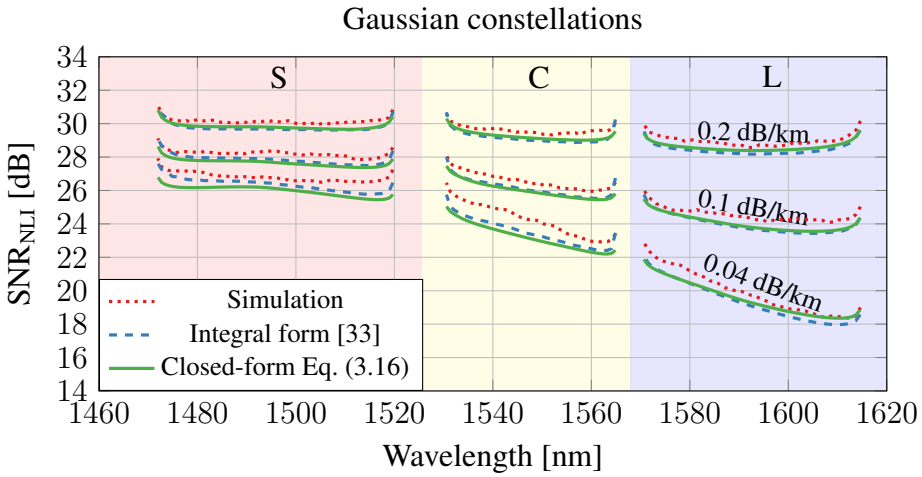

Fig. 3.5: Nonlinear performance for Gaussian constellations after 5 x 80 km spans for different spectrally uniform loss profiles using the closed-form formula in Eq. (3.16) (green), the ISRS GN model in integral form (blue) and SSFM simulation (red).

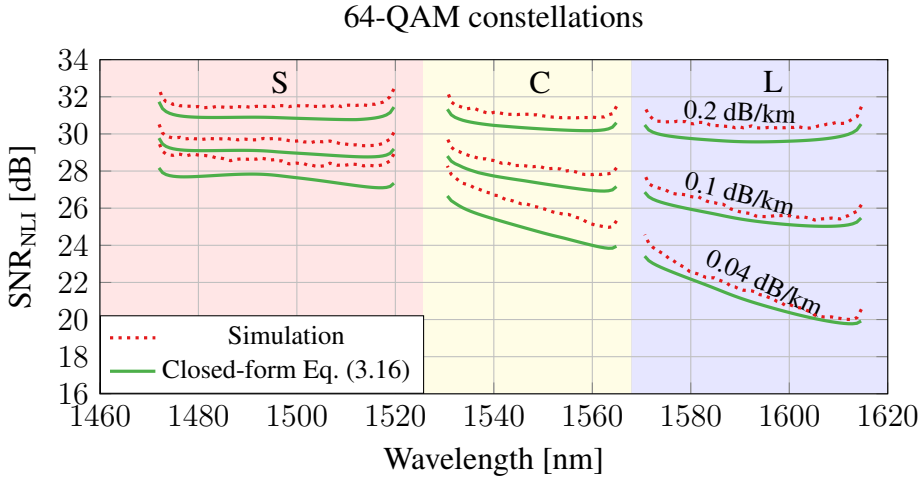

Fig. 3.6: Nonlinear performance for 64-QAM constellations after 5 x 80 km spans for different spectrally uniform loss profiles using the closed-form formula in Eq. (3.16) (green), the ISRS GN model in integral form (blue) and SSFM simulation (red).

To verify the accuracy of the proposed closed-form expression, Eq. (3.16) was compared with the ISRS GN model in integral form, for Gaussian constellation [33] and with SSFM simulations (see Sec 2.5) for both Gaussian and 64-QAM constellations. For the SSFM, a local-error method [62] was used to ensure optimal step size with global local error $\delta_G = 10^{-10}$. This value was found to be sufficient throughout all simulations by comparing simulations with smaller δ_G values and observing insignificant changes in the signal output. The simulations were performed with each channel having 2^{16} random symbols. Due to the relatively short symbol sequence, each result represented an average of eight simulations. The results of these validations are also shown in Figs. 3.3, 3.4, 3.5 and 3.6.

Additionally, for all the scenarios described by each figure, the maximum errors among all curves were computed. For the scenario shown in Fig. 3.3, in which the span length was varied, using Gaussian symbols, the closed-form formula in Eq. (3.16) showed maximum errors of 0.93 dB and 0.58 dB, from integral model and SSFM simulations respectively. For Fig. 3.4, using 64-QAM symbols 1.2 dB maximum error was obtained between Eq. (3.16) and SSFM. The higher inaccuracy for signals using QAM constellations is partly explained by the necessity of adding more correction terms from [28] in Eq. (3.16).

The same analysis was carried out for the scenario where the loss profile was varied. In that case, using Gaussian symbols, Fig. 3.5 shows maximum errors of 1.05 dB and 1.48 dB, respectively, while for 64-QAM symbols Fig. 3.6 shows maximum error of 1.61 dB. For this case, it should be pointed out that the main assumption underlying the GN model is the small perturbation assumption. As discussed in Sec. 2.6, this assumption may fail for links composed of extremely low fibre loss, high power spectral

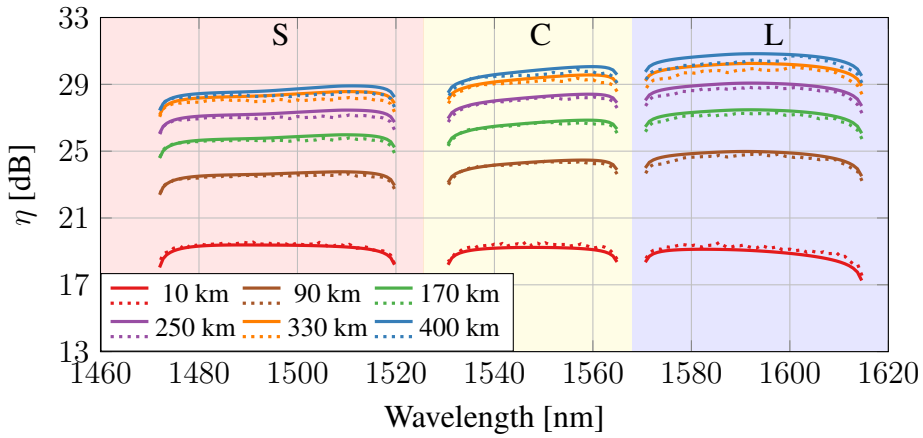

Fig. 3.7: Nonlinear coefficient η_n calculated over portions of an optical fibre link made of 5 x 80 km spans. The portions are chosen as the first 10 km of each span. The results using Eq. (3.16) (continuous lines) are compared with the SSFM simulations (dotted lines).

density, or high γ. Indeed, in these scenarios, higher-order terms have to be included. This fact may justify the large errors presented in Figs. 3.5 and 3.6 for the scenario of 0.04 dB/km. Finally, note that, as this closed-form expression is an extension of the ones in [35, 37], its accuracy for different values of symbol rates for the different NLI contributions, namely, SPM and XPM can be found in [35, Figs. 3,4].

Regarding a rough estimation of the model complexity, using a central processing unit (CPU) without any code parallelisation, one realisation of the closed-form expression in Eqs. (3.13) and (3.12) for all scenarios took less than 1 second, with the majority of the time being spent in the fitting optimisation routine. When using integral model using the same conditions, this time is increased from few to several hours depending on the signal bandwidth and accuracy desired. Results obtained by SSFM simulations took days. For all the cases however, the computational time, could have been reduced to milliseconds by the clever code implementation, parallelisation and utilisation of GPUs.

3.2.3 NLI evolution during propagation in fibre

One of the motivations and importance of the closed-form formula derived in Eq. (3.16) is the possibility of performing an accurate estimate of the NLI in every portion of the fibre link, enabling the calculation of the NLI evolution during propagation in the fibre. The importance of such calculations relies on the ability to account for inline signal impairments, predict failures, and avoid wasting resources as mentioned in this chapter introduction. To illustrate it, the transmission setup described in Sec. 3.2.1 and a 400 km optical fibre link formed of 5 x 80 km spans were considered. Eq. (3.16) was then applied to estimate the NLI for the first 10 km of each span and at the end of the

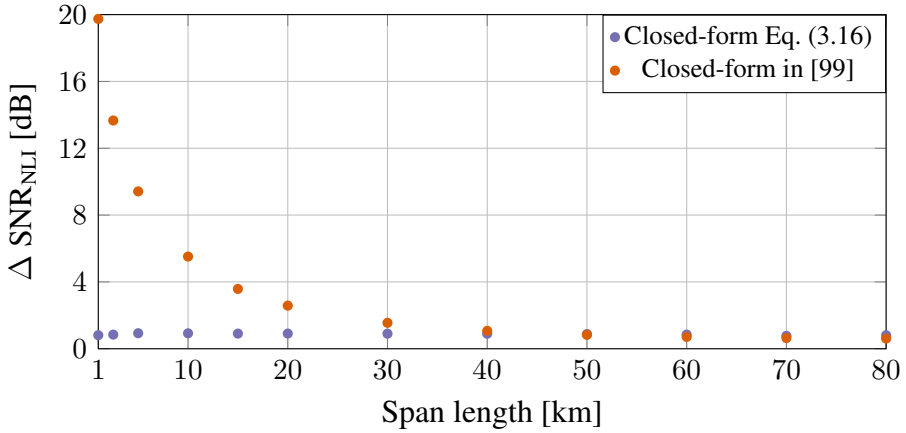

Fig. 3.8: Maximum per-channel $\mathrm{SNR_{NLI}}$ difference ($\Delta\mathrm{SNR_{NLI}}$) between the integral ISRS GN model and the proposed closed-form formula in Eq. (3.16) (purple points) for different span lengths. The $\Delta\mathrm{SNR_{NLI}}$ using the formula in [99] are also shown for comparison (orange points).

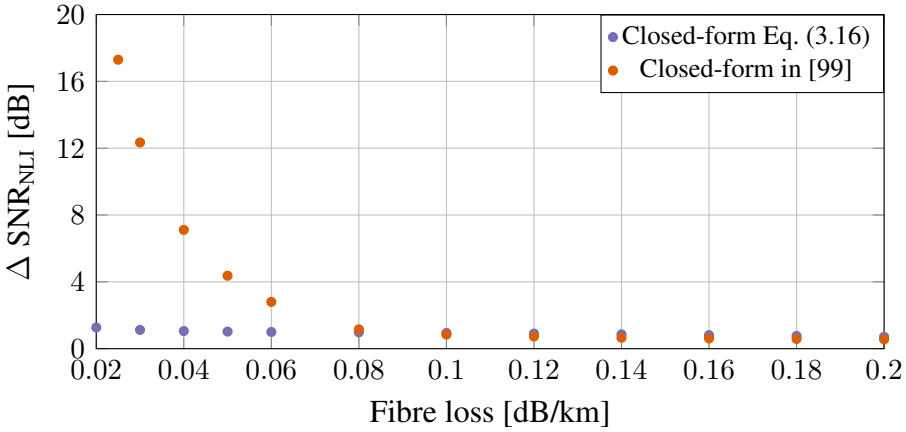

Fig. 3.9: Maximum per-channel $\mathrm{SNR_{NLI}}$ difference ($\Delta\mathrm{SNR_{NLI}}$) between the integral ISRS GN model and the proposed closed-form formula in Eq. (3.16) (purple points) for different fibre losses. The $\Delta\mathrm{SNR_{NLI}}$ using the formula in [99] are also shown for comparison (orange points).

link.

Fig. 3.7 shows the nonlinear coefficient η_n, defined by Eq. (2.54), as a function of wavelength for different distances using Eq. (3.16) (continuous lines). The results were also matched using SSFM simulations (dotted lines); among all the curves a maximum per-channel error of 0.58 dB was found after a propagation distance of 400 km. Note that, the discussion of these results is similar to the ones described in Sec. 3.2 and is omitted in this section.

3.3 Validity range of the closed-form expression and comparison with previously reported expressions

As mentioned in the introduction of this chapter, the closed-form expression derived Sec. 3.1.3 can account for any span length and fibre losses. This is fundamental for modelling short-reach links, ULL fibre technologies, hollow-core fibres, etc. In this section, the accuracy of these expressions, i.e., Eq. (3.16), was compared with that of the closed-form expressions reported in [35, 37, 99] also given by Eqs (2.57) and (2.58). A mathematical justification of the inaccuracy of the later expressions and the validity range of the former is also discussed in this section.

To assess the accuracy of the closed-form expression, the simulation scenario was varied in two different ways. Firstly the span length was swept from 1 km to 80 km and secondly, the span length was fixed at 80 km and a spectrally uniform loss profile ranging from 0.02 dB/km to 0.2 dB/km was considered. The results were obtained considering Gaussian constellations and transmission over 5 spans.

Figs. 3.8 and 3.9 show the maximum per-channel $\mathrm{SNR_{NLI}}$ difference, i.e., the maximum per-channel error in terms of $\mathrm{SNR_{NLI}}$ between the integral ISRS GN model and the proposed closed-form formula in Eq. (3.16) for different span lenghs and fibre losses respectively. For comparison, the same analysis was also carried out with the closed-form expression reported in [99] (Eqs (2.57) and (2.58)). As shown in Figs. 3.8 and 3.9, the new closed-form formula proposed in Sec. 3.1.3 can accurately account for any span length and fibre loss; among all the scenarios considered in Figs. 3.8 and 3.9, maximum errors of 0.93 dB and 1.27 dB were found respectively when considering different span lengths and losses.

A brief discussion is now provided on the validity range of the closed-form formula proposed in Eq. (3.16) and the limitations of that derived in [35, 37, 99]. To that end, consider Eq. (3.7). In the work [35, 37, 99], the following approximation was used

$$\frac{1-e^{-(\alpha_{l,i}-j\phi)L}}{-\alpha_{l,i}+j\phi} \approx \frac{1}{-\alpha_{l,i}+j\phi}, \tag{3.17}$$

where it is easily seen that its accuracy relies on the condition $\alpha_{l,i}L \to \infty$. Note that, the breaking of this condition was the source of the inaccuracy shown in Figs. 3.8 and 3.9 for the closed-form expression published in [35, 37, 99].

On the other hand, Eq. (3.16) relies on the approximation shown in Eq. (3.8), in which a Taylor expansion was performed around $\phi = 0$. This approximation is inaccurate when $\alpha_{l,i}L \to 0$. This is because in this condition, the oscillator function in the numerator $1 - e^{j\phi L} \not\approx 1$, as required by the Taylor expansion around $\phi = 0$. Thus, in order to satisfy the requirement $1 - e^{j\phi L} \approx 1$, the condition $\alpha_{l,i}L \gg 0$ should be satisfied.

Finally, by comparing the requirement of the accuracy of the closed-form formulae published in [35, 37, 99] ($\alpha_{l,i}L \to \infty$) with that of Eq. (3.16) ($\alpha_{l,i}L \gg 0$), it is noted that this last requirement is much less restrictive than that of $\alpha_{l,i}L \to \infty$, justifying the accuracy of Eq. (3.16) for a wide range of scenarios including those of arbitrary span lengths and fibre losses. Additionally, as pointed out in Sec. 3.1.3, in the limit $\alpha_{l,i}L \to \infty$, Eq. (3.16) converges to that in [99].

3.4 Summary

A closed-form formula that can accurately evaluate the NLI in the presence of ISRS at any step of the fibre span and in extremely low loss regimes (~ 0.04 dB/km) was proposed. The formula was applied in modelling an S+C+L band (20 THz) transmission system and its accuracy was verified through comparisons with results obtained using integral model and SSFM simulations. Using the proposed closed-form formula, the NLI could be calculated in a few microseconds, enabling rapid performance evaluations (e.g., SNR, maximum reach, optimum launch power estimations) in UWB transmission systems.

The proposed formula enabled accurate inline NLI estimation of any portion of the optical fibre link, representing an essential step towards the development of intelligent and dynamic optical fibre networks. The latter, together with the computational speed of the proposed closed-form formula, will enable effective network planning tools allowing an online assessment of the data rates, modulation formats, the number of channels and launch power profile, given the fibre, amplifier characteristics and allocated lightpaths. The formula is also useful for NLI estimation using very low-loss fibre technologies, such as ULL fibres and hollow-core fibres. Additionally, it can be used for NLI estimation in short-reach links.

The work presented in this chapter represents the first closed-form expression valid for UWB system with arbitrary span lengths and fibre losses. The work was presented first at 2022 European Conference on Optical Communications (ECOC) [100] and further extended to a journal paper published in the Journal of Lightwave Technology (JLT) [101].

Chapter 4

A closed-form expression for the Gaussian noise model in the presence of Raman amplification

In chapter 3, a closed-form expression for the GN model was derived supporting arbitrary span length and fibre losses. This closed-form expression [100, 101] was an extended version of the closed-form described in Sec. 2.7 [35, 37]. It should be pointed out that the expressions described in Sec. 2.7 and the ones in Chapter 3 are valid for lumped amplifiers only, including EDFAs, TDFAs, BDFAs and SOAs. This is because they were derived by considering Eq. (2.51) as a semi-analytical solution of the coupled Raman equations given by Eq. (2.38). This equation accounts only for the effects of intrinsic fibre loss and ISRS effect and thus cannot model Raman amplifiers. In this chapter, for the first time a semi-analytical solution of the Raman equations in the presence of RA given by Eq. (2.39) is described. This semi-analytical solution was used to derive closed-form expressions that account for any schemes of amplification, including distributed RA technologies.

A wide range of works has shown the benefits of using RA to achieve higher throughputs [6, 10, 11, 12, 14, 15, 16, 19, 20, 104]. RA can be divided into two types, namely distributed RA and discrete RA. For the former, the pumps are injected into the transmission fibre, while for the latter a separate fibre is used as the amplification stage (see Sec. 2.8.2). In both cases, the pumps interact with the signal to provide the desired signal amplification. The complex physics of these systems requires the development of real-time models to optimise the system design maximising the system throughput.

This chapter focuses on the derivation of a closed-form formula to estimate the NLI in Raman-amplified links. Most of the closed-form expressions of the ISRS GN model [34, 35, 36, 37, 38, 61, 96, 100, 101] were valid or tested for lumped-amplified links only, of which some of them were described in Chapters 2 and 3. The exceptions are the closed-form formulas derived in [38, 96]. Despite the closed-form formula in [38, 96] being valid and tested for Raman amplified links, it is limited to FW pumping schemes and was tested only over C-band systems. A closed-form formula limited to BW pumping schemes can be found in [105], however, it is only valid for C-band systems and limited to 2nd order RA, i.e., the utilisation of two or fewer pumps.

A general closed-form expression of the ISRS GN model [33] supporting both

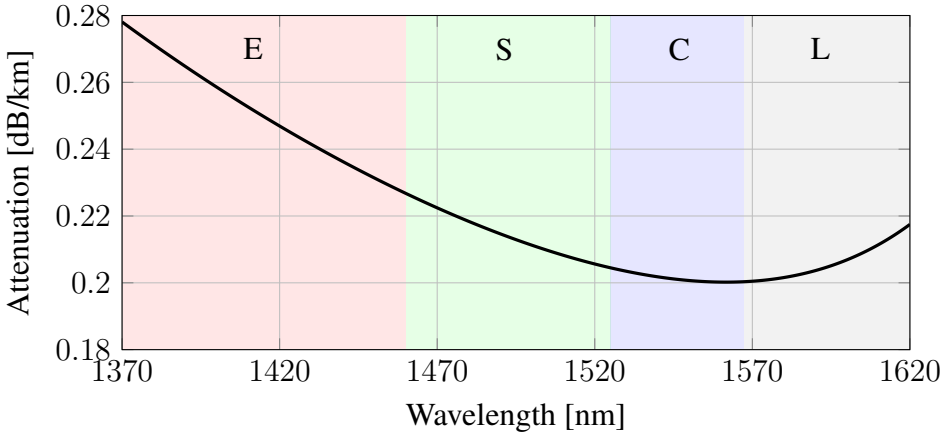

Fig. 4.1: Attenuation coefficient of an ITU-T G652.D fibre.

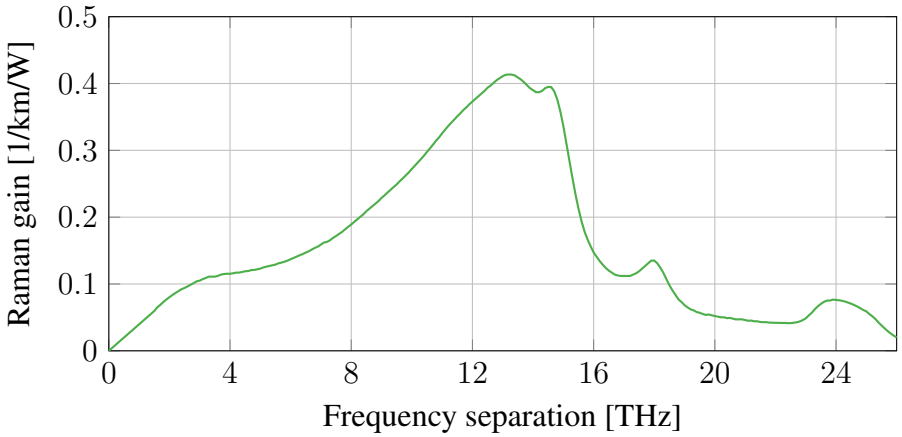

Fig. 4.2: Raman gain spectrum of an ITU-T G652.D fibre for a pump wavelength at 1456 nm and $A_{\text{eff}} = 80\ \mu\text{m}^2$.

FW-RA and BW-RA, ISRS, valid for arbitrary-order RA, i.e., an arbitrary number of pumps was proposed during this PhD research, published in [P3], [P12], [P14], experimentally validated in [P22] and described in this chapter. This expression represents the first closed-form expression of the GN model supporting FW-RA and BW-RA in the presence of ISRS. This was enabled by deriving, for the first time, a semi-analytical solution to model the signal profile in the presence of RA and ISRS. The proposed closed-form formulation is valid for arbitrary constellations, including shaped and square QAM formats, and in this chapter was tested using a distributed RA setup. Its accuracy was verified with numerical integration of the ISRS GN model and SSFM simulations. The formula was also experimentally validated using an S+C+L-band hybrid-amplified long-haul transmission system experiment. Recently, another nonlinear closed-form model also valid for arbitrary Raman setup was independently published by a different group [106, 107].

The closed-form expression presented in this chapter was first presented at the 2023 Optical Fiber Communication Conference (OFC) [108]. The work in [108] was

extended to a journal paper and published in JLT [109]. Another piece of work extended the model in [108, 109] to arbitrary modulation formats and was presented at ECOC 2023. The formula was experimentally validated in [110], and was presented at ECOC 2024. This chapter extensively discusses the validation of this model and presents all the mathematical derivations used to obtain it. A complete discussion on the semi-analytical approach used to obtain an accurate estimation of the fibre signal profile evolution along the fibre length in the presence of RA, given in differential form by Eq. (2.39), is also discussed. Note that, derivations in this chapter were carried out as part of this PhD research and represent novel work. However, to improve readability they were moved to dedicated appendices.

4.1 The signal profile evolution

The first step in obtaining a closed-form expression for NLI noise was to derive a semi-analytical expression for the signal profile evolution along the optical fibre distance, specifically an analytical solution to Eq. (2.39). In the LA scenario, this equation simplifies to Eq. (2.38) with an analytical expression derived in Eq. (2.51) in the work [35], which considered only the ISRS effect. This section introduces a semi-analytical approach for hybrid links where RA is used. The approach is a semi-analytical solution of Eq. (2.38), incorporating both ISRS and RA, where FW and BW pumps are injected in the fibre along with the transmitted signal. The derivation of this semi-analytical expression is a fundamental step which enabled the first UWB closed-form expression applicable to hybrid-amplified links, representing one of the main contributions of this thesis. Additionally, this section evaluates the accuracy of the derived semi-analytical approach.

4.1.1 The derivation of the closed-form expression for signal profile evolution

As mentioned in Secs. 2.6 and 2.7, for NLI estimation expressions based on RP analysis, such as the GN model and its extensions [27, 33, 28], the estimation of the NLI interference is dependent on the signal power profile evolution along the optical fibre distance. Because of this, a fundamental step in deriving any closed-form expression for NLI estimation is to first derive a closed-form expression for the signal power profile evolution.

In the case of C-band systems, such an expression is trivial as the signal power evolution is only loss-dependent [27] and a trivial solution can be obtained as per Eq. (2.20). The situation is more complex in the presence of ISRS as the power of each channel interacts with one another and a set of coupled differential equations must be solved (Eq. (2.38)). Analytical expressions for this case were derived in [102, 103]. These expressions were used in [35] (Eqs. (16) and (17)) to derive a semi-analytical

solution of the signal power profile evolution, given by Eq. (2.51). The solution is semi-analytical because it is further optimised to correctly reproduce the solution of the coupled differential equations.

The situation is even more complicated in the case of RA, where besides the channel-channel interactions, pump-signal and pump-pump interactions must also be considered, not only in the FW direction but also in the BW one. Indeed, for the case of RA and ISRS, the solution of the so-called coupled differential Raman equations in the presence of RA given by Eq. (2.39) must be solved.

The first step in deriving the proposed closed-form expression for NLI estimation in this chapter was to find a semi-analytical expression for Eq. (2.39). Semi-analytical approaches were used in [35, 96, 105, 111] to model specific transmission setups. However, other types of approaches are also possible, e.g. [112]. In this thesis for the first time, a general semi-analytical solution to account for any RA setup scenario with ISRS effect is proposed.

To carry out this derivation, the work in [102] was used as a starting point and all the derivation steps are shown in Appendix D. Recall $\rho(z, f_i)$ represents the signal profile evolution normalised by the input power profile, i.e., $\rho(z, f_i) = \frac{P(z,f_i)}{P(0,f_i)}$ (see Eq.(2.51)). Thus, a semi-analytical solution of Eq. (2.39) is given by

$$\rho(z, f_i) = e^{-\alpha_i z}[1 - (C_{f,i} P_f L_{\text{eff}} + C_{b,i} P_b \tilde{L}_{\text{eff}})(f_i - \hat{f})], \tag{4.1}$$

where

$$L_{\text{eff}}(z) = (1 - e^{-\alpha_{f,i} z})/\alpha_{f,i} \quad ,$$
$$\tilde{L}_{\text{eff}}(z) = (e^{-\alpha_{b,i}(L-z)} - e^{-\alpha_{b,i} L})/\alpha_{b,i} \quad ,$$

α_i, $\alpha_{f,i}$ and $\alpha_{b,i}$ are fibre attenuation coefficients, $\hat{f}$ is the average frequency of the FW and BW pumps, P_f, and P_b are the total launch power respectively from the WDM channels together with any FW pumps, and the BW pumps, $C_{f,i}$ and $C_{b,i}$ is the slope of a linear regression of the normalised Raman gain spectrum. The proof of Eq. (4.1) is given in Appendix D.

The coefficients α_i, $C_{f,i}$, $C_{b,i}$, $\alpha_{f,i}$, and $\alpha_{b,i}$ are channel-dependent parameters and matched using nonlinear least-squares fitting to correctly reproduce the solution of the Raman differential equations in the presence of RA, obtained by numerically solving Eq. (2.39). Note that, three different loss coefficients (α_i, $\alpha_{f,i}$, and $\alpha_{b,i}$) and two different slopes of the Raman gain spectrum ($C_{f,i}$ and $C_{b,i}$) are considered - this enables an increase in the dimension of optimisation space and is essential for modelling all the RA scenarios. The parameters α_i, $C_{f,i}$, $C_{b,i}$, $\alpha_{f,i}$, and $\alpha_{b,i}$ can be interpreted as modelling respectively the fibre loss, the gain/loss due to FW-RA and

Table 4.1: Pump power and wavelength allocations which yields the power profiles shown in Figs. 4.3, 4.4 and 4.5.

	E-band								S-band	
Wavelength [nm]	1402.1	1408.7	1415.4	1422.1	1428.8	1435.7	1442.6	1449.6	1456.6	1463.7	1485.4
Forward Raman Pump Scenario											
FW pumps' power at $z = 0$ [mW]	150.9	331.3	161.2	119.5	34.3	35.8	30.4	25.7	-	63.0	17.2
Backward Raman Pump Scenario											
BW pumps' power at $z = L$ [mW]	-	668.7	64.6	167.7	14.3	58.2	45.3	50.8	-	13.4	58.5
BW pumps' power at $z = 0$ [μW]	-	203.9	40.0	200.9	30.7	198.7	225.6	350.0	-	186.4	5235
Forward + Backward Raman Pump Scenario											
FW pump power at $z = 0$ [mW]	-	-	-	-	-	-	-	-	-	-	393.32
BW pumps' power at $z = L$ [mW]	297.79	123.07	130.92	184.78	-	80.68	17.88	-	24.23	27.41	-
BW pumps' power at $z = 0$ [μW]	53.9	43.7	96.6	263.5	-	327.9	103.9	-	250.8	396.7	-

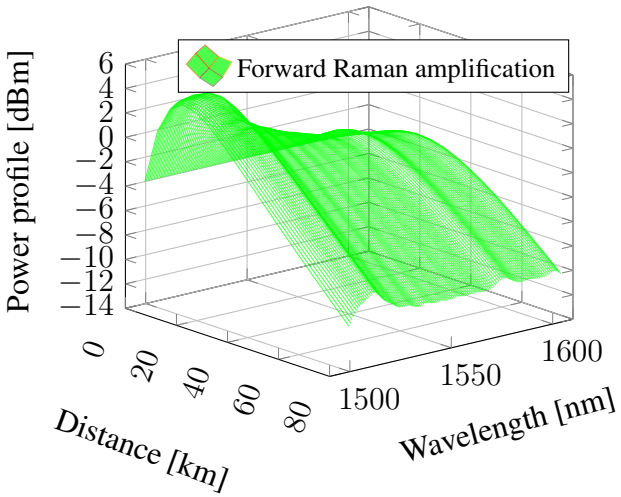

Fig. 4.3: Per-channel launch power evolution with distance for FW-RA.

BW-RA together with ISRS and how fast the channel gain/loss due to the FW-RA and BW-RA together with ISRS extinguishes along the fibre. This fitting optimisation overcomes the restrictive assumptions described in Appendix D, which were used to derive Eq. (4.1) and enables its utilisation in any simulation scenario, such as any number of pumps, launch power profiles and bandwidths.

A main difference between the semi-analytical approach proposed here and the one in [35] (the latter given by Eq. 2.51), is the utilisation of 5 optimisation coefficients, against 3 for the latter. The 2 additional coefficients are essential to model BW-RA. Note that, the approach presented in this section is valid for arbitrary-order RA, i.e., an arbitrary number of Raman pumps. The approach is also a generalisation of Eq. (2.51) [35] as it is also valid for LA - if one sets $C_{b,i} = 0$ and $\hat{f} = 0$, the semi-analytical solution for the normalised signal profile shown in Eq. (2.51) [35] is obtained.

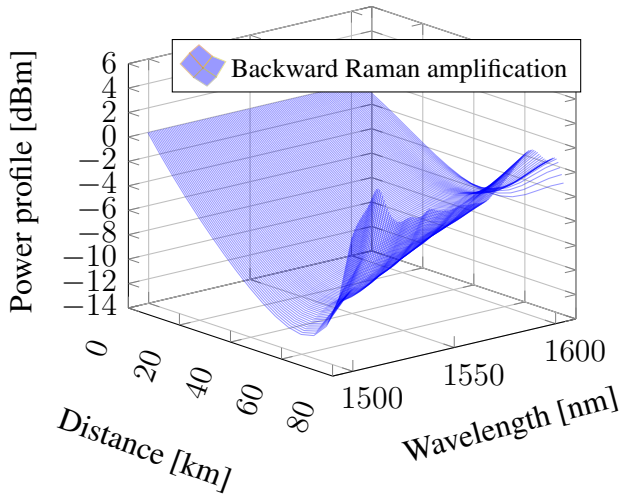

Fig. 4.4: Per-channel launch power evolution with distance for BW-RA.

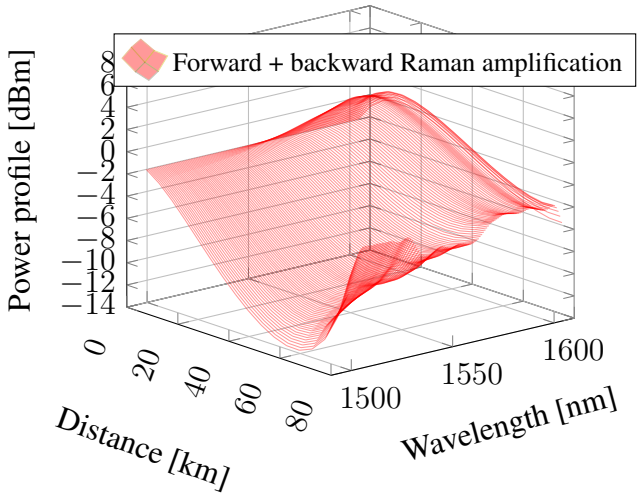

Fig. 4.5: Per-channel launch power evolution with distance for FW+BW-RA.

4.1.2 Accuracy and application of the semi-analytical expression for signal profile evolution estimation

This section illustrates the application of the semi-analytical solution proposed in Eq. (4.1) to reproduce the solution of the differential Raman equations in Eq. (2.39).

Eq. (4.1) was applied over a transmission setup consisting of a WDM signal with N_{ch}=131 channels spaced by 100 GHz and centred at 1550 nm. The signal was amplified using distributed RA. Each channel was modulated at the symbol rate of 96 GBd, resulting in a total bandwidth of 13 THz (105 nm), ranging from 1500 nm to 1605 nm, corresponding to the transmission over the S- (1470 nm - 1530 nm), C- (1530 nm - 1565 nm) and L- (1565 nm - 1615 nm) bands. Gaussian symbols were considered in the transmission. For both scenarios, the span length was 80 km and an ITU-T G652.D fibre was considered with attenuation profile and the Raman gain spectrum (considering a constant $A_{\text{eff}} = 80\ \mu\text{m}^2$ for all the channel) shown in Figs. 4.1 and 4.2 respectively.

Three different simulation scenarios were considered: FW-RA, BW-RA and FW+BW-RA. A spectrally uniform launch power profile, where each channel carries -4 dBm, 0 dBm and -2 dBm was considered, respectively, for each one of the scenarios. For all the cases, the number of pumps, and their wavelengths and powers were chosen based on a "find minimum of constrained nonlinear multivariable" optimisation algorithm implemented in Matlab. Because this section deals only with the SNR_{NLI}, this optimisation was based on the received power and pump powers as the figures of merit (and not the total SNR). In this algorithm, the cost function considered was $\sum_p P_p$, such that the total power of the pumps was minimised. The optimisation was done over a single span. A nonlinear constraint was also considered such that the received per-channel launch power was above a given threshold. Over the E- and S-band 15 pumps spaced from 1 THz apart were placed and the algorithm found the best power allocation. The highest-wavelength pump was chosen to be 2 THz away from the lowest-wavelength channel.

Ideal amplification was assumed such that the received power equals the transmitted power. For FW-RA, pumps were optimised such that at least a quarter of the launch power was recovered at the Rx, for BW-RA and FW+BW-RA, pumps were optimised such that at least half of the launch power was recovered at the Rx. The remaining launch power can be recovered, for instance, with LA. An example of fully recovered launch power using RA can be found in [108]. For all scenarios, the pump allocations with non-zero power found by the described algorithm is shown in Table 4.1.

For the three scenarios, the per-channel power profile along the distance, i.e., the solution of Eq. (2.39), are shown in Figs. 4.3, 4.4 and 4.5 for FW-RA, BW-RA and FW+BW-RA cases, respectively. Note that, for the FW-RA lower per-channel launch

power was chosen (-4 dBm) to limit the per-channel-power peak along the distance to less than 4 dBm as shown in in Fig. 4.3; for this case, such high power may be impractical in currently deployed systems, but still, this scenario was considered as a stress-test of the proposed NLI model.

The goal is now to reproduce the profiles shown in Figs. 4.3, 4.4 and 4.5, obtained from Eq. (2.39) using the semi-analytical solution shown in Eq. (4.1) after the fitting optimisation routine described in Sec. 4.1.1. For better visualisation, Fig. 4.6 shows the results for the worst-performing channel in terms of accuracy between Eq. (2.39) and Eq. (4.1) for (a) FW-RA, (b) BW-RA and (c) FW+BW-RA.

Note that, for the NLI estimation, the effect of the normalised signal profile for each channel is taken into account as an integration over the fibre length (see Eq. (3.3)); this means that the inaccuracies shown in Fig. 4.6 have a negligible impact on the accuracy of the NLI estimation, which is validated in the next section. This is because, for the FW-RA case (Fig. 4.6(a) green), the overestimation of power shown in the first 10 km of fibre was compensated by an underestimation in the remaining kilometres, while for the BW-RA case (Fig. 4.6(b)) the inaccuracies occurred only for reduced-power levels which did not contribute significantly to the result of the integral in Eq. (3.3). Thus, Fig. 4.6 shows that the proposed fitting strategy enabled reproducing Eq. (2.39) by using Eq. (4.1) and accurately capturing the most impactful contributions to the integral in Eq. (3.3).

4.2 Closed-form expression for the NLI estimation valid for Gaussian constellations

This section describes the closed-form expression used to estimate the NLI in the presence of RA. Firstly, $\eta_n(f_i)$ was derived in closed-form, which was then used to calculate $\mathrm{SNR}_{\mathrm{NLI},i}$ in Eq. (2.69). The integral expressions used as a baseline to derive the closed-form expression were presented in Sec. 3.1.1. These expressions depend on the normalised signal power profile evolution $\rho(z, f_i)$, which were derived in closed form in Sec. 4.1.1 and is given by Eq. (4.1). This equation is of fundamental importance to derive all the closed-form expressions presented in this chapter as these expressions were obtained by using this semi-analytical solution. In this section, the closed-form expression was also applied in a transmission system and its accuracy was verified using numerical simulation. Note that, because this section deals only with $\mathrm{SNR}_{\mathrm{NLI}}$, ASE noise contributions were not presented in this section, however, these contributions were discussed in Sec. 2.8.2 and incorporated into the model in Sec. 4.4 and Chapter. 5.

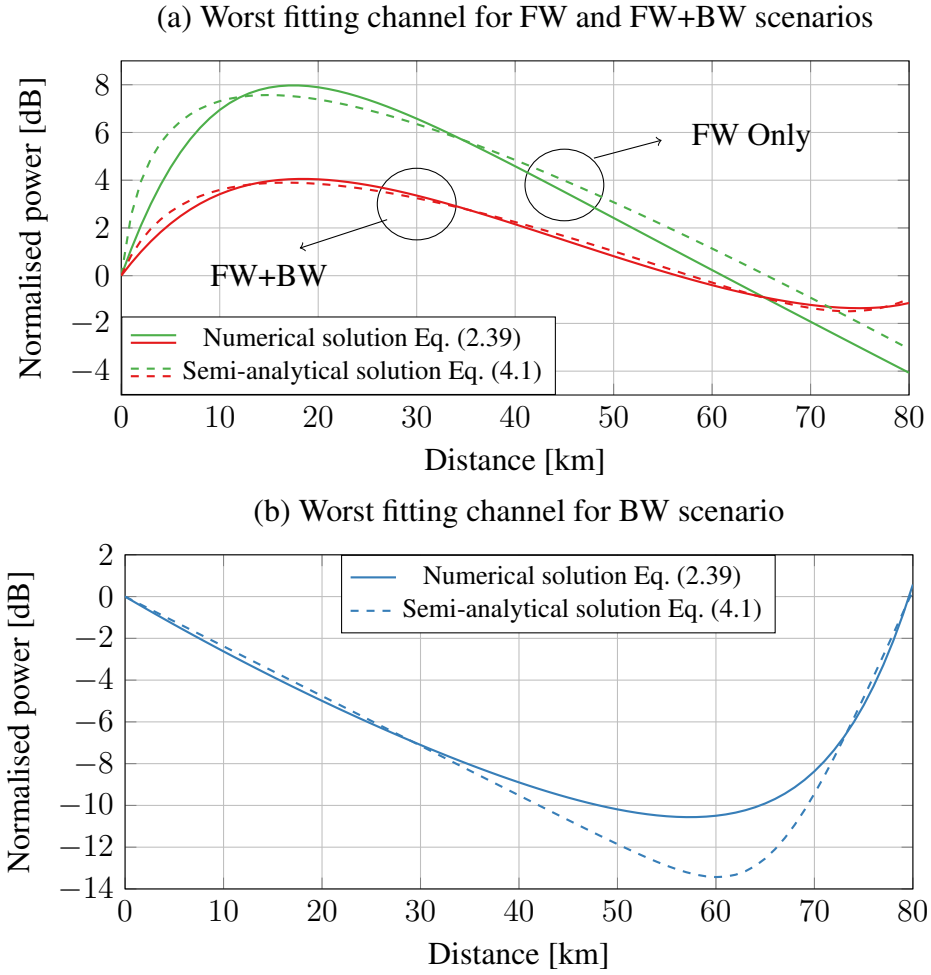

Fig. 4.6: Signal power evolution with distance obtained using the numerical solution of the Raman differential equations in Eq. (2.39) and the semi-analytical solution shown in Eq. (4.1) for (a) FW-RA at 1513.25 nm, FW+BW-RA at 1591.1 nm and (b) BW-RA at 1512.49 nm. In all cases, the results are shown for the worst-performing channel in terms of accuracy between Eq. (2.39) and Eq. (4.1).

4.2.1 Derivation of the closed-form expression

The first step was to derive a closed-form expression of the link function, given in integral form by Eq. (3.3), introduced in Sec. 3.1.1. Let

$$T_{f,i} = -\frac{P_f C_{f,i}(f_i - \hat{f})}{\alpha_{f,i}}, \qquad T_i = 1 + T_{f,i} - T_{b,i} e^{-\alpha_{b,i} L},$$
$$T_{b,i} = -\frac{P_b C_{b,i}(f_i - \hat{f})}{\alpha_{b,i}}, \qquad \alpha_{l,i} = \alpha_i + l_1 \alpha_{f,i} - l_2 \alpha_{b,i},$$
$$\kappa_{f,i} = e^{-(\alpha_i + l_1 \alpha_{f,i}) L},$$
$$\kappa_{b,i} = e^{-l_2 \alpha_{b,i} L}.$$

The link function was approximated in closed form as

$$\mu\left(f_1+f_i,f_2+f_i,f_i\right)\approx\sum_{\substack{0\le l_1+l_2\le 1\\0\le l_1'+l_2'\le 1}}\Upsilon_i\Upsilon_i'\left[\frac{(\kappa_{f,i}\kappa_{f,i}'+\kappa_{b,i}\kappa_{b,i}')(\alpha_{l,i}\alpha_{l,i}'+\phi^2)}{(\alpha_{l,i}^2+\phi^2)(\alpha_{l,i}'^2+\phi^2)}\right.$$
$$\left.-\frac{(\kappa_{f,i}\kappa_{b,i}'+\kappa_{b,i}\kappa_{f,i}')(\alpha_{l,i}\alpha_{l,i}'+\phi^2)}{(\alpha_{l,i}^2+\phi^2)(\alpha_{l,i}'^2+\phi^2)}\cos(\phi L)+\frac{(\kappa_{f,i}\kappa_{b,i}'-\kappa_{b,i}\kappa_{f,i}')(\alpha_{l,i}-\alpha_{l,i}')\phi}{(\alpha_{l,i}^2+\phi^2)(\alpha_{l,i}'^2+\phi^2)}\sin(\phi L)\right], \tag{4.2}$$

where Υ_i is given by

$$\Upsilon_i=T_i\left(\frac{-T_{f,i}}{T_i}\right)^{l_1}\left(\frac{T_{b,i}}{T_i}\right)^{l_2}. \tag{4.3}$$

The proof of Eq. (4.2) is given in Appendix E. The coefficient Υ_i' is the same as the one in Eq. (4.3) with the indices l_1 and l_2 replaced by l_1' and l_2'. The same is valid for the variables $\alpha_{l,i}'$, $\kappa_{f,i}'$ and $\kappa_{b,i}'$ (see Appendix E for details).

Closed-form expressions for the XPM and SPM NLI contributions in Eqs. (3.1) and (3.2), respectively, are presented next. Using Eq. (4.2) as an analytical solution of the link function, closed-form expressions for the XPM and SPM are

$$\eta_{\text{XPM}}^{(k)}(f_i)=\frac{32}{27}\frac{\gamma_i^2}{B_k}\left(\frac{P_k}{P_i}\right)^2\sum_{\substack{0\le l_1+l_2\le 1\\0\le l_1'+l_2'\le 1}}\Upsilon_k\Upsilon_k'\frac{1}{\phi_{i,k}(\alpha_{l,k}+\alpha_{l,k}')}\left\{2(\kappa_{f,k}\kappa_{f,k}'+\kappa_{b,k}\kappa_{b,k}')\right.$$
$$\left[\operatorname{atan}\left(\frac{\phi_{i,k}B_i}{2\alpha_{l,k}}\right)+\operatorname{atan}\left(\frac{\phi_{i,k}B_i}{2\alpha_{l,k}'}\right)\right]+\pi\left[-(\kappa_{f,k}\kappa_{b,k}'+\kappa_{b,k}\kappa_{f,k}')\left(\operatorname{sign}\left(\frac{\alpha_{l,k}}{\phi_{i,k}}\right)e^{-|\alpha_{l,k}L|}\right.\right.$$
$$\left.\left.+\operatorname{sign}\left(\frac{\alpha_{l,k}'}{\phi_{i,k}}\right)e^{-|\alpha_{l,k}'L|}\right)+(\kappa_{f,k}\kappa_{b,k}'-\kappa_{b,k}\kappa_{f,k}')\left(\operatorname{sign}(-\phi_{i,k})\,e^{-|\alpha_{l,k}L|}+\operatorname{sign}(\phi_{i,k})\,e^{-|\alpha_{l,k}'L|}\right)\right]\Bigg\} \tag{4.4}$$

and

$$\eta_{\text{SPM}}(f_i)=\frac{16}{27}\frac{\gamma_i^2}{B_i^2}\sum_{\substack{0\le l_1+l_2\le 1\\0\le l_1'+l_2'\le 1}}\Upsilon_i\Upsilon_i'\frac{\pi}{\phi_i(\alpha_{l,i}+\alpha_{l,i}')}\left\{2(\kappa_{f,i}\kappa_{f,i}'+\kappa_{b,i}\kappa_{b,i}')\left[\operatorname{asinh}\left(\frac{3\phi_iB_i^2}{8\pi\alpha_{l,i}}\right)\right.\right.$$
$$\left.+\operatorname{asinh}\left(\frac{3\phi_iB_i^2}{8\pi\alpha_{l,i}'}\right)\right]+4\ln\left(\sqrt{\frac{\phi_iL}{2\pi}}B_i\right)\left[-(\kappa_{f,i}\kappa_{b,i}'+\kappa_{b,i}\kappa_{f,i}')\left(\operatorname{sign}\left(\frac{\alpha_{l,i}}{\phi_i}\right)e^{-|\alpha_{l,i}L|}\right.\right.$$
$$\left.\left.+\operatorname{sign}\left(\frac{\alpha_{l,i}'}{\phi_i}\right)e^{-|\alpha_{l,i}'L|}\right)+(\kappa_{f,i}\kappa_{b,i}'-\kappa_{b,i}\kappa_{f,i}')\left(\operatorname{sign}\left(-\phi_i\right)e^{-|\alpha_{l,i}L|}+\operatorname{sign}\left(\phi_i\right)e^{-|\alpha_{l,i}'L|}\right)\right]\Bigg\}, \tag{4.5}$$

where

$$\phi_i = -4\pi^2 \left(\beta_2 + 2\pi\beta_3 f_i\right),$$
$$\phi_{i,k} = -4\pi^2 \left(f_k - f_i\right)\left[\beta_2 + \pi\beta_3 \left(f_i + f_k\right)\right].$$

The proofs for Eqs. (4.4) and (4.5) are given respectively in Appendix F and G.

Finally, the $\text{SNR}_{\text{NLI},i}$ can be calculated analytically by substituting Eqs. (2.55), (2.56), (4.4) and (4.5) in Eq. (2.69). The final expression accounts for wavelength-dependent fibre parameters and different launch power per channel. Additionally, the formula is also valid for links made of different span setups - in that case, all the fibre parameters and per-channel launch power depend not only on the channel i but also on the span j.

4.2.2 Accuracy validation of the closed-form expression

This section presents the validation of Eq. (4.5) and Eq. (4.4). The transmission system described in Sec. 4.1.2 was again used, i.e., a distributed RA link consisting of a WDM transmission with N_{ch} = 131 channels spaced by 100 GHz and centred at 1550 nm. Each channel was modulated at the symbol rate of 96 GBd, resulting in a total bandwidth of 13 THz (105 nm). Because the closed-form expression derived in Sec. 4.2 is valid for Gaussian constellations only, Gaussian symbols are considered in the transmission. The span length is 80 km and an ITU-T G652.D fibre is considered with Raman gain spectrum (considering a constant $A_{\text{eff}} = 80\ \mu\text{m}^2$ for all the channel) and attenuation shown in Figs. 4.1 and 4.2, respectively. A constant nonlinear coefficient for all the channels $\gamma_i = 1.16\ \text{W}^{-1}\text{km}^{-1}$ was assumed, dispersion parameter and dispersion slope were $D = 16.5$ ps nm^{-1}km^{-1} and $S = 0.09$ ps nm^{-2}km^{-1}, respectively. A spectrally uniform launch power profile, where each channel carries -4 dBm, 0 dBm and -2 dBm was considered respectively for FW-RA, BW-RA and FW+BW-RA (see Sec. 4.1.2 for details on the choice of the parameters). The power profiles along the fibre length are shown in Figs. 4.3, 4.4 and 4.5 and pump allocations used for each one of the scenarios is shown in Table 4.1. Results were obtained for single-span, 3-span and 10-span transmissions. The amplifiers were assumed to be ideal, such that the launch power profile was the same at the beginning of each span and equal to the transmitted power.

The SNR_{NLI} as a function of wavelength is shown in Fig. 4.7 for FW-RA, Fig. 4.8 for BW-RA and Fig. 4.9 for FW+BW-RA for the cases of a single span, 3-span and 10-span transmissions. To verify the accuracy of the closed-form expression shown in Eqs. (4.4) and (4.5), the SNR_{NLI} was also computed using the integral ISRS GN model [33] and SSFM simulations. For the former, the results were obtained by inserting the power profiles shown in Figs. 4.3, 4.4 and 4.5 in [33, Eq. 4]. For the latter, the same power

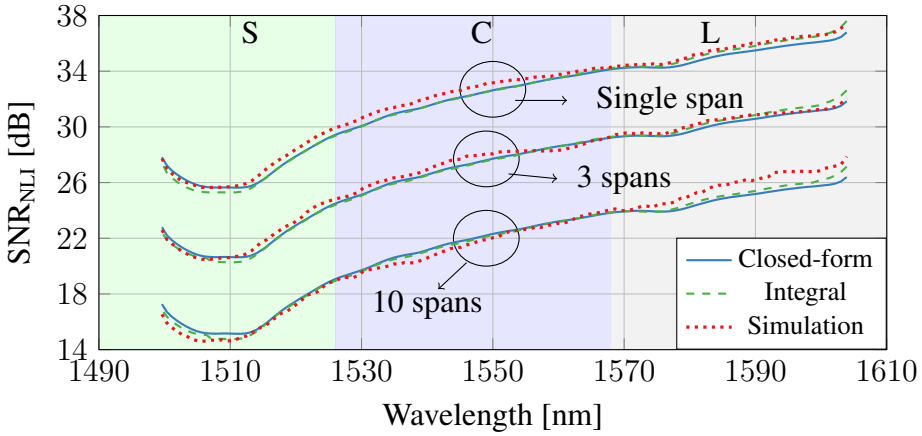

Fig. 4.7: Nonlinear performance after 1 x 80 km, 3 x 80 km and 10 x 80 km transmission for FW-RA.

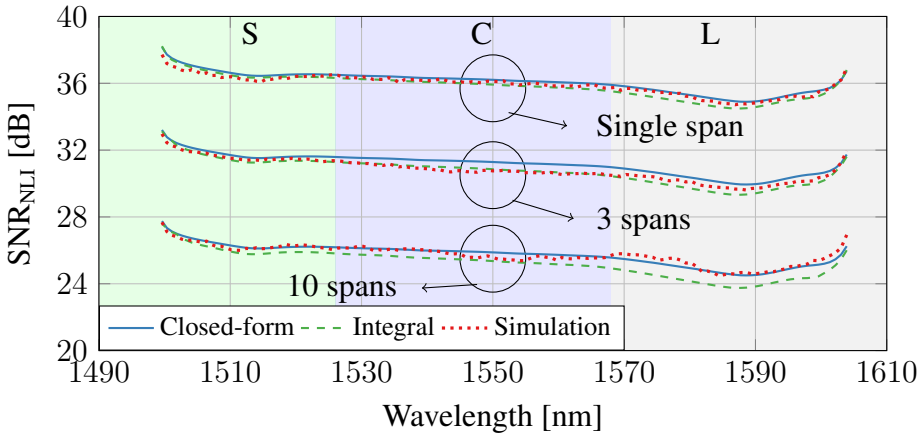

Fig. 4.8: Nonlinear performance after 1 x 80 km, 3 x 80 km and 10 x 80 km transmission for BW-RA.

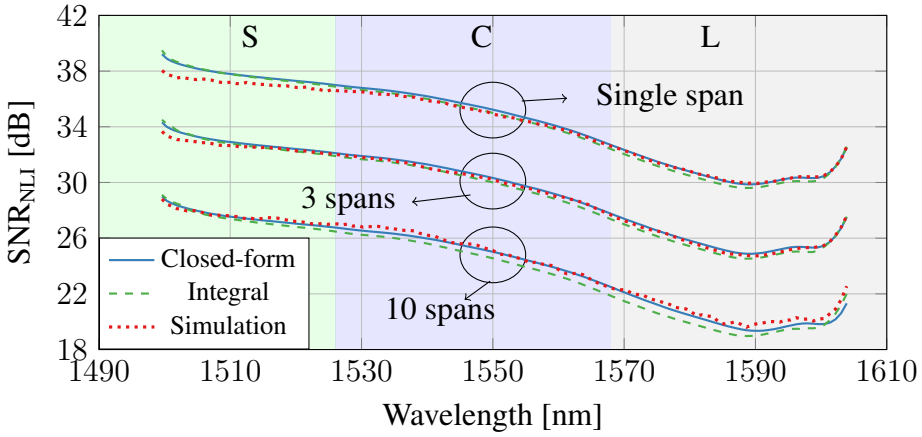

Fig. 4.9: Nonlinear performance after 1 x 80 km, 3 x 80 km and 10 x 80 km transmission for FW+BW-RA.

profiles from Figs. 4.3, 4.4 and 4.5 were used and interpolated along the fibre length for each step in the SSFM simulation. To ensure accurate simulation results, adaptive

step sizes with local-error method [62] were used, where goal local error $\delta_G = 10^{-10}$ and sequence of 2^{17} Gaussian symbols per channel were considered. Note that, for all the results, the XPM generated by the pumps was neglected; as shown in [113], this is a valid assumption when the WDM spectra are sufficiently far from the pumps - in our case, as described in Sec. 4.1.2, the highest-wavelength pump was chosen to be 2 THz away from the lowest-wavelength channel, such that these effects could be neglected. Despite that, the aforementioned effects can be included in this model by considering the pumps as additional interfering channels.

Figs. 4.7, 4.8 and 4.9 shows the SNR_{NLI} respectively for FW-RA, BW-RA and FW+BW-RA. It is interesting to note the correlation of the SNR_{NLI} profile with the power profiles shown in Figs. 4.3, 4.4 and 4.5. Indeed, for the FW-RA case, shown in Fig. 4.7, the high-power levels at short wavelengths (see Fig. 4.3), reduced the SNR_{NLI}, degrading the performance of those channels; on the other hand, the performance of long-wavelength channels was better, due to their reduced power levels, yielding to a tilt in the SNR_{NLI} profile. For the BW-RA case, shown in Fig. 4.8 the interaction between fibre attenuation, dispersion and power profile (see Fig. 4.4) yielded a relatively flat SNR_{NLI} profile; however, a smooth tilt could still be observed, which also correlate with the power profile shown in Fig. 4.4 as high-power levels were observed for the longer wavelengths. Note that, in general, BW-RA performs better in terms of SNR_{NLI} when compared with FW-RA case because of the reduced per-channel power evolution along the fibre. Finally, for the FW+BW-RA case shown in Fig. 4.9, the increased power levels at higher wavelengths (see Fig. 4.5), which is a result of the FW pumping, degraded the performance of those channels when compared to the lower wavelengths channels, where BW pumping dominates. This resulted in higher SNR_{NLI} values for channels located in the S-band when compared to those in the L-band, also yielding a tilt in the SNR_{NLI} profile.

In terms of accuracy, for a single-span FW-RA transmission, maximum per-channel errors of 0.81 dB and 0.64 dB were found between the closed-form expression and the integral ISRS GN model, and between the closed-form expression and the SSFM simulation, respectively. For the transmission over 3 spans, these errors were respectively 0.78 dB and 0.61 dB. For the transmission over 10 spans, these errors were respectively 0.74 dB and 1.47 dB. The same analyses for the BW-RA transmission over a single span yielded errors of 0.47 dB and 0.54 dB respectively, while for the transmission over 3 spans, these errors were both equal to 0.67 dB. Over 10 spans, these errors were respectively 0.80 dB and 0.68 dB. Finally, the same analysis for the FW+BW-RA over a single span yielded errors of 0.31 dB and 1.18 dB respectively, for the transmission over 3 spans, these errors were respectively 0.41 dB and 0.65 dB, and for transmission over 10 spans, these errors were 0.68 dB and 1.23 dB. Note that SSFM simulation accuracy could be improved by averaging

multiple simulations, reducing the discrepancy between closed-form expression and SSFM results. However, given the high computational complexity, each result represents an average of four simulations only.

4.3 Modulation format correction closed-form expression for the NLI estimation for arbitrary constellations

In Sec. 4.2 a closed-form expression valid for RA was presented. This closed-form expression was valid for Gaussian constellations only. In this section, a closed-form expression that estimates the NLI of arbitrary modulation formats in Raman amplified links is presented. The formula was obtained by deriving closed-form expressions of Eqs. (3.5) and (3.6), which were then inserted in Eqs. (3.4), (2.59) and (2.54) enabling the calculation of $\mathrm{SNR}_{\mathrm{NLI}}$ in Eq. (2.69) to be valid for any modulation format, such as shaped or unshaped/square QAM formats. The correction formula derived in this section also accounts for any pumping schemes, ISRS and RA. The baseline to derive this formula was also the utilisation of Eq. (4.1) as the semi-analytical solution for the Raman equations in the presence of RA, given by Eq. (2.39).

To show the application of the closed-form expression for different cases, a different simulation scenario from Sec. 4.2.2 was used to validate the formula. Signal transmission over a 20 THz optical bandwidth was used, making full use of S-, C- and L- bands. The test was done for a 64-QAM signal in a hybrid amplification scheme, where the S-band was fully amplified by launching BW Raman pumps in the transmission fibre. The accuracy of the formula is validated through SSFM simulations using a large 2^{18} symbol sequence per channel.

4.3.1 Closed form expression for modulation format correction term

The modulation format correction term contribution of the nonlinear coefficient is the sum of all COI-interfering-channel pairs present in the transmitted signal, given in integral form by Eqs. (3.5) and (3.6). The link function is given in closed form by Eq. (4.2).

A closed-form expression of Eq. (3.5) for the case of RA is given by

$$\eta_{corr,1}^{(k)}(f_i) = \frac{80}{81}\Phi_k \frac{\gamma_i^2}{B_k}\left(\frac{P_k}{P_i}\right)^2 \sum_{\substack{0\le l_1+l_2\le 1\\ 0\le l_1'+l_2'\le 1}} \Upsilon_k\Upsilon_k' \frac{1}{\phi_{i,k}(\alpha_{l,k}+\alpha_{l,k}')}\left\{2(\kappa_{f,k}\kappa_{f,k}'+\kappa_{b,k}\kappa_{b,k}')\right.$$
$$\left[\operatorname{atan}\left(\frac{\phi_{i,k}B_i}{2\alpha_{l,k}}\right)+\operatorname{atan}\left(\frac{\phi_{i,k}B_i}{2\alpha_{l,k}'}\right)\right]+\pi\left[-(\kappa_{f,k}\kappa_{b,k}'+\kappa_{b,k}\kappa_{f,k}'\left(\operatorname{sign}\left(\frac{\alpha_{l,k}}{\phi_{i,k}}\right)e^{-|\alpha_{l,k}L|}\right.\right.$$
$$\left.\left.\left.+\ \operatorname{sign}\left(\frac{\alpha_{l,k}'}{\phi_{i,k}}\right)e^{-|\alpha_{l,k}'L|}\right)+(\kappa_{f,k}\kappa_{b,k}'-\kappa_{b,k}\kappa_{f,k}')\left(\operatorname{sign}\left(-\phi_{i,k}\right)e^{-|\alpha_{l,k}L|}+\operatorname{sign}\left(\phi_{i,k}\right)e^{-|\alpha_{l,k}'L|}\right)\right]\right\}. \tag{4.6}$$

The proof of Eq. (4.6) is similar to Eq. (4.4) given in Appendix F apart from different multiplication factors, and thus, this proof is omitted. A closed-form for Eq. (3.6) is unnecessary as this equation is already in closed form. For the case of RA, substituting Eq. (4.1) in Eq. (3.6) yields the following expression for $\eta_{corr,a}^{(k)}(f_i)$

$$\eta_{corr,a}^{(k)}(f_i) = \frac{80}{81}\Phi_k \frac{\gamma_i^2}{B_k}\left(\frac{P_k}{P_i}\right)^2 \sum_{\substack{0\le l_1+l_2\le 1\\ 0\le l_1'+l_2'\le 1}} \Upsilon_k\Upsilon_k'$$
$$\left[\frac{2\pi\tilde{n}(\kappa_{f,k}-\kappa_{b,k})(\kappa_{f,k}'-\kappa_{b,k}')}{|\tilde{\phi_k}|B_k^2\alpha_{l,k}\alpha_{l,k}'}\left((2\Delta f-B_k)\ln\left(\frac{2\Delta f-B_k}{2\Delta f+B_k}\right)+2B_k\right)\right]. \tag{4.7}$$

Eq. (4.7) was derived by observing that $\mu(f_i,f_k,f_i)$ yields $\phi(f_i,f_k,f_i)=0$ in Eq. 4.2 and after some algebraic manipulations Eq. (4.7) is obtained. Finally, Eqs. (4.6) and (4.7) can be inserted in Eq. (2.60) to obtain a final expression for the modulation-correction term contribution, which is given by

$$\eta_{\text{corr,n}}(f_i) = \frac{80}{81}\sum_{k=i,k\neq i}^{N_{ch}}\Phi_k \frac{\gamma_i^2}{B_k}\left(\frac{P_k}{P_i}\right)^2 \sum_{\substack{0\le l_1+l_2\le 1\\ 0\le l_1'+l_2'\le 1}} \Upsilon_k\Upsilon_k'\left\{\frac{2(\kappa_{f,k}\kappa_{f,k}'+\kappa_{b,k}\kappa_{b,k}')}{\phi_{i,k}(\alpha_{l,k}+\alpha_{l,k}')}\right.$$
$$\left[\operatorname{atan}\left(\frac{\phi_{i,k}B_i}{2\alpha_{l,k}}\right)+\operatorname{atan}\left(\frac{\phi_{i,k}B_i}{2\alpha_{l,k}'}\right)\right]+\pi\left[-\frac{\kappa_{f,k}\kappa_{b,k}'+\kappa_{b,k}\kappa_{f,k}'}{\phi_{i,k}(\alpha_{l,k}+\alpha_{l,k}')}\left(\operatorname{sign}\left(\frac{\alpha_{l,k}}{\phi_{i,k}}\right)e^{-|\alpha_{l,k}L|}\right.\right.$$
$$\left.\left.+\operatorname{sign}\left(\frac{\alpha_{l,k}'}{\phi_{i,k}}\right)e^{-|\alpha_{l,k}'L|}\right)+\frac{\kappa_{f,k}\kappa_{b,k}'-\kappa_{b,k}\kappa_{f,k}'}{\phi_{i,k}(\alpha_{l,k}+\alpha_{l,k}')}\left(\operatorname{sign}\left(-\phi_{i,k}\right)e^{-|\alpha_{l,k}L|}+\operatorname{sign}\left(\phi_{i,k}\right)e^{-|\alpha_{l,k}'L|}\right)\right]$$
$$\left.+\left[\frac{2\pi\tilde{n}(\kappa_{f,k}-\kappa_{b,k})(\kappa_{f,k}'-\kappa_{b,k}')}{|\tilde{\phi_k}|B_k^2\alpha_{l,k}\alpha_{l,k}'}\left((2\Delta f-B_k)\ln\left(\frac{2\Delta f-B_k}{2\Delta f+B_k}\right)+2B_k\right)\right]\right\}. \tag{4.8}$$

Eqs. (4.4), (4.5) and (4.8) represent a complete set of equations able to calculate the NLI noise in hybrid-amplified links for arbitrary modulation formats.

Table 4.2: Pump power and wavelength allocations which yield the power profile shown in Fig. 4.10.

Wavelength [nm]	1360	1365	1370	1375	1380	1385	1390	1415
Pump power at $z = L$ [mW]	50	250	250	250	249	76	158	250
Pump power at $z = 0$ [mW]	0.0016	0.0155	0.0279	0.0490	0.0817	0.0394	0.1188	1.95

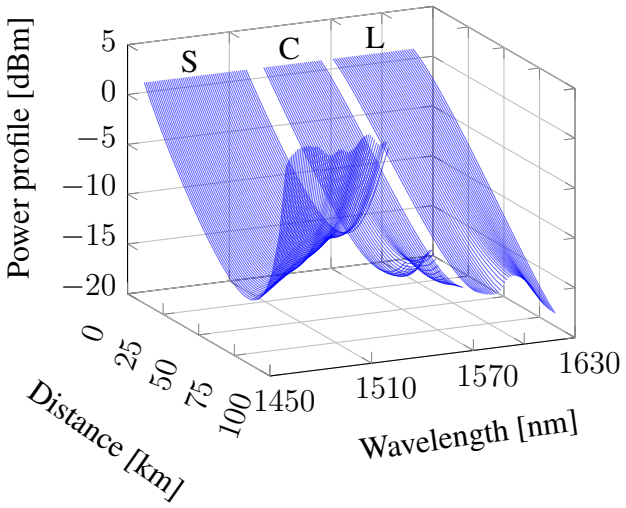

Fig. 4.10: Per-channel launch power evolution along the fibre length for BW-RA, where S-band channels are fully amplified by RA.

4.3.2 Accuracy validation of the closed-form expression for modulation format correction term

This section describes the validation of the accuracy of the closed-form expression derived in Sec. 4.3.1. For this case, the transmission system under investigation consisted of N_{ch}=135 WDM channels with the symbol rate of 140 GBd, spaced by 150 GHz and centred at 1530 nm. A total bandwidth of 20 THz (160 nm) with spectral gaps of 10 nm and 5 nm between the S/C and C/L bands, respectively, was generated. Each channel was modulated using 64-QAM and Gaussian constellations. The transmission link comprised 1 or 10 spans of 100 km ITU-T G652.D fibre with attenuation profile shown in Figs. 4.1 and Raman gain spectrum in 4.2 for a constant effective area. A spectrally uniform launch power profile, with 1 dBm power per channel was considered. The optical fibre nonlinear coefficient was considered constant for all the channels and equal to $\gamma_i = 1.2\,\mathrm{W^{-1}km^{-1}}$, dispersion parameter and dispersion slope were $D = 16.5\ \mathrm{ps\,nm^{-1}km^{-1}}$ and $S = 0.09\ \mathrm{ps\,nm^{-2}km^{-1}}$, respectively.

The link was amplified using hybrid amplification, consisting of a fully BW distributed RA in the S-band to completely recover the transmitted signal, followed by a gain-flattening filter to shape the amplified signal to the input signal. As the RA was not optimised to fully amplify all the bands, ideal LA was also used to amplify the

remaining signals in the C- and L- bands. An example of a full RA system can be found in [108].

For the RA stage, eight BW pumps were placed in the E-band, and their wavelengths were chosen to give the greatest gain in the S-band (see Table 4.2). The pump powers were limited to a maximum of 250 mW (other values are also possible) and they were optimised such that the S-band signal was completely recovered at the Rx - this was set as a nonlinear constraint in the optimisation algorithm. The cost function considered was $\sum_p P_p$, such that the power of each pump (P_p) was minimised. Similarly to Sec. 4.1.2, a function of power was chosen as the cost function because the ASE noise was not considered in this section, and thus, Eq. (2.72) cannot be used. The pump wavelengths and powers are shown in Table 4.2 and the power profile evolution along the fibre span is shown in Fig. 4.10. The latter was obtained by solving the Raman differential equations given by Eq. (2.39), with the pumps shown in Table 4.2. The highest-wavelength pump was 45 nm (6.5 THz) away from the lowest-wavelength channel, such that nonlinearity-induced products generated by the pumps falling within the signal band could be neglected [113].

Using the transmission system described, the $\text{SNR}_{\text{NLI},i}$ was estimated using the closed-form expression derived in Sec. 4.3.1. The results were compared with the integral model [33] (Eq. (2.49)) and SSFM. The integral model in Eq. (2.49) was used to compare results of Gaussian modulated signals as this integral model is only valid for this scenario. The SSFM simulations were used to compare both transmission, i.e., the ones using Gaussian constellations and the ones using 64-QAM.

The $\text{SNR}_{\text{NLI},i}$ is shown in Fig. 4.11 for Gaussian constellations using the equations derived in Sec. 4.2.1, and in Fig. 4.12 for unshaped 64-QAM using equations in Sec. 4.2.1 together with the correction term in closed form shown in Eq. (4.8). The results are shown for 1 and 10 spans. Figs. 4.11 and Fig. 4.12 show a degradation in the S-band performance caused by the increased power levels provided by RA (see Fig. 4.10). This power level in S-band increased the NLI in this band worsening the $\text{SNR}_{\text{NLI},i}$. However, this provides a reduction in the ASE noise in that band increasing the overall performance as shown in Chapter 5.

The accuracy of the closed-form expression in Eqs. (4.4), (4.5) and (4.8) were validated for all the scenarios with SSFM simulations. For Gaussian constellations shown in Fig. 4.11, the results were also validated using the integral model [33]. Over all the scenarios considered, the maximum average errors over channels of 0.78 dB and 0.51 dB were found between the closed-form expression and the SSFM simulations, respectively for Gaussian and 64-QAM constellations, where the most accurate channels were the ones located in the S-band and, therefore, Raman amplified.

For rough estimation of the model complexity, using a CPU without any code parallelisation, one realisation of the closed-form expression in

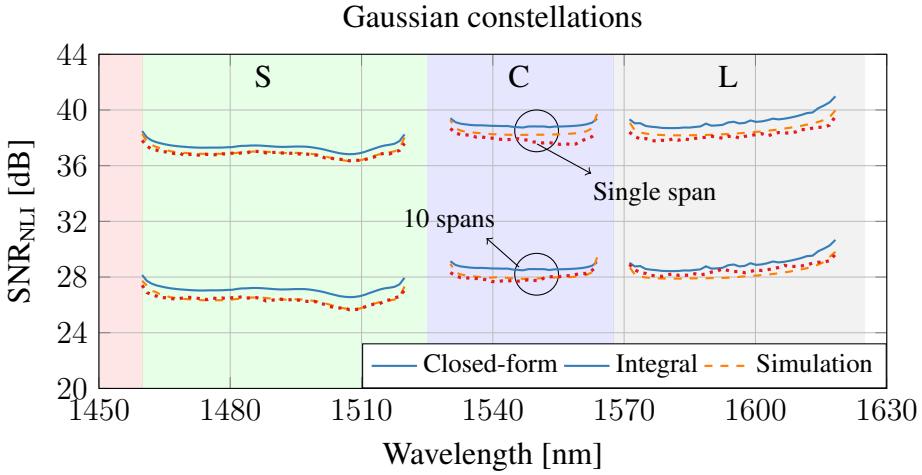

Fig. 4.11: Nonlinear performance after 1 x 100 km and 10 x 100 km transmission for Gaussian constellations.

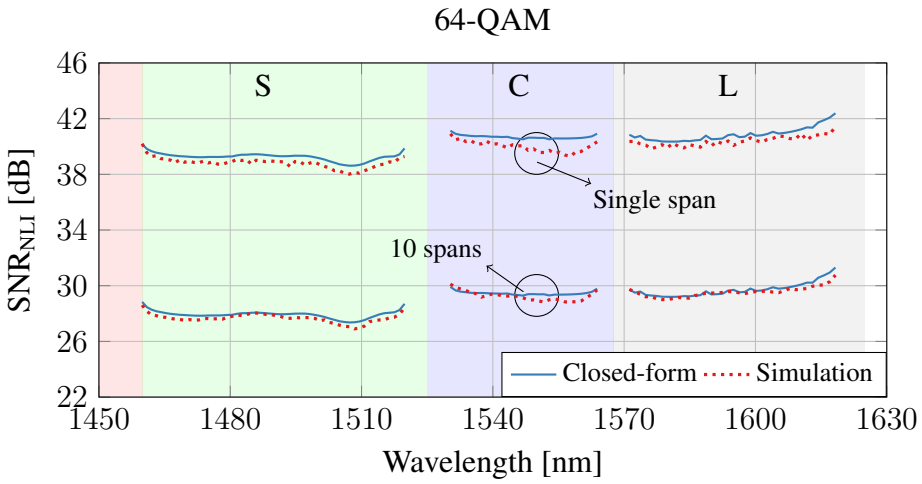

Fig. 4.12: Nonlinear performance after 1 x 100 km and 10 x 100 km transmission for square/unshaped 64-QAM constellations.

Eqs. (4.5), (4.4) and (4.8) for all scenarios took less than 5 seconds, while using integral model and SSFM simulations under the same conditions, yielded similar computational complexity as described in Sec. 3.2.2.

4.4 Experimental validation of the closed-form expression

In this section, the accuracy of the closed-form expressions given by Eqs. (4.4), (4.5) are experimentally assessed. The experiment was conducted by Dr J. Yang [110]. This formula was used to estimate a 12.4 THz S+C+L-band hybrid Raman-EDFA-TDFA amplified long-haul transmission performance in the presence of BW propagating Raman pumps. The pumps had a total power of up to 1.5 W. In the experiment, the TRX noise was minimised by using a relatively low symbol rate of 32 GBaud per

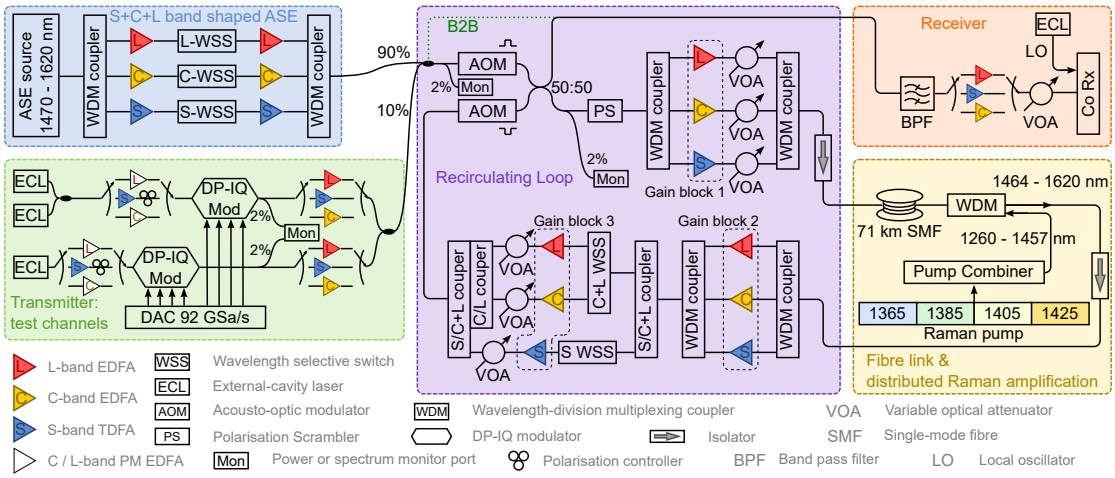

Fig. 4.13: Experimental setup for the S+C+L-band recirculating loop transmission with hybrid Raman-EDFA-TDFA amplification. B2B stands for back-to-back performance.

Table 4.3: Raman pump configuration.

λ (nm)	1365	1385	1405	1425	Total
P (mW)	505.8	374.1	324.3	295.8	1500.0

WDM channel, to highlight the impact of accumulated ASE and NLI noise on the overall performance in the recirculating loop transmission.

As shown in Fig. 4.13, three carriers were generated by tunable external cavity lasers (ECLs), and amplified by polarisation-maintaining EDFAs or TDFAs followed by polarisation controllers. The three signal channels were pre-distorted root-raised-cosine 32 GBaud 64 QAM signals, with a test channel at the centre surrounded by two neighbouring dummy channels with 32.5 GHz channel spacing. Co-propagating WDM channels were emulated by spectrally-shaped ASE noise generated by a wideband ASE source and shaped by WaveShapers® which operated as wavelength selective switches (WSSs). The recirculating loop consisted of a pair of acousto-optic modulators (AOMs) to switch between loading and recirculating states, a polarisation scrambler (PS) to avoid the accumulation of polarisation-dependent losses, three gain blocks (each of which included lumped repeaters: S-TDFA, low-gain C-EDFA and low-gain L-EDFA), a 71-km low OH peak standard SMF, four BW Raman pumps, and WSSs and variable optical attenuators (VOAs) for balancing the loop powers. The Raman pump wavelengths and powers are listed in Table 4.3. After 1065 km transmission, the signal was detected by the coherent Rx, which consisted of a bandpass filter, a pre-amplifier, a 90-degree hybrid for coherent detection, and a 256 GSa/s real-time oscilloscope. Offline pilot-based digital signal processing [114] was based on 2 samples per symbol with a pilot insertion rate of 1/32, and the SNR was evaluated for all WDM channels. The total throughput was based on the generalised mutual information (GMI), calculated using the Monte-Carlo integration

Table 4.4: System and fibre parameters considered in the model.

Parameter	Unit	Value
S/C/L amplifier NF	dB	7.5/5/6
Nonlinear parameter γ	$W^{-1}km^{-1}$	1.4
Effective core area A_{eff}	μm^2	83
Dispersion D at 1550 nm	$ps \cdot nm^{-1}km^{-1}$	16.5
Dispersion slope S	$ps \cdot nm^{-2}km^{-1}$	0.09

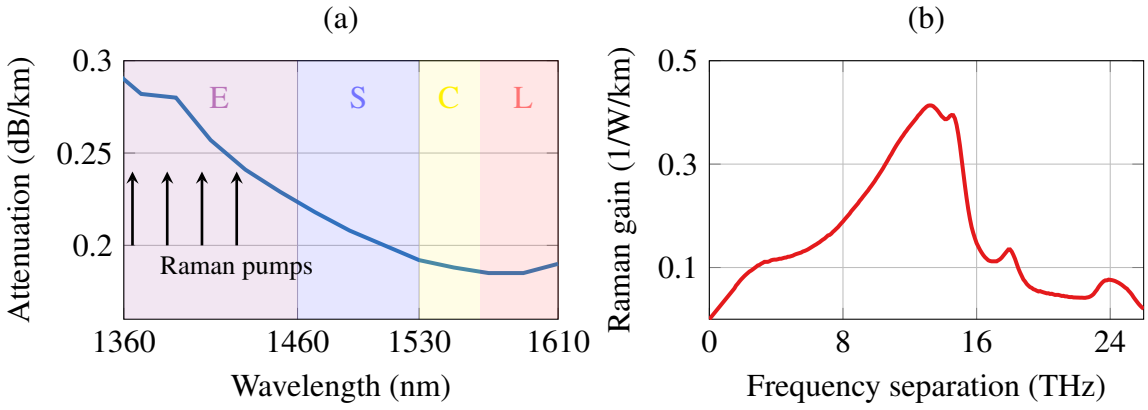

Fig. 4.14: Wavelength-dependent (a) fibre attenuation and (b) Raman gain profile.

as [63, Eq. 36,]. The total throughput, derived from the GMI of each channel, was 121.27 Tb/s over 5 spans (365 km), and 94.28 Tb/s over 15 spans (1065 km).

Eqs. (4.4) and (4.5) were used to estimate the NLI noise. The ASE noise calculation consisted of two components: one generated in the transmission fibre, obtained from the Raman-coupled equations for the signal (Eq. (2.63)) and the noise (Eq. (2.64)), and the other from the lumped amplifiers (gain blocks in Fig. 4.13) obtained from Eq. (2.62). The total ASE is calculated from Eq. (2.66). SNR_{TRX} was measured from the experiment in a back-to-back configuration, as shown in the green dotted path in Fig. 4.13. The parameters of the fibre and components are listed in Table 4.4, and the insertion losses of the optical components in the loop were assumed to be wavelength independent. The wavelength dependence of fibre attenuation and Raman gain are shown in Fig. 4.14. The wavelength dependence of the repeater amplifier gain and loop WSS shaping loss, are shown in Fig. 4.15. The aforementioned parameters were used in the model to accurately reproduce the experimental setup to calculate the NLI and ASE noise. Note that, the measured gains shown in Fig. 4.15 were substituted in Eq. (2.62) to accurately reproduce the ASE noise in the experiment and validated the NLI calculation, i.e., Eqs. (4.4) and (4.5). Additionally, Gaussian constellations are assumed in the model as co-propagating WDM channels were emulated by spectrally-shaped ASE noise generated by a wideband ASE source.

As shown in Fig. 4.15, gain block 1 amplifies the signal by approximately 13 dB

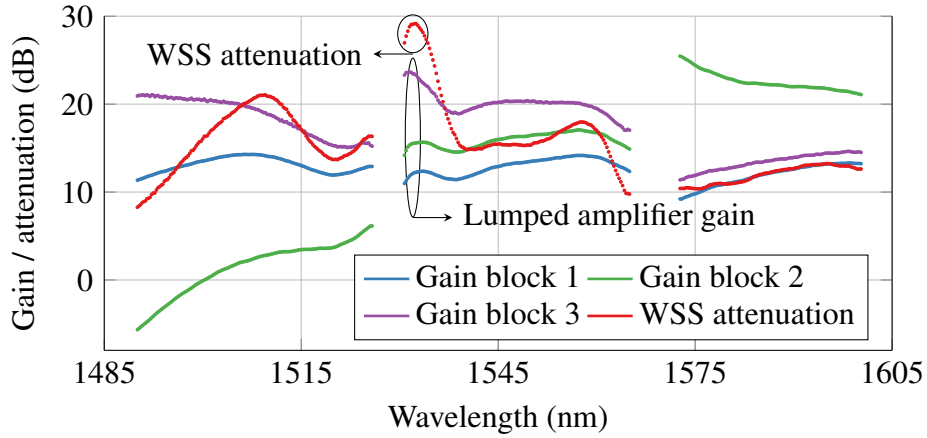

Fig. 4.15: Wavelength-dependent gain of block 1, 2, and 3, and loop WSS attenuation.

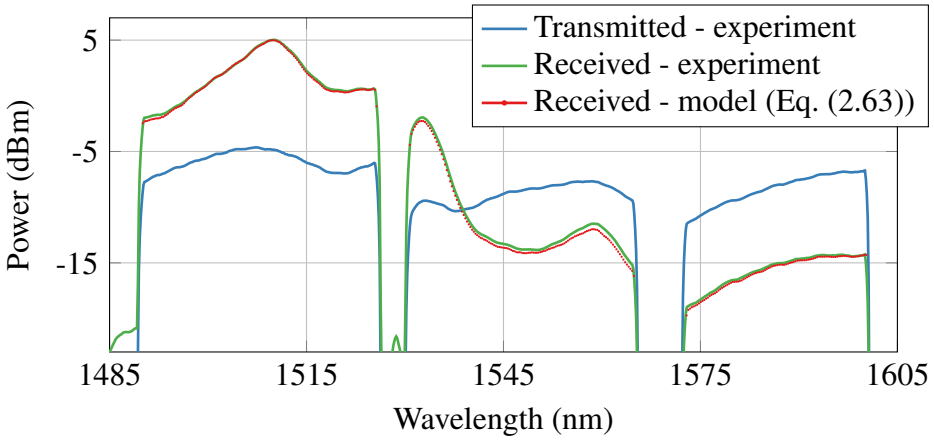

Fig. 4.16: Signal power spectra measured in the experiment (blue and green solid line) and predicted by the model (red dots).

to overcome the insertion loss of AOMs, couplers, and the PS, followed by VOAs to control the launch powers in each band. Gain block 2 compensates for the fibre loss. Since Raman pumps mainly provide gain in the S-band and part of the C-band, gain block 2 gave the most gain in L-band with more than 20 dB, contributing to most of the ASE noise. In contrast, S-band had the lowest gain from LA, and the negative gain at the shortest wavelength means that the Raman pump recovered the signal power to a level higher than the launch power. The C-band behaviour was in the middle, with an average gain of 15 dB. Gain block 3 compensated for the WSS insertion losses of 4.5 dB in S-band and 7 dB in C-, L-bands, and additional shaping loss. The WSS attenuation in Fig. 4.15 approximately reflected the Raman on/off gain, with a peak in the gain at a wavelength of 1505 nm. The other peak at the shortest C-band wavelengths was due to the gain from the 1425 nm pump.

Fig. 4.16 shows the fibre launch spectrum with 18.3 dBm, 15.1 dBm, and 14.8 dBm in the S-, C-, and L-band, respectively. The C- and L-band launch power per channel was set to approximately 2 dB below that of the S-band to reduce the ISRS power

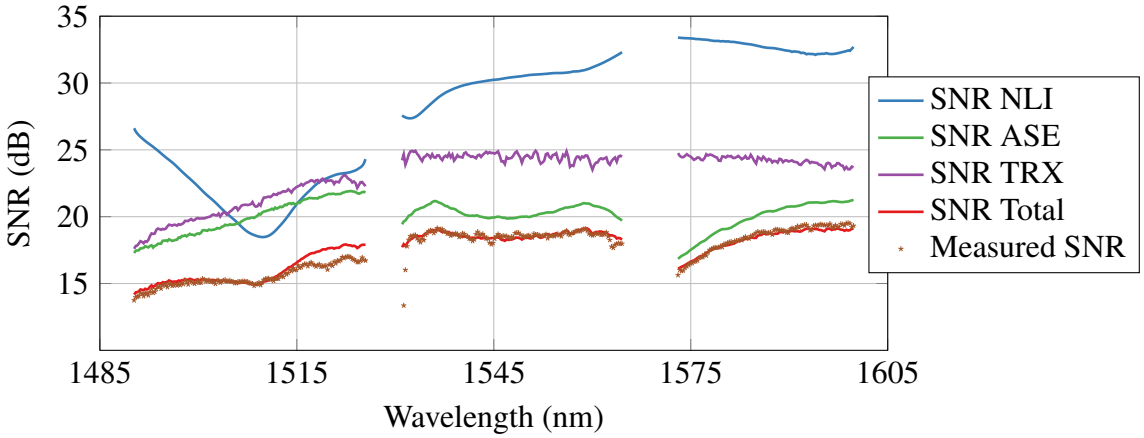

Fig. 4.17: SNR after 5 spans (355 km) from the TRX, ASE, NLI, total SNR estimated from Eqs. (4.4) and (4.5), and measured from the experiment. Solid lines: model prediction. Star markers: experimental results.

transfer, such that the S-band performance would not be fully dominated by ASE noise but would be affected by ASE and NLI noise jointly. The fibre output signal spectrum (green solid line) is shown in Fig. 4.16, together with the predicted output from the Raman coupled equation (red dots) in Eq. (2.63). The model accurately estimated the signal power profile evolution over the 71 km fibre link in the presence of BW-RA, with an average error of only 0.23 dB. This power evolution was further used to calculate the Raman-coupled ASE noise in the fibre link.

Figs. 4.17 and 4.18 show respectively the various noise contributions to the total SNR in 5-span and 15-span transmission, calculated using Eqs. (4.4) and (4.5). The maximum NLI noise was observed at 1505 nm due to the high gain from the RA, while lower NLI was seen in C- and L-bands due to the lower launch power. The ASE noise level was similar in the three bands; in the case of the S-band, the higher NF of the TDFA was offset by the better noise performance of the RA. A clear dip in total SNR due to the NLI at around 1505 nm was accurately predicted in both cases by the model, confirming the accuracy of the NLI noise predicted by the model in Eqs. (4.4) and (4.5). Comparing the experimental results (star markers) and the model predictions (red solid line) in Figs. 4.17 and 4.18, the average SNR estimation errors were 0.38 dB and 0.60 dB for 5- and 15-span transmission, respectively. The discrepancy in the longest wavelength S-band and the shortest wavelength L-band was due to the wavelength dependence of amplifier NFs and the insertion losses of optical components in the loop, which were assumed to be wavelength-independent in the model. These results experimentally validate Eqs. (4.4) and (4.5), confirming its suitability as a key tool in optimising the system design and maximising the throughput of future hybrid-amplified long-haul UWB transmission systems.

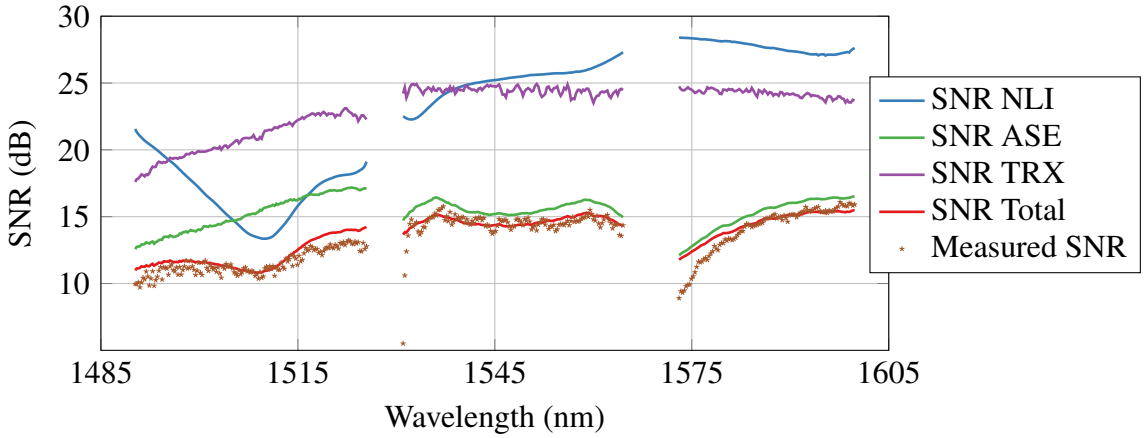

Fig. 4.18: SNR after 15 spans (1065 km) from the TRX, ASE, NLI, total SNR estimated from Eqs. (4.4) and (4.5), and measured from the experiment. Solid lines: model prediction. Star markers: experimental results.

4.5 Summary

In this chapter, a closed-form formula of the GN model was presented. The formula is suitable for UWB transmission systems and tested over a distributed RA setup. This formula is the first to account for any setup of RA technologies (such as an arbitrary number of pumps) together with the ISRS effect. The formula is shown to support FW and BW pumping schemes and accurately predict the NLI for an arbitrary number of pumps and wavelength-dependent fibre parameters and launch power profiles. The formula supports any modulation formats, such as Gaussian constellations, shaped or unshaped QAM formats. A fundamental step to deriving this closed formula was to derive a semi-analytical solution to correctly reproduce the signal power profile evolution along the fibre length in the presence of RA and ISRS effect.

The formula was applied in two scenarios corresponding to transmission over the S-, C-, and L- bands. Firstly considering a 13 THz optical bandwidth and secondly considering 20 THz optical bandwidth, in which for this latter the S-band was fully amplified using BW-distributed RA. Additionally, the formula was capable of estimating the NLI in only a few subseconds, where the majority of the computational time was required to numerically solve the differential Raman equations. Because of the speed of computation, the formula is suitable for real-time estimation of the NLI and can be applied as an enabling tool for future intelligent and dynamic optical fibre networks.

The formula was further validated experimentally, showing its powerful capability for accurate SNR estimation in long-haul WDM transmission. The validation was done over an S+C+L-band recirculating fibre loop WDM transmission experiment, with hybrid Raman-EDFA-TDFA amplification, over standard SMF link lengths of

365 km and 1065 km. The formula showed a discrepancy from experimental measurements of only 0.38 dB and 0.60 dB in the SNR, averaged across all channels respectively for 365 km and 1065 km transmission.

Chapter 5

Physical layer parameter optimisation for throughput maximisation using closed-form expressions-aided algorithms

5.1 Introduction

In Chapters 2, 3 and 4, closed-form expressions able to perform a real-time estimation of the optical system performance in UWB regimes were presented. The accuracy of these formulae was validated in these chapters confirming their effectiveness for application in optimisation algorithms. These algorithms can be used to optimise a desired system metric, such as the maximum throughput for a given transmission system. This can be done by optimising physical layer parameters such as launch power, amplifier gain, etc.

In this chapter, these applications are presented. The real-time formulae described in Chapters 2, 3 and 4 are used to maximising throughput by incorporating them into optimisation algorithms, significantly speeding up computations. The algorithms are applied to various tasks, including launch power optimisation in lumped-amplified and hybrid-amplified links with and without TRX noise; optimising and designing Raman and lumped amplifier, by determining the best pump allocation, such as the number of pumps, their power, wavelength, and direction (FW and/or BW); optimisation of optical networks and topology designs; modelling and designing practical case scenarios; and modelling of transmission experiments.

The topics presented in this chapter were published in Journal of Optical Communications and Networking (JOCN) [P1] and in JLT [P6], and presented at conferences: at 2021 International Conference on Optical Network Design and Modelling (ONDM) [P8], at ECOC 2023 [P16], at OFC 2024 [P17] and at ECOC 2024 [P19].

5.2 Launch power optimisation and the impact of the transceiver noise for lumped-amplified links

This section analyses the impact of launch power optimisation and TRX noise on the throughput of UWB optical fibre transmission systems. As mentioned in Sec. 2.4.4,

ISRS effectively results in the power transfer from shorter wavelengths to longer wavelengths in the signal. This power transfer leads to additional complexity in the estimation of the NLI as this later depends on the evolution of the per-channel launch power (see Eq. (2.49)). Therefore, the combination of signal power transfer due to ISRS together with wavelength-dependent attenuation and amplifier noise levels, the WDM channels, especially from different bands, experience different accumulated distortions. As a consequence, the estimation of the per-channel launch power that maximises the total system performance, also known as launch power optimisation, turns out to be a multidimensional non-convex problem [115].

The importance of launch power setting in UWB systems was already discussed back in the late 90's [39, 40, 41]. However, just with the recent development of fast and accurate models and algorithms, its computation has become possible. Over the recent years, this problem has been addressed for lumped-amplified links by global optimisation algorithms such as evolutionary algorithms (EA) [116, 117], PSO [75], artificial neural network (ANN) [111] and faster but sub-optimal strategies [118, 119, 120, 121]. Most importantly, these algorithms are accelerated and supported by analytical [35, 122], numerical [33, 70], or even ANN [123, 124] models that estimate the NLI in the presence of ISRS. A similarity between these works is the assumption of an ideal TRX subsystem. Although this approach does not detract from the validity of previous works, it does not allow for the assessment of the impact of TRX noise on the per-channel QoT in the presence of ISRS. This analysis is important to help identify potential performance bottlenecks and over-engineered power control strategies.

This section presents a comprehensive analysis of the main noise sources and power optimisation constraints of the UWB transmission experiment published in [11]. The main limitations that dictated the experiment data throughput of 178 Tbit/s were investigated. In particular, the focus is on how the TRX noise together with the launch power profile impacted the per-channel QoT and overall data throughput. This analysis was then broadened to account for different values of TRX noise and other optical fibre transmission system configurations. More specifically, the transmission distance, the span length and the bandwidth were varied. The investigation focused on how different amounts of per-channel transferred power due to ISRS change the QoT and the gains in performance obtained by launch power optimisation in the presence of TRX noise. To measure these gains a spectrally uniform launch power is used as a baseline.

The closed-form formulae in Eqs. (2.55), (2.56), (2.57), (2.58), (2.59) and (2.60) were used to estimate the NLI impact and the resulting per-channel SNR in Eq. (2.69) for assessing the system performance. These equations are well suited for computing the NLI in lumped-amplified UWB transmission systems, and its accuracy compared to the NLSE simulations has been demonstrated in [35, 125] and in Chapter 3. The

analysis presented in this section was first presented at ONDM 2021 [75] and was selected as a top-scored paper and further invited to be extended in a journal paper, published in JOCN [82].

5.2.1 Launch power optimisation algorithm

This section describes the algorithm used for launch power optimisation. Due to the ISRS, the relation between system performance and launch power is nonlinear. This nonlinear relation yields to a N_{ch}-dimensional non-convex optimisation problem [115]. To solve that problem, numerical optimisation algorithms are required.

The goal was to find the optimum launch power allocation P_i for the transmitted channels, maximising total throughput for the transmission system. The total throughput is upper-bounded by the AWGN channel capacity, thus, Eq. (2.72) was chosen as the cost function to be maximised for a set of values of P_i, with SNR_i for the i^{th} channel given by (2.69). For this optimisation, an ideal TRX subsystem is considered, such that $\mathrm{SNR}_{\mathrm{TRX}} \to \infty$. The latter assumption is done because this optimisation is independent of the TRX; i.e., the launch power profile that maximizes Eq. (2.72) is the same for any value of $\mathrm{SNR}_{\mathrm{TRX}}$.

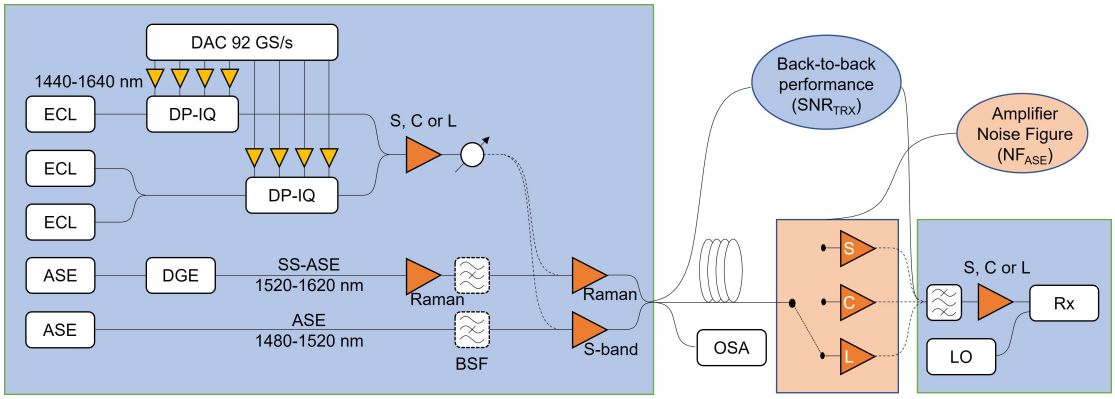

Fig. 5.1: Schematic of the transmission experiment of [11]. Dynamic gain equalizer, DGE; spectrally shaped amplified spontaneous emission noise, SS-ASE; bandstop filter, BSF; external cavity laser, ECL; amplified spontaneous emission noise, ASE noise; dual-polarization in-phase quadrature optical modulator, DP-IQ optical modulator; optical spectrum analyzer, OSA; local oscillator, LO; digital-to-analog converter, DAC; and receiver, Rx.

The numerical optimisation algorithm selected to find a local maximum of Eq. (2.72) was the PSO [126] combined with a gradient descent algorithm with a backtracking line search to determine the step size. The PSO is efficient in exploring the N_{ch}-dimensional space, leading to the surroundings of a good local optimal solution on the N_{ch}-dimensional surface. To accurately find this solution, the gradient descent algorithm was used with the initial condition as the solution of the PSO.

For the PSO, the Matlab function provided by the global optimisation toolbox was used. A total of $10 \cdot N_{ch}$ particles were chosen with their values, i.e., the launch power for each channel, ranging from -15 dBm to 15 dBm. The PSO algorithm begins by assigning to these particles uniform distributed random values in this interval, which represent their locations in the N_{ch}-dimensional space. Initial particle velocities were also randomly picked from the interval $[-30, 30]$ dBm and the initial inertia was set to 1.1. The algorithm evaluates the cost function (Eq. (2.72)) at each particle location, storing the current best solution, which was iteratively used to update particles' velocities and locations. Iterations proceeded until the algorithm reached a stopping criterion, which was chosen to be a maximum of 100 interactions ensuring algorithm convergence to the optimal solution. For the gradient descendent algorithm, a convergence rate of 10^{-3} was chosen and for the backtracking line search $\alpha = 0.15$ and $\beta = 0.8$ [127, Chap. 9,] was set. Additionally, adjacent channels were combined into one super-channel to reduce computational complexity - this approach is justified by the fact that adjacent channels are likely to have similar launch power.

Finally, besides the optimum launch power per channel, this strategy is also used to calculate the optimum spectrally uniform launch profile, such that each channel carries the same launch power. This was computed considering 1 super-channel for the entire bandwidth with the attenuation coefficient and additional fibre parameters equal to the central channel. This approach yields a single-dimensional space and omits the impact of the ISRS as just 1 super-channel is transmitted.

5.2.2 Experimental improvement analysis and performance assessment through analytical modelling

In this section, the model described in Sec. 2.7 and represented by Eqs. (2.55), (2.56), (2.57), (2.58), (2.59) and (2.60) was applied to simulate the UWB experiment reported in [11]. This analysis allowed us to trace general conclusions about this experiment and to search for ways of potential improvements in the total experiment throughput. This section starts by describing the experimental configuration within the simulation parameters considered to model the experiment, followed by the computation of different launch power profiles, which were compared with the one used in the experiment. For these different launch power profiles, the system performance, in terms of SNR and total throughput, was analysed. Finally, the interplay between TRX and launch power optimisation was investigated by analysing how the different cases of launch power profiles, together with the TRX noise, influenced the system performance.

Sub-band [nm]	NF [dB]	Geometrically shaped-QAM	SNR_{TRX} [dB]
1484.86 - 1519.8	7.0	256-QAM	15.80
1520 - 1529	9.0	64-QAM	17.82
1529.2 - 1568	5.5	1024-QAM	21.25
1568.2 - 1607.8	6.0	1024-QAM	21.25
1608 - 1619.67	9.0	256-QAM	17.07

Table 5.1: Sub-bands of the amplification scheme with corresponding amplifier NF and implemented modulation formats, used in the experiment [11] and in its modelling.

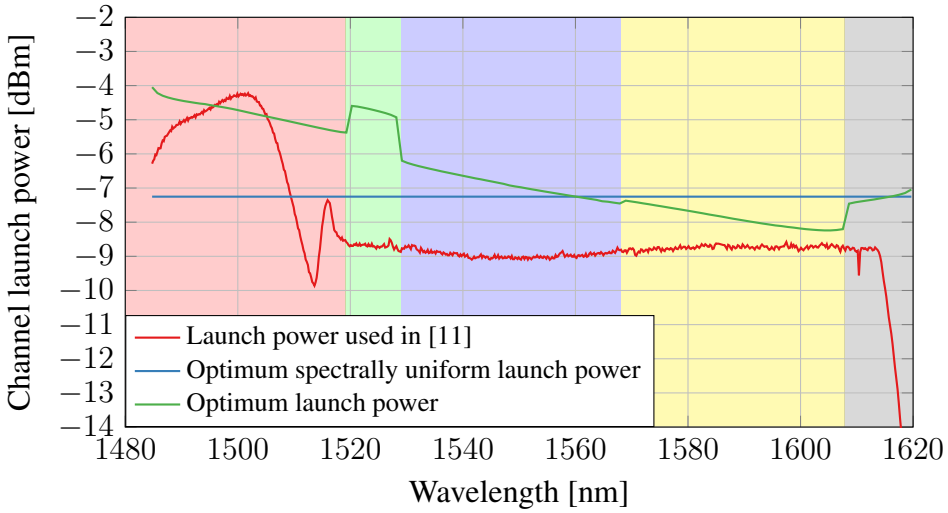

Fig. 5.2: Per-channel launch power obtained from the optimisation strategy described in Sec. 5.2.1, using the model proposed in Sec. 2.7. The launch power used in [11] (red) is also shown for comparison.

5.2.2.1 Transmission system setup

This section describes the parameters of the transmission system used to model the experiment in [11]. The experimental setup is shown in Fig. 5.1, of which the following components can be identified: dynamic gain equaliser (DGE), spectrally shaped (SS)-ASE, band-stop filter (BSF), ECL, ASE noise generator, Dual-Polarization In-phase Quadrature (DP-IQ) optical modulator, optical spectrum analyser (OSA), local oscillator (LO), digital-to-analogue converter (DAC), and Rx. A complete description of the experimental setup can be found in [11, Sec. 2]. As shown in this figure, the Tx and Rx impairments were gathered into $\mathrm{SNR_{TRX}}$, which corresponds to the experimental back-to-back implementation penalty as indicated in this figure as the blue background. Similarly, the impairments of the optical amplifiers used to amplify the signal after fibre propagation were accounted as NF, which is represented by the orange background. Also, to calculate the system performance, the model and the assumptions presented in Eq. (2.69) were used. Note that, the TRX impairment was modelled as AWGN. The $\mathrm{SNR_{TRX}}$ was calculated as $\frac{\mathbb{E}[|X|^2]}{\mathbb{E}[|Y-X|^2]}$, where $\mathbb{E}[\cdot]$ is the expectation operator, X is the transmitted symbols and Y the received symbols after DSP.

The experimental transmission system parameters used in Eqs. (2.57), (2.58), and (2.60) are summarised in Table 5.1. The system was based on [11] and it consisted of a WDM transmission with $\mathrm{N_{ch}}$ = 660 channels spaced by 25.5 GHz. Each channel was modulated at the symbol rate of 25 GBd. This resulted in a total bandwidth of 16.83 THz (134.81 nm), ranging from 1484.86 nm to 1619.67 nm, which corresponded to the continuous transmission over S, C and L bands. The channels were transmitted over a single span of 40 km standard SMF with attenuation profile $\alpha(f_i)$ as [11, Fig. 2] and Raman gain as Fig. 3.2. A total power of 20.4 dBm was launched into the fibre and the power per channel is shown in Fig. 5.2 by the red line. Note that, no DGE was available to equalise the power for lower wavelengths (from 1484.86 nm to 1520 nm), therefore the signal gain followed the amplifier ASE power profile. For the remaining wavelengths, a spectrally uniform power profile was used.

For the in-line amplifiers shown in Fig. 5.1 (orange background), the NF were the ones reported in [11, Sec. 2] and displayed in Table 5.1. The back-to-back implementation penalty $\mathrm{SNR_{TRX}}$ was not measured experimentally for every channel separately. For each amplifier sub-band, the $\mathrm{SNR_{TRX}}$ of 3 channels were measured and their mean value was used, as shown in Table 5.1, as an estimation of the per-channel $\mathrm{SNR_{TRX}}$.

The same geometric shaped (GS)-QAM formats from [11], optimised based on the received SNR, were also used to estimate the $\mathrm{SNR_{NLI}}$ in Eqs. (2.57), (2.58), and (2.60).

This was done by using different values of Φ_k in Eq. (2.60) (see Table 2.1), according to the GS-QAM constellation used per amplification sub-band, which is also shown in Table 5.1. The constellation diagrams of these GS-QAM constellations are shown in [11, Fig. 3]. Furthermore, these constellations were also used to estimate the total throughput of the system based on the GMI [63].

5.2.2.2 Optimised launch power profiles

This section is devoted to finding the optimum and the spectrally uniform launch power profiles, using the strategy described in Sec. 5.2.1. In this estimation, five adjacent channels were combined into joint super-channels to reduce computational complexity.

Fig. 5.2 shows the optimum launch power (green line), with a total power of 21.93 dBm, as well as the signal power profile used on the experiment [11] (red line), with a total launch power of 20.4 dBm. For the spectrally uniform power (blue line), a total launch power of 20.95 dBm, corresponding to a -7.25 dBm per channel, was found. For ease of viewing, different background colours are used to mark the different values of NF for the in-line amplifiers used across different sub-band within the gain bandwidth as shown in Table 5.1.

For the optimum launch power profile (green line), a maximum power of -4 dBm was at 1484.86 nm and minimum power of -8.2 dBm at 1607.8 nm, resulting in a maximum per-channel launch power variation (ΔP) of 4.2 dB across the signal bandwidth. Such variation can be understood by noting that due to ISRS, $\eta_n(f_i)$ in Eq. (2.54) had increased values for longer wavelengths, even though these wavelengths suffer a greater dispersion. In contrast, P_{ASE_i} was higher for shorter wavelengths, as these wavelengths experience more loss due to the attenuation profile combined with the ISRS effect. Thus, higher launch power is expected for shorter wavelengths, as these wavelengths experience more ASE noise and lower nonlinearities. Note that, the shape of the wavelength-dependent attenuation profile used [11, Fig. 2], was also considered in this analysis, which in combination with the power transferred due to the ISRS effect, also changed the distribution of the ASE and NLI noise powers among the channels.

As described in [11], different amplification technologies, such as TDFAs, discrete Raman and EDFAs, were used for different wavelength ranges within the total transmission bandwidth. Each amplifier determined its operational wavelength ranges and demonstrated different NF values, as shown in Table 5.1. Therefore, different levels in the optimal power profile were observed at different sub-bands highlighted by the different background colours, while maintaining the main trend of a downward slope. Indeed, to neutralise the undesired impact of higher ASE noise from the in-line amplifiers, higher launch power is required.

(a) $\mathrm{SNR}_{\mathrm{TRX}}$ as per Table 5.1

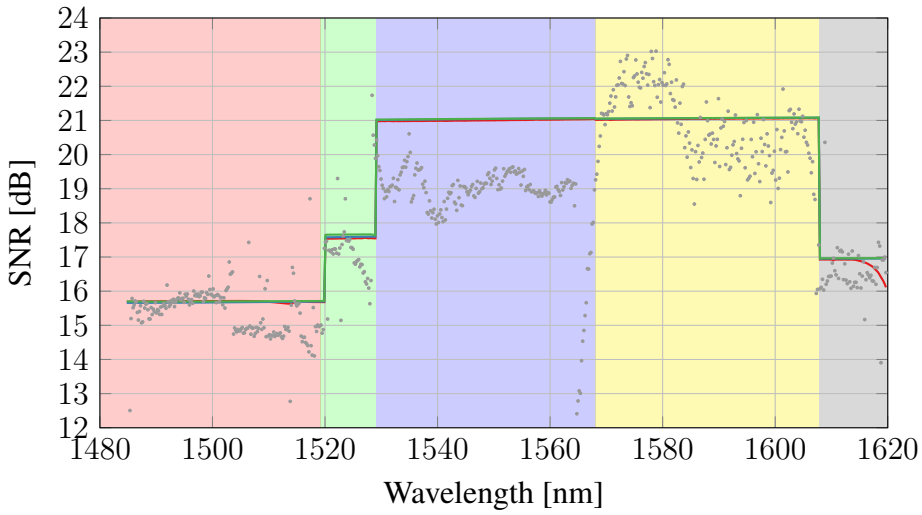

(b) $\mathrm{SNR}_{\mathrm{TRX}} = \infty$

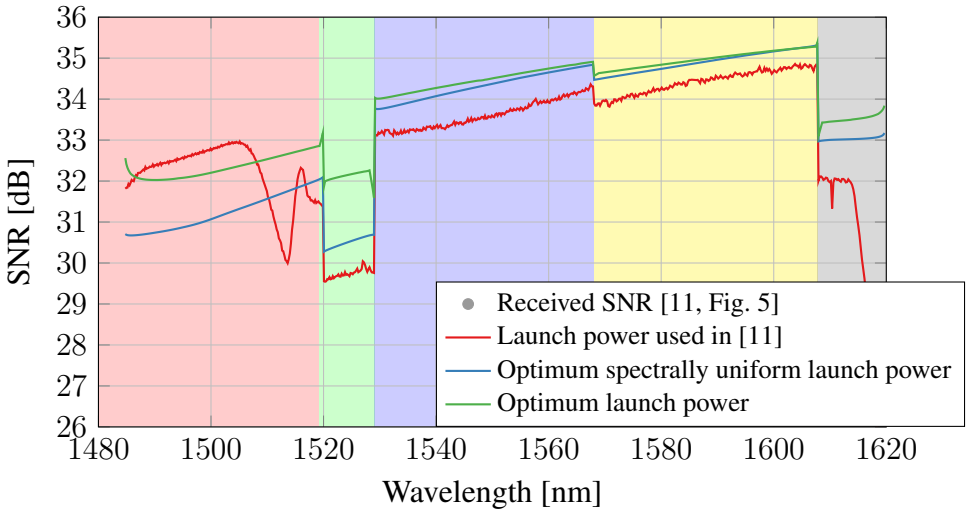

Fig. 5.3: Per-channel SNR profile for the different launch power profiles shown in Fig. 5.2. Two scenarios were considered: (a) TRX noise as Table 5.1 and (b) the case of an ideal TRX. The experimental measurements in [11] (grey marks) are shown for comparison.

5.2.2.3 Transmission system performance

In this section, the experimental and theoretical performance of the transmission system described in Sec. 5.2.2.1 was analysed. The SNR was used as a performance metric and the three launch power profiles shown in Fig. 5.2 were used to estimate the system performance based on Eq. (2.69). Additionally, to analyse how the TRX noise impacts the transmission system performance for each studied launch power profile, the case of an ideal TRX is also considered by setting $\mathrm{SNR}_{\mathrm{TRX}} \rightarrow \infty$ for the entire transmission bandwidth. Both cases are shown in Fig. 5.3.

Fig. 5.3 (a) shows the received SNR with the inclusion of the noise introduced by the experiment back-to-back implementation penalty, as per Table 5.1 for the different launch power profiles. Note that, all the three launch power profiles considered, yielded pretty much the same per-channel SNR, as all the three continuous lines almost overlap completely. This proves that the transmission system performance under investigation was mainly limited by the TRX noise. This is because (2.69) is dominated by the $\mathrm{SNR}_{\mathrm{TRX}}$ term. As the TRX impact is purely characterised by the back-to-back SNR, the launch power optimisation did not make a considerable impact on the system performance after 40 km fibre transmission.

The experimentally measured received SNR from [11] were depicted as grey markers for comparison, an average error of 0.52 dB was found between the continuous lines and the grey markers, showing a good agreement between the analytical model, described by Eqs. (2.58), (2.57) and (2.60) and the experimental results.

In contrast, Fig. 5.3 (b) shows the SNR obtained by considering an ideal TRX ($\mathrm{SNR}_{\mathrm{TRX}} \rightarrow \infty$). For the optimum launch power profile (green line), the SNR varied between 31.59 dB and 35.37 dB. For the spectrally uniform launch power profile (blue line), the SNR varied between 30.28 dB and 35.32 dB. For both cases, the minimum and maximum values of SNR occurred at 1607.8 nm and 1529.2 nm, respectively. This difference is because for an ideal TRX, Eq. (2.69) is dominated by $\mathrm{SNR}_{\mathrm{NLI}}$ and $\mathrm{SNR}_{\mathrm{ASE}}$, which are both dependent on the launch power profile. Similar to Sec. 5.2.2.2, the different levels (green curve) observed in the SNR profile at different sub-bands highlighted by the different background colours, rely on the different in-line amplifier NF used to compensate for fibre loss. Furthermore, the main trend of an upward slope was observed as the lower wavelength channels experienced the lowest SNR values due to ISRS.

For the launch power used in the experiment (red line), the SNR varied between 23.18 dB at 1619.67 nm and 34.86 dB at 1607.8 nm. This represents a maximum per channel SNR variation of 11.68 dB across the entire transmission bandwidth, compared to only 3.78 dB for the optimum launch power profile case. Note that, for channels in the

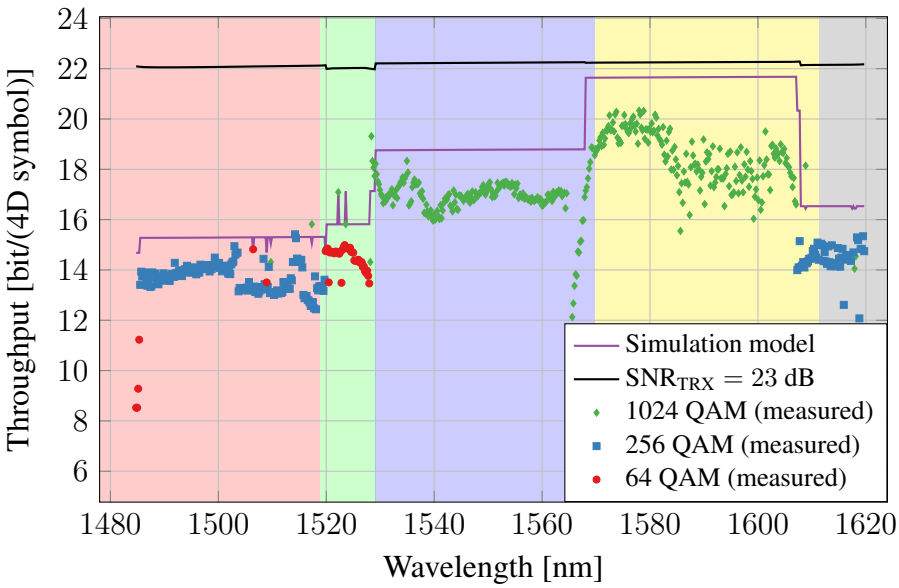

Fig. 5.4: Per-channel data throughput after 40 km transmission, estimated from Eq. (2.72), and measured in the experiment [11]. A scenario of a better TRX performance with $\text{SNR}_{\text{TRX}} = 23$ dB is added for comparison.

range of 1487-1508 nm, the SNR values were higher in the case of the experiment. This was due to the combination of two factors when compared with the optimum launch power per channel profile. Firstly, because of their increased per-channel launch power values at this range of wavelengths. Secondly, these channels transferred less power to the longer wavelength channels. The latter occurs because of the reduced launch power used for channels above 1520 nm. This decreased the performance of these channels in exchange for an increase in performance for the channels between 1487 nm - 1508 nm. As a result, a lower mean SNR was obtained for the launch power used in the experiment compared with the other launch power profiles.

5.2.2.4 Transmission system data throughput

In this section, the system performance in terms of throughput is analysed. The values of SNR estimated for each studied launch power profile were used to calculate the AIR, and the GMI was used as a metric for AIR. The GMI was calculated using the Monte-Carlo integration as [63, Eq. 36], and the GS-QAM constellations designed in [11, Fig. 3] were used depending on the received SNR (see Table 5.1). Additionally, as in the experiment, a pilot overhead of 4.64% was accounted for in the calculations.

Fig. 5.4 shows the experimental measurements and theoretical calculations of the per-channel throughput, obtained by multiplying the estimated GMI by the pilot overhead. A total throughput of 194.55 Tbit/s was obtained, against 178.08 Tbit/s reported in [11]. This discrepancy is explainable by some modelling assumptions, e.g.,

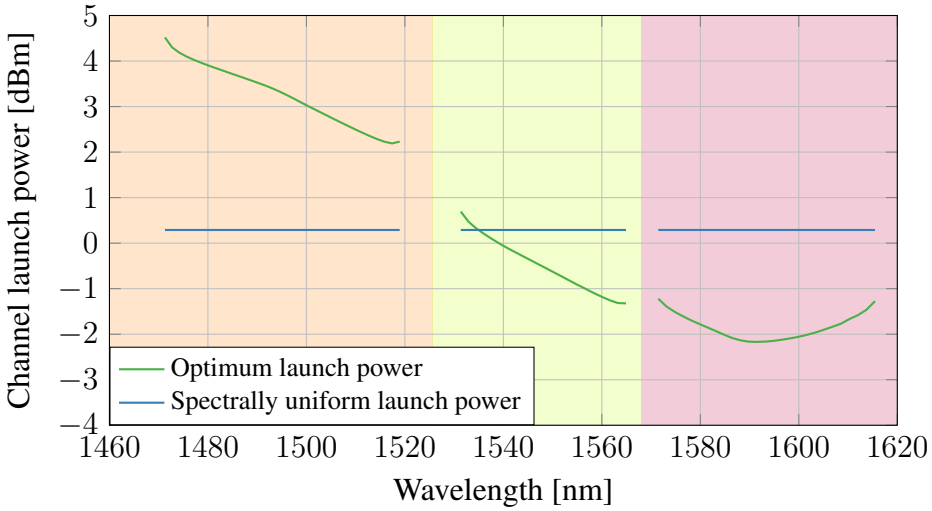

Fig. 5.5: Optimum (green curve) and spectrally uniform (blue curve) launch power per channel optimised for a single span.

flat NFs across each amplifier bandwidth gains, the SNR_{TRX} was measured for a few channels only, and constant NF assumption was made for the other channels.

It is important to stress that this large variation in the back-to-back performance across different bands (see Table 5.1) was mainly due to lab experimental setup constraints, especially for the S-band wavelengths. This is because two different types of lasers for the LO were used in this experiment: ECL with 15.5 dBm output power and 100 kHz linewidth was used for wavelengths between 1529.2 nm to 1607.8 nm. For the remaining wavelengths, ECL with 300 kHz linewidth and 0 dBm output power followed by an optical amplifier was used to operate the Rx at optimum power. Further, due to a limited number of TDFAs, SOAs had to be used to pre-amplify the received signal for S-band wavelengths, incurring an SNR penalty for the S-band channels (1484.86 nm to 1519.8 nm). A significant penalty in the back-to-back performance was also measured for the wavelength bands (from 1520 nm to 1529 nm and from 1608 nm to 1619.67 nm) that used discrete Raman amplifiers to compensate for the Tx and Rx losses. In a deployed system, with individual transponders per channel, a similar level of SNR_{TRX} across all WDM channels would be expected. Therefore, to investigate what could potentially be the throughput if there were no experimental constraints, the throughput for a realistic value SNR_{TRX} = 23 dB for all channels was computed (continuous black line in Fig. 5.4).

For this case, the launch power was optimised for the GS-1024 QAM constellation shown in [11, Fig. 4], which based on the received SNR was found to be the optimum choice out of the three candidate constellations for all the bands. A total throughput of 232.47 Tbit/s was obtained, indicating that a considerable improvement of 54.39 Tbit/s of the total throughput reported in [11] could potentially be achieved.

5.2.3 Interplay between transceiver noise and launch power optimisation impacts on overall system performance

In this section, the impact of launch power optimisation in the per-channel system performance and QoT for different values of $\mathrm{SNR_{TRX}}$ and distances spanning from short to metro, long-haul and trans-Atlantic was investigated. A system configuration, that takes into account commercial optical amplifiers' gain bandwidth and high symbol rate transponders, was taken into consideration.

The transmission system investigated was assumed to have $\mathrm{N_{ch}} = 183$ WDM channels centred at 1540 nm, ranging from 1471.3 nm to 1615.5 nm, corresponding to commercially available amplifiers. Each channel was modulated at the symbol rate of 96 GBd and was spaced by 100 GHz from its neighbour. The transmission over S, C and L bands with spectral gaps between each band was considered. For the S/C and C/L separation bands, gaps of 10 nm and 5 nm were considered, respectively, emulating the amplifier bandwidth coverage range. The NFs of each band were 7 dB, 4 dB, and 6 dB in the S, C and L band, respectively. For simplicity, Gaussian constellations (i.e., $\Phi_k = 0$) were used, such that each span was made of 80 km SMF (same fibre parameters as in Sec. 5.2.2.1) and the fibre launch power of each WDM channel to each span was controlled to the target value by assuming adaptive spectral equalisation and dynamic gain control of the amplifier.

Due to the assumption of coherent accumulation of the nonlinearity ($\epsilon \neq 0$ in Eq. (2.55)), the optimum and the spectrally uniform launch power per channel were not exactly the same for every span. However, $\epsilon \to 0$ as the number of channels increases [27, Fig. 10]. Justified by this fact, the launch power was optimised for a single span and was used as the approximate optimum launch power for every span. The optimum launch power per channel and the spectrally uniform launch power profile used are shown in Fig. 5.5. Both launch power cases were obtained using the same strategy and the same optimisation parameters of Sec. 5.2.1 and 5.2.2.2, except that in this case, each 2 adjacent channels were combined into 1 super-channel to reduce complexity. For the optimum launch power profile (green curve), a total launch power of 23.68 dBm and a maximum per channel power variation of 6.7 dB (4.5 dBm for 1471.47 nm and -2.17 dBm for 1591.47 nm) were found. For the spectrally uniform launch power (blue curve) a total launch power of 22.91 dBm was obtained, with 0.29 dBm per channel. Note that, for the optimum launch power profile case, there was an increase in the channel powers for wavelengths above 1590 nm. This is because the ISRS effect reduces for spectral spacing above 15 THz, as defined by the Raman gain spectrum shown in Fig. 3.2. Both launch power profile strategies are used further in this section to estimate the transmission system performance.

Fig. 5.6 illustrates the per channel SNR for different transmission distances and

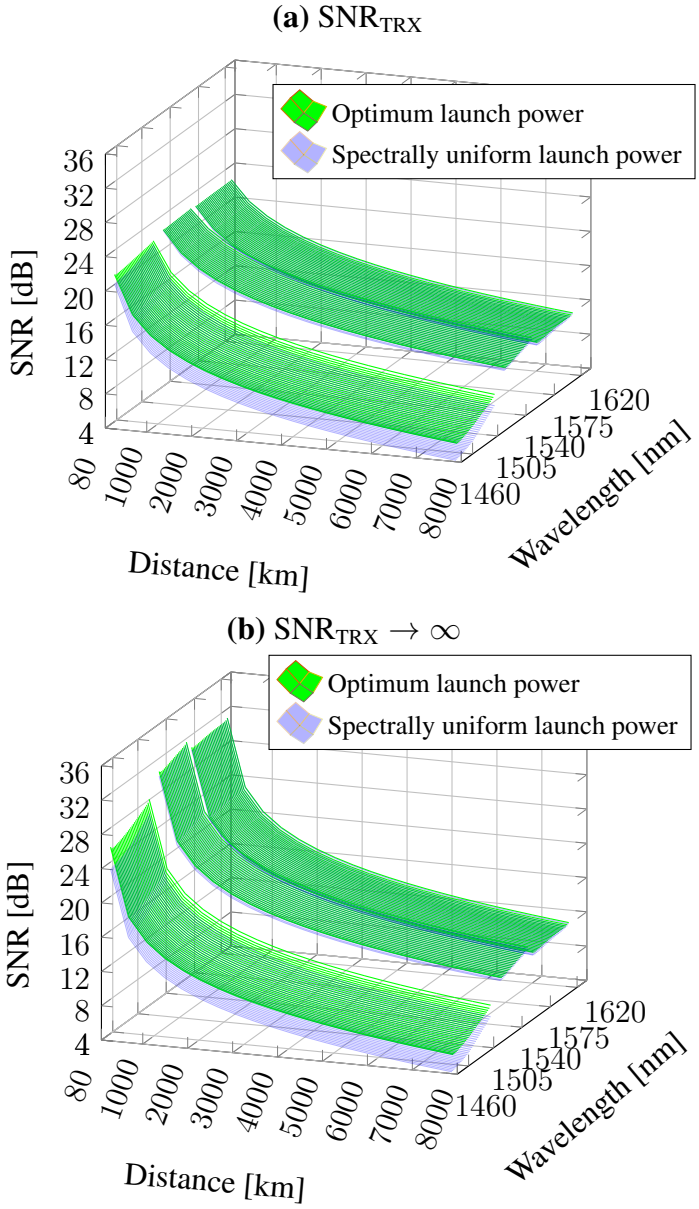

Fig. 5.6: Per channel SNR profile for different distances and for the different launch power profiles shown in Fig. 5.5. Two scenarios are considered: (a) non-ideal TRX with SNR$_{TRX}$ = 23 dB and (b) the case of an ideal TRX.

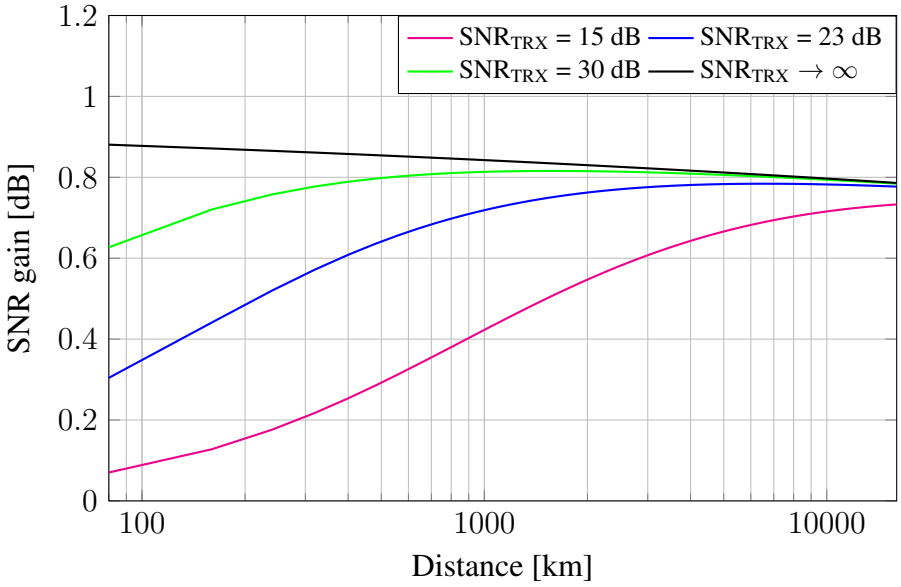

Fig. 5.7: Gain in SNR w.r.t. using the optimum instead of the spectrally uniform launch power profile. The launch power profiles are shown in Fig. 5.5. The gains are averaged over the channels.

launch power profiles. Two cases were considered: (a) per channel $\text{SNR}_{\text{TRX}} = 23$ dB and (b) an ideal TRX, with $\text{SNR}_{\text{TRX}} \rightarrow \infty$ for all the channels. The aim here was twofold. Firstly, to investigate how the SNR_{TRX} value impacted the per-channel SNR for different transmission distances when transmitting the optimum power per channel (green surface) or the spectrally uniform power (blue surface) profiles. Secondly, to investigate how the SNR_{TRX} value impacted the QoT across the entire transmission bandwidth. This was measured by analysing the maximum per channel SNR variation across the entire bandwidth (designated as ΔSNR).

When comparing Fig. 5.6(a) with Fig. 5.6(b), it can be seen that SNR_{TRX} reduced the transmission performance difference between the launch power profile cases. For instance, in case (a), for 80 km, the average SNR values were 21.93 dB and 21.62 dB for the optimum power and spectrally uniform power profile, respectively. This corresponds to a difference of only 0.31 dB SNR, while the same analysis for case (b) resulted in 28.96 dB and 28.08 dB, corresponding to a difference in SNR between both launch power profiles of 0.88 dB. Moreover, it can be seen that SNR_{TRX} yielded a flatter QoT for both launch power profiles by reducing the maximum per channel SNR variation (ΔSNR) across the bandwidth. For instance, in the case (a) for 80 km, the ΔSNR was 1.39 dB and 2.33 dB for the optimum and the spectrally uniform launch power profiles, respectively. The same analysis for the case (b) ($\text{SNR}_{\text{TRX}} \rightarrow \infty$) resulted in a ΔSNR of 6.14 dB and 8.23 dB, respectively.

To further investigate the difference in transmission system performance for both launch power profile cases, Fig. 5.7 shows the SNR gains and Fig. 5.8 the throughput

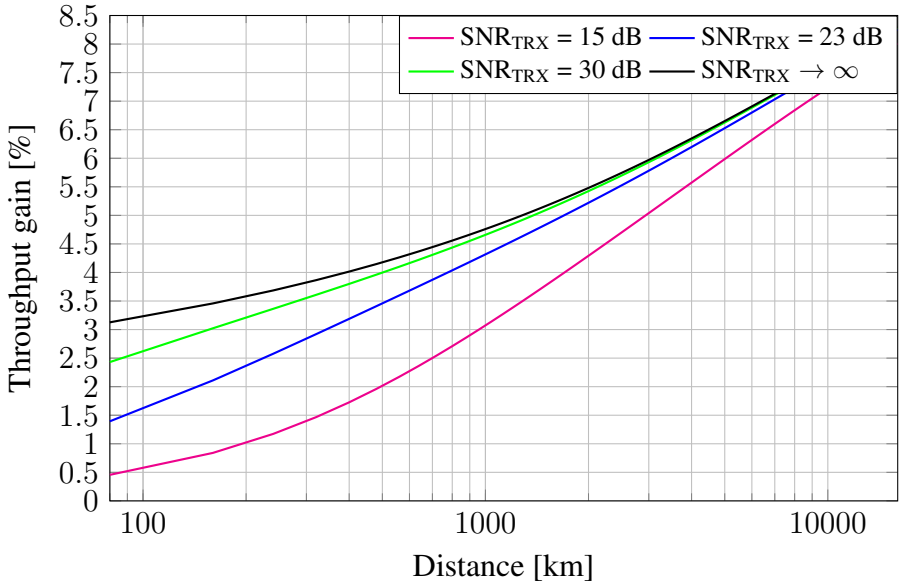

Fig. 5.8: Gain in throughput w.r.t. using the optimum instead of the spectrally uniform launch power profile. The launch power profiles are shown in Fig. 5.5. The gains are averaged over the channels.

gains, relative to the spectrally uniform power profile, for the optimum launch power profile. Different values of SNR_{TRX} and transmission distances were considered. The SNR gains were averaged over all the channels and the throughput was computed using the AWGN capacity (Eq. (2.72)).

It can be noted that in Figs. 5.7 and 5.8, for short distances, the gains in SNR and throughput change considerably depending on the SNR_{TRX} and this change is monotonically reduced for long distance. It can also be observed that, for the case of an ideal TRX ($SNR_{TRX} \to \infty$), the drop in the SNR gain with distance was resulted of the deviation between the launch power used, which was optimised for a single span only. However as previously explained, due to the coherent accumulation, the optimum launch power slightly drops with the number of spans. Also, note that in Fig. 5.8, the throughput gains increase with distance. This is a result of the logarithmic dependence between SNR and the AWGN channel capacity.

To further investigate how the different launch power profiles and the SNR_{TRX} impact the system QoT for different distances, the ΔSNR for different values of SNR_{TRX} and distance was calculated, and the curves are shown in Fig. 5.9. The continuous line illustrates the results for the optimum launch power per channel, while the dashed line shows the results for the spectrally uniform launch power profile. Firstly, it could be noted that the optimum launch power profile improved the QoT by reducing the SNR variation across bandwidth for any distance and SNR_{TRX} value. For the case of an ideal TRX, this difference was approximately 2 dB for any distance. For a TRX-constrained SNR system, this improvement was reduced for short distances and

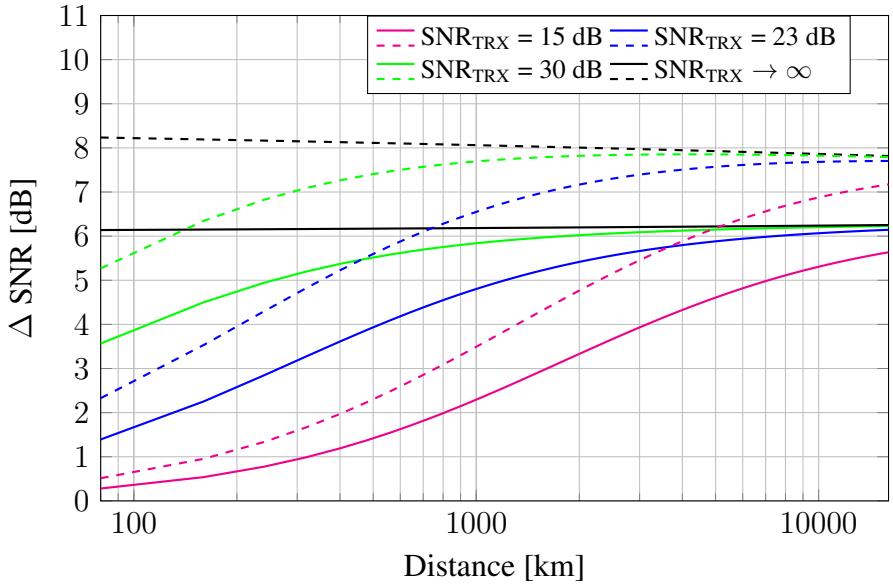

Fig. 5.9: Maximum per channel SNR variation (ΔSNR), i.e., the difference in SNR between the most and the least distorted channel for different values of SNR$_{TRX}$. Both launch power profile cases shown in Fig. 5.5 are considered, optimum launch power profile (continuous lines) and spectrally uniform launch power profile (dashed lines).

grew as the distance increased. Moreover, the lower the SNR$_{TRX}$, the more evenly was the QoT across the channels. This flatness in the QoT was noted with greater impact for short distances and was monotonically reduced as the distance increases.

In summary, when the TRX noise is the main source of impairment in the system, the gains provided by the utilisation of the optimal, instead of the spectrally uniform launch power was reduced as SNR$_{TRX}$ was the same irrespective of the launch power per channel.

5.2.4 Impact of launch power optimisation on different span lengths and transmission bandwidths

This section investigates how the QoT and the gains in performance, obtained by using the optimum instead of the spectrally uniform launch power profile, change for different span lengths and transmission bandwidths. All analyses were carried out in the absence of the TRX noise contribution, (SNR$_{TRX}$ $\rightarrow \infty$) and for a single span. This is because the impact of TRX in the SNR gain and ΔSNR has been demonstrated in Sec. 5.2.3 and can be easily extended for the scenarios considered in this section.

The system configurations considered here were the same as in Sec. 5.2.3, but with span lengths of 60 km, 80 km and 100 km, and bandwidths of 10 THz, 15 THz and 20 THz, corresponding to transmissions of 101, 151 and 201 channels centred at 1540 nm, respectively. For each of these system scenarios, the optimum and the spectrally uniform launch power profiles were computed following the strategy of

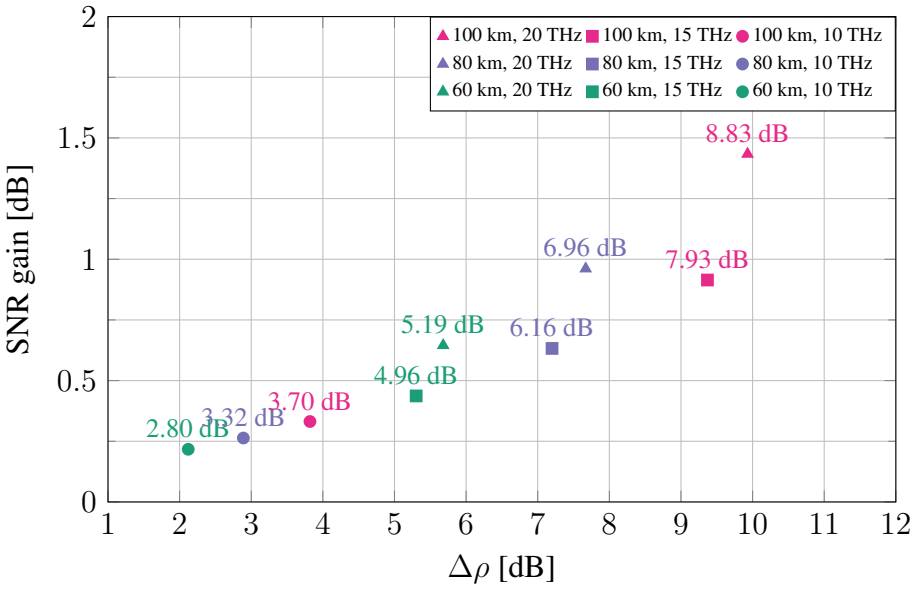

Fig. 5.10: The gain in SNR w.r.t. using the optimum instead of the spectrally uniform launch power profile as function of the maximum transferred power between channels ($\Delta\rho$) due to ISRS, for each of the scenarios shown in the legend. For each scenario, the maximum launch power per channel variation (ΔP) is shown above the marker. The gains in SNR were averaged over the channels and computed for a single span.

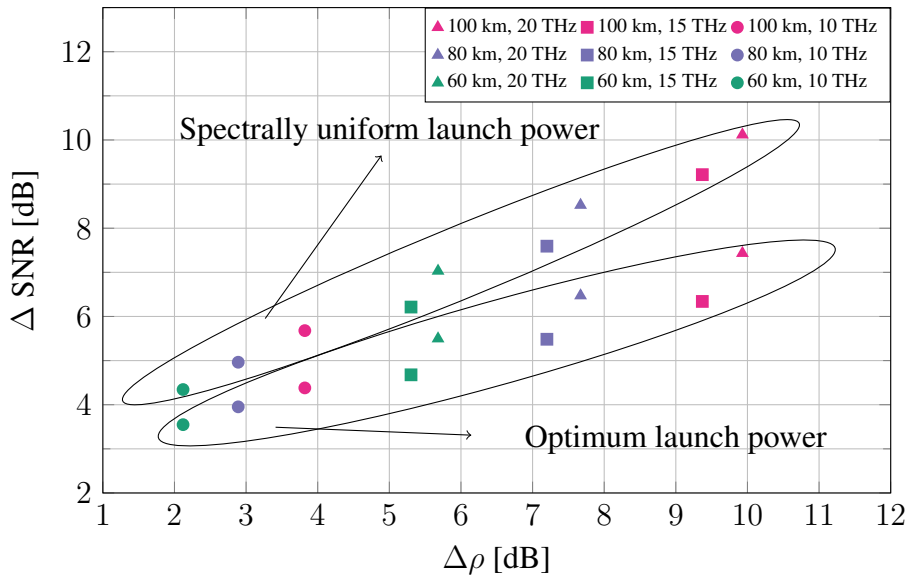

Fig. 5.11: Maximum per channel SNR variation (ΔSNR), i.e., the difference in SNR between the most and the least distorted channel as a function of the maximum transferred power between channels ($\Delta\rho$) due to ISRS, for the different scenarios shown in the legend. For each scenario, ΔSNR is shown for the optimum (lower ellipse) and the spectrally uniform (upper ellipse) launch power profiles.

Sec. 5.2.1, and these launch power profiles were used to estimate the SNR gain and the SNR variation across the bandwidth ΔSNR. To analyse how the different span lengths and bandwidths change the level of the ISRS effect, for each case, the maximum ISRS-transferred power $\Delta\rho$ was also computed. This was done by computing the difference between the maximum and the minimum values of the Raman transfer function.

For the different transmission bandwidths and span lengths considered in this section, Fig. 5.10 shows the gains in terms of SNR between the optimum and the spectrally uniform launch power profiles as a function of the maximum transferred power between channels ($\Delta\rho$) due to ISRS. Also, for each case, the value of per-channel launch power variation (ΔP) above each marker was indicated. It could be noted an upward trend between the strength of ISRS impact measured by the maximum transferred power between channels ($\Delta\rho$) and the SNR gains achieved by the power optimisation. This was because a larger amount of power being transferred between channels due to the ISRS effect needs to be compensated for, increasing ΔP.

Therefore, the greater ΔP, the greater the difference between the per channel launch powers of the optimum and the spectrally uniform profiles, increasing the SNR gains. For instance, for a span length of 60 km and bandwidth of 15 THz, a maximum transferred power between channels $\Delta\rho$ of 5.30 dB and a ΔP of 4.96 dB were found. This provides a SNR gain (difference in SNR between using the optimum and the spectrally uniform launch power profile) of 0.44 dB. On the other hand, for the case of a span length of 100 km and bandwidth of 20 THz a $\Delta\rho$ of 9.93 dB and a ΔP of 8.83 dB was found, providing a SNR gain of 1.43 dB.

From Fig. 5.10, two observations are remarkable. Firstly, note that for the cases of 60 km and 80 km both with 10 THz, the maximum transferred power between channels due to ISRS was lower than the maximum launch power per channel variation, i.e., $\Delta\rho < \Delta$P, while for the remaining scenarios, this trend was reversed, i.e., $\Delta\rho > \Delta$P. This was because the strong ISRS effect flipped the NLI profile [125, Fig. 5], i.e., for increasing ISRS, the magnitude of NLI turned to be higher for the longer wavelengths channels, even with these channels experiencing higher levels of dispersion.

Secondly, it should be noted that for some scenarios, the SNR gain was lower even with higher $\Delta\rho$. For instance, for a span length of 80 km and bandwidth of 20 THz, a $\Delta\rho$ of 7.67 dB provided a SNR gain of 0.96 dB, while for a span length of 100 km and bandwidth of 15 THz, a $\Delta\rho$ of 9.37 dB provided a SNR gain of 0.91 dB. To explain it, Fig. 5.5 should be considered. It is possible to note that, in the spectrally uniform case, the long-wavelength channels experienced a higher impact of NLI, because their per-channel power values were larger than the optimal ones. Therefore, it diminished the SNR gains, despite demonstrating higher values of $\Delta\rho$.

Fig. 5.11 shows the maximum per channel SNR variation (ΔSNR) as a function of

the maximum transferred power between channels ($\Delta\rho$) for the different span length and bandwidths. Similar to Sec. 5.2.3, this variation was computed using the optimum (lower ellipse) and the spectrally uniform (upper ellipse) launch power profiles. As expected the ΔSNR variation was reduced when using the optimum power profile instead of the spectrally uniform launch power profile, improving the QoT. More interestingly here, is that, firstly, this reduction in ΔSNR follows an upward trend as the strength of ISRS increases. Secondly, ΔSNR increases with $\Delta\rho$, deteriorating the QoT for both the optimum and the spectrally uniform launch power profiles. As an example, considering the ΔSNR obtained for the optimum launch power profiles for each case (lower ellipse), it is noted that, for a $\Delta\rho$ of 2.12 dB a ΔSNR of 3.55 dB was obtained, while for a $\Delta\rho$ of 9.93 dB, this value increases to 7.43 dB.

5.3 Impact of launch power optimisation in hybrid-amplified links

In Sec. 5.2 per-channel launch power optimisation for UWB has been extensively analysed for lumped-amplified links. It was shown that relevant gains in performance can be achieved by allocating higher power in the S-band and lower in the L-band to counteract the ISRS effect. In Sec. 5.2, it was also shown that these gains in performance depend on the system configuration including span lengths and optical bandwidths (see Fig. 5.3). For hybrid-amplified links however, because of the very recent availability of real-time models, very little research has been done to quantify the gains in performance obtained by per-channel launch power optimisation compared to using a spectrally uniform one. Such optimisation has now become possible thanks to closed-form expressions derived in the course of this PhD research in the works [P3], [P6], [P12], [P14] and [P17], described in Chapter 4, and also the independent work in [106].

The first theoretical UWB demonstrations of hybrid-link optimisation were reported in [128, 129, 130] for BW pumped Raman systems and in [87] for arbitrary pump pumped systems. In [87, 128], also described in Secs. 5.4 and 5.5, a spectrally uniform launch power profile was used to maximise the system throughput, whereas in [129, 130], per-channel launch power optimisation was performed. However, no quantification of the gains obtained by optimising the launch power was reported in this later. This is important as per-channel launch power optimisation is computationally complex and requires additional shaping components in the deployed systems, increasing overall system cost and power consumption.

In this section, the gains in total throughput obtained by per-channel launch power optimisation in hybrid-amplified links were quantified and compared with these values obtained for lumped systems. A capacity-maximising hybrid amplifier is described, designed using a PSO algorithm, where the launch power, as well as FW and BW

pumps, were optimised in terms of power and wavelength to maximise system throughput (similar to Sec. 5.2.1). The results were compared to an optimum spectrally uniform launch power profile. A similar analysis was carried out for a system with the same parameters but designed to operate using lumped amplifiers only. The analysis presented in this section was presented at ECOC 2024 [P19] [131].

5.3.1 Launch power optimisation and transmission system setup

This section describes the transmission system design, and the amplifier optimisation, including the per-channel launch power optimisation algorithm. It was assumed that the modelled system uses a hybrid amplification technology, consisting of two stages: a FW+BW-distributed Raman amplifier followed by an ideal EDFA. Transmission of N_{ch} = 131 channels spaced by 100 GHz and centred at 1550 nm was modelled. Each channel was modulated at the symbol rate of 96 GBd, resulting in a total bandwidth of 13 THz (105 nm), spanning 1500 nm to 1605 nm (transmission over the S-, C- and L-bands). Spectral gaps of 10 nm and 5 nm were assumed, respectively, between the S/C and C/L bands. The NF of each lumped amplifier placed at the end of each span was 7 dB, 4.5 dB, and 6 dB in the S-, C- and L- bands, respectively. Gaussian constellations, ideal LA, and ideal TRXs were assumed.

The signal transmission was evaluated over 10 $\times$ 100 km spans (total distance of 1000 km). The optical fibre was assumed to have wavelength-dependent attenuation and the Raman gain profile compliant with Figs. 4.1 and 4.2, and a spectrally uniform effective area of 80 μm^2, resulting in a spectrally uniform nonlinear coefficient $\gamma = 1.16$ W^{-1}km^{-1}. Dispersion parameters considered were $D = 16.5$ ps nm^{-1}km^{-1}, $S = 0.09$ ps nm^{-2}km^{-1}. For the distributed RA, FW and BW pumps were placed in the E- and the unoccupied part of the S-band (1405 nm - 1490 nm), and their wavelengths and powers, and the per-channel system launch power were optimised to maximise the system throughput.

Launch power and pump were optimised over a single-span transmission based on the strategy described in Secs. 5.2.1. The optimisation used PSO algorithms only. The cost function to be maximised was the total system throughput, given by Eq. (2.72), where the SNR was calculated using the model in Eqs. (4.5) and (4.4). Given the large number of degrees of freedom of this problem, the optimisation was divided into two steps. Firstly, pump powers and wavelengths were optimised with a spectrally uniform launch power profile. Secondly, the pump powers and wavelengths found previously were kept constant and the channel launch power was optimised.

For the first step, 6 FW plus 6 BW pumps were chosen (other pump numbers are also possible) and placed in the E- and S-bands (1405 nm-1490 nm). The PSO algorithm had 13 variables to be optimised (12 pumps + the total launch power). The

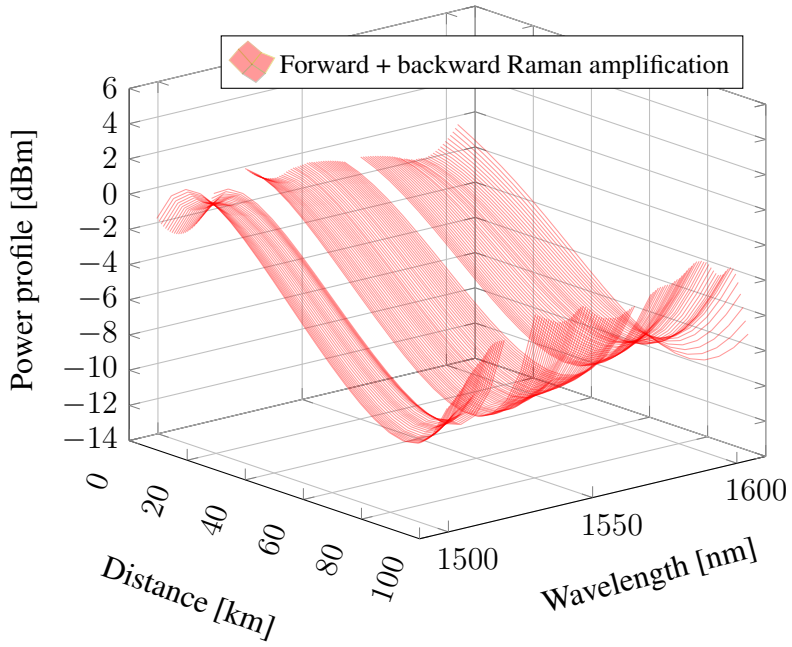

Fig. 5.12: Per-channel launch power evolution with distance for the optimised launch and pump powers and pump wavelengths.

number of particles was chosen to be 50 with a maximum of 50 iterations selected as the stopping criterion. For the algorithm bounds, the total channel launch power varied between 10 dBm and 25 dBm, and the power of each pump from 0 mW to 250 mW. The optimisation resulted in an optimum spectrally uniform launch power of -1.74 dBm per channel, corresponding to a total launch power of 18.75 dBm; 3 FW pumps with non-negligible power, with wavelengths located at 1405 nm, 1410 nm and 1455 nm, and powers of 153.6 mW, 240.1 mW and 31.3 mW, respectively; and 5 BW pumps with non-negligible power, with wavelengths located at 1422 nm, 1428 nm, 1437 nm, 1452 nm, and 1483 nm, and powers of 249.2 mW, 31.7 mW, 250 mW, 80 mW and 225.3 mW, respectively.

In the second step, the pump powers and wavelengths found previously were kept and the per-channel launch power was optimised to maximise the system throughput. In this step, the PSO algorithm had N_{ch} = 131 variables to be optimised, corresponding to the number of WDM channels. The number of particles was chosen to be $10 \cdot N_{ch}$ with their values, i.e., the launch power for each channel, ranging from -10 dBm to 10 dBm. A maximum of 75 iterations was selected as the stopping criterion. The optimum per-channel launch power evolution of the optimised hybrid amplifier with distance is shown in Fig. 5.12. This optimisation was also carried out for a system operating with LA only. In that case, the per-channel launch-power bounds ranged from -5 dBm to 15 dBm, and the remaining parameters were kept the same. Finally to smooth the solution of the PSO algorithm with low complexity, for both cases, the optimum per-channel launch power obtained from the PSO algorithm was passed through a second-

order Savitzky-Golay filter with a 7-channel window, resulting in a smooth per-channel launch power that achieved a total throughput within 0.06 Tb/s of that obtained from the PSO.

5.3.2 Optimum per-channel launch power profile vs spectrally-uniform launch power profile

The optimum per-channel and spectrally uniform launch power profiles for the optimised hybrid amplifier are shown in Fig. 5.13(a) after one span. For the optimum per-channel launch power, a total power of 19.14 dBm was obtained with a total per-channel variation of 2.85 dB. For the optimum spectrally uniform launch power, the total power was 18.75 dBm. The same analysis was carried out and is shown in Fig. 5.13(b) for an optimised system operating with lumped amplifiers only; in that case, these values were 24.44 dBm, with a total per-channel variation of 6.14 dB, and 23.85 dBm, respectively.

Fig. 5.14 shows the system performance after 10 spans for the launch power profiles shown in Fig. 5.13(a). For the optimised hybrid amplifier, using the optimum spectrally uniform launch power, yielded increased values of NLI noise and reduced values of ASE noise in the S-band, resulting mostly from the noise from FW Raman pumps within that band. On the other hand, reduced values of NLI noise and increased values of ASE noise were observed in the C- and L- bands which were most impacted by the noise from the BW Raman pumps. To counteract these noises, the per-channel optimum launch power allocated reduced power levels in the S-band, and increased power levels in the C- and L-bands (see Fig. 5.13(a)), increasing the system performance. The results of the same analysis carried out for the optimised lumped amplified system are shown in Fig. 5.14(b). In this case, similar to Sec. 5.2, the optimum per-channel launch power allocated more power in the S-band to counteract the ISRS effect (see Fig. 5.13(b)).

In terms of performance for the optimised hybrid amplifier (Fig. 5.14(a)), using the per-channel optimum launch power profile, yielded an average total SNR of 19.78 dB, and total throughputs of 213.14 Tb/s and 141.64 Tb/s after 1 and 10 spans respectively. Conversely, using the optimum spectrally uniform launch power profile yielded an average total SNR of 19.65 dB, and a total throughput of 212.48 Tb/s and 140.70 Tb/s, over 1 and 10 spans respectively. The same analysis for the optimised lumped amplifier (Fig. 5.14(b)), yielded an average total SNR value of 15.07 dB and total throughputs of 179.88 Tb/s and 108.66 Tb/s over 1 and 10 spans for the optimum per-channel launch power profile. These values using a spectrally uniform launch power profile are 14.50 dB, 175.72 Tb/s and 104.86 Tb/s respectively.

In terms of gains obtained through the use of per-channel launch power optimisation, compared to the spectrally uniform case, the hybrid-amplified system yielded 0.13 dB in total SNR gain, and 0.66 Tb/s (0.3 %) and 0.94 Tb/s (0.7 %)

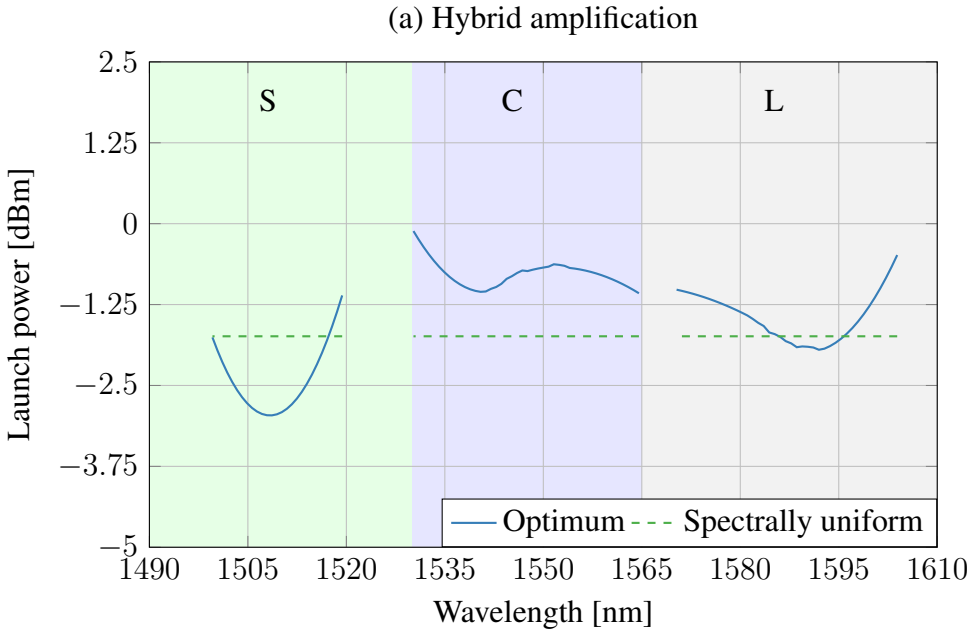

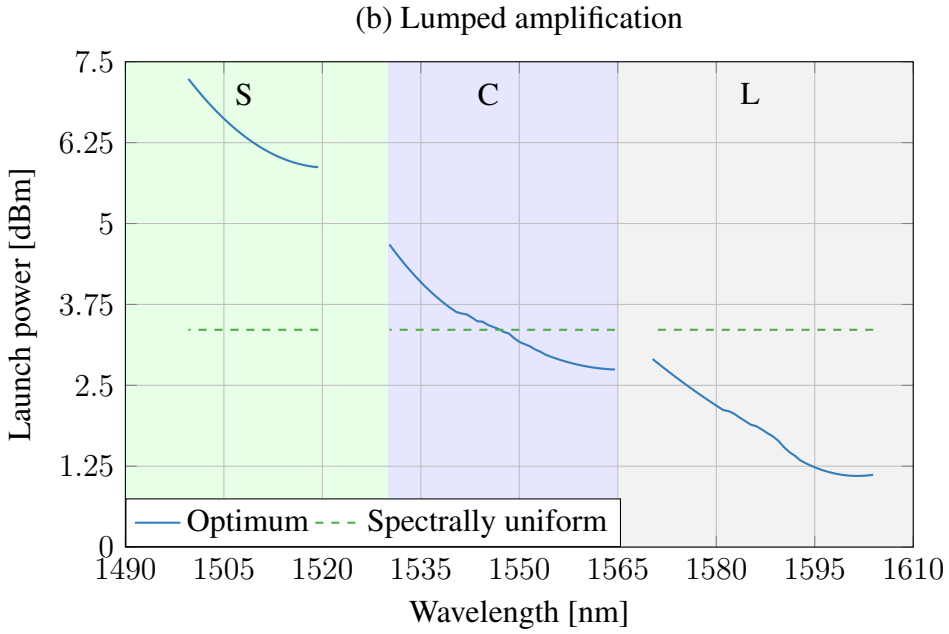

Fig. 5.13: Per-channel and spectrally uniform optimum launch power profiles for (a) hybrid and (b) lumped amplification.

(a) Hybrid amplification

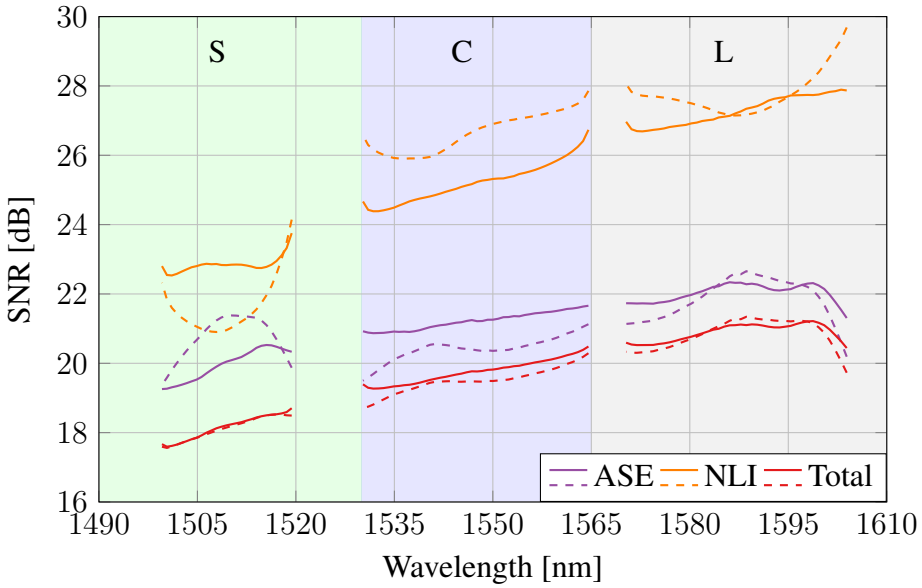

(b) Lumped amplification

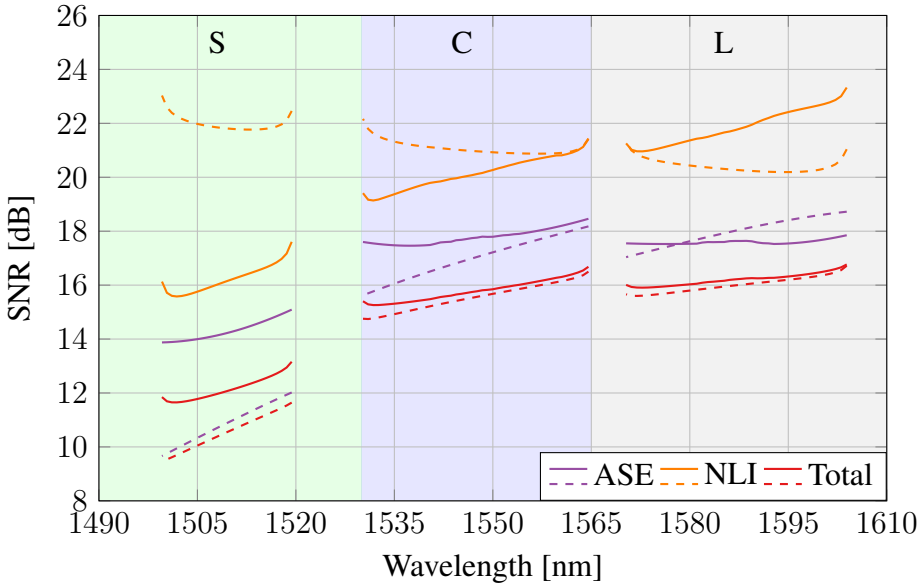

Fig. 5.14: SNR contributions after 10 spans using per-channel (continuous lines) and spectrally uniform (dashed lines) optimum launch power profile for (a) hybrid and (b) lumped amplification.

throughput gains over 1 and 10 spans. For the lumped-amplified system, the gains with per-channel launch power optimisation were significantly larger, at 0.56 dB, 4.16 Tb/s (2.4 %) and 3.80 Tb/s (3.6 %) respectively. Thus, for hybrid-amplified systems, in comparison with lumped-amplified systems, it was found that pump power and wavelength optimisation can compensate for almost all the power fluctuations induced by the combination of Raman, ISRS and wavelength-depend fibre parameters, reducing the further gain in SNR achievable with per-channel launch power optimisation. For the optimised hybrid-amplified system only 0.13 dB SNR gain was due to the per-channel power optimisation. In contrast, per-channel power optimisation in the system with LA was responsible for a larger SNR gain of 0.56 dB. It should finally be noted that these gains also vary with span length and signal bandwidth as pointed out in Sec. 5.2.4.

5.4 Hybrid-amplifier design optimisation

In Secs. 5.2 and 5.3, the impact of launch power optimisation and TRX noise on the system performance was analysed for lumped and hybrid-amplified links using the models in Chapters 2 and 4. In this section, the model derived in Chapter 4, also in [87, 108, 109, 132, 128], was used to model and optimise different configurations of hybrid-amplified links.

More specifically, a detailed characterisation of capacity-maximising hybrid amplifiers is given for different configurations, such as hybrid-FW, hybrid-BW, and hybrid-FW+BW RA. S-, C-, L-band systems are considered with an optical transmission bandwidth of 18.4 THz (145.7 nm). For the designed hybrid amplification transmission systems, launch power, FW and BW pumps are optimised to achieve the maximum system throughput in a distributed Raman pumping configuration. The NLI and ASE noise contributions are calculated using Eqs. (4.4), (4.5), (2.63) and (2.64), where the wavelength-dependent nonlinear parameter (γ) shown in Fig. 2.4 and effective core area (A_{eff}) shown in Fig. (2.6) were included in this model, and validated using the integral ISRS GN model [33]. The overall system performance is presented, identifying each source of noise and its contributions to the total SNR, analysing the relation of these noise sources with the capacity-achieving amplifier characteristics. Finally, a comparison of these optimised systems with one optimised to operate over a lumped amplifier scheme is carried out, enabling us to quantify potential increases in throughput through the use of RA schemes. The topic presented in this section was published in JLT [P6] and led to an emerging young scholar award by the Pacific Telecommunication Council.

Table 5.2: Pump power and wavelength allocations which yields the power profiles shown in Figs. 5.15, 5.16 and 5.17.

Forward Raman pump scenario							
Wavelength [nm]	1370	1370.3	1411	-	-	-	-
FW pumps' power at $z = 0$ [mW]	249.28	250	250	-	-	-	-
Backward raman pump scenario							
Wavelength [nm]	1370	1412.4	1414.7	1423.9	1452.1	-	-
BW pumps' power at $z = L$ [mW]	249.97	249.86	226.43	46.19	73.21	-	-
BW pumps' power at $z = 0$ [mW]	0.03	0.64	0.67	0.29	2.17	-	-
Forward + backward Raman pump scenario							
Wavelength [nm]	1370.4	1395.6	1402.6	1418.1	1423	1451.2	1460
FW pump power at $z = 0$ [mW]	244.28	164.73	-	-	-	-	-
BW pumps' power at $z = L$ [mW]	-	-	194.6	228	200.28	15.93	133.63
BW pumps' power at $z = 0$ [mW]	-	-	0.15	0.90	1.22	0.87	14.97

5.4.1 Transmission system setup for hybrid-amplified transmission

This section describes the transmission system used for hybrid amplifier design optimisation. It consisted of a WDM signal with N_{ch}=185 channels spaced by 100 GHz and centred at 1539 nm. Each channel was modulated at the symbol rate of 96 GBd, resulting in a total bandwidth of 18.4 THz (145.7 nm), ranging from 1470 nm to 1615 nm, corresponding to transmission over the S- (1470 nm - 1520 nm), C- (1530 nm - 1565 nm) and L- (1570 nm - 1615 nm) bands respectively with 6.7 THz, 4.4 THz, and 5.3 THz each. Spectral gaps of 10 nm and 5 nm were considered, respectively between the S/C and C/L band. The NF of each lumped amplifier placed at the end of each span was assumed to be uniform per band with values of 6 dB, 5 dB, and 6 dB in the S-, C- and L- band, respectively. For simplicity, as before, Gaussian constellations were considered, such that Eqs. (4.5) and (4.4) could be directly applied, however, other types of constellations could be easily considered by using the additional NLI correction term given by Eq. (4.8).

A generic SMF corresponding to an ITU-T G652.D fibre with wavelength-dependent parameters was considered. The attenuation profile is shown in Fig. 4.1, the γ profile is shown in Fig. (2.4), and the A_{eff} profile is shown in Fig. (2.6). The wavelength-dependent Raman gain spectrum is shown in Fig. 2.7, which enhances its frequency variation from the frequency variation of the effective area, i.e., the Raman gain spectrum is normalised for each channel i by the corresponding $A_{\text{eff},i}$ shown in Fig. 2.6. The fibre dispersion, and fibre dispersion slope, were assumed to be $D = 16.5$ ps nm^{-1}km^{-1} and $S = 0.09$ ps nm^{-2}km^{-1}, respectively.

A transmission link made of multiple spans of 80 km was studied. Simulations were carried out for 1, 10 and 100 spans to simulate distances ranging from short to metro, long-haul and trans-oceanic. A hybrid amplification scheme made of a distributed Raman amplifier followed by an LA was considered. The LA at the end of

each span is assumed to be ideal, such that the transmitted power is completely recovered at the end of each span. To that end, after distributed RA, the lumped gain at the end of each span is assumed to be controlled to the target value by using adaptive spectral equalisation and amplifier dynamic gain control devices. A spectrally-uniform launch power profile was considered and optimised with the pumps to maximise the system throughput (see Sec. 5.4.2). A per-channel launch power profile could also have been considered as in Sec. 5.2.3, however, in Sec. 5.3 it is shown that in the case of hybrid-amplified links, operating with spectrally uniform launch power profiles does not yield significant performance loss compared to an operation with per-channel optimum launch power profile. Additionally, spectrally uniform launch power profiles enable the reduction of computational time, speeding up the optimisation algorithms described in Sec. 5.4.2.

5.4.2 Throughput maximisation algorithm for hybrid-amplified transmission

This section describes the strategy used to maximise the system performance given by Eq. (2.69) and maximise system throughput. The strategy is similar to Secs 5.2.1 and 5.3.1. Due to the RA and the ISRS effect, the relation between system performance, pump powers and launch power is nonlinear, leading to a $N_{ch} + N_p$-dimensional non-convex optimisation problem [115]. To solve this problem, numerical optimisation algorithms are required.

The goal of this optimisation was to find the optimum pump wavelengths and powers together with the optimum channel launch power, which maximises the total throughput for the hybrid RA transmission system considered in Sec. 5.4.1. The total throughput is bounded by the AWGN channel capacity given by Eq. (2.72). This equation was the cost function considered in the optimisation, where the SNR was calculated from Eq. (2.69). Note that, the ASE generated by the distributed Raman stage and by the lumped amplifiers was calculated using Eqs. (2.64) and (2.62), respectively.

The numerical optimisation algorithm chosen to find a local maximum of Eq. (2.72) was the PSO [126]. As mentioned in Sec. 5.2.1, the PSO is efficient in exploring the $N_{ch} + N_p$-dimensional space leading to the surroundings of a good local optimal solution. For this algorithm, as before, the Matlab PSO function provided by the global optimisation toolbox was used. To reduce the complexity of this algorithm, a spectrally uniform launch power profile, such that each channel carries the same launch power, was chosen to be optimised. This enabled the reduction of the optimisation space from $N_{ch} + N_p$ to $N_p + 1$. Moreover, compared to a per-channel launch power optimisation, the penalty in performance by making this assumption is small as shown in Sec. 5.3.

For this optimisation, transmission over a single span was considered, and the solution of this single-span optimisation was used for pumping all the remaining amplifiers in the multi-span transmission scenarios (see Sec. 5.4.1). As mentioned in Sec. 5.2.1, this approach is not optimum as the optimum amplifier design changes slightly for each span. This is because the NLI and the ASE noises generated in each span accumulate in a nonlinear manner. However, this non-optimal choice reduces the complexity of the optimisation algorithm as Eqs. (2.63) and (2.64) are solved for a single span only.

Three different hybrid-amplification simulation scenarios were considered, each one using the following distributed setup: FW-RA, BW-RA and FW+BW-RA. To amplify the S-, C- and L- bands, Raman pumps have to be placed in the E-band. To that end, over the E- band (1370 nm-1460 nm) 8 FW/BW pumps were placed and the algorithm found the best wavelength and power allocation for these pumps, i.e., the allocation which maximises Eq. (2.72), considering an ideal lumped amplifier at end of the span to give the remaining signal gain to completely recover the transmitted power. The highest-wavelength pump was chosen to be 10 nm away from the lowest-wavelength channel, such that the XPM-induced products from pumps falling into the WDM spectrum could be neglected [113].

For the FW-RA and BW-RA, 17 variables were then optimised, of which 1 variable was the spectrally uniform launch power, 8 were the pump powers (FW or BW) and 8 were their respective wavelengths. For the FW+BW-RA, 33 variables were optimised, of which 1 variable was the spectrally uniform launch power, 16 were the pump powers (FW + BW) and 16 were their respective wavelengths. For the PSO algorithm, the number of particles was chosen to be 50 with a maximum of 50 iterations as the stopping criteria. For the algorithm bounds, total channel launch power varied between 10 dBm and 25 dBm as the optimum launch power is expected to be within this range, and the power of each pump at the beginning of the fibre varied from 0 mW to 250 mW (other choices are also possible). At the end of the optimisation, 0 power was set for all the pumps with negligible power at the beginning of the fibre for the FW case, and at the end of the fibre for BW case. For each one of the scenarios considered, the pump allocations with non-negligible power found by the described algorithm is shown in Table 5.2. For the FW-RA case, an optimum input launch power per channel of -0.97 dBm was found, resulting in a total launch power of 21.23 dBm, yielding a total throughput of 296.48 Tbit/s. For the BW-RA case, an optimum input launch power per channel of 0.28 dBm was found, resulting in a total launch power of 22.48 dBm and yielding a total throughput of 310.72 Tbit/s. For the FW+BW-RA case, an optimum input launch power per channel of -1.39 dBm was found, resulting in a total launch power of 20.81 dBm and yielding a total throughput of 319.72 Tbit/s. These values are discussed and analysed in the next sections.

Finally, note that the optimisation carried out in this section, may not necessarily be the optimum one, as more pumps could be considered at more wavelengths, increasing the degrees of freedom of the transmission system. This could be done by changing the algorithm optimisation bounds. Additionally, other optimisation algorithms different from the PSO could be used. The described setup was chosen to achieve fast computational time for the PSO algorithm within practical system constraints without requiring the utilisation of GPUs.

5.4.3 Hybrid-amplifier characterisation over single span

This section presents the characterisation of the hybrid amplifier. To that end, for both the optimised scenarios described in Sec. 5.4.2, the power profile evolution along the fibre length, and the hybrid amplifier gain, i.e., the distributed Raman on-off gain followed by the gain provided by the lumped amplifier placed at the end of the span, were calculated. The results are shown for transmission after 1 span.

The pump allocations in terms of wavelengths and powers are shown in Table 5.2 for each optimised scenario described in Sec. 5.4.2. For the FW-RA case, the wavelengths of the pump placed in the E-band amplified mostly the S-band signal. For the BW-RA and FW+BW-RA cases, the obtained pump wavelengths amplified both S- and C- band channels and the shorter channels of the L-band. For all the cases, the longer L-band channels were mainly amplified by the lumped amplifier as the longer possible E-band pump wavelength (1460 nm) was 110 nm (14.4 THz) away from the shorter L-band channel (1570 nm), and thus beyond the peak of the Raman gain spectrum which is at 13.4 THz (see Fig. 2.7). Note that the resultant number of pumps in Table 5.2 depends on the total power allowed for each pump and on the total system losses. In this section, the only source of loss considered was the fibre loss, however, in deployed systems, more pumps may be expected due to additional fibre component and equipment losses.

For the three scenarios described in Sec. 5.4.2, the per-channel power profile with distance, i.e., the solution of Eq. (2.63), are shown in Figs. 5.15(a), 5.16(a) and 5.17(a) for FW-RA, BW-RA and FW+BW-RA, respectively. Note that, as shown in Eqs. (2.63) and (2.64), the intensity of ASE noise generated due to the RA, i.e., ASE noise before LA, is proportional to the intensity of the received launch power profiles. Taking the FW-only and BW-only scenarios as examples, this means that for the FW-RA amplification, low levels of ASE noise before LA were expected and higher NLI noise was generated given the higher power levels propagating along the length of the fibre. In the case of BW-RA, the opposite effect occurred: higher ASE noise before LA is expected and then lower NLI noise was produced given the reduced power levels propagating along the fibre length. However, the generated ASE noise before LA was still amplified by the lumped amplifier placed at the end of the span. These effects

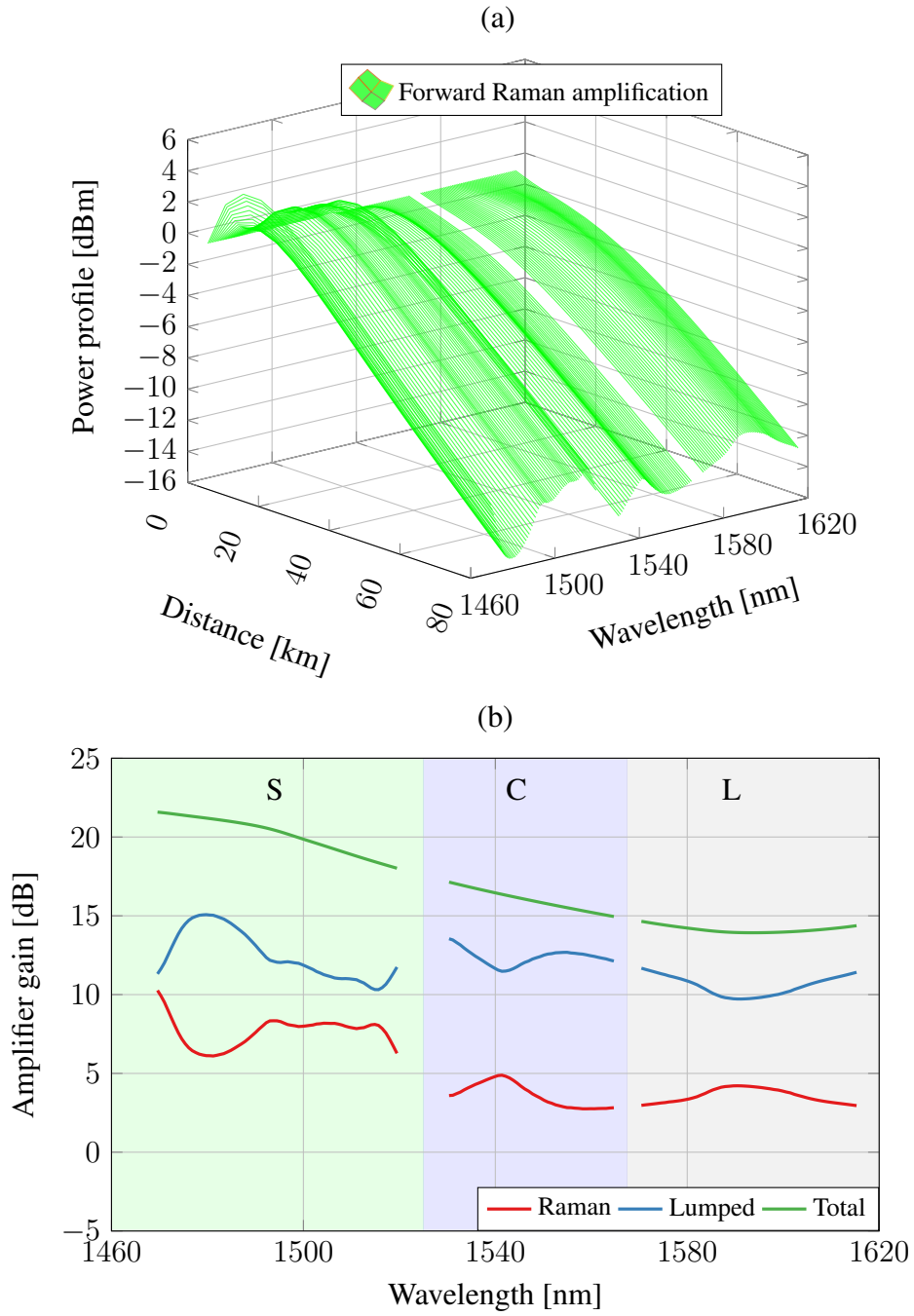

Fig. 5.15: (a) Per-channel launch power evolution along the fibre length after 1 span for FW-RA. (b) Hybrid amplifier gain after 1 span designed in Sec. 5.4.2 for FW-RA. The gains for each one of the amplification stages are shown in red (RA stage) and blue (LA stage); the total gain is shown in green.

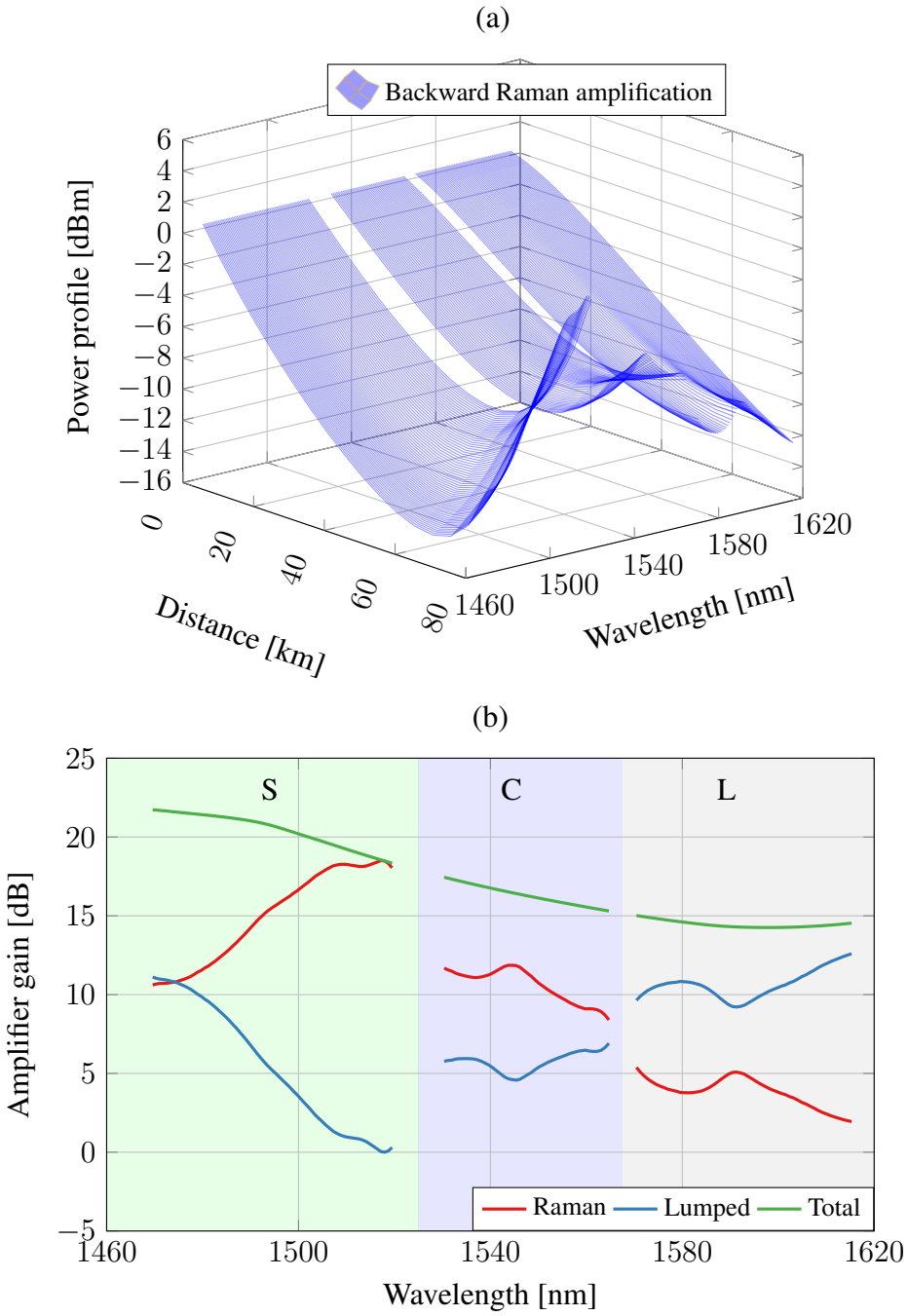

Fig. 5.16: (a) Per-channel launch power evolution along the fibre length after 1 span for BW-RA. (b) Hybrid amplifier gain after 1 span designed in Sec. 5.4.2 for BW-RA. The gains for each one of the amplification stages are shown in red (RA stage) and blue (LA stage); the total gain is shown in green.

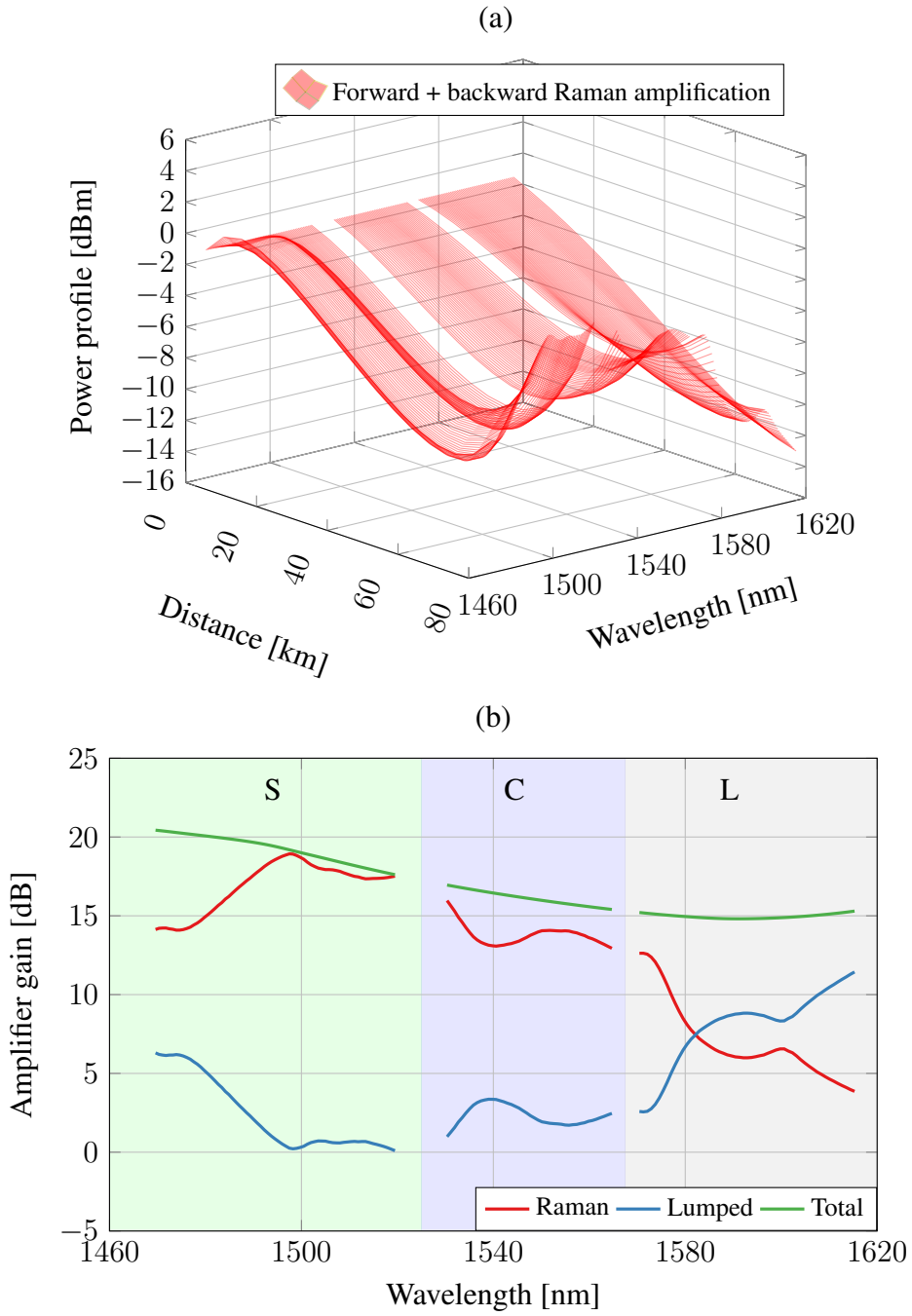

Fig. 5.17: (a) Per-channel launch power evolution along the fibre length after 1 span for FW+BW-RA. (b) Hybrid amplifier gain after 1 span designed in Sec. 5.4.2 for FW+BW-RA. The gains for each one of the amplification stages are shown in red (RA stage) and blue (LA stage); the total gain is shown in green.

were quantified in detail in Sec. 5.4.4.

Figs. 5.15(b), 5.16(b) and 5.17(b) show the amplifier gain for hybrid, FW-RA, BW-RA and FW+BW-RA. The gains are shown for the optimised distributed Raman amplifier (red) and the lumped amplifier (blue) placed at the end of each span. The total gain, i.e., the sum of the gain from the distributed Raman and lumped amplifier stages is also shown in green. For the systems with BW pumps, most of the optimised amplifier gain in the S- and C-bands arose from the distributed Raman stage. L-band channels were far from the pumps and thus did not benefit significantly from the gains in this stage. For FW-RA, most gains come from the LA stage given the high NLI due to the high power levels propagating through the fibre. More interesting is the fact that a full Raman gain in the S- and C- band, with no lumped amplifiers, might not be the best option, as, despite the improved performance of Raman amplifiers in terms of ASE generation, it may massively increase the NLI and ASE noise as a result of high pump powers. Note that, the total gain (green), or effective fibre loss (standard loss + ISRS effect) was different for each scenario - this was because each one of the systems had different values of total launch power (which changed the intensity of the ISRS effect); indeed for the hybrid FW-RA case, the total optimised power was 21.23 dBm, while these values for the hybrid BW-RA and FW+BW-RA cases were respectively 22.48 dBm and 20.81 dBm.

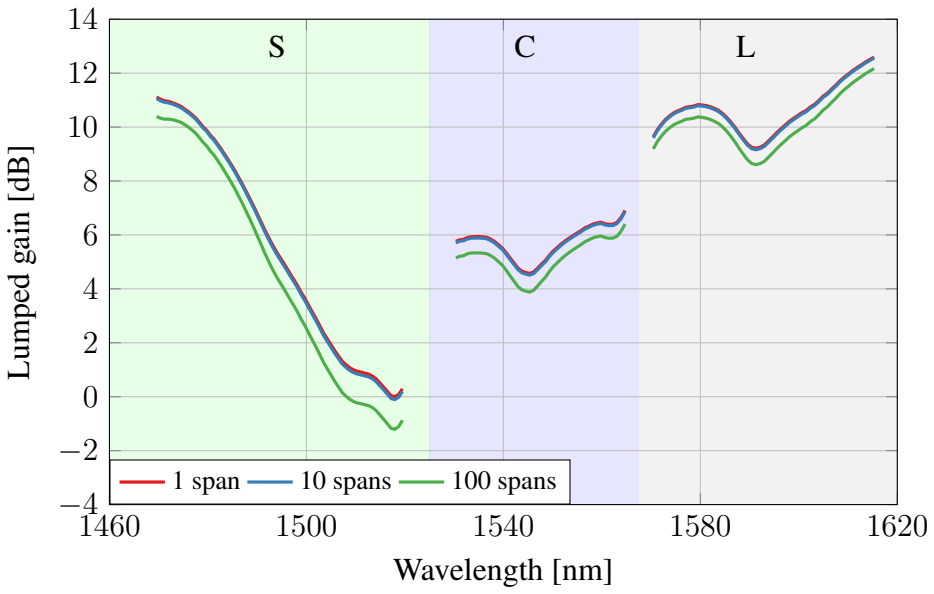

Fig. 5.18: Ideal gain from the lumped amplifiers placed at the end of the 1st, 10th and 100th span for the optimised hybrid BW-RA scenario.

Because the signal profile evolution along the fibre length depends on the ASE noise (see Eqs. (2.63) and (2.64)), its evolution changes slightly in each span, resulting in different Raman and ideal lumped gains depending on the span under consideration. This effect is well known [133] as the "droop" effect [134]. To analyse it, Fig. 5.18

shows the ideal gain, to recover the transmitted power, from the lumped amplifier placed at the end of the 1st, 10th and 100th span for the optimised hybrid BW-RA designed in Sec. 5.4.2. The ideal lumped gain is slightly reduced after each span to maintain the correct input/output power. This change was approximately 0.1 dB after 10 spans and 1.2 dB after 100 spans. Note that, this effect is negligible for a few spans, but relevant for trans-oceanic links. Because this effect is negligible for a few spans, Eq. (2.39), which has no ASE noise coupled on it, could be used. In this chapter, Eq. (2.63) was used in its original form, i.e., considering the coupled ASE noise with the signal (and, thus, accounting for the droop effect), where the ideal lumped gain was adjusted in each span to recover the transmitted power correctly.

5.4.4 System performance for multi-span hybrid-amplified transmission

This section shows the performance of the transmission systems considered in Secs. 5.4.1 and 5.4.2, for the three optimised hybrid-amplified systems. The noise sources, namely, ASE from the Raman amplifier, ASE from the lumped amplifier and NLI from the fibre transmission, were separated and analysed for a single span. The total system performance in terms of ASE, NLI and total SNR were then computed for 1, 10 and 100-span transmissions and a detailed discussion of the results is presented. Furthermore, the accuracy of the NLI SNR levels estimated using the model given by Eqs. (4.5) and (4.4) were verified for all the scenarios presented in this section using the integral ISRS GN model [33]. Note that, the wavelength dependence of γ and A_{eff} were also included in this model.

Fig. 5.19 demonstrates each one of the noise sources in Eq. (2.69) after 1 span transmission. The choice of showing it for 1 span was based on the fact that this is the only scenario where the ASE noise generated from the Raman amplifier could be separated from that generated by LA. This is because after the first span, the total ASE noise (Raman + lumped) was used as the initial condition in Eq. (2.64), and thus, from the second span onwards, noise from both sources was coupled in the transmission and could not be separated.

Fig. 5.19 shows the different noise contributions from Eq. (2.69), for the three hybrid amplifier schemes. The Raman ASE noise is shown before LA (red) and after being amplified by the ideal lumped amplified (blue) placed at the end of the span. The ASE noise from LA (green) obtained from Eq. (2.62) is also shown. The amplified Raman and the lumped ASE noise contributions were then summed and shown as the total ASE (purple). Finally, the NLI noise (orange), and the sum of the total ASE and NLI noises are shown as the total noise (brown). For (a) hybrid FW-RA, the NLI noise was higher in portions of the S-band, because most of the RA happened in this spectral region. On the other hand, for (b) hybrid BW-RA, the ASE noise was the most

(a) Hybrid forward Raman amplification

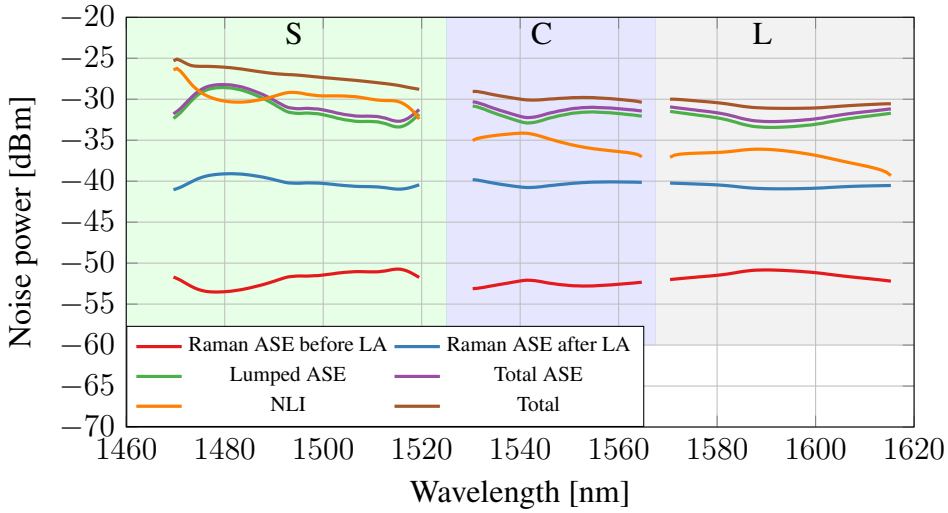

(b) Hybrid backward Raman amplification

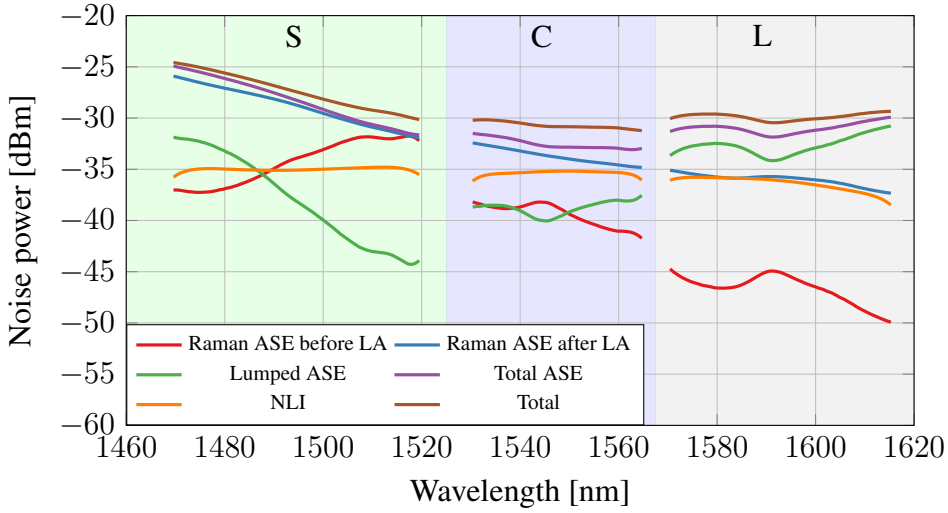

(c) Hybrid forward + backward Raman amplification

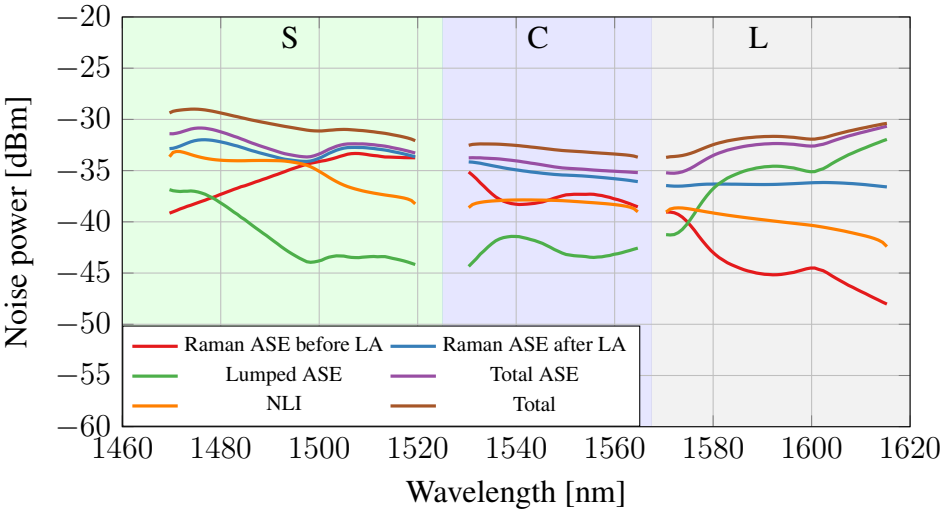

Fig. 5.19: Noise power contributions after the first span for hybrid (a) FW-RA, (b) BW-RA and (c) FW+BW-RA.

impactful contribution while the NLI noise had a smaller contribution in the full spectral region. For (c) hybrid FW+BW-RA, the ASE and NLI contributions in the S-band were more balanced and the total noise power levels were limited by both ASE and NLI contributions; in the C- and L-band the system was more impacted by the ASE noise. The explanation for these levels relies on the amount of power and ASE generated along the fibre transmission for each scenario (see Figs. 5.15, 5.16 and 5.17 and Sec. 5.4.3 for a detailed explanation).

Fig. 5.20 shows the different SNR contributions as a function of wavelength for the transmissions over 1, 10 and 100 spans for (a) FW-RA, (b) BW-RA and (c) FW+BW-RA. The ASE contribution corresponds to the total ASE noise generated by RA and LA.

It is interesting to note the correlation of the SNR profile with the power profiles shown in Figs. 5.15, 5.16 and 5.17 and Sec. 5.4.3. Indeed, for the hybrid FW-RA case, shown in Fig. 5.20(a), the high-power levels at the short wavelengths (see Fig. 5.15) increased the NLI noise, reducing the SNR, and degrading the performance of those channels; on the other hand, the performance of long-wavelength channels was higher, due to their reduced power levels, yielding to a tilt in the SNR profile. For the hybrid BW-RA case, shown in Fig. 5.20(b) the increased received power levels at the short wavelengths (see Fig. 5.16) increased the ASE noise generated by the Raman stage, reducing the SNR and degrading the performance of those channels; on the other hand, the balanced ASE generated from the Raman stage together with the lumped stage increased the performance of the C-band. Almost no Raman gain was obtained in the L-band, worsening the SNR of these channels because most of the ASE noise was generated by the lumped stage. For the hybrid FW+BW-RA case, shown in Fig. 5.20(c) the increased power levels at the short wavelengths (see Fig. 5.17) increased the ASE and NLI noises, reducing the SNR degrading the performance of those channels and yielding a similar SNR curve shape as in the previous case.

NLI SNR estimation using the model in Eqs. (4.5) and (4.4) and the integral ISRS GN model [33] given by Eq. (2.49) are shown as blue curves in Fig. 5.20 for accuracy verification. For (a) hybrid FW-RA and (b) hybrid BW-RA, the maximum per-channel difference between these models was 1.11 dB and 1.03 dB respectively occurring for the channel located at 1546.7 nm. For (c) hybrid FW+BW-RA, this value was 1.10 dB for the channel located at 1469.6 nm. In each scenario, the maximum per-channel differences occurred for the transmission over 100 spans. Furthermore, across all scenarios, the maximum average difference was 0.33 dB and occurred for the transmission over 100 spans using hybrid FW+BW-RA.

Regarding a rough estimation of the model complexity, using a CPU without any code parallelisation, one realisation of the closed-form expression in Eqs. (4.5) and (4.4) for all scenarios took less than 5 seconds, with the majority of the time being spent

(a) Hybrid forward Raman amplification

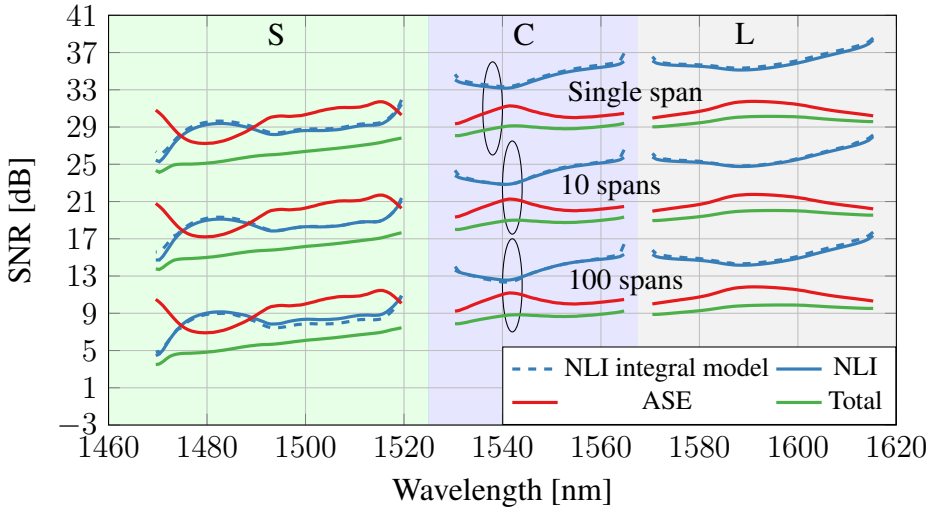

(b) Hybrid backward Raman amplification

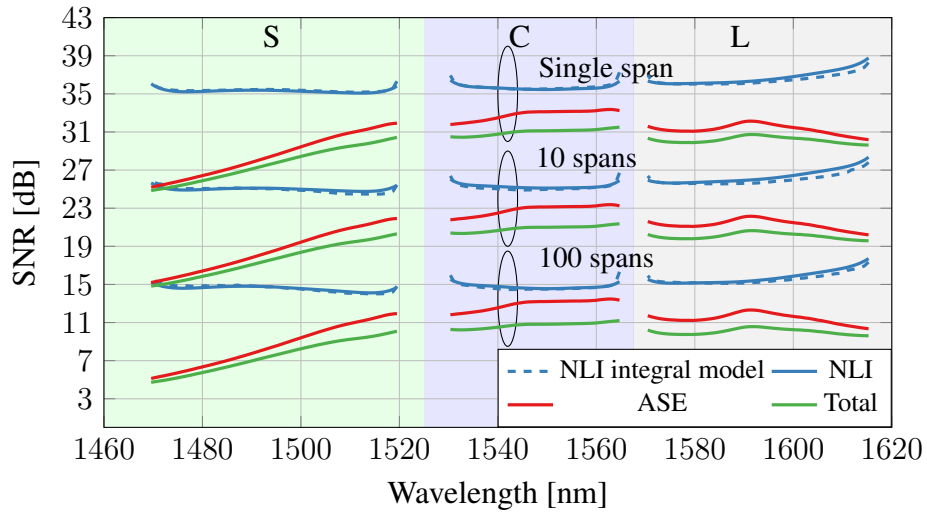

(c) Hybrid forward + backward Raman amplification

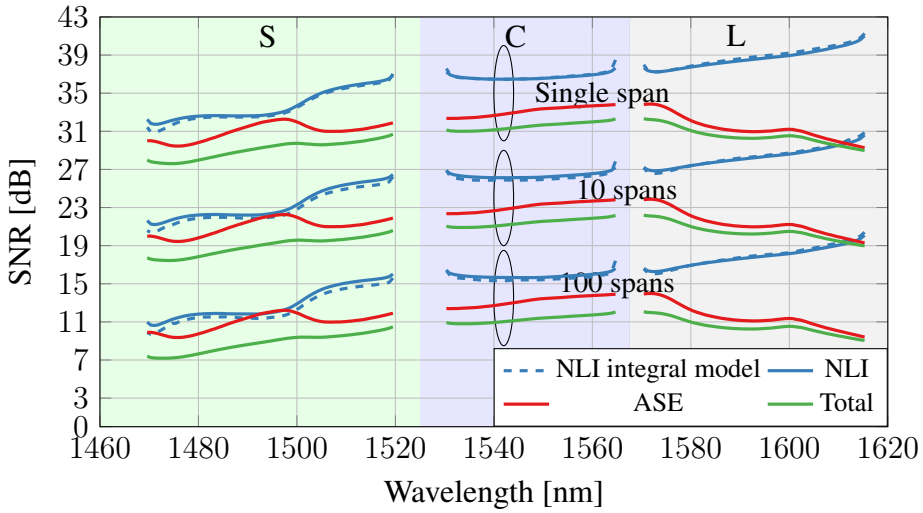

Fig. 5.20: SNR contributions after the 1st, 10th and 100th span for hybrid (a) FW-RA, (b) BW-RA and (c) FW+BW-RA.

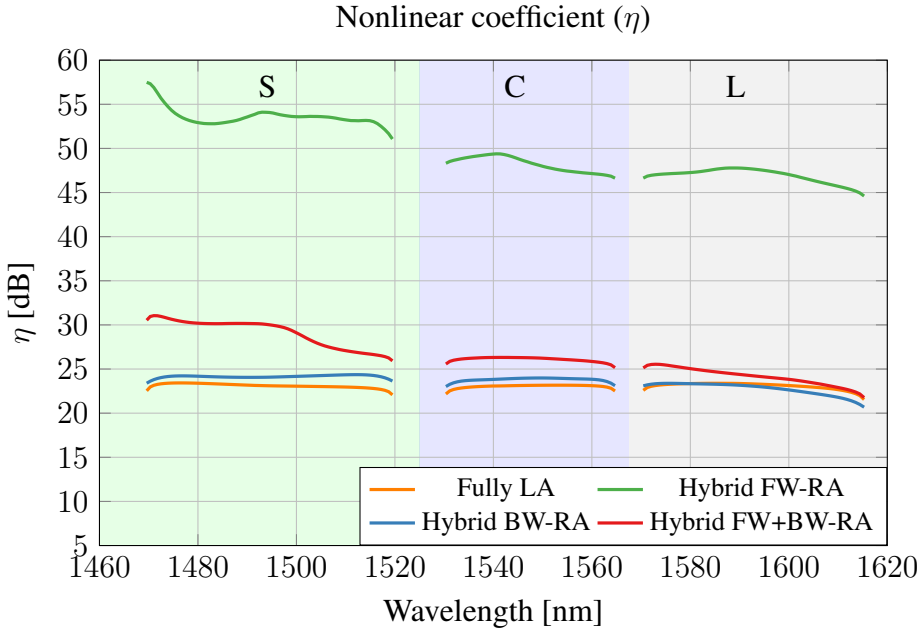

Fig. 5.21: Nonlinear coefficient after 1 span for the transmission system in Sec. 5.4.1 for each amplification scheme.

in the fitting optimisation routine which involves fitting Eq. (4.1) to the power profile obtained by numerically solving Eq. (2.63). The computation time, however, could have been reduced to milliseconds by the clever implementation of the fitting optimisation routine, code parallelisation and utilisation of GPUs, as the fitting can be calculated independently for each channel. On the other hand, integral model simulations, took hours.

5.4.5 Comparison with fully lumped amplification

This section compares the transmission system described in Secs. 5.4.1 and 5.4.2 with a fully lumped amplified link, i.e., without any pumps in the transmission fibre, such that the transmitted power is completely recovered with the ideal lumped amplifier placed at the end of each span. To simulate this transmission system, the NLI model given by Eqs. (2.57) and (2.58) was used with the same transmission setup described in Sec. 5.4.1. Note that the wavelength dependence of γ and A_{eff} was also included in this model. The results, in terms of SNR performance, were then compared with those of Sec. 5.4.4.

The first step for carrying out this simulation was to consider a fully lumped transmission system with the same parameters as described in Sec. 5.4.1. As no pumps were placed in the transmission, the total launch power of the system was the only variable optimised, which resulted in a total optimal launch power of 23.5 dBm, corresponding to 1.3 dBm per channel. This optimisation resulted in a total throughput of 275.29 Tbit/s over a single-span transmission.

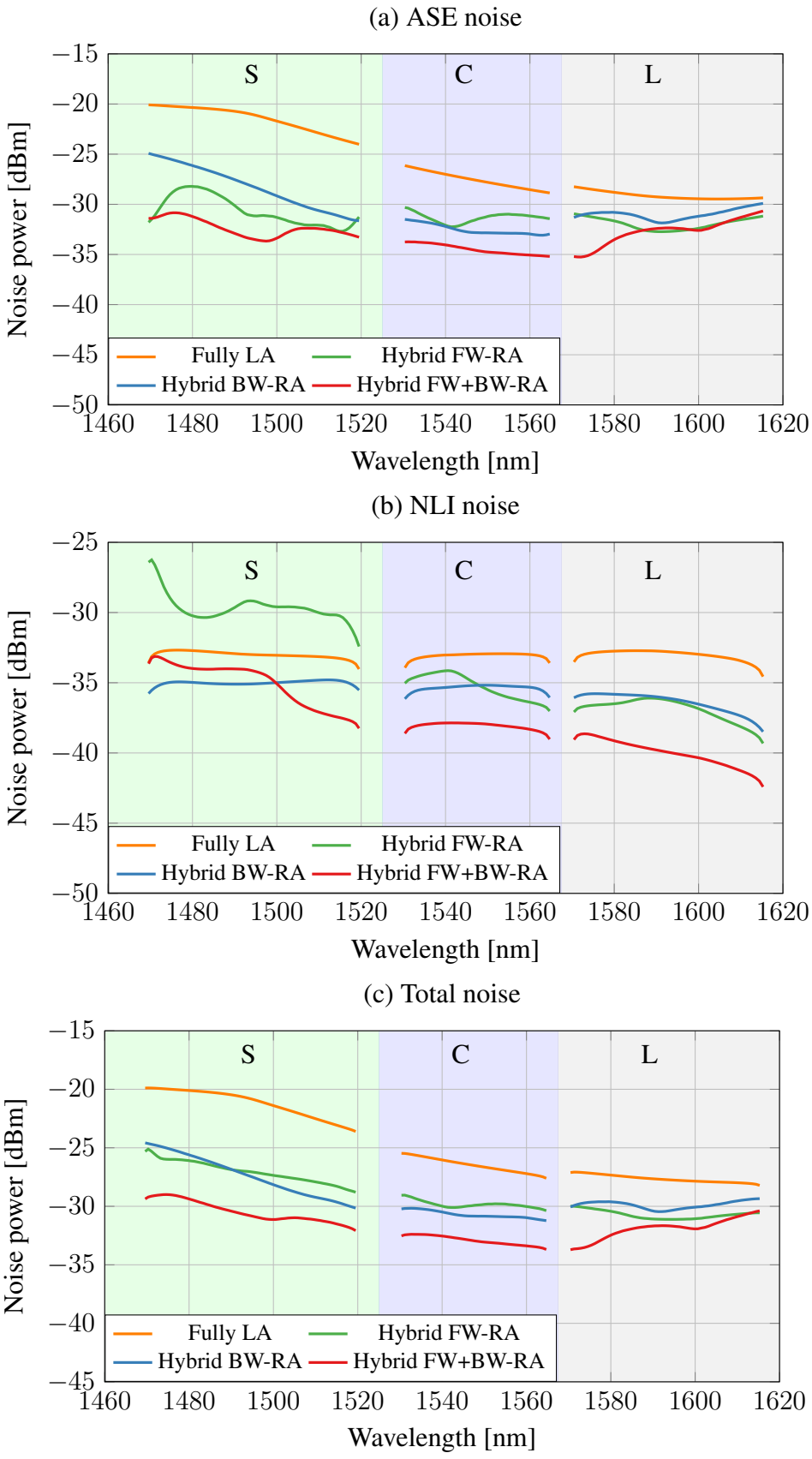

Fig. 5.22: Different noise power contributions after the 1st span for each amplification scheme.

For this lumped system, the nonlinear coefficient η is calculated and compared to the hybrid-amplified links designed in Secs. 5.4.1 and 5.4.2. The same is done for the different noise sources, SNR and total throughput. Fig. 5.21 shows the nonlinear coefficient η (see Eq. (2.69)) obtained from each one of the amplification schemes, namely, hybrid FW-RA, hybrid BW-RA, hybrid FW+BW-RA and fully LA. The motivation for plotting η was to provide a rough estimate of the amount of NLI noise generated by each amplification scheme if the launch power was the same for the optimised amplification schemes considered (this is because η only depends on the normalised launch power profile, and not on its absolute value). This figure shows that the hybrid FW-RA generated higher amounts of NLI noise, because of its increased values of power propagating along the fibre length (see Fig. 5.15), while the LA case generated lower amounts of NLI noise (for the same launch power) because the power was just attenuated by the fibre loss and changed by the ISRS effect, i.e., no pumps were adding additional power in the fibre. Note that, in reality for the systems designed in this section, because the launch power, P_i was different for each amplification scheme and the NLI noise is proportional to the cube of P_i ($P_{\text{NLI}} \propto P_i^3$), the absolute amount of NLI noise generated by each scheme depends on the launch power. Indeed, the higher launch power for the fully LA scenario (23.5 dBm) made this case perform worse than BW-RA and BW+FW-RA cases in terms of NLI noise generation as shown in Fig. 5.22(b).

Fig. 5.22 shows the different noise contributions for each one of the amplification schemes designed in this section. Fig. 5.22(a) shows that the LA case results in greater values of ASE noise, which motivates the utilisation of hybrid amplifiers to achieve higher throughput. Fig. 5.22(b), shows that the increased total launch power of the LA case (23.5 dBm) generated high amounts of NLI noise. Finally, Fig. 5.22(c), shows that, overall, LA is the worst-case scenario in terms of noise generation, followed by the hybrid amplification schemes. However, this is not a complete indication of which amplification scheme is better as the SNR calculation also depends on the launch power.

To assess which amplification scheme is best, Fig. 5.23 shows the total SNR contributions for the transmission over 1, 10 and 100 spans for each one of the designed amplifiers. This figure shows that the hybrid FW+BW-RA presented the best compromise between launch power, ASE and NLI noise, achieving the best performance. The worst performance was obtained by the fully lumped case, which was mainly because of its reduced ASE performance. In this figure, the NLI SNR contribution to the total SNR for the lumped case was also validated using the integral model using Eq. (2.49), however, results were not shown in this figure. The maximum per-channel difference obtained between closed-form expressions and the integral model was 0.76 dB at the channel located at 1612.7 nm for transmission over 100 spans. The maximum average difference obtained was 0.47 dB for transmission over 1

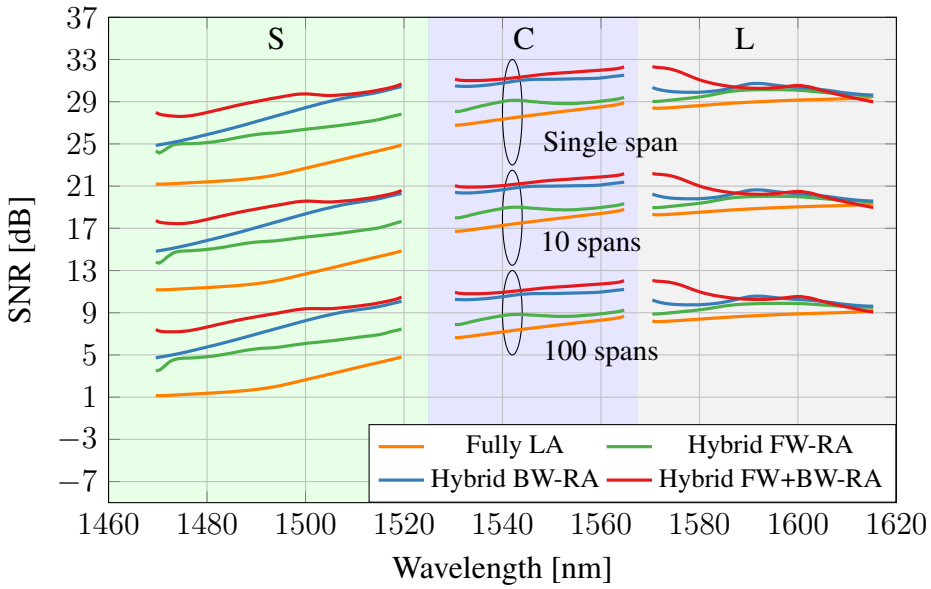

Fig. 5.23: Total SNR contribution after the 1st, 10th and 100th span for each amplification scheme.

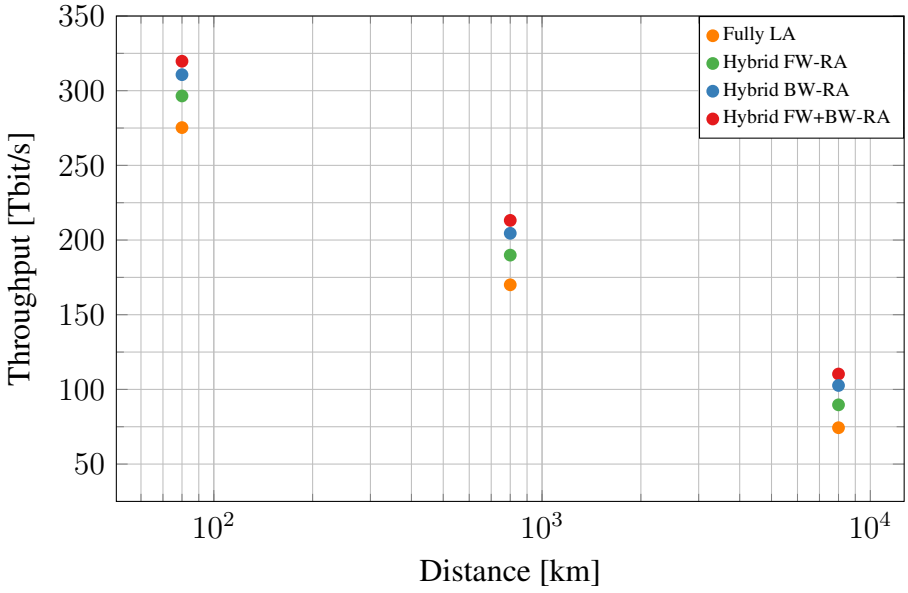

Fig. 5.24: Total throughput for different amplification schemes after 1, 10 and 100 spans.

span. Finally, the results presented in Fig. 5.23 are also shown in terms of total throughput in Fig. 5.24.

Fig. 5.24 shows the total throughput achieved in each of the amplification schemes by using Eq. (2.72). For transmission over a single span, the throughput values obtained were 319.72 Tbit/s, 310.72 Tbit/s, 296.48 Tbit/s, and 275.29 Tbit/s, respectively for the hybrid FW+BW-RA, hybrid BW-RA, hybrid FW-RA and LA. For the transmission after 10 spans, these values were respectively 213.16 Tbit/s, 204.51 Tbit/s, 189.9 Tbit/s, and 170.03 Tbit/s. Finally, for the transmission over 100 spans, these values were respectively 110.29 Tbit/s, 102.63 Tbit/s, 89.66 Tbit/s, and 74.34 Tbit/s.

5.5 Practical case study for UWB hybrid-amplified link design: MAREA submarine cable

In this section, a practical case study was considered. An optimised UWB hybrid-amplified link was designed with the same parameters as the MAREA subsea cable. The MAREA subsea cable is a high-capacity transatlantic communication cable, that stretches over 6600 km (4,000 miles) between Virginia Beach, USA, and Bilbao, Spain. This cable was originally designed to deliver an estimated throughput of 20 Tbit/s over the C-band for a single core [121, 135, 136, 137]. This throughput has been improved to approximately 30 Tbit/s during trials with advanced optical technologies.

The MAREA subsea cable was simulated in this section to operate over UWB regime, using the entire C- and L- band (10.5 THz). The goal was to understand the potential improvements in throughput for a single core, by operating the MAREA submarine cable in UWB regime using BW RA (this is typical of practical systems that use RA), where pumps are placed in the S-band, compared to using lumped amplifiers only. In [121] this cable was simulated over the entire S-, C-, and L- band using LA and per-channel launch power optimisation, where a total throughput of 161.23 Tbit/s was obtained over 18.2 THz bandwidth. In this section, similar fibre parameters were used and two optimised systems operating over 10.5 THz (C- + L-band) were compared: one operating using LA only, and another operating using hybrid-BW-distributed RA. A spectrally uniform launch power was considered for speeding up the optimisation routine for both systems. Note that, although spectrally uniform launch power profile may yield a considerable loss in performance for system operating with LA (see Sec. 5.2), for the case considered here it only yields minor performance degradation because of the relative small UWB bandwidth of 10.5 THz used (see Fig. 5.10). For the case of hybrid amplification, the performance degradation is negligible, as discussed in Sec. 5.3. The topic presented in this section was published in [P17] and presented at OFC 2024.

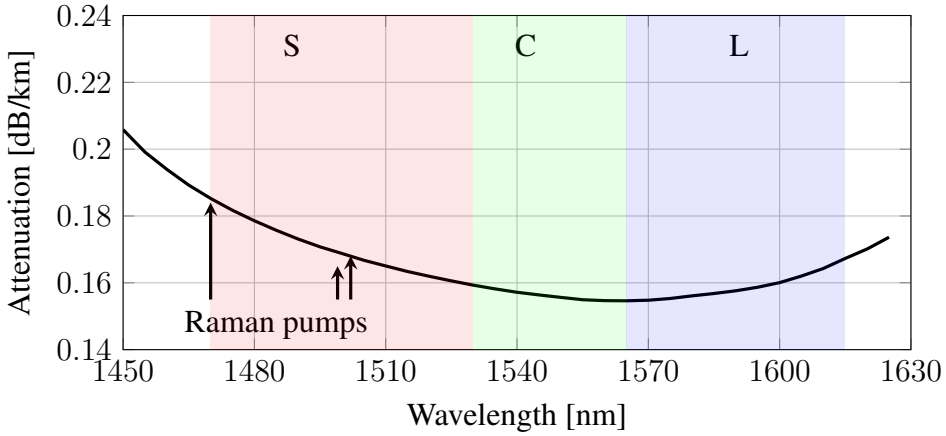

Fig. 5.25: Fibre attenuation coefficient considered to simulate the MAREA subsea cable.

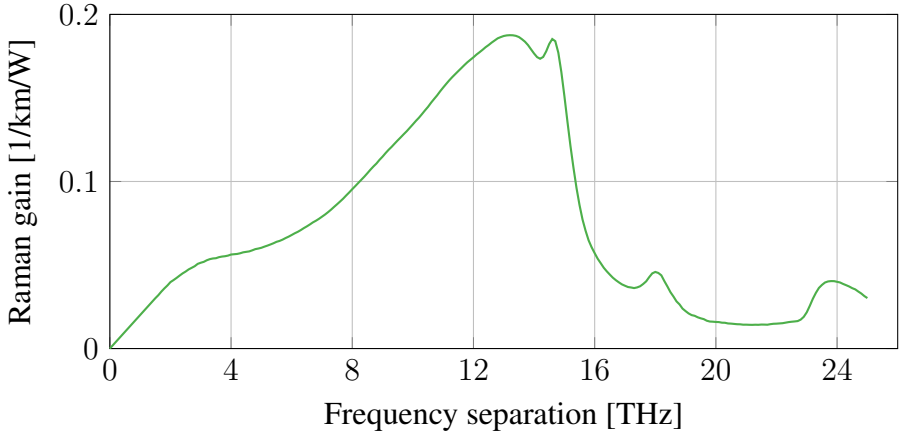

Fig. 5.26: Raman gain spectrum coefficient considered to simulate the MAREA subsea cable for a pump wavelength at 1456 nm and $A_{\text{eff}} = 150\ \mu\text{m}^2$.

5.5.1 Backward hybrid-amplified optimisation and system parameters

The transmission system was assumed to use a hybrid amplification technology, consisting of two stages: a BW-distributed Raman amplifier followed by an ideal EDFA. It was assumed to amplify a WDM signal with N_{ch}=105 Nyquist-spaced channels centred at 1571 nm, where each channel was modulated at the symbol rate of 100 GBd, with Gaussian symbols. This setup resulted in a total bandwidth of 10.5 THz, ranging from 1530 nm to 1615 nm, corresponding to the full utilisation of the C- and L- bands. The transmission system and the fibre parameters were similar (but not identical) to the MAREA subsea cable [135]. The signal transmission was evaluated over 117 x 57 km (a total distance of 6669 km). The transmission optical fibre under consideration was assumed to have wavelength-dependent attenuation and the Raman gain profile compliant with Figs. 5.25 and 5.26, and a spectrally-uniform effective area of 150 μm^2, resulting in a spectrally-uniform nonlinear coefficient

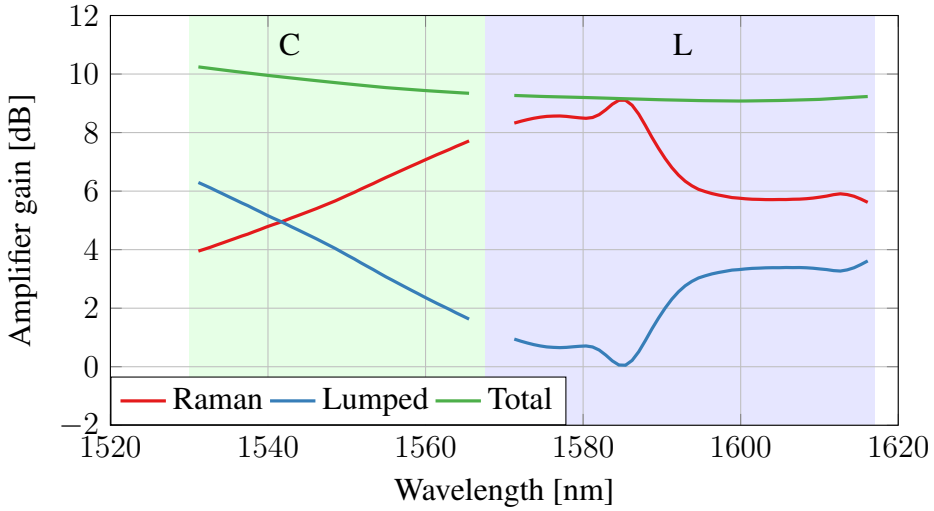

Fig. 5.27: Optimised hybrid amplifier gain for BW distributed RA stage (red) and ideal lumped / EDFA stage (blue).

$\gamma = 0.55$ W^{-1}km^{-1}. Dispersion parameters considered were $D = 21$ ps nm^{-1}km^{-1}, $S = 0.067$ ps nm^{-2}km^{-1}. The NFs of the EDFAs were assumed to be 5 dB and 6 dB, for the C- and L- bands, respectively. For the distributed RA, pumps were placed in the S-band, as shown in Fig. 5.25, and their wavelengths and powers, as well as the total transmitted launch power are optimised to maximise the system throughput.

The optimised hybrid amplifier was designed, based on a PSO algorithm (see Secs. 5.2.1. 5.3.1 and 5.4.2), where a spectrally uniform launch power profile and 6 BW pumps, limited to 500 mW each and placed in the S-band (1470 nm - 1520 nm) were considered. The total launch power and the pump wavelengths and powers were optimised to maximise the cost function in Eq. (2.72), such that the total throughput was maximised. The PSO algorithm had 7 variables to be optimised (6 pumps + total launch power). The number of particles was chosen to be 50 with a maximum of 50 iterations selected as the stopping criterion. For the algorithm bounds, total channel launch power varied between 15 dBm and 25 dBm, and the power of each pump at the end of the fibre from 0 mW to 500 mW. The optimisation resulted in a total launch power of 20.4 dBm, corresponding to 0.49 dBm per channel, and 3 pumps with non-negligible power, with wavelengths 1470 nm, 1499 nm and 1502 nm, and powers of 433 mW, 107 mW and 113 mW, respectively as shown in Fig. 5.25. The optimised hybrid amplifier gain is shown in Fig. 5.27 where the lumped/EDFA gain was assumed to be ideal to completely recover the transmitted power.

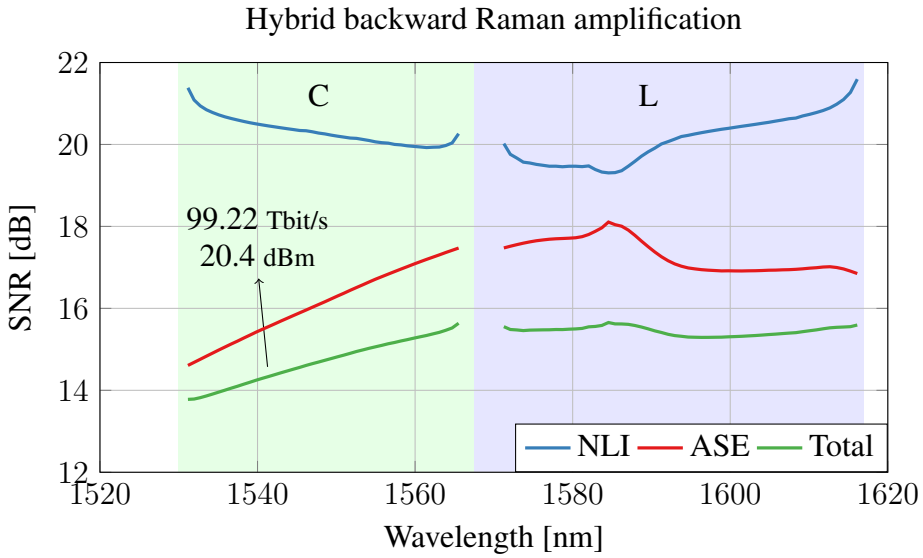

Fig. 5.28: Performance in terms of SNR for the system in Sec. 5.5.1 operating with an optimised hybrid amplification.

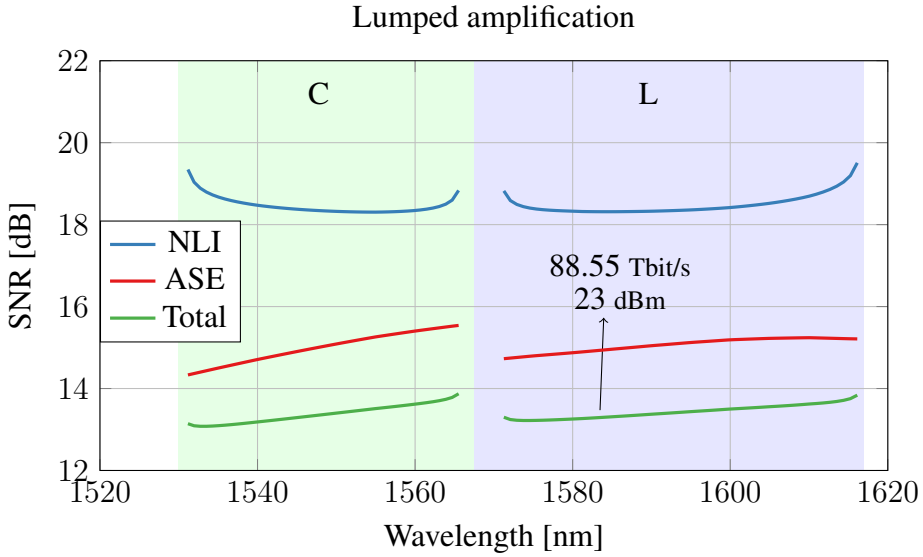

Fig. 5.29: Performance in terms of SNR for the system in Sec. 5.5.1 operating with an optimised LA.

5.5.2 Performance and throughput comparison: backward hybrid-amplified vs lumped-amplified MAREA submarine cable.

Fig. 5.28 shows the transmission system performance of the capacity-achieving hybrid amplifier in terms of SNR. The results were calculated using Eq. (4.5) and (4.4). Because the majority of Raman gain occurred at the shorter wavelengths of the L band (see Fig. 5.27), the NLI noise was worst in this region, due to the increased power levels propagating through the fibre, which reduced the $\mathrm{SNR_{NLI}}$. On the other hand, the better ASE performance of Raman amplifiers when compared to EDFA reduced the ASE noise in this same region increasing the $\mathrm{SNR_{ASE}}$; this is because for those channels almost all the fibre loss was compensated with RA, whereas in the remaining part of the spectrum, greater EDFA gain was required.

To compare the benefits of using hybrid amplification schemes, Fig. 5.29 show the performance results in terms of SNR for the same transmission system described in Sec. 5.5.1 using a fully LA scheme, i.e., without any distributed Raman pumps injected in the transmission fibre. As before, the results were calculated using Eqs. (2.57) and (2.58), and the total launch power was also optimised to maximise the throughput, resulting in a value of 23 dBm total launch power, corresponding to $P_i =$ 3.09 dBm per channel. The increased ASE noise values for this case compared to the hybrid amplification case resulted from the worse performance of EDFAs compared to Raman amplifiers in terms of NF. In the case of NLI noise, despite pump powers also being injected into the transmission fibre for the hybrid amplification case, the increased channel launch powers optimising the system with LA made this case also worse in terms of NLI noise. Indeed, with optimised hybrid amplification, a total throughput of 99.22 Tbit/s was obtained with the total channel launch power of 20.4 dBm, while for the system with optimised LA, this value was 88.55 Tbit/s with 23 dBm total launch power. Using the optimised hybrid amplifier resulted in a 12 % increase when compared to the same system operating with EDFAs only.

5.6 Network throughput maximisation

Throughout this thesis, all the analyses were carried out considering point-to-point links. This section shows an application of analytical models for optical network analysis and optimisation, enabled by the computational speed of closed-form expressions. For ease of understanding and to avoid an extensive list of variables and symbols definitions, some symbols are redefined in this section. Thus, in this section, the reader should not use the list of symbols defined for this thesis.

Optical networks form the backbone of the digital communications infrastructure and enable the transport of 100/1000s Tbit/s of data over many 100/1000s of kilometres. This currently is achieved using WDM, typically within the C-band [138].

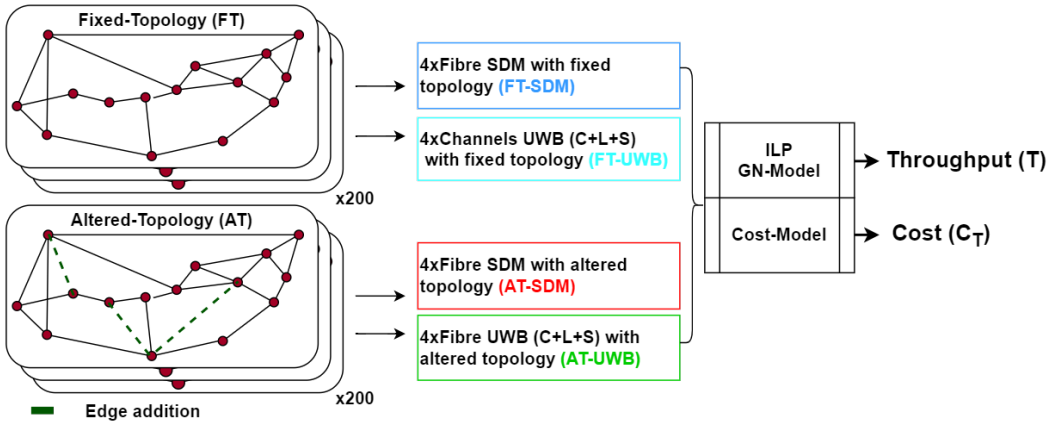

Fig. 5.30: Data generation process for fixed and altered topology scenarios.

However, with data traffic increasing each year, the capacity of conventional WDM networks is expected to be exceeded by demand, as discussed in Chapter 1. As a result, UWB transmission and/or SDM strategies are emerging as potential solutions for optical network upgrades. Despite this, network operators are reluctant to install new fibres due to the high costs involved. Therefore, it is crucial to determine how, when, and where to cost-effectively deploy new resources to meet these demands.

Previous work [139, 140, 141] compared UWB and SDM upgrades, however usually the performance was evaluated for a single topology, with sub-optimal routing heuristics to estimate the network performance. In this section, different upgrade strategies are investigated: SDM, UWB, as well as the addition of new selected network links using a genetic algorithm in parallel with either SDM or UWB. The role of network structure within the upgrade strategies, in conjunction with SDM and UWB, has not previously been evaluated, especially through the use of global optimal methods such as integer integer linear programming (ILP). The upgrade strategies were evaluated via their cost and their maximum achievable throughput using per-channel optimum launch power profile, which was enabled by the utilisation of closed-form expressions from Sec. 2.7. The topic presented in this section was published in [P16] at ECOC 2023. This work was carried out in collaboration, where network generation was performed by R. Matzner [142].

5.6.1 Network topology generation and design

In this section, 200 topologies were sampled from a geometric generative graph model, previously shown to give structures close to those observed in real core optical networks [92], using National Science Foundation Network's node locations [92]. These 200 topologies were changed using fixed topology (FT) and altered topology (AT), resulting in 400 networks.

The following scenarios were then investigated for all the generated 400 networks,

shown in Fig. 5.30: (a) FT, consisting of 200 networks where the topology remained unchanged, and only existing links were upgraded using (i) UWB (C+L+S) on every edge of the base topology, referred to as FT-UWB, or (ii) SDM deployed with multiple-fibre bundles on the base topology, referred to as FT-SDM; and (b) AT consisting of 200 networks where links were added to the FT via a genetic algorithm, with (iii) new edges added to the base topology and implemented using multiple-fibre bundles, referred to as AT-SDM, and (iv) using the same topologies as in (iii), but reducing the number of edges by deploying UWB, referred to as AT-UWB.

For all the scenarios the goal was to increase the resources by approximately a factor of 4. For FT-UWB, this was done by using C+L+S bands, generating four times the number of channels and for FT-SDM this equated to using about four times the original topology's fibre length, also giving four times the original channels. For AT-SDM/UWB three other topologies were designed for each FT via a genetic algorithm within 10% of the original total fibre length of the base topology. These were then combined to form a single SDM topology. The genetic algorithm uses a binary encoding of the topology and optimises the topology according to the demand weighted cost metric [143], previously shown to maximise throughput in networks.

The next step was to determine the routing and wavelength assignments calculated using the following integer ILP formulation. The variable $\delta_{z,k,w}$ describes whether a node-pair z, takes a path k over wavelength w, 1 if so, 0 otherwise. The variable M constrains the number of connections assigned, given some acceptable blocking rate, β, and normalised traffic matrix T_c^z.

The ILP maximises $\sum_{z\in Z}\sum_{k\in K}\sum_{w\in W}\delta_{z,k,w}$ subjected to Eq. (5.1), which constrains the allocated lightpaths (left side) to less than or equal to the requests (right side). Eq. (5.2) ensures that the number of blocked connections is smaller than or equal to the blocking rate, where $\epsilon = \lfloor \beta \cdot \sum_{z\in Z}\lceil M \cdot T_c^z \rceil \rfloor$. Both optimisations were subjected to the wavelength continuity constraint of Eq. (5.3).

$$\sum_{k\in K}\sum_{w\in W}\delta_{z,k,w} \leq \lceil M \cdot T_c^z \rceil \quad \forall z \in Z \tag{5.1}$$

$$\sum_{z\in Z}\lceil M \cdot T_c^z \rceil - \sum_{z\in Z}\sum_{k\in K}\sum_{w\in W}\delta_{z,k,w} \leq \epsilon \tag{5.2}$$

$$\sum_{z\in Z}\sum_{k\in K}\delta_{z,k,w} \cdot I(e \in k) \leq 1 \quad \forall e \in E \quad \forall w \in W \tag{5.3}$$

Using this ILP, the optimal routing and wavelength assignments for each of the 200 FTs and the 200 ATs were found. The next step was to calculate the maximum achievable throughput for each topology, using Eqs. (2.57) and (2.58) to estimate the SNR, given by Eq. (2.69), of the lightpaths allocated. A fully populated C-band (1520-1560 nm) for the SDM-based scenarios and C+L+S-band (1460-1625 nm) for the UWB

scenarios were used, with 50 GHz Nyquist-spaced channels assumed in both cases, and a uniform length of 80 km span considered for all links. Gaussian constellations were assumed. A spectrally uniform attenuation profile with $\alpha = 0.2$ dB/km was assumed. The Raman gain spectrum was assumed to be the same as the one in Fig. 3.2 with a spectrally uniform effective area of 80 μm^2. Nonlinear coefficient $\gamma = 1.21$ W^{-1}km^{-1} was assumed and dispersion parameters considered were $D = 17$ ps nm^{-1}km^{-1} and $S = 0.067$ ps nm^{-2}km^{-1}. Each span was amplified with identical EDFAs for C and L bands (NFs of 5.5 dB and 6 dB, respectively) and TDFAs for the S-band (NF of 7 dB) [144]. They were interfaced with colourless, directionless and contentionless reconfigurable optical add-drop multiplexers. For each one of the lightpaths, the SNR was calculated using the per-channel optimum launch power profile, which is calculated using the optimisation algorithm in [121] with a step size of 0.5 dB. After finding the SNR of lightpaths, the capacity was calculated using the Shannon upper bound formula and summed over all lightpaths as in Eq. (2.72).

The cost was modelled as node cost (C_i) and edge cost ($C_{i,j}$), where $i \in N$ and $(i,j) \in E$. Where $C_i = \lceil \frac{\delta_i}{\text{WSS}_n - 1} \rceil \cdot \delta_i \cdot (C_{\text{WSS}} + C_{\text{tr}})$ and $C_{i,j} = n_s \cdot (C_A + L_s \cdot C_f)$. Here δ_i is the degree of node i, WSS_n is the WSS ports, C_{WSS} is the WSS cost, C_{tr} is the transponder cost, n_s number of spans, C_A is the amplifier cost, L_s is the span length and C_f is the cost of fibre, including deployment cost. Finally, evaluating these costs with values taken from [145, 139], the costs from all nodes and edges are summed.

5.6.2 Impact of topology redesign using space and wavelength domains on network throughput

The topologies were evaluated in terms of cost (C_T) and their maximum achievable throughput (T), over different blocking probabilities (0.1-10%), and the average of the 200 topologies for each blocking rate is plotted in Figs. 5.4 and 5.32.

Fig. 5.31 shows the throughput hierarchy of the different upgrades, where FT-UWB performed worst in terms of throughput, with FT-SDM only showing a 7% marginal throughput increase. However, when altering the topology, it was possible to note a 138% and 132% increase in the mean throughput for the AT-UWB and AT-SDM scenarios over their FT counterparts.

Using the cost to normalise the throughput, the result is re-plotted in Fig. 5.32, where the hierarchy slightly changed. For the FT results, FT-SDM outperforms FT-UWB upgrades by 7%, in terms of throughput, however, with a cost increase of 205%. It is slightly less drastic for the AT, with AT-SDM outperforming the AT-UWB topologies by only 1% in terms of throughput, however costing 33% more. In each case, the throughput per unit cost increased by 260% and 67% for FT-SDM to AT-SDM and FT-UWB to AT-SDM, respectively. This shows that altering the topology structure can be cost-efficient if no dark fibres are available.

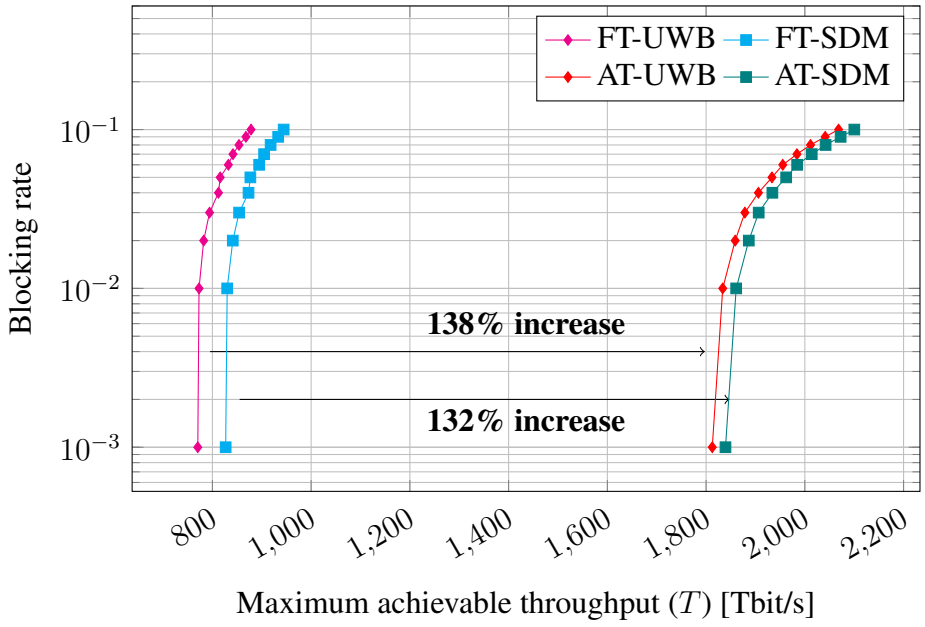

Fig. 5.31: Maximum achievable throughput values for blocking rates between 0.1% and 10%.

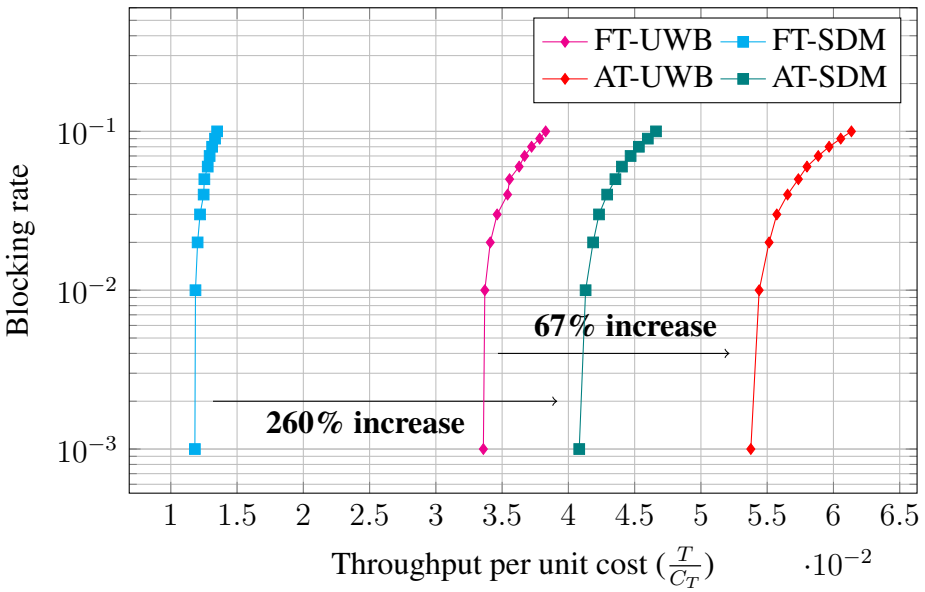

Fig. 5.32: Throughput normalised by the cost of the network for blocking rates between 0.1% and 10%.

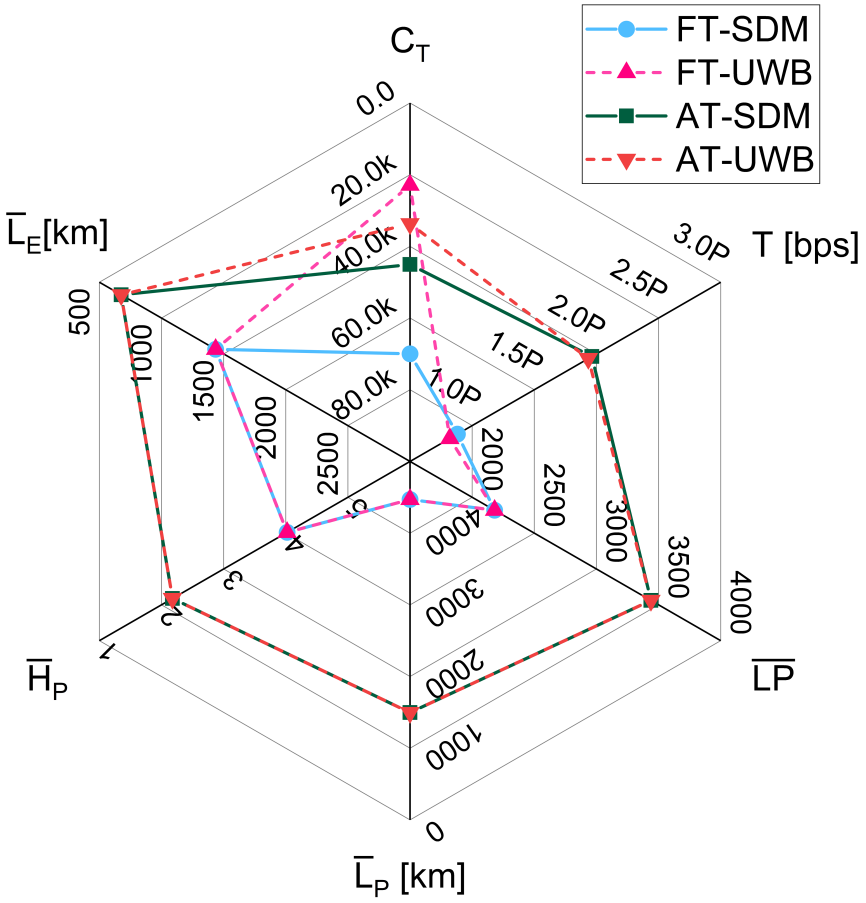

Fig. 5.33: Different network scenarios comparing network cost (C_T), maximum achievable throughput (T), number of connections allocated ($\bar{LP}$), average lightpath length ($\bar{L}_P$), average lightpath hops ($\bar{H}_P$) and average edge length ($\bar{L}_E$).

To demonstrate the impact of introducing new edges, a comparison was made among network cost, maximum achievable throughput, number of connections allocated, average length of routes taken by lightpaths, average number of hops taken by lightpaths and average edge length in Fig. 5.33. It is shown that by minimising the demand weighted cost metric via a genetic algorithm and implementing these new edges via SDM, the average edge length ($\bar{L}_E$) decreased by approximately 52%, in turn reducing the average lightpath length ($\bar{L}_P$) by 66%, with an average 45% fewer hops taken ($\bar{H}_P$), reducing the number of wavelength resources used. This translated into a 63% increase of lightpaths allocated ($\bar{LP}$), generating an increase of 132% in network throughput (T) with a 35% decrease in cost (C_T) compared to the FT-SDM topologies. Comparing the AT-UWB and FT-UWB scenarios one can see 138% higher throughput, however with an increase in cost of 47%. This was due to the new fibres deployed in the AT-UWB scenario, increasing the cost. Therefore, it is clear that if new fibres need to be deployed, altering the network's structure is hugely beneficial.

In summary, by altering the topology one can increase connectivity, and reduce route lengths and hops taken. This resulted in a higher number of allocated demands and, therefore led to increased throughput by 132% at 35% of the cost compared to keeping the same network structure. This showed that if dark fibres are not available, then upgrades via UWB and altering the network structure are better options.

5.7 Summary

In this chapter several applications of the closed-form expressions derived in chapters 2, 3 and 4 were presented. The applications included the analysis of the impact of TRX noise and launch power optimisation in lumped amplified systems; the impact of launch power optimisation in hybrid-amplified links, when RA is used with lumped amplifiers; the optimum design of hybrid amplifiers in terms of launch power, and pump wavelength and pump power; potential performance improvements for an operative submarine cable when increasing the optical bandwidth and using different amplification schemes; and cost and throughput analysis of network topology redesign by using UWB and SDM technologies.

Using the analytical modelling with the results of an experimental investigation, a characterisation of the impact of the ISRS and the TRX noise on the per-channel QoT was carried out. This investigation was extended for different system configurations, such as different span lengths, bandwidths and distances. Launch power optimisation was applied to maximise system throughput and the efficacy of this power optimisation was compared to a spectrally uniform launch power. Up to 0.9 dB gain in SNR was observed for 80 km span and 18.3 THz transmission bandwidth. For the same system configuration, a more even QoT distribution across the fibre bandwidth

was also observed; with a 2 dB improvement on the SNR variation across all transmitted channels. These values for gain in performance assumed an ideal TRX, i.e., $\mathrm{SNR}_{\mathrm{TRX}} = \infty$. However, in practical systems, any TRX will have a constrained SNR, with its upper bound determined by DAC resolution, i.e., its effective number of bits (ENOB).

Analytical modelling for the QoT estimation, combined with the global optimisation algorithms, such as PSO, provided an effective tool for studying practical transmission systems. This strategy was further used to analyse the impact of launch power optimisation for systems operating with hybrid amplifiers using 13 THz bandwidth. For these systems, per-channel launch power optimisation with optimised pump powers and wavelengths was described. Compared to using the optimum spectrally uniform launch power, an average SNR gain, w.r.t using the optimum instead of a spectrally uniform launch power profile, of 0.13 dB was obtained against 0.56 dB for the same system operating with lumped amplifiers only. It is shown that for hybrid links, per-channel launch power optimisation is not needed provided that an unconstrained number of pumps, with tunable powers and wavelengths, is available. If the hybrid system is limited in pump availability, then launch power optimisation gains are relevant and improve the system performance.

Hybrid-amplified links were also characterised showing how to achieve high capacity for these systems using analytical modelling. The analyses were done considering a system with 18.4 THz bandwidth, corresponding to the use of the S-, C- and L-bands. Scenarios ranging from short to metro, long-haul and trans-oceanic transmission systems were considered corresponding to distances of 80, 800 and 8000 km respectively. For these scenarios, the best hybrid Raman amplifier was also designed based on a PSO algorithm, where the optimised pump wavelengths and powers were calculated to maximise the total system throughput of a multi-span system, with 80 km standard SMF spans. Launch power optimisation was also carried out to maximise the performance. A comparison with an optimised fully lumped amplifier was presented showing how and why hybrid amplifiers can outperform EDFAs and TDFAs. Throughput increases of 16.17 %, 12.87 % and 7.69 % were obtained, respectively, for optimised FW + BW, BW, and FW hybrid Raman amplifiers compared to a fully lumped optimised amplifier.

These analyses were also extended to practical system configurations. The MAREA submarine cable was taken as an example and a total throughput of 99.22 Tbit/s was achieved by operating this cable over the C+L band with BW Raman amplifiers. This corresponded to a 12 % increase when compared to the same system operating with EDFAs only.

Finally, in the optical network context, performance optimisation is an interesting and challenging research topic, as realistic networking aspects, such as different span

lengths on an end-to-end connection, adding/dropping of channels, and dynamic traffic should be considered. Plus, individual links can be populated with a variable number of channels, data rates, modulation formats, and launch power profiles, given the fibre, the in-line amplifier characteristics, and the wavelength routing path. In this context, the point-to-point throughput gains analysed throughout this chapter were extended to network scenarios, i.e., the models derived in the previous chapters were also used to study the benefits of network re-design using UWB and SDM strategies. A total of 200 topologies were generated, and the resulting optimal routing configurations revealed the throughput-cost trade-offs involved in redesigning networks using these strategies.

Chapter 6

Conclusions and future work

6.1 Conclusions

In this thesis, advanced semi-analytical mathematical models of nonlinear distortions arising in fibre transmission were developed to estimate the system performance of SMFs. Because of their closed-form or semi-analytical formulation, these models can perform real-time estimations of the system QoT being suitable to design optimum system architectures, improve system operation, and quantify expected throughput gains. Two main strategies to increase the throughput of SMF optical transmission systems were explored. The first involves expanding the optical transmission bandwidth, known as UWB transmission, by using the wide low-attenuation transmission window of silica, and the second focuses on improving the channel SNR through improved amplification techniques, such as the combination of RA with LA, and the use of fibre technologies such as ULL fibres.

In chapter 2, the theory and the literature review needed to understand the work carried out during this PhD research was presented. Closed-form nonlinear models valid for UWB transmission were presented in this chapter. These models account for the ISRS effect, a nonlinear effect that impairs the transmitted signal when expanding the optical bandwidth beyond the C-band. Nevertheless, the models presented in this chapter are constrained to the use of LA and do not capture the intricate physics associated with Raman amplifiers, which is fundamental for increasing the throughput of next-generation optical fibre transmission systems. Additionally, they are limited to specific span lengths and fibre attenuation coefficients.

The first UWB semi-analytical model constrained to LA but able to account for arbitrary span length and fibre losses were presented in Chapter 3. In addition to currently deployed fibres, the model can estimate the performance of new low-loss fibre technologies, such as ULL fibres and hollow core fibres. It can also estimate the performance of arbitrary link lengths, ranging from submarine links to very short-reach links such as fibres connecting data centres. The model was validated over a total bandwidth of 20 THz occupying the S-, C-, and L- bands. A good agreement was found between the proposed closed-form model and its numerical version for a

variety of scenarios considered. Because of its computational speed, the proposed formula enables accurate inline NLI estimation of any portion of the optical fibre link, representing an essential step towards the development of intelligent and dynamic optical fibre networks, enabling effective network planning tools.

However, the models described in Chapters 2 and 3 are not able to account for hybrid-amplified links, where Raman amplifiers are used in combination with lumped amplifiers such as EDFAs and TDFAs. In Chapter 4, the first UWB semi-analytical model valid for arbitrary hybrid-amplified links was developed. Among the general characteristics of this model, it accounts for the ISRS effect, FW and BW pumping schemes, arbitrary number of pumps, wavelength-dependent fibre parameters and launch power profiles. The model was validated over 13 THz and 20 THz optical bandwidth corresponding to transmission over the S-, C-, and L- bands and using a variety of pump configurations, modulation formats and launch power profiles. The proposed closed-form model was validated by numerical simulations showing good agreement for most of the simulated scenarios. The complex physics of Raman-amplified links makes it challenging to determine the optimal launch power, pump power and pump wavelength allocation that maximises a desired system metric. However, the real-time performance estimation enabled by the proposed closed-form expression allows for the exploration of these various characteristics of hybrid-amplified systems, including the optimisation of pumps and launch power to achieve the best system performance metric under interest, such as maximum throughput.

In Chapter 5 the characteristics were explored by applying these models to practical system scenarios. The formulae were used for throughput maximisation by incorporating them into optimisation algorithms such as PSO algorithm, enabling real-time calculations. Firstly, the impact of launch power optimisation, ISRS and TRX on the per-channel QoT is evaluated for the system operating with LA. It was found that launch power optimisation gains change considerably with system bandwidth and span length and these gains are strongly dependent on the TRX noise. For an ideal TRX, up to 0.9 dB gain in SNR was observed for 80 km span and 18.3 THz transmission bandwidth, and a 2 dB improvement on the SNR variation across all transmitted channels. This approach was also applied to assess the impact of launch power optimisation in systems operating with hybrid amplifiers over a 13 THz bandwidth, where it was found that pump power and wavelength optimisation can compensate for almost all the power fluctuations induced by the combination of Raman, ISRS and wavelength-depend fibre parameters, and per-channel launch power optimisation is not needed, provided that unconstrained number of pumps, with tunable powers and wavelengths, is available.

These algorithms were further used for hybrid-amplified link optimisation, where

Raman pumps and launch power were optimised to maximise the system throughput. This was done by finding the best pump allocation, i.e., the number of pumps, their power and wavelength, and their direction (FW and/or BW). It was shown a hybrid FW + BW Raman amplifier achieving 319.82 Tbit/s over a single 80 km span transmission and 18.4 THz optical bandwidth, a hybrid BW Raman amplifier achieving 310.72 Tbit/s, and a hybrid FW Raman amplifier achieving 296.48 Tbit/s, both over the same system. These values represent increases over a fully lumped optimised amplifier system with a maximum throughput of 275.29 Tbit/s, under the same conditions. The model was validated and a maximum average discrepancy of 0.47 dB was found against integral simulations. Additionally, the model was also used to simulate a hypothetical scenario of a hybrid-BW-amplified submarine cable using C+L band over 6669 km. It was shown a performance with a total throughput of 99.22 Tbit/s against to 88.55 Tbit/s for the same system operating with EDFAs only.

Finally, these models were used to study the benefits of network re-design, where a comprehensive study of 200 generated topologies and optimal routings was performed with UWB and SDM architectures. For each of these topologies, the per-channel optimum launch power was calculated enabled by the speed of computation of these models. The study highlighted the throughput-cost trade-offs associated with re-designing networks incorporating both technologies, illustrating scenarios where using SDM outperforms UWB and vice versa.

In conclusion, the research described in this thesis resulted in new real-time mathematical models and significant contributions to modelling of nonlinear distortions in UWB optical fibre systems operating with lumped and Raman amplifiers. The findings enable an understanding of the potentials and limitations of next-generation high-capacity optical transmission systems, helping to pave the way for future system design and optimisation. More importantly, the proposed models lay the groundwork for developing optimal system designs, optimisation strategies, and advanced system architectures for UWB optical networks operating in nonlinear regimes with different types of amplification and fibre technologies. These advancements are crucial for further enhancing the capacity of new and already deployed optical fibre systems, essential to meeting the unprecedented data throughput demands of contemporary society.

6.2 Future work

6.2.1 NLI induced by pump-signal and pump in the COI

In the closed-form expressions derived in Chapter 4, the NLI contributions considered for calculation of the COI NLI SNR were the SPM generated by the COI and XPM generated by the remaining WDM spectra (FWM effects were neglected). The XPM-

and FWM- induced products from pumps alone, or pumps interacting with signal spectral lines falling into the WDM spectrum were also neglected. This approach is valid when placing pumps far away from the transmitted channels. However, when placing pumps close to the WDM spectra or even in the middle of it, these contributions may be the main limiting factor of the system performance. This analysis is fundamental to be carried out if one has an interest in placing pumps in any part of the WDM signal spectra and understand its impact on the total system performance.

6.2.2 O- and OESCLU- band transmission using LA or hybrid amplification

The closed-form models in Chapters 2, 3 and 4 considers only SPM generated by the COI and XPM generated by the remaining WDM spectra. This approach is accurate for transmission over standard SMF using ESCLU- band, where fibre dispersion is high. However, when moving to the O- band where dispersion values are low or even zero, FWM contributions must be considered as these contributions have a substantial effect on the system performance. To make the closed-form expressions of this thesis valid for O- band and thus be able to simulate OESCLU- band transmission, FWM contributions must be included. A recent work in this direction can be found in [146]. Further research should also be done to validate the GN model for close-to-zero dispersion regimes.

6.2.3 Impact of TRX noise in hybrid-amplified links

In chapter 5, the analysis of TRX noise in the signal transmission was analysed for lumped-amplified links. This analysis has not yet been characterised for hybrid-amplified links. The importance of this analysis relies on understanding the necessity of optimising launch power, pump wavelength and power for constrained-TRX systems. These optimisations are costly in terms of computational complexity and require expensive shaping components. It is expected that the TRX noise reduces the gains in performance achieved by launch power and pump optimisation. Thus, analysing the interplay between TRX noise, pump power, pump wavelength, and launch power is important, as it provides valuable insights for cost reduction and optimised system design.

6.2.4 Network optimisation using closed-form models

While most of the analysis carried out in this thesis was done for point-to-point links, the speed of computation of closed-form models derived in Chapters 2, 3 and 4 enable their utilisation for network optimisation proposes. These models can be used for both lumped- and hybrid-amplified links, in a network context by considering variable characteristics for individual links, such as numbers of channels, data rates,

modulation formats, launch power profiles, span lengths on an end-to-end connection, fibre parameters, in-line amplifier characteristics, wavelength routing paths, and dynamic traffics. An example of such analysis was done in Chapter 5 for lumped-amplified links.

6.2.5 New strategies for fitting optimisation routine for UWB closed-form expressions

The closed-form formulae derived in Chapters 2, 3 and the one in Chapter 4 use a fitting optimisation routine to semi-analytically reproduce the signal power profile evolution over the fibre length, obtained by solving the coupled Raman equations. This is a fundamental step for closed-form expressions accounting for RA and operating in UWB regimes. It is important to note that most of the speed of computation of these models comes from this fitting optimisation. In this thesis, the fitting optimisation routine was performed using simple optimisation algorithms, such as nonlinear least-squares fitting. Another direction of research is to implement more sophisticated optimisation routines, such as the use of machine learning algorithms to predict these power profiles, speeding up the computational time and improving the accuracy of these models. Recent work in this direction can be found in [147].

6.2.6 Impact of RA in the ASE noise generated by EDFAs and TDFAs

The ASE generation for LA shown in Chapter 2, assumes that the EDFAs/TDFAs are operating in the small-signal gain regime, such that the input power is low enough that the gain remains relatively constant, and is not affected by variations in input signal power. In reality, the EDFAs/TDFAs characteristics, such as its NF and ASE generation, change if the input power is high. This is particularly the case for hybrid-amplified links, where after RA, the input signal to the EDFAs/TDFAs may not be low enough to neglect these variations. Thus, an important research direction is to include these variations in a EDFA/TDFA model to accurately reproduce the ASE noise generated in hybrid-amplified links.

Bibliography

[1] ITU. ITU-D ICT statistics. https://www.itu.int/en/ITU-D/Statistics/Pages/stat/default.aspx (2023). Accessed: 01/10/2024.

[2] Ericsson. Mobile data traffic outlook. https://www.ericsson.com/en/reports-and-papers/mobility-report/dataforecasts/mobile-traffic-forecast (2023). Accessed: 01/10/2024.

[3] Puttnam, B. J. *et al.* 402-Tb/s GMI data-rate OESCLU-band transmission. In *Optical Fiber Communications Conference and Exhibition (OFC)* (IEEE, 2024).

[4] Puttnam, B. J., Luís, R. S., Huang, Y., Phillips, I., Chung, D., Fontaine, N. K., Rademacher, G., Mazur, M., Dallachiesa, L., Chen, H., Forysiak, W., Man, R., Ryf, R., Neilson, D. T. and Furukawa, H. 301 Tb/s E, S, C+L-band transmission over 212 nm bandwidth with E-band Bismuth-doped fiber amplifier and gain equalizer. In *European Conference on Optical Communication (ECOC)* (2023).

[5] Puttnam, B. J., Luís, R. S., Huang, Y., Phillips, I., Chung, D., K. Fontaine, N., Boriboon, B., Rademacher, G., Mazur, M., Dallachiesa, L., Chen, H., Forysiak, W., Man, R., Ryf, R., T. Neilson, D. and Furukawa, H. 264.7-Tb/s E+S+C+L-band transmission over 200 km. In *Optical Fiber Communications Conference and Exhibition (OFC)* (IEEE, 2024).

[6] Puttnam, B. J., Luís, R. S., Rademacher, G., Mendez-Astudillio, M., Awaji, Y. and Furukawa, H. S-, C- and L-band transmission over a 157nm bandwidth using doped fiber and distributed Raman amplification. *Opt. Express* **30**, 10011–10018 (2022). URL https://opg.optica.org/oe/abstract.cfm?URI=oe-30-6-10011.

[7] He, Q., Ge, D., Luo, M., Zhang, X., Wu, Y., Mei, L., Du, P., Wang, D., Zhang, H., Li, H. and Xiao, X. 150.27-Tb/s capacity over 150-km in S+C+L band using 156-channel 115-GBaud signals with doped fiber amplification. In *Optical Fiber Communications Conference and Exhibition (OFC)* (IEEE, 2024).

[8] Hamaoka, F., Nakamura, M., Takahashi, M., Kobayashi, T., Miyamoto, Y. and Kisaka, Y. 173.7-Tb/s triple-band WDM transmission using 124-channel 144-

GBaud signals with SE of 9.33 b/s/Hz. In *Optical Fiber Communications Conference and Exhibition (OFC)* (IEEE, 2023).

[9] Hamaoka, F., Nakamura, M., Sasai, T., Sugawara, S., Kobayashi, T., Miyamoto, Y. and Yamazaki, E. 110.7-Tb/s single-mode-fiber transmission over 1040 km with high-symbol-rate 144-GBaud PDM-PCS-QAM signals. In *Optical Fiber Communications Conference and Exhibition (OFC)* (IEEE, 2024).

[10] Puttnam, B. J., Luís, R. S., Rademacher, G., Mendez-Astudilio, M., Awaji, Y. and Furukawa, H. S, C and extended L-band transmission with doped fiber and distributed Raman amplification. *Optical Fiber Communication Conference (OFC)* Th4C.2 (2021). URL `http://www.osapublishing.org/abstract.cfm?URI=OFC-2021-Th4C.2`.

[11] Galdino, L., Edwards, A., Yi, W., Sillekens, E., Wakayama, Y., Gerard, T., Pelouch, W. S., Barnes, S., Tsuritani, T., Killey, R. I. *et al.* Optical fibre capacity optimisation via continuous bandwidth amplification and geometric shaping. *IEEE Photonics Technology Letters* **32**, 1021–1024 (2020).

[12] Zhao, X. and et. al. 200.5 Tb/s transmission with S+C+L amplification covering 150 nm bandwidth over 2×100 km PSCF spans. *European Conference on Optical Communication (ECOC)* Th3C.4 (2022).

[13] Yang, J., Aparecido, R., Buglia, H., Hazarika, P., Sillekens, E., Sohanpal, R., Tan, M., Pratiwi, D., S. Luis, R., J. Puttnam, B., Wakayama, Y., Forysiak, W., Bayvel, P. and I. Killey, R. 122.6-Tb/s S+C+L band unrepeated transmission over 223 km link with optimised bidirectional Raman amplication. In *Optical Fiber Communications Conference and Exhibition (OFC)* (IEEE, 2024).

[14] Puttnam, B. J., Luis, R. S., Rademacher, G., Awaji, Y. and Furukawa, H. Investigation of long-haul S-, C- + L-band transmission. In *Optical Fiber Communications Conference and Exhibition (OFC)* (2022).

[15] Hamaoka, F., Nakamura, M., Okamoto, S., Minoguchi, K., Sasai, T., Matsushita, A., Yamazaki, E. and Kisaka, Y. Ultra-wideband WDM transmission in S-, C-, and L-bands using signal power optimization scheme. *Journal of Lightwave Technology* **37**, 1764–1771 (2019).

[16] Renaudier, J., Arnould, A., Gac, D. L., Ghazisaeidi, A., Brindel, P., Makhsiyan, M., Verdier, A., Mekhazni, K., Blache, F., Debregeas, H., Boutin, A., Fontaine, N., Neilson, D., Ryf, R., Chen, H., Achouche, M. and Charlet, G. 107 Tb/s transmission of 103-nm bandwidth over 3×100 km SSMF using ultra-wideband

hybrid Raman/SOA repeaters. *Optical Fiber Communication Conference (OFC)* Tu3F.2 (2019).

[17] Renaudier, J., Meseguer, A. C., Ghazisaeidi, A., Tran, P., Muller, R. R., Brenot, R., Verdier, A., Blache, F., Mekhazni, K., Duval, B., Debregeas, H., Achouche, M., Boutin, A., Morin, F., Letteron, L., Fontaine, N., Frignac, Y. and Charlet, G. First 100-nm continuous-band WDM transmission system with 115Tb/s transport over 100km using novel ultra-wideband semiconductor optical amplifiers. In *European Conference on Optical Communication (ECOC)* (2017).

[18] Ghazisaeidi, A., Arnould, A., Ionescu, M., Aref, V., Mardoyan, H., Etienne, S., Duval, M., Bastide, C., Bissessur, H. and Renaudier, J. 99.35 Tb/s ultra-wideband unrepeated transmission over 257 km using semiconductor optical amplifiers and distributed Raman amplification. *Journal of Lightwave Technology* **40**, 7014–7019 (2022).

[19] Galdino, L., Semrau, D., Ionescu, M., Edwards, A., Pelouch, W., Desbruslais, S., James, J., Sillekens, E., Lavery, D., Barnes, S., Killey, R. I. and Bayvel, P. Study on the impact of nonlinearity and noise on the performance of high-capacity broadband hybrid Raman-EDFA amplified system. *Journal of Lightwave Technology* **37**, 5507–5515 (2019).

[20] Ionescu, M., Lavery, D., Edwards, A., Sillekens, E., Semrau, D., Galdino, L., Killey, R. I., Pelouch, W., Barnes, S. and Bayvel, P. 74.38 Tb/s transmission over 6300 km single mode fibre enabled by C+L amplification and geometrically shaped PDM-64QAM. *Journal of Lightwave Technology* **38**, 531–537 (2020).

[21] Shannon, C. E. A mathematical theory of communication. *ACM SIGMOBILE mobile computing and communications review* **5**, 3–55 (2001).

[22] Agrawal, G. *Nonlinear Fiber Optics*. Optics and Photonics (Elsevier Science, 2013). URL `https://books.google.co.uk/books?id=xNvw-GDVn84C`.

[23] Turitsyn, S. K., Prilepsky, J. E., Le, S. T., Wahls, S., Frumin, L. L., Kamalian, M. and Derevyanko, S. A. Nonlinear Fourier transform for optical data processing and transmission: advances and perspectives. *Optica* **4**, 307–322 (2017). URL `http://opg.optica.org/optica/abstract.cfm?URI=optica-4-3-307`.

[24] Vasylchenkova, A., Prilepsky, J., Shepelsky, D. and Chattopadhyay, A. Direct nonlinear Fourier transform algorithms for the computation of solitonic spectra in focusing nonlinear Schrödinger equation. *Communications in*

Nonlinear Science and Numerical Simulation **68**, 347–371 (2019). URL https://www.sciencedirect.com/science/article/pii/S1007570418302855.

[25] Vannucci, A., Serena, P. and Bononi, A. The RP method: a new tool for the iterative solution of the nonlinear Schrodinger equation. *Journal of Lightwave Technology* **20**, 1102–1112 (2002).

[26] Bosco, G., Poggiolini, P., Carena, A., Curri, V. and Forghieri, F. Analytical results on channel capacity in uncompensated optical links with coherent detection. *Opt. Express* **19**, B440–B451 (2011). URL http://opg.optica.org/oe/abstract.cfm?URI=oe-19-26-B440.

[27] Poggiolini, P. The GN model of non-linear propagation in uncompensated coherent optical systems. *Journal of Lightwave Technology* **30**, 3857–3879 (2012).

[28] Carena, A., Bosco, G., Curri, V., Jiang, Y., Poggiolini, P. and Forghieri, F. EGN model of non-linear fiber propagation. *Opt. Express* **22**, 16335–16362 (2014). URL http://opg.optica.org/oe/abstract.cfm?URI=oe-22-13-16335.

[29] Mecozzi, A. and Essiambre, R.-J. Nonlinear Shannon limit in pseudolinear coherent systems. *Journal of Lightwave Technology* **30**, 2011–2024 (2012).

[30] Forestieri, E. and Secondini, M. Solving the nonlinear Schrödinger equation. In *Optical Communication Theory and Techniques*, 3–11 (Springer, 2005).

[31] Oliari, V., Agrell, E. and Alvarado, A. Regular perturbation on the group-velocity dispersion parameter for nonlinear fibre-optical communications. *Nature Communications* **11** (2020).

[32] Forney, G. and Ungerboeck, G. Modulation and coding for linear Gaussian channels. *IEEE Transactions on Information Theory* **44**, 2384–2415 (1998).

[33] Semrau, D., Killey, R. I. and Bayvel, P. The Gaussian noise model in the presence of inter-channel stimulated Raman scattering. *Journal of Lightwave Technology* **36**, 3046–3055 (2018).

[34] Poggiolini, P., Zefreh, M. R., Bosco, G., Forghieri, F. and Piciaccia, S. Accurate non-linearity fully-closed-form formula based on the GN/EGN model and large-data-set fitting. In *Optical Fiber Communications Conference and Exhibition (OFC)*, 1–3 (2019).

[35] Semrau, D., Killey, R. I. and Bayvel, P. A closed-form approximation of the Gaussian noise model in the presence of inter-channel stimulated Raman scattering. *Journal of Lightwave Technology* **37**, 1924–1936 (2019).

[36] Ranjbar Zefreh, M., Forghieri, F., Piciaccia, S. and Poggiolini, P. Accurate closed-form real-time EGN model formula leveraging machine-learning over 8500 thoroughly randomized full C-band systems. *Journal of Lightwave Technology* **38**, 4987–4999 (2020).

[37] Semrau, D., Sillekens, E., Killey, R. I. and Bayvel, P. A modulation format correction formula for the Gaussian noise model in the presence of inter-channel stimulated Raman scattering. *Journal of Lightwave Technology* **37**, 5122–5131 (2019).

[38] Zefreh, M. R. and Poggiolini, P. A real-time closed-form model for nonlinearity modeling in ultra-wide-band optical fiber links accounting for inter-channel stimulated Raman scattering and co-propagating Raman amplification (2020). arXiv:2006.03088[eess.SP].

[39] Kani, J., Hattori, K., Jinno, M., Kanamori, T. and Oguchi, K. Triple-wavelength-band WDM transmission over cascaded dispersion-shifted fibers. *IEEE Photonics Technology Letters* **11**, 1506–1508 (1999).

[40] Hoshida, T., Terahara, T., Kumasako, J. and Onaka, H. Optical SNR degradation due to stimulated Raman scattering in dual-band WDM transmission systems and its compensation by optical level management. *Fifth Asia-Pacific... and Fourth Optoelectronics and Communications Conference on Communications* **1**, 342–345 (1999).

[41] Krummrich, P., Gottwald, E., Mayer, A., Weiske, C.-J. and Fischer, G. Influence of stimulated Raman scattering on the channel power balance in bidirectional WDM transmission. *Optical Fiber Communication Conference (OFC), and the International Conference on Integrated Optics and Optical Fiber Communication (IOOC)* **2**, 171–173 (1999).

[42] Ip, E., Lau, A. P. T., Barros, D. J. F. and Kahn, J. M. Coherent detection in optical fiber systems. *Opt. Express* **16**, 753–791 (2008). URL https://opg.optica.org/oe/abstract.cfm?URI=oe-16-2-753.

[43] Savory, S. J. Digital filters for coherent optical receivers. *Opt. Express* **16**, 804–817 (2008). URL https://opg.optica.org/oe/abstract.cfm?URI=oe-16-2-804.

[44] Poggiolini, P., Bosco, G., Carena, A., Curri, V., Jiang, Y. and Forghieri, F. The GN-model of fiber non-linear propagation and its applications. *Journal of Lightwave Technology* **32**, 694–721 (2014).

[45] Sillekens, E., Liga, G., Lavery, D., Bayvel, P. and Killey, R. I. High-cardinality geometrical constellation shaping for the nonlinear fibre channel. *Journal of Lightwave Technology* **40**, 6374–6387 (2022).

[46] Secondini, M. Chapter 20 - information capacity of optical channels. In Willner, A. E. (ed.) *Optical Fiber Telecommunications VII* (Academic Press, 2020). URL `https://www.sciencedirect.com/science/article/pii/B9780128165027000233`.

[47] Agrell, E. and Karlsson, M. Influence of behavioral models on multiuser channel capacity. *Journal of Lightwave Technology* **33**, 3507–3515 (2015).

[48] Secondini, M. and Forestieri, E. Analytical fiber-optic channel model in the presence of cross-phase modulation. *IEEE Photonics Technology Letters* **24**, 2016–2019 (2012).

[49] Secondini, M. and Forestieri, E. Scope and limitations of the nonlinear Shannon limit. *Journal of Lightwave Technology* **35**, 893–902 (2017).

[50] Secondini, M., Agrell, E., Forestieri, E. and Marsella, D. Fiber nonlinearity mitigation in WDM systems: Strategies and achievable rates. In *European Conference on Optical Communication (ECOC)*, 1–3 (2017).

[51] Liga, G., Alvarado, A., Agrell, E., Secondini, M., Killey, R. I. and Bayvel, P. Optimum detection in presence of nonlinear distortions with memory. In *European Conference on Optical Communication (ECOC)*, 1–3 (2015).

[52] García-Gómez, F. J. and Kramer, G. Mismatched models to lower bound the capacity of dual-polarization optical fiber channels. *J. Lightwave Technol.* **39**, 3390–3399 (2021). URL `https://opg.optica.org/jlt/abstract.cfm?URI=jlt-39-11-3390`.

[53] Semrau, D., Sillekens, E., Killey, R. I. and Bayvel, P. Modelling the delayed nonlinear fiber response in coherent optical communications. *Journal of Lightwave Technology* **39**, 1937–1952 (2021).

[54] Blow, K. and Wood, D. Theoretical description of transient stimulated Raman scattering in optical fibers. *IEEE Journal of Quantum Electronics* **25**, 2665–2673 (1989).

[55] Makovejs, S., Roberts, C. C., Palacios, F., Matthews, H. B., Lewis, D. A., Smith, D. T., Diehl, P. G., Johnson, J. J., Patterson, J. D., Towery, C. R. and Ten, S. Y. Record-low (0.1460 dB/km) attenuation ultra-large Aeff optical fiber for submarine applications. In *Optical Fiber Communication Conference Post Deadline Papers*, Th5A.2 (Optica Publishing Group, 2015). URL `https://opg.optica.org/abstract.cfm?URI=OFC-2015-Th5A.2`.

[56] Chen, Y., Petrovich, M., Fokoua, E. N., Adamu, A., Hassan, M., Sakr, H., Slavík, R., Gorajoobi, S. B., Alonso, M., Ando, R. F., Papadimopoulos, A., Varghese, T., Wu, D., Ando, M. F., Wisniowski, K., Sandoghchi, S., Jasion, G., Richardson, D. and Poletti, F. Hollow core dnanf optical fiber with <0.11 dB/km loss. In *Optical Fiber Communication Conference (OFC) 2024*, Th4A.8 (Optica Publishing Group, 2024). URL `https://opg.optica.org/abstract.cfm?URI=OFC-2024-Th4A.8`.

[57] ITU. ITU-D G.652 Recommendation. `https://www.itu.int/rec/T-REC-G.652-202408-P/en` (2024). Accessed: 01/10/2024.

[58] D'Amico, A., Correia, B., London, E., Virgillito, E., Borraccini, G., Napoli, A. and Curri, V. Scalable and disaggregated GGN approximation applied to a C+L+S optical network. *Journal of Lightwave Technology* **40**, 3499–3511 (2022).

[59] Mukasa, K., Imamura, K., Shimotakahara, I. and et al. Dispersion compensating fiber used as a transmission fiber: inverse/reverse dispersion fiber. *J Optic Comm Rep 3* 292–339 (2006).

[60] Jarmolovičius, M., Semrau, D., Buglia, H., Shevchenko, M., Ferreira, F. M., Sillekens, E., Bayvel, P. and Killey, R. I. Optimising O-to-U band transmission using fast ISRS Gaussian noise numerical integral model. *Journal of Lightwave Technology* 1–8 (2024).

[61] Poggiolini, P. and Ranjbar-Zefreh, M. Closed form expressions of the nonlinear interference for UWB systems. In *European Conference on Optical Communication (ECOC)* (2022).

[62] Sinkin, O., Holzlohner, R., Zweck, J. and Menyuk, C. Optimization of the split-step Fourier method in modeling optical-fiber communications systems. *Journal of Lightwave Technology* **21**, 61–68 (2003).

[63] Alvarado, A., Fehenberger, T., Chen, B. and Willems, F. M. J. Achievable information rates for fiber optics: Applications and computations. *Journal of Lightwave Technology* **36**, 424–439 (2018).

[64] Xu, B. and Brandt-Pearce, M. Comparison of FWM- and XPM-induced crosstalk using the Volterra series transfer function method. *Journal of Lightwave Technology* **21**, 40–53 (2003).

[65] Tang, J. A comparison study of the Shannon channel capacity of various nonlinear optical fibers. *Journal of Lightwave Technology* **24**, 2070–2075 (2006).

[66] Dar, R., Feder, M., Mecozzi, A. and Shtaif, M. Properties of nonlinear noise in long, dispersion-uncompensated fiber links. *Opt. Express* **21**, 25685–25699 (2013). URL `https://opg.optica.org/oe/abstract.cfm?URI=oe-21-22-25685`.

[67] Poggiolini, P. and Jiang, Y. Recent advances in the modeling of the impact of nonlinear fiber propagation effects on uncompensated coherent transmission systems. *Journal of Lightwave Technology* **35**, 458–480 (2017).

[68] Splett, A., Kurtzke, C. and Petermann, K. Ultimate transmission capacity of amplified optical fiber communication systems taking into account fiber nonlinearities. In *European Conference on Optical Communication (ECOC)* (1993).

[69] Vacondio, F., Rival, O., Simonneau, C., Grellier, E., Bononi, A., Lorcy, L., Antona, J.-C. and Bigo, S. On nonlinear distortions of highly dispersive optical coherent systems. *Opt. Express* **20**, 1022–1032 (2012). URL `https://opg.optica.org/oe/abstract.cfm?URI=oe-20-2-1022`.

[70] Cantono, M., Pilori, D., Ferrari, A., Catanese, C., Thouras, J., Augé, J.-L. and Curri, V. On the interplay of nonlinear interference generation with stimulated Raman scattering for QoT estimation. *Journal of Lightwave Technology* **36**, 3131–3141 (2018).

[71] Bosco, G. Complexity versus accuracy tradeoffs in nonlinear fiber propagation models. *Optical Fiber Conference (OFC)* (2023).

[72] Arpanaei, F., Zefreh, M. R., Hernandez, J. A., Carena, A. and Larrabeiti, D. Link and network-wide study of incoherent GN/EGN models. In *European Conference on Optical Communication (ECOC) 2022*, We1A.3 (Optica Publishing Group, 2022). URL `https://opg.optica.org/abstract.cfm?URI=ECEOC-2022-We1A.3`.

[73] Fludger, C., Handerek, V. and Mears, R. Pump to signal RIN transfer in Raman fiber amplifiers. *Journal of Lightwave Technology* **19**, 1140–1148 (2001).

[74] Bromage, J. Raman amplification for fiber communications systems. *J. Lightwave Technol.* **22**, 79 (2004). URL `https://opg.optica.org/jlt/abstract.cfm?URI=jlt-22-1-79`.

[75] Buglia, H., Sillekens, E., Vasylchenkova, A., Yi, W., Killey, R., Bayvel, P. and Galdino, L. Challenges in extending optical fibre transmission bandwidth beyond C+L band and how to get there. In *2021 International Conference on Optical Network Design and Modeling (ONDM)*, 1–4 (2021).

[76] Sillekens, E., Semrau, D., Liga, G., Shevchenko, N. A., Li, Z., Alvarado, A., Bayvel, P., Killey, R. I. and Lavery, D. A simple nonlinearity-tailored probabilistic shaping distribution for square QAM. In *Optical Fiber Communications Conference and Exposition (OFC)*, 1–3 (2018).

[77] Ghazisaeidi, A. A theory of nonlinear interactions between signal and amplified spontaneous emission noise in coherent wavelength division multiplexed systems. *Journal of Lightwave Technology* **35**, 5150–5175 (2017).

[78] Essiambre, R.-J., Kramer, G., Winzer, P. J., Foschini, G. J. and Goebel, B. Capacity limits of optical fiber networks. *Journal of Lightwave Technology* **28**, 662–701 (2010).

[79] Secondini, M., Civelli, S., Forestieri, E. and Khan, L. Z. New lower bounds on the capacity of optical fiber channels via optimized shaping and detection. *Journal of Lightwave Technology* **40**, 3197–3209 (2022).

[80] Agrell, E. Conditions for a monotonic channel capacity. *IEEE Transactions on Communications* **63**, 738–748 (2015).

[81] Ip, E. and Kahn, J. M. Compensation of dispersion and nonlinear impairments using digital backpropagation. *Journal of Lightwave Technology* **26**, 3416–3425 (2008).

[82] Buglia, H., Sillekens, E., Vasylchenkova, A., Bayvel, P. and Galdino, L. On the impact of launch power optimization and transceiver noise on the performance of ultra-wideband transmission systems. *Journal of Optical Communications and Networking* **14**, B11–B21 (2022).

[83] Vasylchenkova, A., Sillekens, E., Killey, R. I. and Bayvel, P. Mutual shaping and pre-emphasis gain magnification in the throughput maximisation for ultrawideband transmission. In *Optical Fiber Communication Conference (OFC)*, Th1H.4 (Optica Publishing Group, 2022).

[84] Hoshida, T., Curri, V., Galdino, L., Neilson, D. T., Forysiak, W., Fischer, J. K., Kato, T. and Poggiolini, P. Ultrawideband systems and networks: Beyond $C + L$ -band. *Proceedings of the IEEE* (2022).

[85] Shevchenko, N. A., Nallaperuma, S. and Savory, S. J. Maximizing the information throughput of ultra-wideband fiber-optic communication systems. *Opt. Express* **30**, 19320–19331 (2022). URL `https://opg.optica.org/oe/abstract.cfm?URI=oe-30-11-19320`.

[86] Poggiolini, P. and Zefreh, M. R. Closed form expressions of the nonlinear interference for UWB systems. *European Conference on Optical Communication (ECOC)* (2022).

[87] Buglia, H., Killey, R. I. and Bayvel, P. Ultra-wideband modelling of optical fibre nonlinearity in hybrid-amplified links. *Journal of Lightwave Technology* 1–14 (2024).

[88] Wu, Y., Tian, F., Lin, Z., Gu, Y., Wang, J., Zhang, Q., Tian, Q. and Wang, Y. Research on the compensation scheme for spectral power tilt from stimulated Raman scattering in multi-band transmission system. In *20th International Conference on Optical Communications and Networks (ICOCN)* (2022).

[89] Iqbal, M. A., Tan, M., Forysiak, W. and Lord, A. Opportunities and challenges for discrete Raman amplifiers in ultrawideband transmission systems. In *IEEE Photonics Society Summer Topicals Meeting Series (SUM)* (2022).

[90] Vasylchenkova, A., Buglia, H., Sillekens, E., Galdino, L., Killey, R. I. and Bayvel, P. Analytical modelling of system impairments in ultrawideband transmission context. In *Photonic Networks and Devices*, NeTu3D–1 (Optica Publishing Group, 2022).

[91] Buglia, H. and Galdino, L. Unleashing the optical fiber transmission bandwidth: From theory to experiments. In *Signal Processing in Photonic Communications*, SpTh2J–7 (Optica Publishing Group, 2022).

[92] Matzner, R., Semrau, D., Luo, R., Zervas, G. and Bayvel, P. Making intelligent topology design choices: understanding structural and physical property performance implications in optical networks. *J. Opt. Commun. Netw.* **13**, D53–D67 (2021).

[93] Luo, R., Matzner, R., Ottino, A., Zervas, G. and Bayvel, P. Exploring the relationship among traffic, topology, and throughput: towards a traffic-optimal optical network topology design. *Journal of Optical Communications and*

Networking **15**, B1–B10 (2023). URL https://opg.optica.org/jocn/abstract.cfm?URI=jocn-15-5-B1.

[94] Rabbani, H., Beygi, L., Ghoshooni, S., Rabbani, H. and Agrell, E. Quality of transmission aware optical networking using enhanced Gaussian noise model. *Journal of Lightwave Technology* **37**, 831–838 (2019).

[95] Ives, D., Yan, S., Galdino, L., Wang, R., Elson, D., Wakayama, Y., Vaquero Caballero, F. J., Saavedra, G., Lavery, D., Nejabati, R., Bayvel, P., Simeonidou, D. and Savory, S. Distributed abstraction and verification of an installed optical fibre network. *Scientific Reports* **11**, 10750 (2021).

[96] Zefreh, M. R., Forghieri, F., Piciaccia, S. and Poggiolini, P. A closed-form nonlinearity model for forward-Raman-amplified WDM optical links. In *Optical Fiber Communication Conference (OFC) 2021*, M5C.1 (Optica Publishing Group, 2021).

[97] Zefreh, M. R. and Poggiolini, P. A GN-model closed-form formula supporting ultra-low fiber loss and short fiber spans. *arXiv:2111.04584 [eess.SP]* (2021).

[98] Klaus, W. and Winzer, P. J. Hollow-core fiber capacities with receiver noise limitations. In *Optical Fiber Communications Conference and Exhibition (OFC)* (2022).

[99] Semrau, D., Galdino, L., Sillekens, E., Lavery, D., Killey, R. I. and Bayvel, P. Modulation format dependent, closed-form formula for estimating nonlinear interference in S+C+L band systems. In *European Conference on Optical Communication (ECOC)*, 1–4 (2019).

[100] Buglia, H., Sillekens, E., Vasylchenkova, A., Killey, R., Bayvel, P. and Galdino, L. An extended version of the ISRS GN model in closed-form accounting for short span lengths and low losses. In *European Conference on Optical Communication (ECOC)*, 1–4 (2022).

[101] Buglia, H., Jarmolovičius, M., Vasylchenkova, A., Sillekens, E., Galdino, L., Killey, R. I. and Bayvel, P. A closed-form expression for the Gaussian noise model in the presence of inter-channel stimulated Raman scattering extended for arbitrary loss and fibre length. *Journal of Lightwave Technology* **41**, 3577–3586 (2023).

[102] Christodoulides, D. and Jander, R. Evolution of stimulated Raman crosstalk in wavelength division multiplexed systems. *IEEE Photonics Technology Letters* **8**, 1722–1724 (1996).

[103] Zirngibl, M. Analytical model of Raman gain effects in massive wavelength division multiplexed transmission systems. *Electronics Letters* **34**, 789–790 (1998).

[104] Souza, A., Costa, N., ao Pedro, J. and ao Pires, J. Benefits of counterpropagating Raman amplification for multiband optical networks. *J. Opt. Commun. Netw.* **14**, 562–571 (2022). URL `https://opg.optica.org/jocn/abstract.cfm?URI=jocn-14-7-562`.

[105] Semrau, D., Saavedra, G., Lavery, D., Killey, R. I. and Bayvel, P. A closed-form expression to evaluate nonlinear interference in Raman-amplified links. *Journal of Lightwave Technology* **35**, 4316–4328 (2017).

[106] Jiang, Y., Nespola, A., Straullu, S., Tanzi, A., Piciaccia, S., Forghieri, F., Pilori, D. and Poggiolini, P. Closed-form EGN model with comprehensive Raman support. In *European Conference on Optical Communication (ECOC)*, 1–4 (2024).

[107] Jiang, Y. and Poggiolini, P. CFM6, a closed-form NLI EGN model supporting multiband transmission with arbitrary Raman amplification. *arXiv:2405.08512 [eess.SP]* (2024).

[108] Buglia, H., Jarmolovičius, M., Vasylchenkova, A., Sillekens, E., Galdino, L., Bayvel, P. and Killey, R. A closed-form expression for the ISRS GN model supporting distributed Raman amplification. In *Optical Fiber Communications Conference and Exhibition (OFC)*, 1–3 (2023).

[109] Buglia, H., Jarmolovičius, M., Galdino, L., Killey, R. I. and Bayvel, P. A closed-form expression for the Gaussian noise model in the presence of Raman amplification. *Journal of Lightwave Technology* **42**, 636–648 (2024).

[110] Yang, J., Buglia, H., Sillekens, E., Tan, M., Hazarika, P., Pratiwi, D., Sohanpal, R., Jarmolovičius, M., Aparecido, R., Stolte, R., Forysiak, W., Bayvel, P. and Killey, R. Experimental validation of the closed-form GN model accounting for distributed Raman amplification in an S+C+L-band hybrid amplified long-haul transmission system. In *European Conference on Optical Communication (ECOC)*, 1–4 (2024).

[111] Brusin, A. M. R., Zefreh, M. R., Poggiolini, P., Piciaccia, S., Forghieri, F. and Carena, A. Machine learning for power profiles prediction in presence of inter-channel stimulated Raman scattering. In *European Conference on Optical Communication (ECOC)* (2021).

[112] Lasagni, C., Serena, P., Bononi, A. and Antona, J.-C. A generalized Raman scattering model for real-time SNR estimation of multi-band systems. *Journal of Lightwave Technology* 1–11 (2023).

[113] Iqbal, M. A., Rosa, G. D., Krzczanowicz, L., Phillips, I., Harper, P., Richter, A. and Forysiak, W. Impact of pump-signal overlap in S+C+L band discrete Raman amplifiers. *Opt. Express* **28**, 18440–18448 (2020). URL `https://opg.optica.org/oe/abstract.cfm?URI=oe-28-12-18440`.

[114] Wakayama, Y., Gerard, T., Sillekens, E., Galdino, L., Lavery, D., Killey, R. I. and Bayvel, P. 2048-QAM transmission at 15 GBd over 100 km using geometric constellation shaping. *Optics Express* **29**, 18743–18759 (2021).

[115] Roberts, I., Kahn, J. M., Harley, J. and Boertjes, D. W. Channel power optimization of WDM systems following Gaussian noise nonlinearity model in presence of stimulated Raman scattering. *Journal of Lightwave Technology* **35**, 5237–5249 (2017).

[116] Nallaperuma, S., Shevchenko, N. A. and Savory, S. J. Parameter optimisation for ultra-wideband optical networks in the presence of stimulated Raman scattering effect. In *International Conference on Optical Network Design and Modeling (ONDM)* (2021).

[117] Correia, B., Sadeghi, R., Virgillito, E., Napoli, A., Costa, N., Pedro, J. and Curri, V. Optical power control strategies for optimized C+L+S-bands network performance. In *Optical Fiber Communications Conference* (2021).

[118] Correia, B., Sadeghi, R., Virgillito, E., Napoli, A., Costa, N., Pedro, J. and Curri, V. Power control strategies and network performance assessment for C+L+S multiband optical transport. *Journal of Optical Communications and Networking* **13**, 147–157 (2021).

[119] Landero, S. E., de Jauregui Ruiz, I. F., Ferrari, A., Gac, D. L., Frignac, Y. and Charlet, G. Link power optimization for S+C+L multi-band WDM coherent transmission systems. In *Optical Fiber Communications Conference and Exhibition (OFC)* (2022).

[120] Luo, H., Lu, J., Huang, Z., Yu, C. and Lu, C. Optimization strategy of power control for C+L+S band transmission using a simulated annealing algorithm. *Opt. Express* **30**, 664–675 (2022). URL `https://opg.optica.org/oe/abstract.cfm?URI=oe-30-1-664`.

[121] Semrau, D. Modeling of fiber nonlinearity in wideband transmission. In *Optical Fiber Communications Conference and Exhibition (OFC)* (2022).

[122] Poggiolini, P. A generalized GN-model closed-form formula. *arXiv: 1810.06545 [eess.SP]* (2018).

[123] de Moura, U. C., Ros, F. D., Brusin, A. M. R., Carena, A. and Zibar, D. Experimental characterization of Raman amplifier optimization through inverse system design. *Journal of Lightwave Technology* **39**, 1162–1170 (2021).

[124] Soltani, M., Da Ros, F., Carena, A. and Zibar, D. Distance and spectral power profile shaping using machine learning enabled Raman amplifiers. In *IEEE Photonics Society Summer Topicals Meeting Series (SUM)* (2021).

[125] Semrau, D., Sillekens, E., Bayvel, P. and Killey, R. I. Modeling and mitigation of fiber nonlinearity in wideband optical signal transmission. *Journal of Optical Communications and Networking* **12**, C68–C76 (2020).

[126] Kennedy, J. and Eberhart, R. Particle swarm optimization. *Proceedings of ICNN'95 - International Conference on Neural Networks* **4**, 1942–1948 (1995).

[127] Boyd, S., Boyd, S. P. and Vandenberghe, L. *Convex optimization* (Cambridge university press, 2004).

[128] Buglia, H., Sillekens, E., Galdino, L., Killey, R. and Bayvel, P. Throughput maximisation in ultra-wideband hybrid-amplified links. In *Optical Fiber Communication Conference (OFC) 2024*, Tu3H.5 (Optica Publishing Group, 2024). URL `https://opg.optica.org/abstract.cfm?URI=OFC-2024-Tu3H.5`.

[129] Ivanov, V. V., Galdino, L. and Downie, J. D. Optimization of channel powers, Raman pumps and EDFAs in the wideband fiber optic transmission systems. In *Optical Fiber Communications Conference*, W2B.1 (2024).

[130] Jiang, Y., Nespola, A., Tanzi, A., Piciaccia, S., Zefreh, M. R., Forghieri, F. and Poggiolini, P. Performance enhancement of long-haul C+L+S systems by means of CFM-assisted optimization. In *Optical Fiber Communication Conference (OFC) 2024*, M1F.2 (Optica Publishing Group, 2024). URL `https://opg.optica.org/abstract.cfm?URI=OFC-2024-M1F.2`.

[131] Buglia, H., Sillekens, E., Galdino, L., Killey, R. I. and Bayvel, P. Impact of launch power optimisation in hybrid-amplified links. In *European Conference on Optical Communications (ECOC)*, vol. 2024, 1–4 (2024).

[132] Buglia, H., Jarmolovičius, M., Galdino, L., Killey, R. I. and Bayvel, P. A modulation-format dependent closed-form expression for the Gaussian noise

model in the presence of Raman amplification. In *European Conference on Optical Communications (ECOC)*, vol. 2023, 64–67 (2023).

[133] Giles, C. and Desurvire, E. Propagation of signal and noise in concatenated erbium-doped fiber optical amplifiers. *Journal of Lightwave Technology* **9**, 147–154 (1991).

[134] Bononi, A., Antona, J.-C., Serena, P., Carbo-Meseguer, A. and Lasagni, C. The generalized droop model for submarine fiber-optic systems. *Journal of Lightwave Technology* **39**, 5248–5257 (2021).

[135] Varughese, S., Semrau, D., Lavery, D., Yao, D., Stephens, M., Bravi, E., Torbatian, M. and Mertz, P. Improving capacity predictions for subsea open cables employing modern coherent transceivers. In *European Conference on Optical Communication (ECOC) 2022*, We5.37 (Optica Publishing Group, 2022). URL `https://opg.optica.org/abstract.cfm?URI=ECEOC-2022-We5.37`.

[136] Stephens, M. F. C., Mertz, P., Grubb, S. G., Shartle, G., Kumpera, A., O'Connor, J., Maher, R., Chitgarha, M. R., Doggart, C., Thomson, S., Edirisinghe, S., Afonso, A., Elam, M., Gelov, K., Boyanov, B., Dominic, V., Sanders, S. and Kandappan, P. Trans-atlantic real-time field trial using super-Gaussian constellation-shaping to enable 30Tb/s+ capacity. In *Optical Fiber Communication Conference (OFC) 2021*, F4G.2 (Optica Publishing Group, 2021). URL `https://opg.optica.org/abstract.cfm?URI=OFC-2021-F4G.2`.

[137] Varughese, S., Edirisinghe, S., Stephens, M., Boyanov, B. and Mertz, P. SDM enabled record field trial achieving 300+ Tbps trans-atlantic transmission capacity. In *Optical Fiber Communication Conference (OFC) 2022*, M1F.2 (Optica Publishing Group, 2022). URL `https://opg.optica.org/abstract.cfm?URI=OFC-2022-M1F.2`.

[138] Simmons, J. M. *Optical Network Design and Planning* (Springer Publishing Company, Incorporated, 2008), 1 edn.

[139] Kumar Jana, R., Asif Iqbal, M., Parkin, N., Srivastava, A., Mishra, A., Balakrishnan, J., Coppin, P., Lord, A. and Mitra, A. Multifiber vs. ultra-wideband upgrade: A techno-economic comparison for elastic optical backbone network. In *European Conference on Optical Communication (ECOC)*, 1–4 (2022).

[140] Virgillito, E., Sadeghi, R., Ferrari, A., Borraccini, G., Napoli, A. and Curri, V. Network performance assessment of C+L upgrades vs. fiber doubling SDM

solutions. In *Optical Fiber Communications Conference and Exhibition (OFC)*, 1–3 (2020).

[141] Jana, R. K., Mitra, A., Pradhan, A., Grattan, K., Srivastava, A., Mukherjee, B. and Lord, A. When is operation over $\mathrm{C} + \mathrm{L}$ bands more economical than multifiber for capacity upgrade of an optical backbone network? In *European Conference on Optical Communications (ECOC)*, 1–4 (2020).

[142] Matzner, R., Buglia, H. and Bayvel, P. Evolving optical core networks: understanding the impact of topology redesign using space and wavelength domains on network throughput. In *European Conference on Optical Communications (ECOC)*, vol. 2023, 1043–1046 (2023).

[143] Luo, R., Matzner, R., Zervas, G. and Bayvel, P. Towards a traffic-optimal large-scale optical network topology design. In *2022 International Conference on Optical Network Design and Modeling (ONDM)*, 1–3 (2022).

[144] Sambo, N., Ferrari, A., Napoli, A., Costa, N., Pedro, J., Sommerkohrn-Krombholz, B., Castoldi, P. and Curri, V. Provisioning in multi-band optical networks: A C+L+S-band use case. In *European Conference on Optical Communication (ECOC)*, 1–4 (2019).

[145] Nakagawa, M., Seki, T. and Miyamura, T. Techno-economic potential of wavelength-selective band-switchable OXC in S+C+L band optical networks. In *Optical Fiber Communications Conference and Exhibition (OFC)*, 01–03 (2022).

[146] Balasis, F., Elson, D. J., Jarmolovičius, M., Buglia, H., Sillekens, E., Killey, R., Bayvel, P., Yoshikane, N., Tsuritani, T. and Wakayama, Y. An extended closed form of the ISRS GN model for the zero-dispersion regime. In *European Conference on Optical Communication (ECOC)*, 1–4 (2024).

[147] Rosa Brusin, A. M., Nespola, A., Zefreh, M. R., Piciaccia, S., Poggiolini, P., Forghieri, F. and Carena, A. ML-based spectral power profiles prediction in presence of ISRS for ultra-wideband transmission. *Journal of Lightwave Technology* **42**, 37–47 (2024).

Appendices

Appendix A

Derivation of Eq. (3.11)

This appendix describes the derivation of Eq. (3.11) presented in Sec. 3.1.3. The derivation was peer-reviewed and published in [P2]. Let $x(\zeta) = 1 - [P_{\text{tot}} C_{r,i} f_i L_{\text{eff}}(\zeta)]$ with $L_{\text{eff}}(\zeta) = \frac{1-e^{-\tilde{\alpha}_i \zeta}}{\tilde{\alpha}_i}$, Eq. (2.51) can then be written as

$$\rho(z, f_i) = e^{-\alpha_i z} \left[1 - x(\zeta)\right]. \tag{A.1}$$

Inserting Eq. (A.1) in Eq. (3.3) yields

$$\mu\left(f_1, f_2, f_i\right) = \left| \int_0^L d\zeta \; e^{-\alpha_i z} x(\zeta) e^{j\phi(f_1, f_2, f_i)\zeta} \right|^2, \tag{A.2}$$

The term $x(\zeta)$ can be written as

$$x(\zeta) = 1 - \left[\left(\frac{P_{\text{tot}} C_{r,i}}{\tilde{\alpha}_i} f_i \right) \left(1 - e^{-\tilde{\alpha}_i \zeta}\right) \right]. \tag{A.3}$$

Letting $\tilde{T}_i = \frac{-P_{\text{tot}} C_{r,i} f_i}{\tilde{\alpha}_i}$, $T_i = 1 + \tilde{T}_i$, the term $x(\zeta)$ is written as

$$x(\zeta) = T_i \left[1 - \frac{\tilde{T}_i}{T_i} e^{-\tilde{\alpha}_i \zeta} \right]. \tag{A.4}$$

Eq. (A.4) can be conveniently rewritten in terms of a summation using identity (H.1), which will facilitate all the mathematical derivations,

$$x(\zeta) = T_i \sum_{0 \leq l \leq 1} \left(\frac{-\tilde{T}_i}{T_i} \right)^l e^{-l\tilde{\alpha}_i \zeta}. \tag{A.5}$$

Now, inserting Eq. (A.5) in Eq. (A.2)

$$\mu\left(f_1, f_2, f_i\right) = \left| T_i \sum_{0 \leq l \leq 1} \left(\frac{-\tilde{T}_i}{T_i} \right)^l \int_0^L d\zeta \; e^{-(\alpha_i \zeta + l\tilde{\alpha}_i \zeta) + j\phi\zeta} \right|^2. \tag{A.6}$$

Solving the integral in (A.6) yields

$$\mu\left(f_1, f_2, f_i\right) = \left| T_i \sum_{0 \leq l \leq 1} \left(\frac{-\tilde{T}_i}{T_i} \right)^l \frac{e^{-(\alpha_i + l\tilde{\alpha}_i)L + j\phi L} - 1}{-(\alpha_i + l\tilde{\alpha}_i) + j\phi} \right|^2 . \tag{A.7}$$

Now, define $\alpha_{l,i} = \alpha_i + l\tilde{\alpha}_i$. Eq. (A.7) can then be written as

$$\mu\left(f_1, f_2, f_i\right) = \left| -T_i \sum_{0 \leq l \leq 1} \left(\frac{-\tilde{T}_i}{T_i} \right)^l \frac{1 - e^{-(\alpha_{l,i} - j\phi)L}}{-\alpha_{l,i} + j\phi} \right|^2 . \tag{A.8}$$

Despite Eq. (A.8) being in closed form, it needs to be further integrated in frequency to obtain the XPM and SPM contributions to the NLI as shown in Eqs. (3.1), (3.2), (3.5) and (3.6). To solve these integrals in closed-form, the approach in [97] is used, i.e., the fraction with exponential terms in Eq. (A.8) is approximated as

$$\frac{1 - e^{-(\alpha_{l,i} - j\phi)L}}{-\alpha_{l,i} + j\phi} \approx \frac{\kappa_{l,i}}{-\tilde{\alpha}_{l,i} + j\phi}, \tag{A.9}$$

where $\kappa_{l,i}$ and $\tilde{\alpha}_{l,i}$ are chosen such that the first-order Taylor approximations of both the left and the right side of Eq. (A.9) around the variable $\phi = 0$ become equal. This yields Eq. (3.9) and Eq. (3.10). Inserting the approximation shown in Eq. (A.9) into Eq. (A.8) and using identity (H.6), yields

$$\mu\left(f_1, f_2, f_i\right) = \left(T_i \sum_{0 \leq l \leq 1} \left(\frac{-\tilde{T}_i}{T_i} \right)^l \frac{\kappa_{l,i}}{-\tilde{\alpha}_{l,i} + j\phi} \right) \left(T_i \sum_{0 \leq l' \leq 1} \left(\frac{-\tilde{T}_i}{T_i} \right)^{l'} \frac{\kappa_{l',i}}{-\tilde{\alpha}_{l',i} - j\phi} \right). \tag{A.10}$$

Finally, performing the multiplication in Eq. (A.10) together with the identity (H.4), yields Eq. (3.11), concluding the proof.

Appendix B

Derivation of Eq. (3.12)

This appendix presents the derivation of Eq. (3.12). The derivation was peer-reviewed and published in [P2]. The derivation consists of finding an analytical approximation of the integral form in Eq. (3.1) which models the nonlinear interference caused on channel i by a single interfering channel k.

The first step is approximating the phase mismatch term in Eq. (3.3). For the XPM contribution, let $\Delta f = f_k - f_i$ be the frequency separation between channels k and i. Assuming that frequency separation is much larger than half of the bandwidth of channel k, i.e., $|\Delta f| \gg \frac{B_k}{2}$, the assumption that $f_2 + \Delta f \approx \Delta f$ holds. Also, the dispersion slope β_3 is assumed constant over the channel bandwidth. Thus, the phase mismatch term can be approximated as [35, Eq. 15]

$$\begin{aligned}
&\phi(f_1 + f_i, f_2 + f_k, f_i) = \\
&= -4\pi^2 f_1 \Delta f \left[\beta_2 + \pi\beta_3(f_1 + f_2 + f_i + f_k)\right] \approx \\
&\approx -4\pi^2 (f_k - f_i) \left[\beta_2 + \pi\beta_3(f_i + f_k)\right] f_1 = \\
&= \phi_{i,k} f_1,
\end{aligned} \tag{B.1}$$

with $\phi_{i,k} = -4\pi(f_k - f_i)\left[\beta_2 + \pi\beta_3(f_i + f_k)\right]$. The channels most impacted by this approximation are those near the COI. The error relative to this approximation is given by [35, Eq. 25].

Now, Eq. (3.1) is considered. For notation brevity, the factor $\frac{32}{27}\frac{\gamma^2}{B_k^2}\left(\frac{P_k}{P_i}\right)^2$ is omitted. Also, the term $\Pi\left(\frac{f_1+f_2}{B_k}\right)$ is neglected - this is equivalent to approximating the integration domain of the GN model to a rectangle [27]. Inserting Eq. (3.11) in Eq. (3.1)

$$\eta_{\text{XPM}}^{(k)}(f_i) = T_k^2 \sum_{\substack{0\le l\le 1\\ 0\le l'\le 1}} \left(\frac{-\tilde{T}_k}{T_k}\right)^{l+l'} \kappa_{l,k}\kappa_{l',k} \int_{\frac{-B_i}{2}}^{\frac{B_i}{2}} df_1 \int_{\frac{-B_k}{2}}^{\frac{B_k}{2}} df_2 \, \frac{\tilde{\alpha}_{l,k}\tilde{\alpha}_{l',k} + \phi_{i,k}^2 f_1^2}{(\tilde{\alpha}_{l,k}^2 + \phi_{i,k}^2 f_1^2)(\tilde{\alpha}_{l',k}^2 + \phi_{i,k}^2 f_1^2)}. \tag{B.2}$$

Because of the approximation in Eq. (B.1), ϕ no longer depends on f_2. Thus, Eq. (B.2)

can be written as

$$\eta_{\text{XPM}}^{(k)}(f_i) = T_k^2 \sum_{\substack{0\leq l\leq 1\\ 0\leq l'\leq 1}} \left(\frac{-\tilde{T}_i}{T_k}\right)^{l+l'} \kappa_{l,k}\kappa_{l',k} 2B_k \int_0^{\frac{B_i}{2}} df_1 \, \frac{\tilde{\alpha}_{l,k}\tilde{\alpha}_{l',k} + \phi_{i,k}^2 f_1^2}{(\tilde{\alpha}_{l,k}^2 + \phi_{i,k}^2 f_1^2)(\tilde{\alpha}_{l',k}^2 + \phi_{i,k}^2 f_1^2)}. \tag{B.3}$$

The integral in Eq. (B.3) can be solved using identity (H.5), yielding

$$\eta_{\text{XPM}}^{(k)}(f_i) = T_k^2 \sum_{\substack{0\leq l\leq 1\\ 0\leq l'\leq 1}} \left(\frac{-\tilde{T}_k}{T_k}\right)^{l+l'} \frac{2B_k\kappa_{l,k}\kappa_{l',k}}{\phi_{i,k}(\tilde{\alpha}_{l,k} + \tilde{\alpha}_{l',k})} \left[\operatorname{atan}\left(\frac{\phi_{i,k}B_i}{2\tilde{\alpha}_{l,k}}\right) + \operatorname{atan}\left(\frac{\phi_{i,k}B_i}{2\tilde{\alpha}_{l',k}}\right)\right]. \tag{B.4}$$

By inserting again the pre-factor $\frac{32}{27}\frac{\gamma^2}{B_k^2}\left(\frac{P_k}{P_i}\right)^2$ in Eq. (B.4), Eq. (3.12) is obtained, concluding the proof.

Appendix C

Derivation of Eq. (3.13)

This appendix presents the derivation of Eq. (3.13). The derivation was peer-reviewed and published in [P2]. The derivation consists of finding an analytical approximation of the integral form in Eq. (3.2) which models the nonlinear interference caused by the channel i on itself.

The first step is approximating the phase mismatch term. A constant dispersion slope β_3 over the channel bandwidth is assumed. Thus, the phase mismatch term can be approximated as

$$\begin{aligned}&\phi(f_1+f_i, f_2+f_i, f_i) = \\ &-4\pi^2 f_1 f_2 \left[\beta_2 + \pi\beta_3(f_1+f_2-2f_i)\right] \\ &\approx -4\pi^2 f_1 f_2(\beta_2 + 2\pi\beta_3 f_i) \\ &= \phi_i f_1 f_2,\end{aligned} \tag{C.1}$$

with $\phi_i = -4\pi^2(\beta_2 + 2\pi\beta_3 f_i)$. Now, using Eq. (3.2) together with Eq. (3.1) with $k=i$, and omitting the pre-factor of $\frac{16}{27}\frac{\gamma^2}{B_i^2}$, it is possible to write

$$\eta_{\text{SPM}}(f_i) = T_i^2 \sum_{\substack{0\le l\le 1\\ 0\le l'\le 1}} \left(\frac{-\tilde{T}_i}{T_i}\right)^{l+l'} \kappa_{l,i}\kappa_{l',i} \int_{\frac{-B_i}{2}}^{\frac{B_i}{2}} df_1 \int_{\frac{-B_i}{2}}^{\frac{B_i}{2}} df_2 \, \frac{\tilde{\alpha}_{l,i}\tilde{\alpha}_{l',i} + \phi_i^2 f_1^2 f_2^2}{(\tilde{\alpha}_{l,i}^2 + \phi_i^2 f_1^2 f_2^2)(\tilde{\alpha}_{l',i}^2 + \phi_i^2 f_1^2 f_2^2)}. \tag{C.2}$$

Note that, similarly to Appendix B, the term $\Pi\left(\frac{f_1+f_2}{B_i}\right)$ is neglected. The integral in Eq. (C.2) can be rewritten in polar coordinates (r,φ) as

$$\begin{aligned}\eta_{\text{SPM}}(f_i) \approx T_i^2 \sum_{\substack{0\le l\le 1\\ 0\le l'\le 1}} \left(\frac{-\tilde{T}_i}{T_i}\right)^{l+l'} 4\kappa_{l,i}\kappa_{l',i} \int_0^{\sqrt{\frac{3}{\pi}}\frac{B_i}{2}} dr \\ \int_0^{\frac{\pi}{2}} d\varphi \frac{r\left[\tilde{\alpha}_{l,i}\tilde{\alpha}_{l',i} + \frac{\phi_i^2}{4}(r^4\sin^2(\varphi))\right]}{\left[\tilde{\alpha}_{l,i}^2 + \frac{\phi_i^2}{4}r^4\sin^2(\varphi)\right]\left[\tilde{\alpha}_{l',i}^2 + \frac{\phi_i^2}{4}r^4\sin^2(\varphi)\right]^2},\end{aligned} \tag{C.3}$$

where the relations $f_1 = r\cos(\varphi/2)$, $f_2 = r\sin(\varphi/2)$ and

$\sin(\varphi/2)\cos(\varphi/2) = \frac{\sin(\varphi)}{2}$ were used. Also, the integration domain of Eq. (3.2) was approximated by a circular domain such that the area of both domains are equal [35, Fig. 3]. This yields the variation of the radius in the outer integral as shown in Eq. (C.3). The inner integral in Eq. (C.3) can be solved using identity (H.6), yielding

$$\eta_{\text{SPM}}(f_i) \approx T_i^2 \sum_{\substack{0\le l\le 1\\ 0\le l'\le 1}} \left(\frac{-\tilde{T}_i}{T_i}\right)^{l+l'} 4\kappa_{l,i}\kappa_{l',i} \int_0^{\sqrt{\frac{3}{\pi}}\frac{B_i}{2}} dr \\ \frac{r\pi}{\tilde{\alpha}_{l,i}+\tilde{\alpha}_{l',i}} \left[\frac{1}{\sqrt{4\tilde{\alpha}_{l,i}^2+\phi_i^2 r^4}} + \frac{1}{\sqrt{4\tilde{\alpha}_{l',i}^2+\phi_i^2 r^4}}\right]. \tag{C.4}$$

This integral can be rewritten as

$$\eta_{\text{SPM}}(f_i) \approx T_i^2 \sum_{\substack{0\le l\le 1\\ 0\le l'\le 1}} \left(\frac{-\tilde{T}_i}{T_i}\right)^{l+l'} \frac{2\pi\kappa_{l,i}\kappa_{l',i}}{\tilde{\alpha}_{l,i}+\tilde{\alpha}_{l',i}} \\ \int_0^{\sqrt{\frac{3}{\pi}}\frac{B_i}{2}} dr \left[\frac{r}{\tilde{\alpha}_{l,i}\sqrt{1+\frac{\phi_i^2 r^4}{4\tilde{\alpha}_{l,i}^2}}} + \frac{r}{\tilde{\alpha}_{l',i}\sqrt{1+\frac{\phi_i^2 r^4}{4\tilde{\alpha}_{l',i}^2}}}\right]. \tag{C.5}$$

The integral in Eq. (C.5) is solved using identity (H.7) as

$$\eta_{\text{SPM}}(f_i) \approx T_i^2 \sum_{\substack{0\le l\le 1\\ 0\le l'\le 1}} \left(\frac{-\tilde{T}_i}{T_i}\right)^{l+l'} \frac{2\pi\kappa_{l,i}\kappa_{l',i}}{\phi_i(\tilde{\alpha}_{l,i}+\tilde{\alpha}_{l',i})} \left[\operatorname{asinh}\left(\frac{3\phi_i B_i^2}{8\pi\tilde{\alpha}_{l,i}}\right) + \operatorname{asinh}\left(\frac{3\phi_i B_i^2}{8\pi\tilde{\alpha}_{l',i}}\right)\right]. \tag{C.6}$$

By inserting again the pre-factor of $\frac{16}{27}\frac{\gamma^2}{B_i^2}$, Eq. (3.13) is obtained, concluding the proof.

Appendix D

Derivation of Eq. (4.1)

This appendix presents the derivation of Eq. (4.1). The derivation was peer-reviewed and published in [P3]. The derivation consists of finding a semi-analytical approximation of Eq. (2.39) which models the transmitted power evolution along the optical fibre distance in the presence of RA.

It should be noted that some assumptions made in this appendix are not exact, however, this is not an issue as this equation is used as a semi-analytical solution of the Raman equations, which is further fitted and optimised to correct reproduce the solution of Eq. (2.39).

The derivation starts with Eq. (2.39) and follows a method similar to [103]. A constant attenuation α is assumed for all the channels, and energy loss during the conversion of a high-frequency photon into a low-frequency photon is neglected, i.e., $\frac{f_k}{f_i} \approx 1$ and $\frac{f_p}{f_i} \approx 1$. Additionally, the triangular approximation of the Raman spectrum is assumed, i.e., $g_r(\Delta f) \approx C_r \Delta f$, where C_r is the slope of the linear regression (normalized by the effective core area A_{eff}) and Δf is the frequency separation between the channels and between the channels and the pumps. Under these assumptions, Eq. (2.39) can be written as

$$\begin{aligned}\frac{\partial P_i}{\partial z} &= \sum_{k=1}^{N_{\text{ch}}} C_r(f_k - f_i)P_k P_i + \sum_{p=1}^{N_p} C_r(f_p - f_i)P_k P_i - \alpha P_i \\ &= C_r P_i \left(\sum_{k=1}^{N_{\text{ch}}} (f_k - f_i)P_k + \sum_{p=1}^{N_p} (f_p - f_i)P_k \right) - \alpha P_i.\end{aligned} \tag{D.1}$$

The coupled differential equations are now combined into a single equation, by replacing the N_{ch} signals and N_p pumps with a signal and pump density spectrum. Additionally, the summation is replaced with an integration over the entire frequency spectrum of the signal and the pumps. Thus, Eq. (D.1) can be written as

$$\begin{aligned}\frac{dP(z,f)}{dz} = C_r P(z,f) \Bigg(&\int_{f_{ch,min}}^{f_{ch,max}} (\Lambda_{ch} - f)P(z,\Lambda_{ch})\, d\Lambda_{ch} \\ &+ \int_{f_{p,min}}^{f_{p,max}} (\Lambda_p - f)P(z,\Lambda_p)\, d\Lambda_p \Bigg) - \alpha P(z,f),\end{aligned} \tag{D.2}$$

where $f_{ch,max}$, $f_{ch,min}$, $f_{p,max}$ and $f_{p,min}$ are respectively the maximum and minimum frequencies of the channels, and the pumps. Dividing both sides of Eq. (D.2) by $P(z,f)$ and taking the derivative with respect to the frequency f, yields to

$$\frac{d}{df}\left(\frac{dP(z,f)/dz}{P(z,f)}\right) = -C_r \left(\underbrace{\int_{f_{ch,min}}^{f_{ch,max}} P(z,\Lambda_{ch})\, d\Lambda_{ch}}_{P_{total,ch}} + \underbrace{\int_{f_{p,min}}^{f_{p,max}} P(z,\Lambda_p)\, d\Lambda_p}_{P_{total,p}} \right). \tag{D.3}$$

Note that, the integrals represent the total launch power ($P(z)$), i.e., a sum of the channel ($P_{total,ch}$), the forward pump ($P_{total,fw}$) and backward pump ($P_{total,bw}$) launch powers. Moreover, $P_{total,ch}$ and $P_{total,fw}$ must decay with $e^{-\alpha z}$, while $P_{total,bw}$ decays with $e^{-\alpha(L-z)}$. Thus, Eq. (D.3) can be written as

$$\frac{d}{df}\left(\frac{dP(z,f)/dz}{P(z,f)}\right) = -C_r P(z) = -C_r \left(P_{total,ch}e^{-\alpha z} + P_{total,fw}e^{-\alpha z} + P_{total,bw}e^{-\alpha(L-z)}\right). \tag{D.4}$$

To apply this equation in more general scenarios and overcome the assumptions done so far, a separate wavelength-dependent attenuation to model channels together with FW pumps ($\alpha_{f,i}$) and together with BW pumps ($\alpha_{b,i}$) is defined. These parameters can be interpreted as modelling respectively how fast the channel gain/loss due to the FW-RA and BW-RA together with ISRS extinguishes along the fibre. Similarly, a separate wavelength-dependent C_r, i.e., $C_{f,i}$ and $C_{b,i}$, respectively for channels together with FW pumps and BW pumps is defined. These two parameters model respectively the gain/loss due to FW-RA and BW-RA together with the ISRS effect. Note that, a more rigorous approach would be to define 3 wavelength-dependent C_r and α for each one of the terms on the right-hand side of Eq (D.4) (as they occupy different locations of the frequency spectrum); however, as ISRS + FW pumping have effectively the same effect (a power transfer from pumps/channels to the COI) they can be modelled together, resulting in a total of 2 wavelength-dependent C_r and α. Thus, by letting $P_f = P_{total,ch} + P_{total,fw}$ and $P_b = P_{total,bw}$, Eq. (D.4) is rewritten as

$$\frac{d}{df}\left(\frac{dP(z,f)/dz}{P(z,f)}\right) = -(C_{f,i}P_f e^{-\alpha_{f,i}z} + C_{b,i}P_b e^{-\alpha_{b,i}(L-z)}). \tag{D.5}$$

Next, integration is performed with respect to z and f. For the integration in f, note that, the WDM spectra and the pumps occupy different parts of the frequency spectrum. This fact massively complicates the derivation of the closed-form expression. To address this issue, without loss of generality, a new central frequency (common to the WDM spectra and the pumps) is introduced as the average frequencies of the pumps, which is denoted

by $\hat{f}$ (other choices are also possible). Thus, integrating over z and f yields

$$P(z,f) = \quad e^{-[C_{f,i}P_f L_{\text{eff}}(f-\hat{f})+C_{b,i}P_b\tilde{L}_{\text{eff}}(f-\hat{f})]+A(z)+B(f)}, \tag{D.6}$$

where $L_{\text{eff}} = \frac{1-e^{-\alpha_{f,i}z}}{\alpha_{f,i}}$ and $\tilde{L}_{\text{eff}} = \frac{e^{-\alpha_{b,i}(L-z)}-e^{-\alpha_{b,i}L}}{\alpha_{b,i}}$, and $A(z)$, $B(f)$ arbitrary functions which their values determined by requiring that $P(z=0,f) = P(0,f)$, which immediately implies that $e^{B(f)} = P(0,f)$, and, by requiring $\int P(z,f)\,df = P(z)$, the value of $e^{A(z)}$ is obtained. The evolution of the power $P(z)$ is assumed to be modelled as $P(z) = P_{total}e^{-\alpha_i z}$, where P_{total} is the sum of WDM channel and pump powers. This is not strictly true as a power gain at the end of the fibre is expected because of the presence of BW pumps. However, in addition to facilitating the derivation of the closed-form expression, this assumption is also overcome by the wavelength-dependent fitting parameters $\alpha_{b,i}$ and $C_{b,i}$, which are responsible for giving gains at the end of the fibre. Thus, Eq. (D.6) is written as

$$\rho(z,f) = \frac{P(z,f)}{P(0,f)} = \frac{P_{total}e^{-\alpha_i z}e^{-(C_{f,i}P_f L_{\text{eff}}+C_{b,i}P_b\tilde{L}_{\text{eff}})(f-\hat{f})}}{\int G_{\text{Tx}}(\nu)e^{-(C_{f,i}P_f L_{\text{eff}}+C_{b,i}P_b\tilde{L}_{\text{eff}})\nu}d\nu}, \tag{D.7}$$

where $G_{Tx}(f)$ is the input signal spectra including the WDM channels and the pumps and P_{total} is the sum of its launch power. Moreover, the coefficient α is also considered a wavelength-dependent loss α_i. Let $x_i = C_{f,i}P_f L_{\text{eff}} + C_{b,i}P_b\tilde{L}_{\text{eff}}$. By assuming that the input power $G_{Tx}(f)$ is uniformly distributed over the optical bandwidth B with power P_{total} it is possible to write,

$$\int G_{\text{Tx}}(\nu)e^{-x_i\nu}d\nu = \frac{2P_{total}\sinh\left(\frac{x_iB}{2}\right)}{x_iB}. \tag{D.8}$$

Replacing Eq.(D.8) in Eq.(D.7) leads to

$$\rho(z,f) = e^{-\alpha_i z}\frac{x_iBe^{-x_i(f-\hat{f})}}{2\sinh\left(\frac{xB}{2}\right)}. \tag{D.9}$$

Finally, by expanding Eq. (D.9) using a 1st order Taylor approximation around the point $x_i = 0$, yields

$$\rho(z,f) = e^{-\alpha_i z}[1-x(f-\hat{f})], \tag{D.10}$$

and setting $f = f_i$, Eq. (4.1) is obtained concluding the proof.

In the derivation of Eq. (D.10), 5 wavelength-dependent coefficients are introduced, namely, α_i, $\alpha_{f,i}$, $\alpha_{b,i}$, $C_{f,i}$ and $C_{b,i}$. These coefficients are chosen to overcome the restrictive assumptions used to derive Eq. (D.10) and to enable a simplified derivation of the closed-form expression in the following appendices. The restrictive assumptions overcome by the aforementioned fitting parameters are: the

constant attenuation α for all the channels; the energy that is lost whenever a high-frequency photon is transformed into a low-frequency photon; the triangular approximation of the Raman spectrum; the different spectrum locations of FW pumps, BW pumps and channels through a new central frequency of the spectrum $\hat{f}$ and the joint consideration of the FW amplification and ISRS effect; the power evolution along the distance $P(z) = P_{total}e^{-\alpha_i z}$; the spectrally uniform input power profile $G_{Tx}(f)$; and the 1st order Taylor approximation.

Appendix E

Derivation of Eq. (4.2)

This appendix shows the derivation of Eq. (4.2). The derivation was peer-reviewed and published in [P3]. The derivation consists of finding a closed-form expression for the link function in the presence of RA given by Eq. (3.3).

Let $x_i(\zeta) = C_{f,i}P_f L_{\text{eff}} + C_{b,i}P_b \tilde{L}_{\text{eff}}$, $\tau_i(\zeta) = 1 - x_i(\zeta)(f_i - \hat{f})$ with $L_{\text{eff}}(\zeta) = \frac{1-e^{-\alpha_{f,i}\zeta}}{\alpha_{f,i}}$ and $\tilde{L}_{\text{eff}}(\zeta) = \frac{e^{-\alpha_{b,i}(L-\zeta)} - e^{-\alpha_{b,i}L}}{\alpha_{b,i}}$. The first step is to insert Eq. (4.1) in Eq. (3.3) and use the approximation in Eq. (D.8) yielding

$$\mu\left(f_1, f_2, f_i\right) = \left| \int_0^L d\zeta \; e^{-\alpha_i \zeta} \frac{x_i B e^{-x_i(f_1+f_2-f_i-\hat{f})}}{2\sinh\left(\frac{x_i B}{2}\right)} e^{j\phi(f_1,f_2,f_i)\zeta} \right|^2 . \tag{E.1}$$

Now, the link function for the XPM contribution in Eq. (3.1), i.e., $\mu\left(f_1 + f_i, f_2 + f_k, f_i\right)$ is considered (the derivation for the link function for SPM is analogous and one simply needs to replace $f_k = f_i$ and the indices $k = i$). Assuming that the frequency separation between channels k and i ($\Delta f = f_k - f_i$) is much larger than half of the bandwidth of channel k ($|\Delta f| \gg \frac{B_k}{2}$), yields to $f_2 + \Delta f \approx \Delta f$. Additionally, the signal power profile is assumed to be constant over the channel bandwidth (see Appendices in [35] for additional details). Then, using the 1 $^{\text{st}}$ order Taylor approximation shown in Eq. (D.10), yields to

$$\mu\left(f_1 + f_i, f_2 + f_k, f_i\right) = \left| \int_0^L d\zeta \; e^{-\alpha_k \zeta} \tau_k(\zeta) e^{j\phi(f_1+f_i,f_2+f_k,f_i)\zeta} \right|^2 . \tag{E.2}$$

The term $\tau_k(\zeta)$ can be written as

$$\tau_k(\zeta) = 1 - \left[\left(\frac{C_{f,k}P_f}{\alpha_{f,k}} \right) \left(1 - e^{-\alpha_{f,k}\zeta}\right) + \left(\frac{C_{b,k}P_b}{\alpha_{b,k}} \right) e^{-\alpha_{b,k}L} \left(e^{\alpha_{b,k}\zeta} - 1\right) \right] (f_k - \hat{f}). \tag{E.3}$$

Let $T_{f,k} = \frac{-P_f C_{f,k}(f_k - \hat{f})}{\alpha_{f,k}}$, $T_{b,k} = \frac{-P_b C_{b,k}(f_k - \hat{f})}{\alpha_{b,k}}$, $T_k = 1 + T_{f,k} - T_{b,k}e^{-\alpha_{b,k}L}$. Thus, the term $\tau_k(\zeta)$ is written as

$$\tau_k(\zeta) = T_k \left[1 - \frac{T_{f,k}}{T_k} e^{-\alpha_{f,k}\zeta} + \frac{T_{b,k}}{T_k} e^{-\alpha_{b,k}L} e^{\alpha_{b,k}\zeta} \right]. \tag{E.4}$$

Eq. (E.4) can be conveniently rewritten in terms of a summation using identity (H.2), which will facilitate all the mathematical derivations,

$$\tau_k(\zeta) = T_k \sum_{0\leq l_1+l_2\leq 1} \left(\frac{-T_{f,k}}{T_k}\right)^{l_1} \left(\frac{T_{b,k}}{T_k}\right)^{l_2} e^{-(l_1\alpha_{f,k}\zeta + l_2\alpha_{b,k}L - l_2\alpha_{b,k}\zeta)}. \tag{E.5}$$

Now, defining

$$\Upsilon_k = T_k \left(\frac{-T_{f,k}}{T_k}\right)^{l_1} \left(\frac{T_{b,k}}{T_k}\right)^{l_2}, \tag{E.6}$$

Eq. (E.5) is written as

$$\tau_k(\zeta) = \sum_{0\leq l_1+l_2\leq 1} \Upsilon_k e^{-(l_1\alpha_{f,k}\zeta + l_2\alpha_{b,k}L - l_2\alpha_{b,k}\zeta)}. \tag{E.7}$$

Note that Υ_k is a variable which depends on the indices of the summation. Now, inserting Eq. (E.7) in Eq. (E.1), yields to

$$\mu\left(f_1+f_i, f_2+f_k, f_i\right) = \left| \sum_{0\leq l_1+l_2\leq 1} \Upsilon_k \int_0^L d\zeta\, e^{-(\alpha_k\zeta + l_1\alpha_{f,k}\zeta + l_2\alpha_{b,k}L - l_2\alpha_{b,k}\zeta) + j\phi\zeta} \right|^2, \tag{E.8}$$

and solving the integral in Eq. (E.8) yields to

$$\mu\left(f_1+f_i, f_2+f_k, f_i\right) = \left| \sum_{0\leq l_1+l_2\leq 1} \Upsilon_k \frac{e^{-(\alpha_k + l_1\alpha_{f,k})L + j\phi L} - e^{-l_2\alpha_{b,k}L}}{-(\alpha_k + l_1\alpha_{f,k} - l_2\alpha_{b,k}) + j\phi} \right|^2. \tag{E.9}$$

Now, let define $\alpha_{l,k} = \alpha_k + l_1\alpha_{f,k} - l_2\alpha_{b,k}$, $\kappa_{f,k} = e^{-(\alpha_k + l_1\alpha_{f,k})L}$ and $\kappa_{b,k} = e^{-l_2\alpha_{b,k}L}$. Eq. (E.9) can then be written as

$$\mu\left(f_1+f_i, f_2+f_k, f_i\right) = \left| \sum_{0\leq l_1+l_2\leq 1} \Upsilon_k \frac{\kappa_{f,k}e^{j\phi L} - \kappa_{b,k}}{-\alpha_{l,k} + j\phi} \right|^2. \tag{E.10}$$

The last step of the derivation is to calculate the modulus of Eq. (E.10). Using the identity (H.3), Eq. (E.10) is written as

$$\mu\left(f_1+f_i, f_2+f_k, f_i\right) = \left(\sum_{0\leq l_1+l_2\leq 1} \Upsilon_k \frac{\kappa_{f,k}e^{j\phi L} - \kappa_{b,k}}{-\alpha_{l,k} + j\phi} \right) \left(\sum_{0\leq l_1'+l_2'\leq 1} \Upsilon_k' \frac{\kappa_{f,k}'e^{-j\phi L} - \kappa_{b,k}'}{-\alpha_{l,k}' - j\phi} \right). \tag{E.11}$$

Finally, performing the multiplication in Eq. (E.11) together with the identity (H.4) and considering the channel $f_k = f_i$, Eq. (4.2) is obtained, concluding the proof.

Appendix F

Derivation of Eq. (4.4)

This appendix presents the derivation of Eq. (4.4). The derivation was peer-reviewed and published in [P3]. The derivation consists of finding an analytical approximation of the integral form Eq. (3.1) which models the nonlinear interference caused on channel i by a single interfering channel k.

The phase mismatch term in Eq. (3.3) is firstly approximated. For the XPM contribution, let $\Delta f = f_k - f_i$ be the frequency separation between channels k and i - here the pumps are also included as additional indices k. Assuming that frequency separation is much larger than half of the bandwidth of channel k ($|\Delta f| \gg \frac{B_k}{2}$), yields to $f_2 + \Delta f \approx \Delta f$. Additionally, the dispersion slope β_3 is assumed to be constant over the channel bandwidth. Thus, the phase mismatch term can be approximated as [35, Eq. (15)],

$$\begin{aligned}
&\phi(f_1 + f_i, f_2 + f_k, f_i) = \\
&= -4\pi^2 f_1 \Delta f \left[\beta_2 + \pi\beta_3(f_1 + f_2 + f_i + f_k)\right] \approx \\
&\approx -4\pi^2 (f_k - f_i) \left[\beta_2 + \pi\beta_3(f_i + f_k)\right] f_1 = \\
&= \phi_{i,k} f_1,
\end{aligned} \tag{F.1}$$

with $\phi_{i,k} = -4\pi(f_k - f_i)\left[\beta_2 + \pi\beta_3(f_i + f_k)\right]$. The most impacted channels by this approximation are the ones near the COI. The error relative to this approximation is given by [35, Eq. (25)].

Now, Eq. (3.1) giving us the XPM contribution is considered. For notation brevity, the factor $\frac{32}{27}\frac{\gamma^2}{B_k^2}\left(\frac{P_k}{P_i}\right)^2$ is omitted. Also, the term $\Pi\left(\frac{f_1+f_2}{B_k}\right)$ is neglected - this is equivalent to approximating the integration domain of the GN model to a rectangle [27]. Because of the approximation in Eq. (F.1), ϕ no longer depends on f_2, and the double integral in Eq. (3.1) turns to be a single integral. Thus, inserting Eq. (4.2) in Eq. (3.1), three terms can be identified as follows

$$\eta_{\text{XPM}}^{(k)}(f_i) = \sum_{\substack{0\le l_1+l_2\le 1\\ 0\le l_1'+l_2'\le 1}} \Upsilon_k\Upsilon_k'[(\kappa_{f,k}\kappa_{f,k}' + \kappa_{b,k}\kappa_{b,k}')\eta_{\text{XPM,main}}^{(k)}(f_i) - (\kappa_{f,k}\kappa_{b,k}' + \kappa_{b,k}\kappa_{f,k}')\eta_{\text{XPM,cos}}^{(k)}(f_i) + (\kappa_{f,k}\kappa_{b,k}' - \kappa_{b,k}\kappa_{f,k}')\eta_{\text{XPM,sin}}^{(k)}(f_i)], \tag{F.2}$$

with

$$\eta_{\text{XPM,main}}^{(k)}(f_i) = 2B_k \int_0^{\frac{B_i}{2}} df_1 \frac{\alpha_{l,k}\alpha_{l,k}' + \phi_{i,k}^2 f_1^2}{(\alpha_{l,k}^2 + \phi_{i,k}^2 f_1^2)(\alpha_{l,k}'^2 + \phi_{i,k}^2 f_1^2)}, \tag{F.3}$$

$$\eta_{\text{XPM,cos}}^{(k)}(f_i) = 2B_k \int_0^{\frac{B_i}{2}} df_1 \frac{\alpha_{l,k}\alpha_{l,k}' + \phi_{i,k}^2 f_1^2}{(\alpha_{l,k}^2 + \phi_{i,k}^2 f_1^2)(\alpha_{l,k}'^2 + \phi_{i,k}^2 f_1^2)} \cos(\phi_{i,k} L f_1) \tag{F.4}$$

and

$$\eta_{\text{XPM,sin}}^{(k)}(f_i) = 2B_k \int_0^{\frac{B_i}{2}} df_1 \frac{(\alpha_{l,k} - \alpha_{l,k}')\phi_{i,k} f_1}{(\alpha_{l,k}^2 + \phi_{i,k}^2 f_1^2)(\alpha_{l,k}'^2 + \phi_{i,k}^2 f_1^2)} \sin(\phi_{i,k} L f_1). \tag{F.5}$$

In the following, the above three integrals are solved. Eq. (F.3) is solving using identity (H.5) as

$$\eta_{\text{XPM,main}}^{(k)}(f_i) = \frac{2B_k}{\phi_{i,k}(\alpha_{l,k} + \alpha_{l,k}')} \left[\arctan\left(\frac{\phi_{i,k}B_i}{2\alpha_{l,k}}\right) + \arctan\left(\frac{\phi_{i,k}B_i}{2\alpha_{l,k}'}\right)\right]. \tag{F.6}$$

Eqs. (F.4) and (F.5) do not have analytical solutions in their current form. To derive an analytical solution of these equations, the channel bandwidth $B_i \to \infty$ and the integrals are solved using identities (H.8) and (H.9), yielding to

$$\eta_{\text{XPM,cos}}^{(k)}(f_i) = \frac{\pi B_k}{\phi_{i,k}(\alpha_{l,k} + \alpha_{l,k}')} \left[e^{-|\alpha_{l,k}L|} \operatorname{sign}\left(\frac{\phi_{i,k}}{\alpha_{l,k}}\right) + e^{-|\alpha_{l,k}'L|} \operatorname{sign}\left(\frac{\phi_{i,k}}{\alpha_{l,k}'}\right)\right] \tag{F.7}$$

and

$$\eta_{\text{XPM,sin}}^{(k)}(f_i) = \frac{\pi B_k}{\phi_{i,k}(\alpha_{l,k} + \alpha_{l,k}')} \left[e^{-|\alpha_{l,k}L|} \operatorname{sign}(-\phi_{i,k}) + e^{-|\alpha_{l,k}'L|} \operatorname{sign}(\phi_{i,k})\right]. \tag{F.8}$$

Finally, by inserting Eqs. (F.6), (F.7) and (F.8) in Eq. (F.2) together with the pre-factor $\frac{32}{27}\frac{\gamma^2}{B_k^2}\left(\frac{P_k}{P_i}\right)^2$, Eq. (4.4) is obtained concluding the proof.

Appendix G

Derivation of Eq. (4.5)

This appendix presents the derivation of Eq. (4.5). The derivation was peer-reviewed and published in [P3]. The derivation consists of finding an analytical approximation of the integral form in Eq. (3.2) which models the nonlinear interference caused by the channel i on itself.

The phase mismatch term is firstly approximated. To that end, the dispersion slope β_3 is assumed to be constant over the channel bandwidth. Thus, the phase mismatch term can be approximated as

$$\begin{aligned}
&\phi(f_1+f_i, f_2+f_i, f_i) = \\
&= -4\pi^2 f_1 f_2 \left[\beta_2 + \pi\beta_3(f_1+f_2-2f_i)\right] \approx \\
&\approx -4\pi^2 f_1 f_2 (\beta_2 + 2\pi\beta_3 f_i) = \\
&= \phi_i f_1 f_2,
\end{aligned} \tag{G.1}$$

with $\phi_i = -4\pi^2(\beta_2 + 2\pi\beta_3 f_i)$.

Now, using Eq. (3.2) together with Eqs. (3.1) and (4.2) with $k=i$, and omitting the pre-factor of $\frac{16}{27}\frac{\gamma^2}{B_i^2}$, yields to

$$\begin{aligned}
\eta_{\text{SPM}}(f_i) = \sum_{\substack{0\le l_1+l_2\le 1 \\ 0\le l_1'+l_2'\le 1}} \Upsilon_i \Upsilon_i' \Big[&(\kappa_{f,i}\kappa'_{f,i} + \kappa_{b,i}\kappa'_{b,i})\eta_{\text{SPM,main}}(f_i) - \\
&-(\kappa_{f,i}\kappa'_{b,i} + \kappa_{b,i}\kappa'_{f,i})\eta_{\text{SPM,cos}}(f_i) + (\kappa_{f,i}\kappa'_{b,i} - \kappa_{b,i}\kappa'_{f,i})\eta_{\text{SPM,sin}}(f_i) \Big],
\end{aligned} \tag{G.2}$$

where $\eta_{\text{SPM}}(f_i)$, $\eta_{\text{SPM,cos}}(f_i)$ and $\eta_{\text{SPM,sin}}(f_i)$ are given respectively by

$$\eta_{\text{SPM,main}}(f_i) = \int_{-\frac{B_i}{2}}^{\frac{B_i}{2}} df_1 \int_{-\frac{B_i}{2}}^{\frac{B_i}{2}} df_2 \frac{\alpha_{l,i}\alpha'_{l,i} + \phi_i^2 f_1^2 f_2^2}{(\alpha_{l,i}^2 + \phi_i^2 f_1^2 f_2^2)(\alpha_{l,i}'^2 + \phi_i^2 f_1^2 f_2^2)}, \tag{G.3}$$

$$\eta_{\text{SPM,cos}}(f_i) = \int_{-\frac{B_i}{2}}^{\frac{B_i}{2}} df_1 \int_{-\frac{B_i}{2}}^{\frac{B_i}{2}} df_2 \frac{\alpha_{l,i}\alpha'_{l,i} + \phi_i^2 f_1^2 f_2^2}{(\alpha_{l,i}^2 + \phi_i^2 f_1^2 f_2^2)(\alpha_{l,i}'^2 + \phi_i^2 f_1^2 f_2^2)} \cos(\phi_i L f_1 f_2) \tag{G.4}$$

and

$$\eta_{\text{SPM,sin}}(f_i) = \int_{-\frac{B_i}{2}}^{\frac{B_i}{2}} df_1 \int_{-\frac{B_i}{2}}^{\frac{B_i}{2}} df_2 \frac{(\alpha_{l,i} - \alpha'_{l,i})\phi_i f_1 f_2}{(\alpha_{l,i}^2 + \phi_i^2 f_1^2 f_2^2)(\alpha_{l,i}'^2 + \phi_i^2 f_1^2 f_2^2)} \sin(\phi_i L f_1 f_2). \quad \text{(G.5)}$$

Note that, similar to Appendix F, the term $\Pi\left(\frac{f_1+f_2}{B_i}\right)$ is neglected.

In the following, the three integrals above are solved. The integral in Eq. (G.3) is rewritten in polar coordinates (r, φ) as

$$\eta_{\text{SPM,main}}(f_i) \approx 4 \int_0^{\sqrt{\frac{3}{\pi}}\frac{B_i}{2}} dr \int_0^{\frac{\pi}{2}} d\varphi \, \frac{r\left[\alpha_{l,i}\alpha'_{l,i} + \frac{\phi_i^2}{4}(r^4 \sin^2(\varphi))\right]}{\left[\alpha_{l,i}^2 + \frac{\phi_i^2}{4}(r^4 \sin^2(\varphi))\right]\left[\alpha_{l,i}'^2 + \frac{\phi_i^2}{4}(r^4 \sin^2(\varphi))\right]}, \quad \text{(G.6)}$$

where it was used the relations $f_1 = r\cos(\varphi/2)$, $f_2 = r\sin(\varphi/2)$ and $\sin(\varphi/2)\cos(\varphi/2) = \frac{\sin(\varphi)}{2}$. Also, the integration domain of Eq. (3.2) was approximated by a circular domain such that the area of both domains is equal [35, Fig. 3]. This yields the variation of the radius in the outer integral as shown in Eq. (G.6). The inner integral in Eq. (G.6) can be solved using identity (H.6), yielding to

$$\eta_{\text{SPM,main}}(f_i) \approx 4 \int_0^{\sqrt{\frac{3}{\pi}}\frac{B_i}{2}} dr \frac{r\pi}{\alpha_{l,i} + \alpha'_{l,i}} \left[\frac{1}{\sqrt{4\alpha_{l,i}^2 + \phi_i^2 r^4}} + \frac{1}{\sqrt{4\alpha_{l,i}'^2 + \phi_i^2 r^4}}\right]. \quad \text{(G.7)}$$

This integral can be rewritten as

$$\eta_{\text{SPM,main}}(f_i) = \frac{2\pi}{\alpha_{l,i} + \alpha'_{l,i}} \int_0^{\sqrt{\frac{3}{\pi}}\frac{B_i}{2}} dr \left[\frac{r}{\alpha_{l,i}\sqrt{1 + \frac{\phi_i^2 r^4}{4\alpha_{l,i}^2}}} + \frac{r}{\alpha'_{l,i}\sqrt{1 + \frac{\phi_i^2 r^4}{4\alpha_{l,i}'^2}}}\right]. \quad \text{(G.8)}$$

The integral in Eq. (G.8) is solved using identity (H.7) as

$$\eta_{\text{SPM,main}}(f_i) = \frac{2\pi}{\phi_i(\alpha_{l,i} + \alpha'_{l,i})} \left[\operatorname{asinh}\left(\frac{3\phi_i B_i^2}{8\pi\alpha_{l,i}}\right) + \operatorname{asinh}\left(\frac{3\phi_i B_i^2}{8\pi\alpha'_{l,i}}\right)\right]. \quad \text{(G.9)}$$

To solve the integrals in Eqs. (G.4) and (G.5), a similar approach as in [105] is used. The integrals are converted to hyperbolic coordinates using the relations $\nu_1 = \sqrt{f_1 f_2}$, $\nu_2 = -\frac{1}{2}\ln\left(\frac{f_1}{f_2}\right)$, $f_1 = \nu_1 e^{\nu_2}$ and $f_2 = \nu_1 e^{-\nu_2}$ [27, Sec. VIII-A]; this change of coordinates yields a one-dimensional integral in ν_1. The change of variable $\nu = \nu_1^2$ [105] is also

used to rewrite Eqs. (G.4) and (G.5) as

$$\eta_{\text{SPM,cos}}(f_i) = 8\int_0^{\frac{B_i}{2}} d\nu \ln\left(\frac{B_i}{2\sqrt{\nu}}\right) \frac{\alpha_{l,i}\alpha'_{l,i} + \phi_i^2\nu^2}{(\alpha_{l,i}^2 + \phi_i^2\nu^2)(\alpha_{l,i}'^2 + \phi_i^2\nu^2)} \cos(\phi_i L\nu) \tag{G.10}$$

and

$$\eta_{\text{SPM,sin}}(f_i) = 8\int_0^{\frac{B_i}{2}} d\nu \ln\left(\frac{B_i}{2\sqrt{\nu}}\right) \frac{(\alpha_{l,i} - \alpha'_{l,i})\phi_i\nu}{(\alpha_{l,i}^2 + \phi_i^2\nu^2)(\alpha_{l,i}'^2 + \phi_i^2\nu^2)} \sin(\phi_i L\nu). \tag{G.11}$$

The integrals in Eqs. (G.10) and (G.11) do not have analytical solutions in their current form. In order to obtain an integral that yields an analytical solution the logarithm functions are evaluated in the point $\nu = \frac{\pi}{2\phi_i L}$, where this point was chosen such that the cosine function achieves its minima and the sine function achieves its maxima. This yields to

$$\eta_{\text{SPM,cos}}(f_i) = 8\ln\left(\sqrt{\frac{\phi_i L}{2\pi}}B_i\right)\int_0^{\frac{B_i}{2}} d\nu \frac{\alpha_{l,i}\alpha'_{l,i} + \phi_i^2\nu^2}{(\alpha_{l,i}^2 + \phi_i^2\nu^2)(\alpha_{l,i}'^2 + \phi_i^2\nu^2)} \cos(\phi_i L\nu) \tag{G.12}$$

and

$$\eta_{\text{SPM,sin}}(f_i) = 8\ln\left(\sqrt{\frac{\phi_i L}{2\pi}}B_i\right)\int_0^{\frac{B_i}{2}} d\nu \frac{(\alpha_{l,i} - \alpha'_{l,i})\phi_i\nu}{(\alpha_{l,i}^2 + \phi_i^2\nu^2)(\alpha_{l,i}'^2 + \phi_i^2\nu^2)} \sin(\phi_i L\nu). \tag{G.13}$$

The integrals in Eqs. (G.12) and (G.13) can now be solved similar to Appendix F, i.e., by letting $B_i \to \infty$. This yields to

$$\eta_{\text{SPM,cos}}(f_i) = 4\pi\ln\left(\sqrt{\frac{\phi_i L}{2\pi}}B_i\right)\left[e^{-|\alpha_{l,i}L|}\operatorname{sign}\left(\frac{\phi_i}{\alpha_{l,i}}\right) + e^{-|\alpha'_{l,i}L|}\operatorname{sign}\left(\frac{\phi_i}{\alpha'_{l,i}}\right)\right] \tag{G.14}$$

and

$$\eta_{\text{SPM,sin}}(f_i) = 4\pi\ln\left(\sqrt{\frac{\phi_i L}{2\pi}}B_i\right)\left[e^{-|\alpha_{l,i}L|}\operatorname{sign}\left(-\phi_i\right) + e^{-|\alpha'_{l,i}L|}\operatorname{sign}\left(\phi_i\right)\right]. \tag{G.15}$$

Finally, by inserting Eqs. (G.9), (G.14) and (G.15) in Eq. (G.2) together with the prefactor of $\frac{16}{27}\frac{\gamma^2}{B_i^2}$, Eq. (4.5) is obtained concluding the proof.

Appendix H

Mathematical identities

$$(x+y)^i = \sum_{0\le l\le i} \frac{i!}{l!(i-l)!} x^l y^{i-l}. \tag{H.1}$$

$$(x+y+z)^i = \sum_{0\le 1_1+1_2\le i} \frac{i!}{l_1!l_2!(i-l_1-1_2)!} x^{l_1} y^{l_2} z^{i-l_1-l_2}. \tag{H.2}$$

$$|z_k|^2 = \Re(z_k \cdot \overline{z}_k) = z_k \cdot \overline{z}_k. \tag{H.3}$$

$$z_i \cdot \overline{z}_j + z_j \cdot \overline{z}_i = 2\Re(z_i \cdot \overline{z}_j),\ j < i. \tag{H.4}$$

$$\int_0^x d\xi\ \frac{ab + c^2\xi^2}{(a^2 + c^2\xi^2)(b^2 + c^2\xi^2)} = \frac{1}{c(a+b)} \left[\arctan\left(\frac{cx}{a}\right) + \arctan\left(\frac{cx}{b}\right)\right]. \tag{H.5}$$

$$\int_0^{\frac{\pi}{2}} d\xi\ \frac{ab + c^2\sin^2\xi}{[a^2 + c^2\sin^2\xi][b^2 + c^2\sin^2\xi]} = \frac{\pi}{2(a+b)} \left(\frac{1}{\sqrt{a^2+c^2}} + \frac{1}{\sqrt{b^2+c^2}}\right). \tag{H.6}$$

$$\int_0^x d\xi\ \frac{\xi}{\sqrt{1 + a^2\xi^4}} = \frac{1}{2a} \operatorname{asinh}(ax^2). \tag{H.7}$$

$$\int_0^\infty d\xi\ \frac{ab + c^2\xi^2}{(a^2 + c^2\xi^2)(b^2 + c^2\xi^2)} \cos(c\xi L) = \frac{\pi}{2} \frac{e^{-|aL|}\operatorname{sign}(c/a) + e^{-|bL|}\operatorname{sign}(c/b)}{c(a+b)}. \tag{H.8}$$

$$\int_0^\infty d\xi \, \frac{(a-b)c\xi}{(a^2+c^2\xi^2)(b^2+c^2\xi^2)} \sin(c\xi L) = \frac{\pi}{2} \frac{e^{-|aL|}\,\mathrm{sign}(-c) + e^{-|bL|}\,\mathrm{sign}(c)}{c(a+b)}. \quad \text{(H.9)}$$